

Hee-Gweon Woo

Hong Li

*Editors*

# Advanced Functional Materials



ZHEJIANG UNIVERSITY PRESS

浙江大学出版社



Springer

Hee-Gweon Woo  
Hong Li

**Advanced Functional Materials**



Hee-Gweon Woo  
Hong Li

# Advanced Functional Materials

With 109 figures

 ZHEJIANG UNIVERSITY PRESS  
浙江大学出版社

 Springer

*Authors*

Prof. Hee-Gweon Woo  
Chonnam National University  
500-757, the Republic of Korea  
E-mail: hgwoo@chonnam.ac.kr

Prof. Hong Li  
Key laboratory of Functional Polymer Materials  
of Education Ministry, Institute of Polymer  
Chemistry, Nankai University  
300071, Tianjin, P. R. China  
E-mail: hongli@nankai.edu.cn

ISBN 978-7-308-08166-5  
Zhejiang University Press, Hangzhou

ISBN 978-3-642-19076-6 e-ISBN 978-3-642-19077-3  
Springer Heidelberg Dordrecht London New York

Library of Congress Control Number: 2011920982

© Zhejiang University Press, Hangzhou and Springer-Verlag Berlin Heidelberg 2011

This work is subject to copyright. All rights are reserved, whether the whole or part of the material is concerned, specifically the rights of translation, reprinting, reuse of illustrations, recitation, broadcasting, reproduction on microfilm or in any other way, and storage in data banks. Duplication of this publication or parts thereof is permitted only under the provisions of the German Copyright Law of September 9, 1965, in its current version, and permission for use must always be obtained from Springer. Violations are liable to prosecution under the German Copyright Law.

The use of general descriptive names, registered names, trademarks, etc. in this publication does not imply, even in the absence of a specific statement, that such names are exempt from the relevant protective laws and regulations and therefore free for general use.

Printed on acid-free paper

Springer is a part of Springer Science+Business Media ([www.springer.com](http://www.springer.com))

---

## Preface

Humankind has achieved dramatic advancement of technology over the Stone Age, the Bronze Age, the Iron Age, the Plastic Age, and the Advanced Materials Age since their advent. Now we are living in the world of advanced materials including plastics, ceramics, renewable energy, sensors, etc. Literally we cannot live in daily life without using millions of products produced from the advanced technology. The developing rate of new technology is very fast. Global community really needs it for prosperity promotion.

There are great interests in six advanced technologies: nano-technology, bio-based technology, sensor technology, energy-based technology, high performance material-based technology, and fuel cell technology. During the past decades major progress in the synthesis, characterization, and applications of functional polymers has been accomplished along with the recent development of nanobioscience and environment technology. This monograph titled *Advanced Functional Materials* contains six chapters spanning from polymers to ceramics, sensor, and to fuel cell: high performance organic polymers, biodegradable organic polymers, inorganic polymers, ceramic composite formation, sensor, and fuel cell.

Chapter 1 deals with the synthesis and applications of high performance polymers including polyimides and other polymers. The high performance polymers are engineered for use in especially harsh environments with the virtue of a long life span, ease of maintenance and low cost of production. Standard common polymers (PE (polyethylene), PMMA (polymethyl methacrylate), PVC (polyvinyl chloride), etc.) have a thermal resistance below 100 °C and are less suitable for sliding/rolling surfaces. Examples of hard wearing high performance polymers, having a thermal resistance over 150 °C, are polyetheretherketon, polyethersulfon and polyimide. Engineering polymers are classified by a temperature resistance within 100 to 150 °C. The engineering polymers include polyamide, polycarbonate, polyoxymethylene, polyethylene terephthalate, ultra high molecular weight polyethylene, and polybutylene terephthalate. The authors hope to discuss polyimides with major emphasis since they are one of the most recent advanced materials of their kind while briefly describing other high performance organic polymers.

Chapter 2 discusses on the controlled synthesis of biodegradable organic polymers such as polylactic acid, polyglycolic acid and related copolymers. These polymers have found many significant applications in the field of biomedical science as drug-delivery carriers, resorbable sutures, artificial-tissue materials, and

so forth. The discussion is hence centered on the living and stereospecific or stereoselective ring-opening polymerization of lactides, particularly which uses low-toxic/non-toxic metal catalysts and metal-free organic catalysts/initiators to conduct the controlled polymerizations.

Chapter 3 describes the high functional inorganic polymers containing main group 13 – 16 elements in the polymer backbone chain. Polymers can be largely divided into two categories: organic polymers and inorganic polymers. Organic polymers tend to lose their advantageous material properties (light weight, flexibility, fabricability, elasticity, mechanical strength, conductivity, optoelectricity, etc.) in the presence of oxygen, ozone, corrosion, ultraviolet radiation or at extreme high/low temperatures. Nonetheless, most organic polymers used heavily and widely in modern daily life, hardly decompose in the natural environment and burn releasing toxic chemicals as well, creating serious environmental pollution. Furthermore, the availability of raw materials for organic polymers, whose backbone chains consist mainly of carbon atoms linked together or separated by heteroatoms, such as oxygen or nitrogen, is limited by the anticipated shortage of natural petroleum/coal resources. Therefore, research on the design, synthesis, characterization and applications of inorganic polymers, inorganic-organic hybrid polymers or organometallic polymers is needed to avoid these problems. Inorganic polymers have main group non-metallic or sub-metallic elements (Si, Ge, Sn, B, P, N, O, S, etc.), main group metals (Mg, Al, etc.) or transition metals (i.e., d-block or f-block elements) within the polymers. Main group metal-based and transition metal-containing inorganic polymers have been extensively reviewed by many authors and are not covered here because they are beyond the scope of this article, due to the limit of space and interest. Main group non-metallic or sub-metallic inorganic polymers are composed of mainly boron (polyboranes, polyborazines, polycarboranes, etc.), silicon/germanium/tin (polysilanes, polysilane-co-germane, polycarbosilanes, polysiloxanes, polysilathianes, polysilazanes, polygermanes, polystannanes, etc.), phosphorous (polyphosphazenes, etc.) and sulfur (polysulfur, polysulfur nitrides, etc.) atoms, which do not originate from petroleum/coal resources.

Chapter 4 covers the preparation of various ceramic composites using various hybrid preceramic polymeric precursors, including super-resistant Si-C-B-N, electrically conducting MoSi<sub>2</sub>/SiC, superhard Ti-B-N and highly thermally conducting Al-B-N nanocomposites, thermally insulating Al-Cr-phosphates. Moreover, some application examples of preceramic polymers are introduced to demonstrate their utility in structural ceramic materials as an alternative preparative route to the conventional powder sintering process, such as ceramic matrix composites and ceramic film. In addition, the authors summarize the recent development of porous SiC materials from templated preceramic polymers and the fabrication of small and complicated ceramic features using near net shape processing techniques, such as lithography.

Chapter 5 discusses chemical and biological sensors based on porous silicon nanomaterials. It was not until 1990, when L. T. Canham first reported efficient, tunable, room temperature luminescence in the visible range from porous silicon,

that interest in the field grew exponentially. From this point on, a large number of academic and industrial researchers from all over the world began to study the porous silicon pore structure, light emission mechanism, surface chemistry, and feasibility for optoelectronic applications. The many favorable characteristics and the vast interest in porous silicon have given rise to a variety of new applications, such as light emitting devices, multilayer structure, solar energy conversion, chemical and biological sensors, drug delivery application, ultrasound generators, microengineering, astrophysics, signal processing and nuclear science.

Chapter 6 covers a critical prospective on the recent advances in microbial fuel cell (MFC) with an emphasis on the performances of MFC, materials, operational factors and applications of MFCs in the future. The article includes the following: MFC designs, characterizations and performance, the recent advances in MFC configurations and performances, the microbial metabolism and parameters defining the performance of MFC, electricity producing bacterial communities, the primary mechanism for electron transfer of electricigens to electrodes, the characteristics of electrochemically active bacteria in a mediator-less system, microbial physiology and engineering approaches regarding Benthic Unattended Generators for powering remote-sensing or monitoring devices, the inherent constraints of MFCs and suggestions for MFC performance improvement, the anodic electron transfer mechanisms in electrochemically active bacteria, improved cathode reactions and the application of new electrode materials.

As matter of fact, this book is oriented to give general and specific knowledge to the readers working in the field of material science and engineering, not to the casual readers. Nonetheless we hope that the readers can expand their knowledge while enjoying the book with relaxing and fruitful mind. We left some space for the readers' imagination.

Finally, the editors of the book would like to appreciate their coworkers for the dedicated contribution described in the respective chapter. We should particularly thank Prof. Xiaojia Chen, vice president of Zhejiang University Press for inviting us to compile the book.

Hee-Gweon Woo  
Gwangju, the Republic of Korea

Hong Li  
Tianjin, P.R. China  
January, 2011





---

# Contents

<b>1 Polyimides and High Performance Organic Polymers.....</b>	<b>1</b>
1.1 Introduction.....	1
1.2 Aromatic Polyimides.....	2
1.2.1 Polyimides .....	3
1.2.2 Classification.....	4
1.2.3 Aromatic Polyimides.....	5
1.2.4 Synthesis of Aromatic Polyimides.....	6
1.2.5 Properties of Aromatic Polyimides.....	7
1.2.6 Applications for Aromatic Polyimides.....	8
1.3 Aliphatic Polyimides.....	9
1.3.1 Monomers for Fully Aliphatic Polyimides .....	10
1.3.2 Synthesis of Fully Aliphatic Polyimides.....	11
1.3.3 Structural Confirmation of Fully Aliphatic Polyimides.....	12
1.3.4 Properties of Fully Aliphatic Polyimides.....	14
1.4 Polyimides for Organic Light-Emitting Devices and Flexible Substrates.....	17
1.4.1 Semi-conducting Polyimides .....	17
1.4.2 Polyimides as Plastic Substrate for the Flexible OLED.....	19
1.5 Polyimide-Based Nanohybrids.....	20
1.6 Other General High Performance Polymers.....	22
1.6.1 Polyetheretherketon (PEEK) .....	22
1.6.2 Polysulphone (PSU) .....	23
1.6.3 Polysulfides.....	25
1.6.4 Polycarbonates (PC) .....	26
1.6.5 Polyamides (PA) .....	27
1.6.6 Poly(Butylene Terephthalate) (PBT) .....	29
1.6.7 Poly(Phenylene Oxides) .....	29
1.6.8 Polynorbornene (PNB) .....	30
1.7 Summary.....	31
References.....	32
<b>2 Advanced Biodegradable Organic Polymers.....</b>	<b>37</b>
2.1 Introduction.....	37
2.2 Synthesis of Biodegradable Polymers by Polycondensation.....	38
2.2.1 General Polycondensation Technique.....	39

2.2.2	Post Polycondensation Technique.....	40
2.2.3	Chain-Extension Technique.....	41
2.2.4	Enzyme-Catalyzed Polycondensation.....	42
2.3	Synthesis of Biodegradable Polymers by Ring-Opening Polymerization.....	42
2.3.1	Monomers.....	42
2.3.2	Polymerization with Metal Catalysts.....	43
2.3.3	Polymerization Using Metal-Free Organic Catalysts.....	55
2.3.4	Enzyme-Catalyzed Ring-Opening Polymerization.....	60
2.4	Concluding Remarks.....	61
	References.....	61
<b>3</b>	<b>High Functional Inorganic Polymers Containing Main Group 13 - 16 Elements in the Polymer Backbone Chain.....</b>	<b>65</b>
3.1	Introduction.....	65
3.2	Group 14 Inorganic Polymers: Polysilanes, Polygermanes, Polystannanes, and their Copolymers.....	66
3.2.1	Dehydrocatenation of Group 14 Hydrides to Polymers.....	67
3.2.2	Redistributive Catenation of Group 14 Hydrides to Polymers...77	
3.2.3	Exhaustive Hydrosilylation, Hydrogermylation and Hydrostannylation of Group 14 Hydrides on Vinyl Derivatives...85	
3.2.4	Formation of Polysilane-Metal Nanoparticle Composites.....	89
3.3	Group 13 Inorganic Polymers: Polyborazines.....	89
3.4	Group 15 Inorganic Polymers: Polyphosphazenes.....	91
3.5	Group 16 Inorganic Polymers: Polysulfur and Poly(sulfur nitride).....	92
3.6	Summary.....	93
	References.....	93
<b>4</b>	<b>Preparation and Applications of Ceramic Composite Phases from Inorganic Polymers.....</b>	<b>103</b>
4.1	Introduction.....	103
4.2	Preparation of Composite Phases from Inorganic Polymers.....	105
4.2.1	Si-C-B-N Ceramics via Hydroboration from Borazine Derivatives and Trivinylcyclotrisilazane.....	105
4.2.2	SiC/MoSi <sub>2</sub> Ceramic Composites Prepared by Polymer Pyrolysis.....	111
4.2.3	Ti-B-N Composite from a Hybrid Precursor of Polyborazine and TiH <sub>2</sub> .....	117
4.2.4	Al-B-N Nanocomposite from Polyborazine and Al Metal...120	
4.2.5	Al-Cr-Phosphates as Low Temperature Curable Binders...124	
4.3	Applications of Preceramic Polymers.....	130
4.3.1	Preparation of Carbon Fiber Reinforced BN Matrix Composite...130	
4.3.2	BN Film by Spin-Coating Process of a Polymeric Precursor...137	
4.3.3	Fabrication of SiC-Based Ceramic Microstructures.....	140
4.4	Summary.....	150
	References.....	152

**5 Chemical and Biological Sensors Based on Porous Silicon Nanomaterials.....157**

5.1 Introduction.....157

5.2 Interferometric Sensors Based on Porous Silicon Nanomaterials.....158

    5.2.1 Fabrication of Porous Silicon.....158

    5.2.2 Chemical Sensing Application of Porous Silicon.....173

    5.2.3 Biological Sensing Application of Porous Silicon.....183

5.3 Summary.....189

References.....190

**6 Microbial Fuel Cells as the Real Source of Sustainable Energy.....195**

6.1 Introduction.....195

6.2 Configurations and Designs of Microbial Fuel Cells.....196

    6.2.1 MFC Components.....196

    6.2.2 Two-Chambered MFCs.....197

    6.2.3 Single-Chambered MFCs.....198

    6.2.4 Up-Flow Mode MFCs.....199

    6.2.5 Stacked MFCs.....200

6.3 Electrode Materials and Catalysts.....201

    6.3.1 Electrode Materials.....201

    6.3.2 Cathodic Catalysts.....202

6.4 Performance of Microbial Fuel Cells.....204

    6.4.1 Parameters Defining the Performance of MFCs.....204

    6.4.2 Effects of Conditions When Operating MFCs.....206

6.5 Metabolism in Microbial Fuel Cells.....212

6.6 Applications.....213

6.7 Summary.....215

References.....215

**Index.....221**



---

# Polyimides and High Performance Organic Polymers

**Chang-Sik Ha\*, Anu Stella Mathews**

Department of Polymer Science and Engineering, Pusan National University,  
Pusan 609-735, the Republic of Korea

Tel.: +82-51-510-2407; Fax: +82-51-514-4331

\*E-mail: csha@pnu.edu

## 1.1 Introduction

The amazing scope of wartime applications accelerated the development and growth of polymers to meet the diverse needs of special materials in different fields of activity.<sup>[1,2]</sup> Polyurethanes were developed in 1937, polyepoxides in 1947 and acrylonitrile-butadiene-styrene (ABS) terpolymer in 1948.<sup>[3,4]</sup> The discovery of the Zeigler-Natta catalyst in the 1950s brought about the development of linear polyethylene and stereoregular polypropylene.<sup>[4]</sup> Thereafter, the emergence of polyacetal, polyethylene terephthalate, polycarbonate, and many new copolymers, was noted. Commercial requirements paved the way for the development of highly temperature-resistant materials, which include polyphenylene oxides, polysulphones, polyimides, poly(amide-imide)s and polybenzimidazoles. These high performance polymers to which standard metal engineering equations can be applied are widely commercialized now. Polymers with properties of strength, heat-resistance or flame-resistance or chemical-resistance that far exceed those of more conventional polymers are termed “High Performance Polymers”. They are capable of sustaining high loads and stresses and are dimensionally stable.<sup>[5-7]</sup>

For any applications, the prime importance is given to three factors: life span, maintenance and cost.<sup>[7]</sup> In this regard, high performance polymers are engineered for use in especially harsh environments with the virtue of a long life span, ease of

maintenance and low cost of production. These merits have accelerated the application of these polymers. Standard polymers have a thermal resistance  $<100\text{ }^{\circ}\text{C}$  and are less suitable for sliding/rolling surfaces. Examples of these polymers include high density polyethylene (HDPE), low density polyethylene (LDPE), poly(methyl methacrylate) (PMMA), and poly(vinyl chloride) (PVC). They have low melting points and therefore cannot operate at elevated temperature and the majority of these polymers decompose or readily oxidize at high temperatures. The current demand is for polymers which retain useful properties for a long period at higher temperature with high thermo-oxidative stability, i.e., they should withstand degraded properties over long periods at high temperature in the air. High performance polymers show high temperature-resistance and high mechanical strength. Examples of hard-wearing high performance polymers, having a thermal resistance  $>150\text{ }^{\circ}\text{C}$ , are polyetheretherketon (PEEK), polyethersulfon (PES) and polyimide (PI). Engineering polymers are classified by a temperature resistance within  $100\text{ to }150\text{ }^{\circ}\text{C}$ . The engineering polymers include polyamide (PA), polycarbonate (PC), polyoxymethylene (POM), poly(ethylene terephthalate) (PET), ultra high molecular weight polyethylene (UHMWPE), and poly(butylene terephthalate) (PBT). One basic factor which determines the stability is the strength of the bonds which join different groups in the backbone. For instance, a polymer chain with Si-O bonds would be more stable than one with C-C bonds, due to the higher bond energy of Si-O. A phenylene unit in the backbone also shows more stability than a chain with an alkenylene backbone owing to the stiffness and deformation-resistance of the phenylene ring. Based on the above arguments, several high performance polymers are synthesized and successfully applied. Firstly, we wish to discuss polyimides since they are one of the most recent advanced materials of their kind. Then we will briefly describe other high performance polymers.

A considerable amount of research work is being carried out into the development of high performance polymers and to improve their efficiency. The main stimulus has come from the development and characterization of new materials for space exploration. Construction of a spacecraft or a satellite, for instance, needs materials that can withstand high surface temperature, are light weight and have high dimensional stability. Modern military and civil aircraft use a high percentage of such polymers. Conventional materials like metals, glass and ceramics are being fast replaced. Polymers also find applications in the microelectronics and optoelectronics industries. In the next section we wish to discuss more advances of polyimides among the high performance polymers mentioned above.

## **1.2 Aromatic Polyimides**

In this section, we will introduce polyimides and their classification, as well as synthesis, properties and applications of aromatic polyimides.

### 1.2.1 Polyimides

Polyimides (PIs) are a new generation of polymers with inherently rigid chains and of high commercial importance.<sup>[8]</sup> PIs possess excellent thermal, mechanical and electrical properties and thus have found immense applications in many technologies, ranging from microelectronics to high temperature matrices and adhesives for gas separation membranes.<sup>[9-24]</sup> These materials are prepared by incorporating highly stable and rigid heterocyclic ring systems into the polymer chain. PIs are available for use as plastics, films, laminating resins, insulating coatings and high temperature structural adhesives. Thermal stability of polyimides is attributed to the presence of an inert imide ring and high interchain interaction, i.e., high cohesion among the polymer chains. A representative structure of a polyimide is shown in Fig. 1.1.

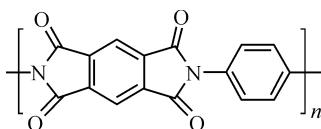


**Fig. 1.1.** Representative structure of aromatic polyimide

The first synthesis of a polyimide from 4-aminophthalic acid was performed by Bogert and Renshaw in 1908.<sup>[25]</sup> However, a high-molecular weight aromatic polyimide was first synthesized in 1955 by Edwards and Robinson.<sup>[26]</sup> Poly(4,4'-oxydiphenylene pyromellitimide) (PMDA-ODA PI), widely known as Kapton<sup>®</sup> which can remain stable in a wide range of temperatures from  $-269$  to  $400$  °C, was first commercialized in the early 1960s.<sup>[27]</sup> Kapton<sup>®</sup> film is used in, among other things, flexible printed circuits (flexible electronics) and spacesuits. Kapton<sup>®</sup> insulated wiring has been widely used in civil and military avionics (electrical wiring for aircraft) because of its very light weight compared to other insulator types, as well as possessing good insulating and temperature characteristics. The NASA Jet Propulsion Laboratory has considered Kapton<sup>®</sup> as a good plastic support for solar sails because of its long duration in the space environment.<sup>[28]</sup> Kapton<sup>®</sup> is also used to monitor the flux on X-ray sources. A number of PIs have been synthesized and investigated extensively in aspects of structure and property relationships and applications after the success with Kapton<sup>®</sup>.<sup>[29]</sup> PIs are known to be thermally stable due to their heterocyclic imide rings on the backbone, and the thermal stability is further significantly improved by incorporating aromatic rings on the backbone and/or side groups. In addition to such high thermal stability, the nature of the chemical structure consisting of rigid imide and aromatic rings always provides excellent mechanical and dielectric properties as well as high chemical resistance. Beyond these advantageous properties, a variety of functionalities (for example, photo reactivity, molecular recognition ability, nonlinear optical responsibility, light emitting ability, and so on) can be added into the backbone and/or side groups of PIs, depending on their application demands.<sup>[30-41]</sup>



Due to these advantageous properties as well as the functionalities, PIs have found diverse applications in the microelectronics, flat panel display, aerospace and chemical and environmental industries as flexible circuitry carriers, stress buffers, inter dielectric layers, passivation layers, liquid crystal alignment layers, varnishing resins, fibers, matrix materials, and gas and chemical separation membranes.<sup>[42-48]</sup>

## 1.2.2 Classification

According to the monomers from which polyimides are derived, they can be broadly classified as fully aromatic polyimides, semi-aromatic polyimides and fully aliphatic polyimides (Fig. 1.2).<sup>[8]</sup> Aromatic polyimides are derived from an aromatic dianhydride and diamine. Semi-aromatic ones contain any one of the monomer aromatics: i.e., either the dianhydride or diamine is aromatic and the other part is aliphatic. Finally, the third category consists of the polymers formed as a result of the combination of aliphatic dianhydride and diamine.

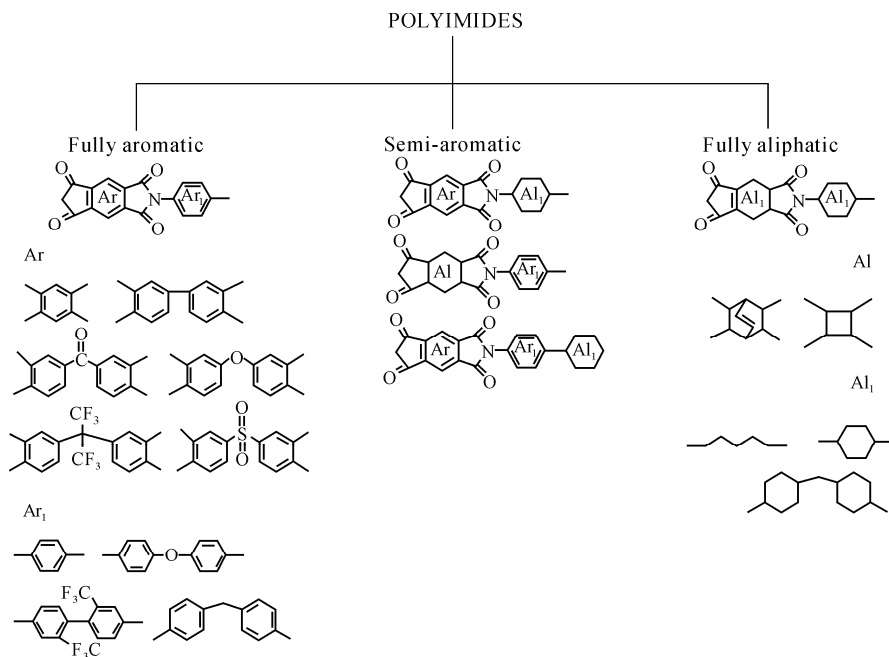


**Fig. 1.2.** Classification of polyimides into three broad categories, depending upon the chemical structure of the backbone (Adapted from Ref. 8. Copyright (2007), with permission from the Polymer Society of Korea)

### 1.2.3 Aromatic Polyimides

Aromatic polyimides (PIs) are typical of most commercial polyimides, such as Ultem from G.E. and DuPont's Kapton<sup>®</sup>. These polymers have such incredible mechanical and thermal properties that they are used in place of metals and glass in many high performance applications in the electronics, automotive, and even the aerospace industries. These properties come from strong intermolecular forces between the polymer chains. A polymer which contains a charge transfer complex consists of two different types of monomers, a donor and an acceptor (Fig. 1.3).<sup>[49]</sup> The donor has plenty of electrons to go around because of its nitrogen groups and the acceptor with its carbonyl group draws away its electron density. So the donor lends some of its electrons to the acceptor, holding them tightly together. Thus, the polymer chains will stack together like strips of paper, with donors and acceptors paired up due to the formation of a charge transfer complex between adjacent units in the polymer chain as shown in Fig. 1.3(b). This charge transfer complex holds the chains together very tightly, not allowing them to move around very much. When things cannot move around on the molecular level, they cannot move around in the whole material. This is the reason why polyimides are so robust. The charge transfer complex is so strong that it sometimes becomes necessary to make the polymer a little softer, leading it to be processable. Aromatic polyimides synthesized from only aromatic monomers are often insoluble in their fully imidized form, thus having a low processability. In addition, as most of the aromatic polyimides absorb visible light intensely, they cannot be used in areas where colorlessness is an important requirement. It is well known that the origin of coloration in aromatic polyimides is caused by the inter- and intra-molecular charge transfer (CT) interactions between the five membered ring of the imide group and the aromatic ring, as explained above in Fig. 1.3. The high dielectric constant also arising from these interactions is also a demerit of aromatic polyimides. Despite its excellent properties, low processability, high dielectric constant and light or dark yellow coloration hinders its successful application in optoelectric materials and high-speed multilayer printed wiring boards. Efforts to suppress the CT interactions have included the use of siloxane,<sup>[50]</sup> sulfonyl,<sup>[51]</sup> fluorinated<sup>[52]</sup> and aliphatic<sup>[53]</sup> moieties. Among these, aliphatic structures display a lower dielectric constant and higher transparencies which result from their lower molecular density and polarity and low probability of undergoing inter or intra-molecular charge transfer. Thus, incorporation of aliphatic units to enhance the desired properties was applied widely.

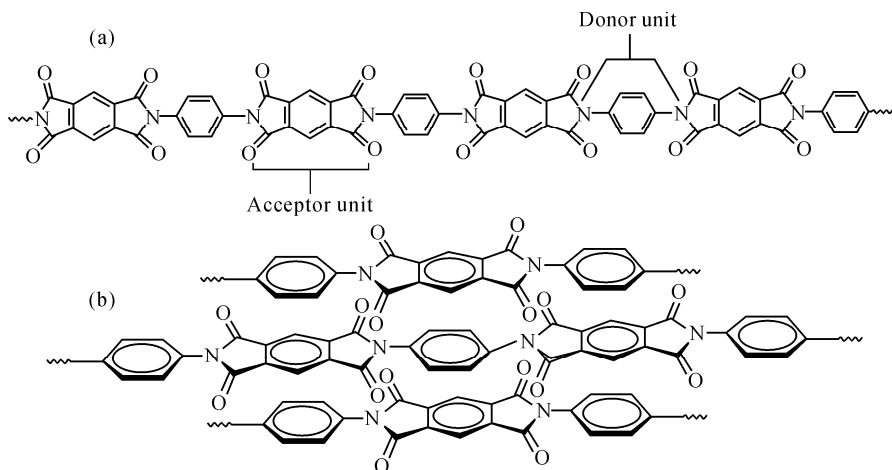
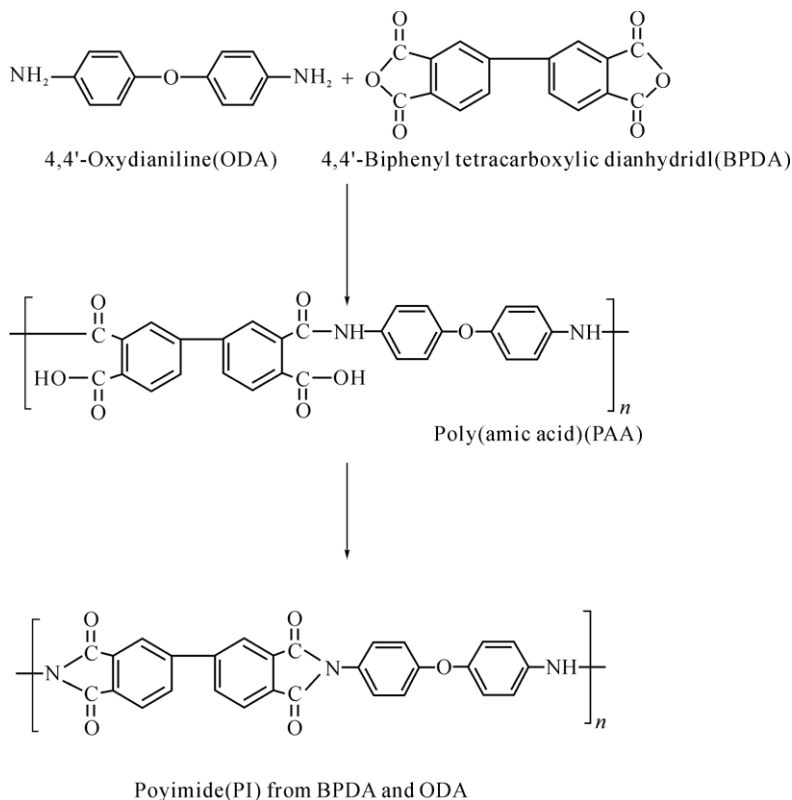


**Fig. 1.3.** Donor-acceptor system prevailing in PIs and the resulting interchain locking. (a) Nitrogen atoms having a higher electron density than the carbonyl groups lend some of their electrons to the acceptor while carbonyl groups draw electron density away from the acceptor unit; (b) Interchain interlocking of PI backbones. Polyimides may stack like this allowing the carbonyl of the acceptor on one chain to interact with the nitrogens of the donor on the adjacent chains (Modified from Ref. 49)

### 1.2.4 Synthesis of Aromatic Polyimides

Aromatic polyimides are generally prepared through a two-step procedure by the ring opening polyaddition of aromatic polyimides to aromatic tetracarboxylic dianhydrides in *N*-methyl pyrrolidone (NMP) or *N,N*-dimethyl acetamide (DMAc) solution giving soluble polyamic acid. The polyamic acid thus formed is imidized into polyimides by thermal cyclodehydration. The polyimides thus formed are insoluble in their fully imidized form. The multi-step process makes the materials applicable in the state of soluble polymeric intermediate. The schematic representation of two-step synthesis of the polyimide is given in Scheme 1.1.<sup>[22]</sup> Direct preparation of polyimides without the isolation of polyamic acid at elevated temperature is another route of synthesis. This is widely known as one step synthesis since it does not have an intermediate stage.



**Scheme 1.1.** Schematic representation of two-step synthesis of aromatic polyimides, where 3,3'-4,4'-biphenyl tetracarboxylic dianhydride (BPDA)-4,4'-oxydianiline (ODA) poly(amic acid) (PAA) precursor is thermally imidized to BPDA-ODA PI (Adapted from Ref. 22. Copyright (2003), with permission from Elsevier)

### 1.2.5 Properties of Aromatic Polyimides

Polyimide parts and laminates can serve continuously in air at 260 °C; the service temperature for intermittent exposure can range from cryogenic to as high as 482 °C. Glass-fiber reinforced versions retain over 70% of their flexural strength and modulus at 249 °C. Creep is almost nonexistent, even at high temperatures and deformation under load (28 MPa) is less than 0.05% at room temperature for 24 h.<sup>[49]</sup> These materials have good wear resistance and low coefficients of friction, both of which are further improved by polytetrafluoroethylene (PTFE) fillers. Self-lubricating parts containing graphite powders have flexural strengths above 69 MPa, which are considerably higher than those of typical thermoplastic bearing compounds. Electrical properties of PI moldings are outstanding over a wide range of temperature and humidity conditions. Polyimide parts are unaffected by

exposure to dilute acids, aromatic and aliphatic hydrocarbons, hydraulic fluids, JP-4 fuel and kerosene.<sup>[48]</sup> Polyimides are attacked, however, by dilute alkalis and concentrated inorganic acids. Polyimide abrasives maintain useful properties for over 12,000 h at 260 °C, 9,000 h at 302 °C, 500 h at 343 °C, and 100 h at 371 °C. Resistance of these abrasives to combined heat (to 302 °C) and salt water exposure is excellent. The basic properties of these polymers can be varied by choosing the diamine and dianhydride, incorporation of functional groups like fluorine, sulfur, silicon, oxygen, aliphatic chain, etc. Fluorination provides unique properties to polyimides, such as reduction of dielectric constants and refractive indices, improvement of the transparency in the visible and near IR region, lowering of glass transition temperature, change in reactivity of compounds (in particular, that of diamine), increase in free volume, decrease in water absorption, and rise in thermal decomposition temperature. This increases solubility, gas permeability, radiation-durability and thermal expansion coefficients.<sup>[54]</sup> On the other hand, increasing the importance of polyimides for gas-separation, microelectronics and optoelectronics applications has paved the way for the introduction of silicon moieties into the backbone of PIs, promoting a significant increase in permeability, perm-selectivity and adhesive ability.<sup>[55]</sup> Thus, more recently, silicon containing aromatic polymers has attracted much scientific and technological interest because of its superior permeability and adhesive ability between substrates and polyimides, together with low dielectric constant.<sup>[56]</sup> Polyimide-siloxanes (PISiOs), the segmented co-polymers containing siloxane segment along the intractable backbone chain of aromatic polyimides, maintain some of the excellent properties of PIs, e.g., high thermal stability and mechanical strength, and some of the desirable properties of siloxanes, such as ductility and adhesion as well as low moisture permeability. Superior solubility, even in organic solvents with low boiling point meliorate the processibility of fully imidized PISiOs by replacing a prolonged polymer curing step at elevated temperature with a baking procedure at a lower one, while maintaining the thermal and mechanical stability.<sup>[57]</sup> These excellent properties, imparted by fluorine and siloxane group, motivated researchers to incorporate them in aliphatic backbones and compare the variations they bring to the basic traits of these polyimides.

### ***1.2.6 Applications for Aromatic Polyimides***

When compared to most other organic or polymeric materials, polyimides exhibit an exceptional combination of thermal stability (>460 °C), mechanical toughness and chemical resistance. In addition, they have excellent dielectric properties. Because of their high degree of ductility and inherently low coefficient of thermal expansion (CTE), polyimides can be readily implemented into a variety of microelectronic applications. Multilayer thin and thick film applications on large silicon or ceramic substrates can be readily achieved.<sup>[54-57]</sup> Polyimide films are

frequently used as a “stress buffer” or protective overcoat for semiconductors. Polyimide stress buffers are typically 4 – 6 microns in thickness, and protect the delicate thin films of metal and oxides on the chip surface from damage during handling and from induced stress after encapsulation in plastic molding compound. Patterning is simple and straightforward. Because of the low defect density and robust plasma etch resistance inherent in polyimide films, a “single mask” process can be implemented, which permits the polyimide layer to function both as a stress buffer and as a dry etch mask for the underlying silicon nitride passivation layer.<sup>[50]</sup> In addition, polyimide layers have been readily used for flip chip bonding applications, including both C-4 and dual-layer bond pad redistribution (BPR) applications. Polyimides may also serve as an interlayer dielectric in both semiconductors and thin film multichip modules (MCM-D’s). The low dielectric constant, low stress, high modulus and inherent ductility of polyimide films make them well suited for these multiple layer applications. Other uses for polyimides include alignment and/or dielectric layers for displays, and as a structural layer in micromachining applications.<sup>[9-14]</sup> In the fabrication of microelectronic devices, polyimides are typically applied as a liquid on a substrate, and then thermally cured into a smooth, rigid, intractable polymeric film or structural layer. The film can be patterned using a lithographic (photographic) process in conjunction with liquid photoresists. “Photodefinable” polyimides are light-sensitive and readily patterned without the use of photoresists, further simplifying the fabrication process. The need for thermally stable membranes has raised the possibility of using polyimides with appropriate ion-conducting sites. However, it is well known that in order to obtain polymers that exhibit high selectivity and permeability, it is necessary to synthesize structures with stiff backbone chains and with chain packing so as to produce a very narrow free-volume distribution. In other words, it is necessary to generate polymeric molecular sieves. The high rigidity of polyimides, their suitable polarity and their high chemical resistance due to high thermal and chemical stability, plus the capability of forming hydrogen bonds, explain why these polymers can be used as membranes.

### 1.3 Aliphatic Polyimides

Although aromatic polyimides possess excellent thermal stability, chemical resistance, and mechanical properties, there are a number of obstacles that hinder extending their applications in optoelectric materials and high-speed multilayer printed wiring boards—their insolubility in common solvents in the fully imidized form, the light- or dark-yellow color of their films caused by intra- and intermolecular charge transfer interactions, and their high dielectric constants. As a result, fully aliphatic and alicyclic polyimides (APIs) are currently being considered for applications in optoelectronics and interlayer dielectric materials because of their higher transparencies and lower dielectric constants, which result from their

low molecular density and polarity and low probability of undergoing interior intramolecular CT.<sup>[8]</sup> Nevertheless, polyimides derived from aliphatic monomers are most suitable for applications that have less stringent thermal requirements. The high flexibility and low rigidity, resulting in low bond strength of their backbone due to the aliphatic moieties, make their thermal and dimensional properties inferior to those of aromatic ones. It is well known that rigid-rod structures reduce the CTE of polyimides.<sup>[58]</sup> Adamantane (tricyclo [3.3.3.1.1.<sup>3,7</sup>] decane), a rigid alicyclic compound composed of three cyclohexane rings in chair conformations,<sup>[59]</sup> is the most salutary alicyclic candidate for incorporation into aliphatic polyimide, to enhance their thermal stability without sacrificing their high transparency, solubility and low dielectric constants. Chern et al.<sup>[60-62]</sup> and Watanabe et al.<sup>[63-65]</sup> reported the synthesis of relatively thermally stable polyimides, semi-aromatic polyimides, containing damantly and biadamantane moieties. Seino et al.<sup>[66,67]</sup> and Mathews et al.<sup>[68,69]</sup> reported the synthesis and characterization of a series of fully aliphatic polyimides with good thermal and dimensional stabilities. Oishi et al.<sup>[70,71]</sup> reported fully alicyclic polyimides containing fluorine groups, while Mathews et al.<sup>[69]</sup> focused on the synthesis of siloxane containing aliphatic polyimides.

### 1.3.1 Monomers for Fully Aliphatic Polyimides

The structures of aliphatic monomers commonly used for synthesis of aliphatic polyimides in previous studies are given in Fig. 1.4.<sup>[8,66-72]</sup>

Dianhydrides A and B have proved to impart excellent thermal and optical properties to polyimides. The demerit of B is the presence of a double bond which can impart polarity decreasing transparency. So compound B is oxidized to C to get more useful results. Dianhydrides F and G are asymmetric and thus can provide more free volume and lessen interchain interactions. Mathews et al.<sup>[8]</sup>. Utilizes diamines **1** – **4** to study the impact of long chain and highly flexible backbones in polyimides. **5** and **6** attract attention due to the formation of ortho and para linkage of the imide group. Diamine **7** is non-coplanar and can decrease the dielectric constant more. The synthesis of damantly containing diamines **12** and **13** was reported.<sup>[66-71]</sup> Structures of the diamines used to synthesize alicyclic polyimides containing fluorine and siloxane groups are shown as **14** – **17** in Fig. 1.4. The influence of fluorine and siloxane moieties upon fully aliphatic polyimides can be drawn using those diamines.

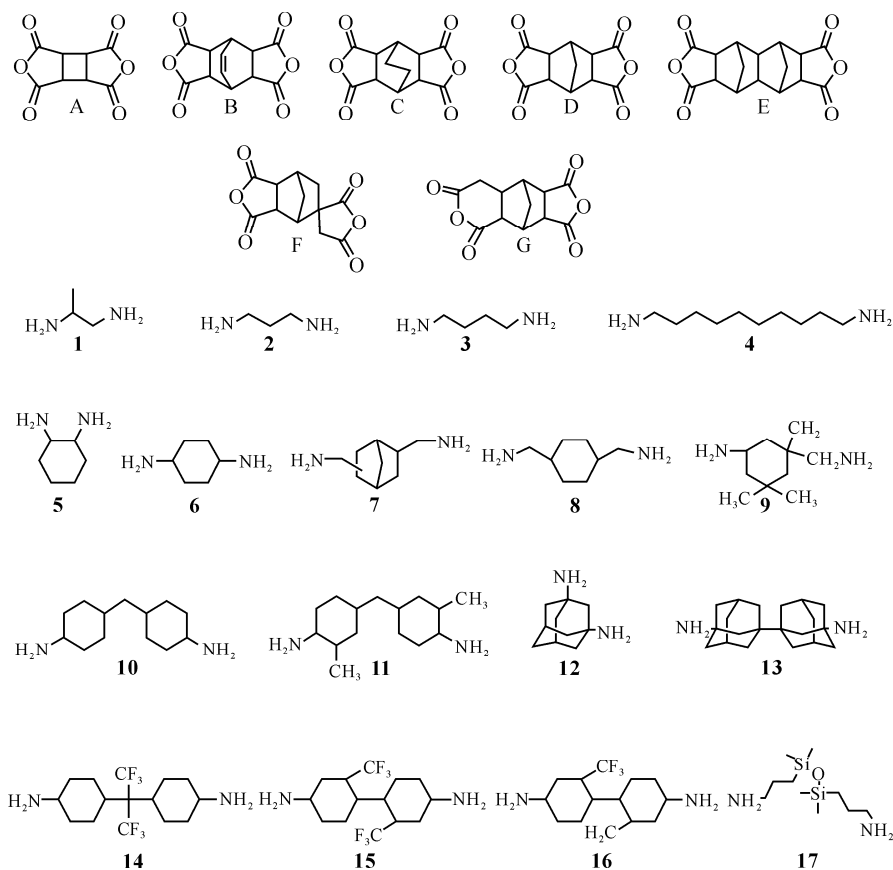


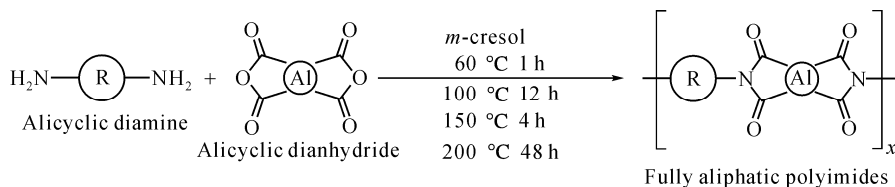
**Fig. 1.4.** Monomers selected for the synthesis of APIs (Adapted from Ref. 8. Copyright (2007), with permission from the Polymer Society of Korea)

### 1.3.2 Synthesis of Fully Aliphatic Polyimides

Generally, the reaction of anhydrides with highly basic diamines, such as aliphatic and alicyclic diamines, provides amic acids, and then free amines form carboxylic acid salts with a carboxyl group of amic acids due to their high basicity. In the polymerization, salt formation prevents the attainment of high molecular weight poly(amic acid) (PAA). So a one-pot PI synthesis without isolation of PAA at high reaction temperature is used for preparing high molecular weight aliphatic polyimides, because the amines used for the salt formation can be generated during the formation of imide.<sup>[73,74]</sup> The synthetic method used for the preparation of fully aliphatic polyimides by Mathews et al. is given in Scheme 1.2. A typical example of the polymer synthesis procedure is as follows. A solution of an



equimolar amount of diamine and dianhydride in *m*-cresol was heated in the following steps: 100 °C for 12 h, 150 °C for 4 h, and 200 °C for 48 h. The solution was then cooled to ambient temperature, diluted with *m*-cresol, and poured into methanol. The polymer was filtered off and dried in vacuo at 60 °C.

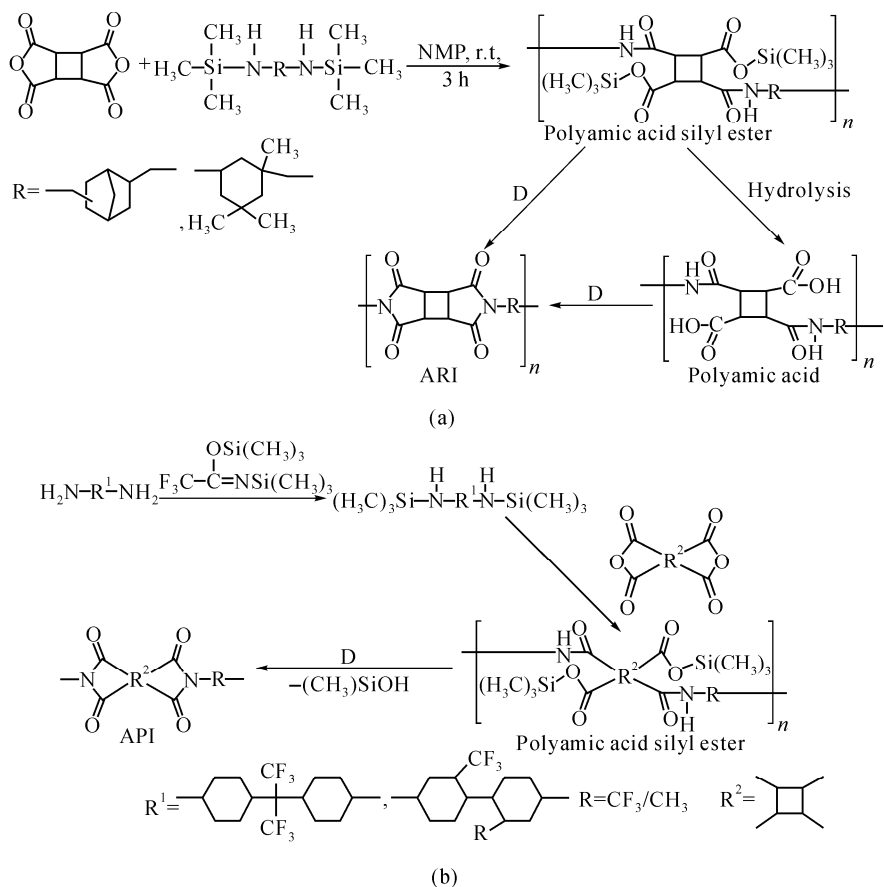


**Scheme 1.2.** Scheme of synthesis of fully aliphatic polyimides (Adapted from Ref. 8. Copyright (2007), with permission from the Polymer Society of Korea)

Watanabe et al.<sup>[63-65]</sup> and Oishi et al.<sup>[70,71]</sup> reported the synthesis of fully aliphatic polyimides by silylation. The reaction procedure is demonstrated in Scheme 1.3. The silylation method employs two steps: the ring opening polyaddition of the *N*-silylated alicyclic diamines to alicyclic dianhydrides, producing polyamic acid silyl ester (PASE), which in turn undergo subsequent thermal imidization to form APIs. The first step of polymerization proceeded smoothly in homogeneous solutions without any salt formation, giving clear and viscous PASE solutions. The inherent viscosity of the polyamic acid silyl ester ranged from 0.3 to 0.74 dL·g<sup>-1</sup> indicating enough molecular weights to form cast films. Thus formed, polyamic acid silyl ester was subjected to thermal imidization by heating at 200 °C for 1 h, 250 °C for 1 h and 300 °C for 1 h, to be converted to wholly alicyclic polyimide films by the elimination of trimethyl silanol.

### 1.3.3 Structural Confirmation of Fully Aliphatic Polyimides

Structural confirmation of a fully aliphatic polyimide can be done using FT-IR and NMR spectroscopies and by elemental analysis. The characteristic peaks occur at 1,780 (C=O symmetric stretching), 1,716 (C=O asymmetric stretching), 1,375 (C-N-C stretching), 739 (imide ring deformation), 2,800 – 2,900 (aliphatic C-H stretching), 1,465 (CH<sub>2</sub> bending), and 1,450 and 1,395 cm<sup>-1</sup> (CH<sub>3</sub> bending). The slight shifts of the absorption peaks from the usual wave number values can be attributed to non-conjugation due to the absence of an aromatic ring. For silicon containing fully aliphatic polyimidodisiloxanes (APISiOs), the bands of Si domain stretching are observed at between 1,000 cm<sup>-1</sup> and 1,180 cm<sup>-1</sup> together with around 850 cm<sup>-1</sup> (Si-O-Si asymmetric stretching), around 1,400 cm<sup>-1</sup> (Si-H<sub>3</sub>), and at 787 cm<sup>-1</sup> (Si-C). The intensities of these bands gradually increase as the amount of siloxane residue increased in the polyimide backbone, while the intensity of the absorption bands, corresponding to that of aliphatic moieties, decreased.<sup>[69]</sup>



**Scheme 1.3.** Synthesis of wholly alicyclic polyimides. (a) From *N*-silylated alicyclic diamines; (b) In situ *N*-silylated fluorinated alicyclic diamines (Adapted from Ref. 8. Copyright (2007), with permission from the Polymer Society of Korea)

In addition, NMR spectra can also be utilized for the structural confirmation of synthesized fully aliphatic polyimides. The APIs show all the characteristic peaks corresponding to the dianhydride and diamine residues which constitute their backbone. The homopolyimides give a single peak around  $176 \times 10^{-6}$  in  $^{13}\text{C}$  NMR spectra, while in the case of copolyimides those  $\text{C}=\text{O}$  peak splits, due to the difference in the carbons attached to the two sides of the imide group. The NMR integration method can be also utilized to determine the exact ratio of the monomer residues in the polyimide backbones.

Fully aliphatic polyimidosiloxanes can be characterized using  $^{29}\text{Si}$ -MAS NMR spectra.<sup>[69]</sup> The  $^{29}\text{Si}$ -MAS NMR spectroscopy showed the signals of the internal silicon atoms of the polymer backbone around  $+7.6 \times 10^{-6}$  corresponding to  $\text{Si}(\text{CH}_3)_2-\text{O}-\text{Si}(\text{CH}_3)_2$ . The signal located around  $+7.6 \times 10^{-6}$  is attributed to the silicon atom close to the methylene group. The  $^{29}\text{Si}$ -MAS NMR spectrum of

homopolyimides with only dianhydride and siloxane residues exhibits a narrow single peak at  $+7.6 \times 10^{-6}$ . The narrow peak results from a single ordered environment around Si. The spectrum of copolymers exhibits two broad peaks around  $+17.5$  and  $+7.6 \times 10^{-6}$ . Multiple peaks are the result of a disordered atmosphere around Si atom. The peak widths increase with increasing alicyclic diamine components, which suggests increasing disorder accompanying the addition of cyclohexane or damantly moieties. The peak near  $+17.5 \times 10^{-6}$  is due to the enhanced segmental motions.

### 1.3.4 Properties of Fully Aliphatic Polyimides

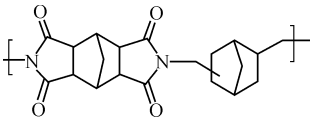
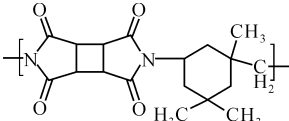
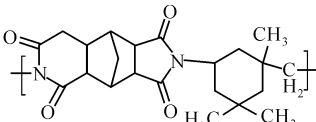
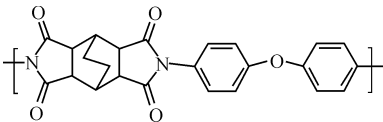
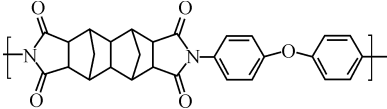
The intrinsic viscosities of fully aliphatic polyimides synthesized via one step synthesis ranged from 0.16 to  $0.56 \text{ dL}\cdot\text{g}^{-1}$ . According to the gel permeation chromatography (GPC) data,  $M_n$  and polydispersity index (PDI) of the polyimides ranged from 2,400 to 45,200, and 1.1 to 2.4, respectively. The lower  $M_w/M_n$  values comparative to those of conventional Pis may be due to the somewhat low reactivity of monomers containing the rigid and bulky groups. The polyamic acid silyl esters which are the intermediate for the synthesis of fully aliphatic polyimides via silylation method give intrinsic viscosities between  $0.51 \text{ dL}\cdot\text{g}^{-1}$  and  $0.99 \text{ dL}\cdot\text{g}^{-1}$ . The chromatogram indicated that the  $M_n$  and  $M_w$  values were in the range of 29,000 and 64,000, respectively, with respect to polystyrene standards and the ratio  $M_w/M_n$  was found around 2.2.<sup>[8]</sup>

The good solubility of fully aliphatic polyimides is their first advantage over aromatic ones. All of the APIs exhibited peaks in the region  $2\theta < 20^\circ$ , which indicates that they possess crystalline structures as well as intermolecular regularity when evaluated through wide-angle X-ray diffraction (WAXD) measurements.<sup>[8]</sup> The linear aliphatic diamine-based APIs presented patterns in the region  $2\theta < 20^\circ$  that are different from those of the alicyclic APIs. The broad peak centered at  $2\theta = 16.02^\circ$  ( $d$ -space =  $5.5 \text{ \AA}$ ) shifted to a lower position and split into several smaller peaks when the diamine changed from **1** to **2** (Fig. 1.4). In addition, the peak intensity increased as the chain length of the polyimide backbone increased; this finding suggests a high degree of internal order. Alicyclic APIs exhibited a peak at  $2\theta = 16.54^\circ$ , which corresponds to a  $d$ -spacing of  $5.3 \text{ \AA}$ . Incorporation of damantly moieties into the alicyclic and APIs resulted in a lowering of the peak intensity and broadening of the peaks at  $2\theta < 20^\circ$ . As the siloxane unit was incorporated, the peaks at  $2\theta < 20^\circ$  disappeared and the amorphous halo was evident at  $9^\circ < 2\theta < 40^\circ$ .<sup>[8]</sup>

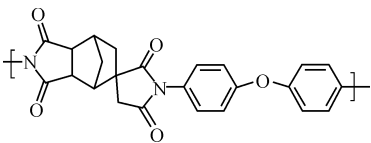
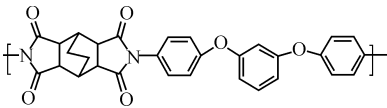
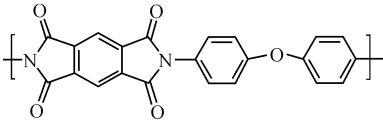
A lower dielectric constant ( $\epsilon$ ) is the second advantage of fully aliphatic polyimides over aromatic polyimides. The homopolyimides derived from aliphatic linear diamines had comparatively high  $\epsilon$  (2.92 – 2.56) values and copolyimides containing damantly moieties possessed the lowest values of  $\epsilon$  (2.8 – 2.4).<sup>[8]</sup> As the amount of the siloxane group increased in the polymer chain, the dielectric

constant decreased first. This can be explained in terms of an overall enhancement of small scale molecular mobility by the incorporation of silica domains in the polyimidosiloxanes backbone, arising from loosened molecular packing of APISiO chains as compared to API chains. However, as the amount of siloxane units increased no further, a decrease in  $\epsilon$  value was seen owing to the improved degree of close chain packing. The decreasing aromatic character of polyimides decreases the refractive index and birefringency thereby decreasing the dielectric constant. The average refractive indices ( $n_{AV}$ ) of the polyimides prepared via the silylation method were determined between 1.5173 and 1.4977.<sup>[8]</sup> The  $n_{AV}$  of 1.5173 and 1.4977 can be translated into dielectric constants of 2.53 and 2.47, respectively. These values are slightly lower than the optically estimated  $\epsilon$  of an alicyclic polyimide (2.55)<sup>[75]</sup> and a fluorinated semi-aromatic polyimide (2.6)<sup>[76]</sup> and significantly lower than that of a semi-aromatic polyimide (2.83).<sup>[75]</sup> In addition, the in-plane/out-of-plane birefringences ( $\Delta n$ ) of the polyimides were estimated as 0.0000 – 0.0004. The fluorinated polyimides synthesized by Oishi et al. display  $\Delta n$ ,  $n_{AV}$  and  $\epsilon$  in the range of 0.0016 – 0.0128, 1.471 – 1.478 and 2.38 – 2.40 respectively.<sup>[70,71]</sup> For the effective comparison of the dielectric constants and refractive indices and birefringency of fully aliphatic, semi-aromatic and fully aromatic polyimides we have tabulated the results<sup>[72,65]</sup> in Table 1.1.

**Table 1.1** Optical properties of polyimide films (Adapted from Ref. 8. Copyright (2007), with permission from the Polymer Society of Korea)

Polyimide	Category	$n_{AV}$	$\Delta n$	$\epsilon$	Ref.
	Fully aliphatic	1.52	0.000	2.55	72
	Fully aliphatic	1.49	0.000	2.47	65
	Fully aliphatic	1.51	0.004	2.53	65
	Semi-aromatic	1.61	0.000	2.87	72
	Semi-aromatic	1.60	0.013	2.83	72

(Continued)

Polyimide	Category	$n_{AV}$	$\Delta n$	$\epsilon$	Ref.
	Semi-aromatic	1.61	0.015	2.85	72
	Semi-aromatic	1.59	0.017	2.81	72
	Fully aromatic	1.68	0.079	3.13	72

It was observed that the transparency of APIs is much better than that of aromatic polyimides.<sup>[8,72]</sup> The high transparency of APIs may come from a few factors such as low molecular density, polarity and the rare probability of inter- and intra-molecular charge transfers. All the synthesized APIs were above 80% transparent.<sup>[8,72]</sup>

The APIs containing linear aliphatic chains on their backbones were found to be the least sensitive to temperature and their stability decreased as the thermally fragile alkyl chain length increased.<sup>[8]</sup> The polymers showed 5% weight loss ranging from 242 to 270 °C. The temperatures for 10% gravimetric loss ( $T_{10}$ ), which are an important criterion for the evaluation of thermal stability, were in the range of 304 – 320 °C. The polyimides derived from alicyclic monomers showed 5% weight loss ranging above 400 °C in nitrogen and above 350 °C in air. The temperatures for 10% gravimetric loss ( $T_{10}$ ) were above 450 °C in nitrogen and above 400 °C in air.<sup>[8]</sup> Fluorine containing wholly alicyclic polyimides, derived from monomers **14**, **15** and **16** (shown in Fig. 1.4), exhibited thermal decomposition temperatures ( $T_{10}$ ) in the range of 395 – 400 °C in air and 430 – 440 °C in nitrogen. The polymers containing siloxane groups underwent their 5% weight loss within the temperature range of 325 – 455 °C. The temperatures for 10% gravimetric loss ( $T_{10}$ ), were in the range of 353 – 476 °C. Thermal stability was further improved when silica was introduced. The APISiO containing 50% silica had the maximum  $T_d$  in the range 460 – 470 °C.  $T_g$ s of the polyimides were in the range of 110 – 250 °C, although no  $T_g$  was detected for the most rigid homo APIs derived from **5**, **6** and **12** (shown in Fig. 1.4). Polyimides containing linear aliphatic residues of **1**, **2**, **3** and **4** (shown in Fig. 1.4) showed a melting temperature around 320 – 380 °C and  $T_g$  in the range 110 – 190 °C, which reappeared with repeated scans. This means that these polyimides have a semi-crystalline nature. The fluorinated APIs showed higher  $T_g$ s in the range of 306 – 335 °C. As the amount of siloxane increased in the polyimide backbone, the glass transition temperature showed an increasing trend followed by a decrement when the siloxane amount further

increased. The API films possess a tensile modulus of 1.3 – 3.0 GPa, tensile strength in the range of 78.7 – 145 MPa and elongation at break around 3.4% – 30%. Most of the polyimides exhibited appreciable tensile strength, indicating they are mechanically stringent.<sup>[8]</sup>

World-wide research is progressing for a practically applicable polyimide candidate devoid of demerits; despite the bewildering number of candidate materials under investigation, a clear winner has yet to emerge. The balance between stiffness, polarity, free volume, flexibility and silicon or fluorine content of their backbone units enables APIs to find an immense range of applications in flexible polymer light emitting diode substrates, soft-printed circuit boards, interlevel dielectric insulators, high-speed passivation or dielectric films and alignment films.

## 1.4 Polyimides for Organic Light-Emitting Devices and Flexible Substrates

In this section, we will introduce semi-conducting polyimides, as well as polyimides as plastic substrate for the flexible Organic Light-Emitting Device (OLED).

### 1.4.1 *Semi-conducting Polyimides*

Applications of aromatic polyimides such as a mechanically rubbed alignment layer for liquid crystals in a passive and active matrix liquid crystal display (LCD) and a dielectric interlayer for insulating electrons in microelectronic devices, require good electrical insulating characteristics of polyimide films. Most of the research and development concentrated on lowering the dielectric constant (permittivity) of polyimide films.<sup>[77-79]</sup> Therefore, polyimides have been generally considered as an insulating material. However, we can simply change this insulating property to an electrically semi-conducting property in polyimide films and not at the expense of other favored physical (mechanical), chemical and thermal characteristics. The only change is in the electrical characteristics.

To achieve an electrically semi-conducting polyimide (SPI) we need to replace one of the constituents (repeating units) with a charge carrier transporting unit like a triarylamine unit as a diamine constituent in the polyimide backbone. The basic structure of SPI is shown in Fig. 1.5, where we can decouple the repeating units into two parts by role: The triarylamine moiety as an electronic unit for delivering charge carrier transportability and the imide moiety as a physicochemical unit for keeping other physical (mechanical) and chemical characteristics, though the triarylamine moiety also contributes to the physical properties of SPI. Fig. 1.6 shows a typical representative SPI which was synthesized in our group.

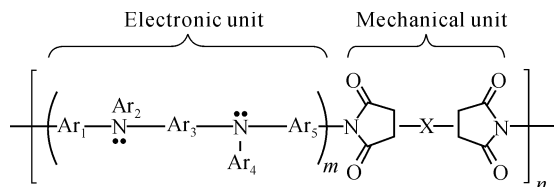


**Fig. 1.5.** Basic chemical structure of semi-conducting polyimide (SPI) (Adapted from Ref. 77. Copyright (2007), with permission from Science Publishers, Inc.)

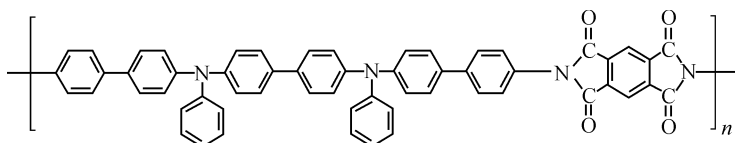


**Fig. 1.6.** A typical example of synthesized semi-conducting polyimide (SPI): Poly[*N,N'*-diphenyl-*N,N'*-bis(4-aminobiphenyl)-(1,1'-biphenyl)-4,4'-diamine pyromellitimide] (PMDA-DBABBD PI) (Adapted from Ref. 81. Copyright (2007), with permission from the American Chemical Society)

The final electrical characteristics of SPIs indeed strongly depend on the kinds of diamine and dianhydride units. Although most of these SPIs can form organic nanolayers (nanofilms) by wet and dry processes,<sup>[80-86]</sup> wet processes to make nanolayers of this SPI need a corresponding poly(amic acid) precursor, which is soluble in organic solvents such as NMP and dimethylformamide (DMF), whereas dry processes do not need the precursor polymer in advance because it is in-situ prepared upon depositing monomers onto a substrate in a vacuum.<sup>[80-86]</sup> Whether wet or dry processes, the precursor nanolayers are converted into SPI nanolayers via thermal imidization process. The conductivity of this SPI was measured between  $10^{-9}$  and  $10^{-6}$  s/cm, depending on the process conditions, which were obtained using a parallel two-electrode (probe) voltage-current (V-I) method.

The maximum hole mobility of this SPI was approximately  $10^{-5}$  cm<sup>2</sup>/Vs, which was calculated using the Child law in a space charge limited current (SCLC) regime from measured current-voltage characteristics for the sandwiched hole only device (ITO/SPI/Al).<sup>[87]</sup> This hole mobility is 10 – 100 times lower than that of a well-known *p*-type organic semiconductor, which was measured with time-of-flight (ToF) method<sup>[88,89]</sup> due to the existence of many charge trapping sites (carbonyl groups). Further improvement in the charge carrier mobility of this SPI is expected by replacing the imide unit with less charge trapping characteristics.

Recent developments in the use of photosensitive polyimide (PSPI) and in the associated exposure equipment have expanded the applications of photosensitive polyimide in the semi-conductor industry.<sup>[90,91]</sup> The thermal and dielectric characteristics of photosensitive polyimide are compatible with the requirements of semiconductor devices. The advanced development of photosensitive polyimide has opened a new door for semi-conductor manufacturers to realize significant cost savings. Using photosensitive polyimide can substantially reduce the total number of process steps used in the traditional polyimide process. For some applications, the use of photosensitive polyimide consolidates the passivation and

polyimide lithography steps into one process level. This translates into process simplification and manufacturing cost reduction. Consequently, there has been a rapid increase in the use of photosensitive polyimide in the semi-conductor industry.

### ***1.4.2 Polyimides as Plastic Substrate for the Flexible OLED***

With the recent development of semiconductor techniques, it is feasible to fabricate semiconductor devices on organic flexible substrates. OLEDs can be also fabricated on flexible plastic substrates, creating the potential to reduce the weight of flat panel displays (FPDs). Flexible polymeric electroluminescent (EL) devices based on  $\pi$ -conjugated polymers have been demonstrated on polyaniline substrates and indium tin oxide (ITO)-coated plastic substrates, which further spurred interest in FPDs. So far, the use of the flexible substrates for OLEDs has been restricted mainly to the polyester films due to their excellent transparent property. However, up until now, the plastic substrates can be severely damaged at high temperature (200 – 300 °C for sputtering method) during the deposition process, mainly due to their intrinsic low thermal and mechanical properties compared with other inorganic or metal substrates. In this case, therefore, it is impossible to use a common sputtering method at high temperature. Consequently, reduced electrical resistance and long-term stability of the ITO surface cannot be achieved and maintained, which is directly related to the performance of applied devices. The syntheses of colorless transparent PIs have been achieved by the introduction of non-aromatic, fluorine, or sulfone groups into the polymer main chain, whose systems minimize the formation of the intra- and/or inter-molecular CT complex in the molecules. It leads aromatic PIs to be applied in optical components. Aliphatic cyclic polyimide (alicyclic polyimide) was synthesized from alicyclic dianhydride and was used as flexible transparent substrate for the deposition of ITO thin films by Lim et al.<sup>[92]</sup> ITO thin films were prepared at a typically high substrate deposition temperature with an r.f. planar magnetron sputtering system. The plastic substrates with transparent ITO thin films have been successfully prepared with aliphatic bicyclic polyimide (PI) synthesized from bicyclo[2.2.2]-oct-7-ene-2,3,5,6-tetracarboxylic dianhydride (BCOEDA) and 4,4'-oxydianiline (ODA) monomers.<sup>[92]</sup> It was summarized that the BCOEDA-ODA PI substrates with ITO thin film have good electrical conductivity, in spite of their relatively lower optical transmission property. The substrate can be applicable for display devices possessing yellow to red emission properties, except for blue or green emission devices. Other colorless polyimide substrates with ITO thin films have also been prepared by Lim et al.<sup>[93]</sup> with a novel fluorine-containing colorless aromatic PI derived from 2,2'-bis-(3,4-dicarboxyphenyl) hexafluoropropane dianhydride (6FDA) and 2,2'-bis (trifluoromethyl)-4,4'-diaminobiphenyl (TFDB), which has been used as a transparent flexible substrate for OLED. The PI substrate has high glass transition and decomposition temperature, low water absorption, good transmission and low optical loss. It was also found that the electrical sheet



resistance, optical transmission, grain size and structural orientation significantly depend on the substrate temperatures. Most of all, the sheet resistance value was the lowest value of the ITO films coated onto polymer substrates that has been reported in the previous literature. From the dependence of the sheet resistance on the grain size, it can be considered that the predominant scattering mechanism limiting the mobility is the grain boundary scattering mechanism for the ITO films deposited onto the PI substrates.

## 1.5 Polyimide-Based Nanohybrids

The dispersion of inorganic nanoparticles into a polymer matrix has been proved to be effective in the improvement of the performances of the organic polymers by yielding so-called organic-inorganic hybrid nanocomposites. These nanocomposites are one of the hottest issues among today's materials scientists since their unique combinational properties from organic and inorganic materials could not be obtained by a single component. The sol-gel reaction has been one of the most widely used approaches to obtain hybrid nanocomposites. In particular, an important advantage of the sol-gel synthesis route for polyimide/silica hybrid composites is that the poly(amic acid) organic matrix acts to prevent agglomeration of the silica, which can lead to nanometer scale silica clusters in the composites or, as often stated, "nanocomposites."

It is of the utmost importance to improve the compatibility between the two phases to prepare polyimide-inorganic composites with good properties. There are several approaches for making compatibilized composites: (1) by adding a coupling agent which makes a bond with the growing inorganic oxides and PI chains; (2) functionalizing the PI chains at their end groups; (3) choosing a polymer with appropriate groups within the repeating units; (4) using appropriate functional groups; (5) choosing judiciously the silsesquioxane, which can also make a bond with the carbonyl groups of PI; (6) interestingly, introducing titania to be able to reduce particles of silica/silsesquioxane through Si-O-Ti bonding. A few methods employed for preparing compatibilized hybrid composites have been discussed in this chapter.

Ha et al.<sup>[41,94]</sup> introduced fluorescence spectroscopy to interpret the interfacial interaction between the inorganic particles and PI, as shown in Fig. 1.7. In this figure, silica was prepared by sol-gel reaction of tetraethoxysilane (TEOS) as a silica precursor.<sup>[95]</sup> The peaks were obtained with an excitation wavelength of 350 nm. The results can be summarized as follows: On increasing the amount of silica, the wavelength of the emission peak for the 3,3'-4,4'-biphenyltetracarboxylic anhydride (BPDA)-phenylenediamine (PDA) PI/silica composite films increases. A large red shift was observed for the BPDA-PDA PI/silica hybrid system (up to 50 – 70 nm) at high silica loadings (22 wt%). The result suggests that the interaction between silica and polyimide is important and the interfacial interaction between BPDA-PDA PI and silica is strong. We found that in the

BPDA-4,4'-oxydianiline (ODA) PI/silica composite there is no specific interaction or chemical bonding holding the silica to the polyimide matrix.

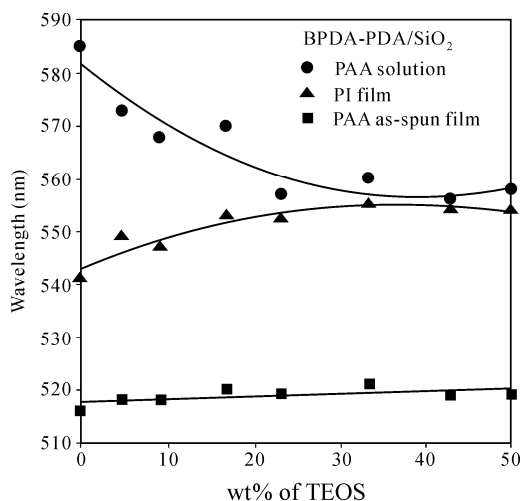


**Fig. 1.7.** Emission wavelength change of BPDA-PDA PAA/TEOS hybrid solution in NMP, BPDA-PDA PAA/TEOS hybrid as-spun film and BPDA-PDA polyimide/silica composites (Adapted from Ref. 41. Copyright (2000), with permission from the American Chemical Society)

Highly compatibilized BPDA-ODA PI/silica films can be, however, successfully prepared if one uses 3-aminopropyltriethoxysilane (3-APS) or polyvinylsilsesquioxane (PVSSQ). For instance, in Fig. 1.8, 3-APS produced a very compact and fine microstructure as well as improved optical transparencies in the hybrid composites of PI with silica from TEOS, in comparison to the PI/silica hybrid composite without 3-APS, which exhibits gross phase separation. In this figure, the silica content was fixed at 30 wt%. The enhancement of phase compatibility brought via PVSSQ was also clearly observed as for the case of 3-APS. The result was ascribed to the better interfacial interaction in the PI/PVSSQ hybrids in comparison to that of the PI/silica (from TEOS) hybrid system. The end hydrogen of PVSSQ and the hydrogen of Si-OH also provided hydrogen bonds in the carbonyl group of the PI matrix, leading to compatibilized morphology.

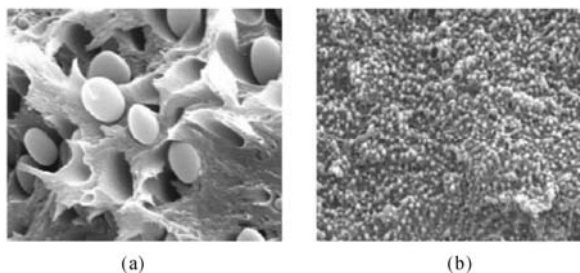


**Fig. 1.8.** SEM images of the PI/silica hybrid composites containing 30 wt% of silica without (a) and with (b) 3-APS

It was found that nanocomposites with BPDA-PDA PI can be obtained up to 30 wt% of PVSSQ, whereas  $\leq 20$  wt% of PVSSQ is the maximum composition to give nanocomposites for the BPDA-ODA PI. The mechanical properties of the nanocomposites were improved by the introduction of fine silica particles into a polymer matrix and better adhesion as well as strong interaction between PI and PVSSQ. It is noteworthy that the flexible organic phase of PVSSQ played a significant role in the interfacial adhesion between polyimide and the PVSSQ. It was also found that the addition of silica or PVSSQ affected the dielectric constant of hybrid films, which was explained in terms of increasing free volume as well as domain sizes of PVSSQ and an inherently higher dielectric value of silica.

Meanwhile, it is known that titania possesses very fast hydrolysis and ultimately produces an inhomogeneous and large agglomeration of domains, which can significantly impact on the polymer matrix. The introduction of titania into the PI/silica hybrid composites was, however, found to improve the interfacial interaction between silica and PI.<sup>[96]</sup>

## 1.6 Other General High Performance Polymers

In this section, we will introduce some other general high performance polymers, including polyetheretherketon (PEEK), polysulphone (PSU), polysulfide, polycarbonates (PC), polyamides (PA), poly(butylene terephthalate) (PBT), polynorbornene (PNB), and poly(phenylene oxides).

### 1.6.1 Polyetheretherketon (PEEK)

Fig. 1.9 illustrates chemical structure of polyetheretherketones (PEEKs), which is also referred to as polyketones.

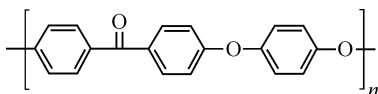


Fig. 1.9. Representative structure of polyetheretherketon

PEEKs are obtained from aromatic dihalides and bisphenolate salts by nucleophilic substitution (Fig. 1.10). The bisphenolate salt is formed in situ from bisphenol and either added sodium or added alkali metal carbonate or hydroxide.<sup>[97]</sup>

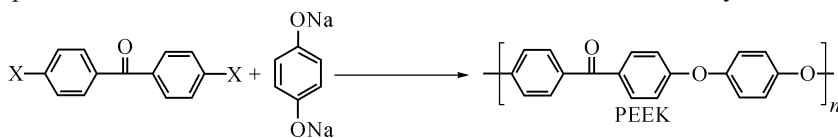


Fig. 1.10. Synthetic route of PEEK

PEEK is a thermoplastic with extraordinary mechanical properties. The Young's modulus is 3.6 GPa and its tensile strength 170 MPa. PEEK is partially crystalline, and is highly unusual in exhibiting two glass transition temperatures at around 140 °C and around 275 °C, depending on cure cycle and precise formulation. PEEK melts at around 350 °C and is highly resistant to thermal degradation.<sup>[98]</sup> The material is also resistant to both organic and aqueous environments, and is used in bearings, piston parts, pumps, compressor plate valves and cable insulation applications. It is one of the few plastics compatible with ultra-high vacuum applications. PEEK is considered as an advanced biomaterial used in medical implants, often in reinforced format using biocompatible fibre fillers such as carbon. In carbon fibre reinforced form, PEEK has also come under consideration as an aerospace structural material due to its high strength-to-weight ratio. Electronic circuitry has a high demand for PEEK's large temperature range.<sup>[99]</sup> PEEK also exhibits good chemical resistance in many environments, including alkalis (i.e., sodium, potassium and ammonium hydroxides), aromatic hydrocarbons, alcohols (i.e., ethanol, propanol), greases, oils and halogenated hydrocarbons. However, its performance in acids is dependent on the type of acid-PEEK, showing poor resistance in concentrated sulfuric, nitric, hydrochloric, hydrobromic and other mineral acids, though performance may be adequate for short-term use with these acids in very dilute form. Its resistance to hydrofluoric acid and oleum is very poor. PEEK shows good resistance to phosphoric acid and organic acids (acetic, citric, oxalic, tartaric, etc.), but varying resistance in the presence of halogens. PEEK is resistant to dissolution by some formaldehydes and ketones such as acetone, but not (at higher temperature) methylethyl ketone.<sup>[97]</sup>

### 1.6.2 Polysulphone (PSU)

Chemically, polysulfone consists of repeating units of  $C_{27}H_{22}O_4S$  (Fig. 1.11). It is produced by step polymerization of bisphenol-A and bis(4-chlorophenyl) sulfone, forming a polyether by elimination of hydrogen chloride.

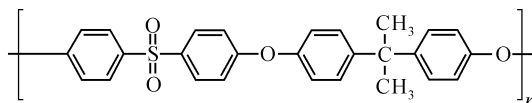
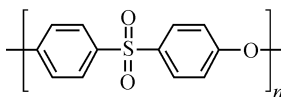


Fig. 1.11. Representative structure of polysulphones

This thermoplastic material is tough, rigid, high-strength and transparent, retaining its properties between  $-100$  and  $150$  °C. It has very high dimensional stability; the size change when exposed to boiling water or  $150$  °C air or steam generally falls below 0.1%. Its glass transition temperature is  $185$  °C.<sup>[100]</sup> The sulfur in the oxidized state gives this polymer a high affinity for water. This discourages absorption of organic substances. The sulfur atoms in this oxidation state make the polymer quite polar and thus hydrophilic. As much of the fouling

in water comes from hydrophobic organic particles, they are not attracted to the polysulfone. The pH and temperature ranges are wide when using this polymer. Polysulfone is highly resistant to mineral acids, alkalis and electrolytes, in pH ranging from 2 to 13. It is resistant to oxidizing agents, and therefore it can be cleaned by bleaches. It is also resistant to surfactants and hydrocarbon oils. It is not resistant to low-polar organic solvents (e.g., ketones and chlorinated hydrocarbons), and aromatic hydrocarbons. Due to its excellent electrical properties, polysulfone is used as a dielectric in capacitors.<sup>[101]</sup> Mechanically, polysulfone has fairly high compaction resistance, allowing its use under high pressure. Polysulfone allows easy manufacturing of membranes, with reproducible properties and controllable size of pores. Such membranes can be used in applications like hemodialysis, waste water recovery, food and beverage processing, and gas separation. Polysulfone can be reinforced with glass fibers. The resulting composite material has twice the tensile strength and a three-time increase of its modulus. Polysulfone can be used in Food and Drug Administration (FDA)-recognized devices.<sup>[102]</sup> It is used in medical devices, food processing, feeding systems and the automotive and electronics industries. Polysulfone has the highest service temperature of all melt-processable thermoplastics. Its resistance to high temperatures gives it the role of a flame retardant, without compromising its strength, which usually results from the addition of flame retardants. Its high hydrolysis stability allows its use in medical applications requiring autoclave and steam sterilization. However, it has low resistance to some solvents and undergoes weathering, while the weathering instability can be offset by adding other materials into the polymer. Polysulfone was introduced in 1965 by Union Carbide.<sup>[100-103]</sup> It is a speciality material with a very small share of the total plastics market. It is very expensive both as a raw material and to process; therefore it is generally not used in applications that do not call for its special properties. In such applications, it is often a superior replacement for polycarbonates. Polysulfone is also used as a copolymer. Polysulfone is resistant to compression- and temperature-induced deformation (boiling water). It is also stable in aqueous acids and bases and many non-polar solvents; however, it is soluble in strong polar solvents such as dichloromethane and *N*-methylpyrrolidinone. Polyethersulfone (PES) is a common thermoplastic belonging to the group of polysulfones. They have the chemical structure as shown in Fig. 1.12.<sup>[103]</sup>



**Fig. 1.12.** Representative structure of polysulfones (Adapt from Ref. 103, Copyright (1985), with permission from Wiley)

PES is transparent, hydrolysis-resistant and chemically steady. PES is superior to PSU in stability opposite chemicals and in the impact strength. Thus it finds applications in thermally highly loaded parts of medical instruments, automobile and aircraft construction, electrical and electronic components.

### 1.6.3 Polysulfides

They are a class of chemical compounds containing chains of sulfur atoms. In their simplest form, polysulfides are anions with the general formula  $S_n^{2-}$ . In the commercial world, however, polysulfide usually refers to a class of polymers with alternating chains of several sulfur atoms and hydrocarbon. The general formula for the repeat unit is  $\text{-(CH}_2\text{)}_m\text{-S}_x\text{-(CH}_2\text{)}_n\text{-}$ , where  $x$  indicates the number of sulfur atoms (or rank), and  $n$  indicates the number of repeat units. Polymers containing sulfur atoms separated by hydrocarbon sequences are not polysulfides, e.g., polyphenylene sulfide  $(C_6H_4S)_n$ . Polysulfide polymers can be synthesized by condensation polymerization reactions between organic dihalides and alkali metal salts of polysulfide anions. The dihalide species that are reportedly used in the condensation polymerization method are dichloroalkanes such as 1,2-dichloroethane  $(ClCH_2CH_2Cl)$ , bis-(2-chloroethyl)formal  $(ClCH_2CH_2OCH_2OCH_2CH_2Cl)$ , and 1,3-dichloropropane  $(ClCH_2CH_2CH_2Cl)$ , whereas sodium polysulfides  $(Na_2S_x)$  are the alkaline polysulfides of choice.<sup>[104]</sup> In some cases, polysulfide polymers can be formed by ring-opening polymerization reactions. Polysulfide polymers are insoluble in water, oils and many other organic solvents and therefore are often used as sealants. These sealants have been used to fill the joints in pavements, automotive window glass and aircraft structures. A primary reason for using the polysulfide sealants in these applications is to prevent water intrusion.<sup>[105]</sup> Many commercial elastomers currently have polysulfide crosslinks. These crosslinks interconnect neighboring polymer chains, thereby conferring rigidity. The degree of rigidity is related to the number of crosslinks. Elastomers therefore have a characteristic ability to snap back to their original shape after being stretched or compressed. Because of this memory for their original cured shape, elastomers are commonly referred to as rubbers. The process of crosslinking the polymer chains in these polymers with sulfur is called vulcanization. Fig. 1.13 shows polysulfide linkage in vulcanized rubber.<sup>[104]</sup> The sulfur chains attach themselves to the “allylic” carbon atoms, which are adjacent to  $C=C$  linkages. Vulcanization is applied to the processing of several classes of rubbers, including polychloroprene (Neoprene<sup>TM</sup>), styrene-butadiene and polyisoprene, which is natural rubber.<sup>[104]</sup> Charles Goodyear’s discovery of vulcanization, involving the heating of polyisoprene with sulfur, was revolutionary because it converted a sticky and almost useless material into an elastomer which could be fabricated into useful products.<sup>[104]</sup> Inorganic polysulfides are common, the most useful one being lime sulfur  $CaS_n$ , which is used as a pesticide in agriculture. Well-defined polysulfide compounds have been widely discussed in the research literature.<sup>[104-106]</sup> Examples include polysulfide complexes of the transition metals such as  $(C_5H_5)_2TiS_5$ ,  $[Ni(S_4)_2]^{2-}$ , and  $[Pt(S_5)_3]^{2-}$ .<sup>[106]</sup> Main group elements also form polysulfides.

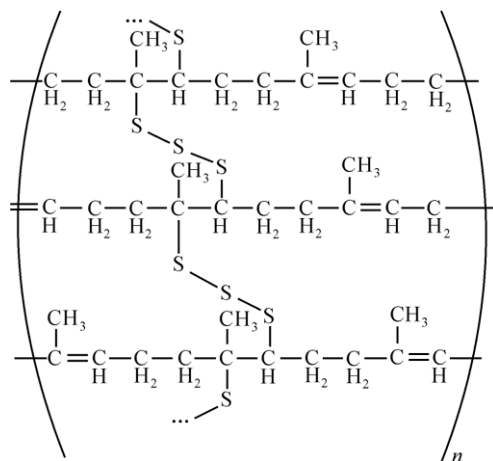


**Fig. 1.13.** Polysulfide linkage in vulcanized rubber (Adapted from Ref. 104, with permission from Wikipedia)

### 1.6.4 Polycarbonates (PC)

They are a particular group of thermoplastic polyesters which can be easily worked, molded and thermoformed. As such, these plastics are very widely used in modern manufacturing. Their interesting features (temperature resistance, impact resistance and optical properties) position them between commodity plastics and engineering plastics.

Polycarbonates got their name because they are polymers having functional groups linked together by carbonate groups  $\text{+O-(C=O)-O+}$  in a long molecular chain. Fig. 1.14 shows their repeating units.

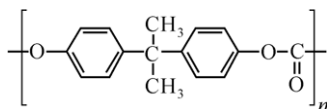


**Fig. 1.14.** Representative structure of polycarbonates

The characteristics of polycarbonates are quite like those of polymethyl methacrylate (PMMA; acrylic), but polycarbonate is stronger and more expensive. This polymer is highly transparent to visible light and has better light transmission characteristics than many kinds of glass.

Polycarbonates can be divided into poly(aromatic carbonate)s and poly(aliphatic carbonate)s. The second one, poly(aliphatic carbonate)s are a product of the reaction of carbon dioxide with epoxides which, owing to the thermodynamical stability of carbon dioxide, requires the use of a catalyst. Poly(aliphatic carbonate)s display promising characteristics, have a better biodegradability than

the aromatic ones and could be employed to develop other specialty polymers.<sup>[107]</sup> The most common type of polycarbonate plastic is one made from bisphenol A, in which groups from bisphenol A are linked together by carbonate groups in a polymer chain. This polycarbonate is characterized as a very durable material, and can be laminated to make bullet-proof “glass”, though “bullet-resistant” would be more accurate. Although it has high impact-resistance, polycarbonate has low scratch-resistance and so a hard coating is applied to polycarbonate eye-wear lenses.<sup>[108]</sup> General properties of polycarbonate are a density of  $1.20 \text{ g}\cdot\text{cm}^{-3}$ , a use range from  $-100$  to  $135 \text{ }^\circ\text{C}$ , a melting point around  $250 \text{ }^\circ\text{C}$ , a refractive index equal to  $1.585 \pm 0.001$ , a light transmission index equal to  $(90 \pm 1)\%$ , poor weathering in an ultraviolet (UV) light environment.<sup>[107-110]</sup> Main transformation techniques for polycarbonate resins are injection moulding into ready articles, extrusion into tubes, rods and other profiles, extrusion with calenders into sheet ( $1 - 15 \text{ mm}$ ) and film (below  $1 \text{ mm}$ ), which can be used as such, or manufactured into other shapes using thermoforming or secondary fabrication techniques, such as bending, drilling, routing, and laser cutting. Polycarbonate is becoming more common in houseware as well as laboratories and in industry, mainly where at least two of its three main features are required: high impact resistance, temperature resistance and optical properties. Typical injected applications are: lighting lenses, sunglass/eyeglass lenses, compact discs, DVDs, automotive headlamp lenses, Nalgene bottles. It is also used for animal enclosures and cages used in research. Typical sheet/film applications are found in industry: machined or formed cases, machine glazing, riot shields, visors, instrument panels. In advertisements: signs, displays, poster protection. In buildings: domelights, flat or curved glazing, sound walls. Polycarbonate may be appealing to manufacturers and purchasers of food storage containers due to its clarity and toughness. Polycarbonate has been described as lightweight and highly break resistant particularly when compared to silica glass. Polycarbonate may be seen in the form of both single use and refillable plastic water bottles.<sup>[107-110]</sup>

### 1.6.5 Polyamides (PA)

Polyamides are large molecules formed by the condensation polymerization of diamines with dicarboxylic acids. These complementary molecules give the same type of amide linkage as that found in natural protein fibres, such as silk and wool, where the monomers are amino acids. The early development of polyimides started when nylon-6,6 was first synthesized from 1,6-diaminohexane,  $\text{H}_2\text{N}-\text{CH}_2-\text{CH}_2-\text{CH}_2-\text{CH}_2-\text{CH}_2-\text{CH}_2-\text{NH}_2$  with 1,6-hexanedioic acid (adipic acid),  $\text{HOOC}-\text{CH}_2-\text{CH}_2-\text{CH}_2-\text{CH}_2-\text{COOH}$ . Polyamides as hot melt adhesives are used in a variety of industrial applications. Most polyamide adhesives possess a broad range of adhesive properties, and are characterized as exhibiting excellent adhesion to a wide variety of substrates, bonding well to porous substrates. They also demonstrate good chemical and oil resistance, and show good adhesion over a



wide range of service temperatures. Fig. 1.15 shows the structure of aromatic polyamide known as Nomex.

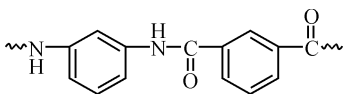


**Fig. 1.15.** Representative structure of aromatic polyamide known as Nomex

They are broadly classified into aliphatic and aromatic polyimides.<sup>[111]</sup> The term nylon refers to a family of polymers called linear polyamides. There are two common methods of making nylon for fiber applications. In one approach, molecules with an acid (COOH) group on each end react with molecules containing amine (NH<sub>2</sub>) groups on each end. The resulting nylon is named on the basis of the number of carbon atoms separating the two acid groups and the two amines.<sup>[112]</sup> Thus nylon-6,6, which is widely used for fibers, is made from adipic acid and hexamethylene diamine. The two compounds form a salt, known as nylon salt, an exact 1:1 ratio of acid to base. This salt is then dried and heated under vacuum to eliminate water and form the polymer. In another approach, a compound containing an amine at one end and an acid at the other is polymerized to form a chain with repeating units of  $\text{[-NH-(CH}_2\text{)]}_n\text{-CO-}$ . If  $n=5$ , the nylon is referred to as nylon 6, another common form of this polymer. The commercial production of nylon 6 begins with caprolactam using a ring-opening poly-merization. In both cases the polyamide is melt spun and drawn after cooling to give the desired properties for each intended use. Nylon is exceptionally strong, elastic, abrasion resistant, lustrous and easy to wash, resistant to damage from oil and many chemicals, can be pre-colored or dyed in a wide range of colors, resilient, low in moisture absorbency. Filament yarns provide smooth, soft, long-lasting fabrics, spun yarns lend fabrics light weight and warmth. Hence nylons are used as tire cord, hoses, conveyer and seat belts, parachutes, racket strings, ropes and nets, sleeping bags, tarpaulins, tents, thread, monofilament fishing lines, dental floss. Aromatic polyamides derived from aromatic monomers are better known as aramid fibres and are commercialized as Kevlar.<sup>[113]</sup> When Kevlar is spun in the same way that a spider spins a web, the resulting fiber has tremendous strength. The fibers do not rust or corrode. When woven together, they form a good material for mooring lines and other underwater objects. There are three common grades of Kevlar: Kevlar, Kevlar 29, and Kevlar 49. Kevlar is typically used as reinforcements in tires and other mechanical rubber goods. Kevlar 29 is used in industrial applications such as cables, asbestos replacement, brake linings and body armor. Kevlar 49 is considered to have the greatest tensile strength of all the aramids, and is used in applications such as plastic reinforcement for boat hulls, airplanes and bikes. Kevlar is susceptible to breakdown from ultraviolet light (such as sunlight) and hence is almost never used unprotected or unsheathed. Fibers of Kevlar consist of long molecular chains produced from poly-paraphenylene terephthalamide. There are many inter-chain bonds making the material extremely strong. Kevlar derives a portion of its improved strength from inter-molecular hydrogen bonds

formed between the carbonyl groups and protons on neighboring polymer chains and the partial  $\pi$  stacking of the benzenoid aromatic stacking interactions between stacked strands. These interactions have a greater influence on Kevlar than van der Waals interactions and chain length that typically influence the properties of other synthetic polymers and fibers like Dyneema. The presence of salts and certain other impurities, especially calcium, could interfere with the strand interactions and caution is used to avoid inclusion in its production. Kevlar's structure consists of relatively rigid molecules, which tend to form mostly planar sheet-like structures that have similarities to silk protein.

### 1.6.6 Poly(Butylene Terephthalate) (PBT)

PBT is a plastic that is used as an insulator in the electrical and electronics industries.<sup>[114,115]</sup> Fig. 1.16 shows the structure of poly(butylene terephthalate) repeating units. It is a thermoplastic crystalline polymer, and a type of polyester. PBT is resistant to solvents, shrinks very little during forming, is mechanically strong, heat-resistant up to 150 °C (or 200 °C with glass-fibre reinforcement) and can be treated with flame retardants to make it noncombustible.

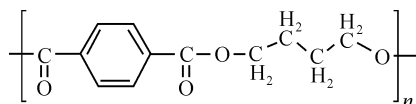


Fig. 1.16. Representative structure of poly(butylene terephthalate)

### 1.6.7 Poly(Phenylene Oxides)<sup>[3]</sup>

One more promising class of polymers which has found commercialization is the polyphenylene oxide type. Fig. 1.17 shows its structure. These polymers are synthesized by oxidative coupling of 2,6-substituted phenols. The advantage of these polymers, over other thermally stable polymers, is that they can be melt-fabricated and have a melting temperature of the order of 350 °C. They can be processed on conventional moulding and extrusion equipment, and a particularly notable physical property is their low thermal expansion rate. This property makes them fit for use where high dimensional tolerance is the prime requirement.

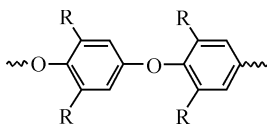


Fig. 1.17. Representative structure of polyphenylene oxide. R represents an alkyl group

### 1.6.8 Polynorbornene (PNB)

Polynorbornenes are the latest high performance polymers. Polymers derived from norbornene have attracted special interest due to their applications in oil spill recovery or as a sound barrier. Polynorbornene has excellent dielectric properties and a cost advantage over other materials currently being used as interlevel dielectrics. Polynorbornene has been found to be an excellent binder for the preparation of solid fuel materials and solid propellants. Its structure is shown in Fig. 1.18.

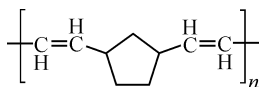


Fig. 1.18. Representative structure of polynorbornene

The bicyclic variation of polynorbornene is a polymer currently under investigation for a number of applications, including deep ultraviolet photoresists and interlevel dielectrics in microelectronics applications.<sup>[116-122]</sup> The 2,3-norbornene monomer undergoes a vinyl-like polymerization that preserves the bicyclic conformation in the backbone of the resulting polymer, as seen in Fig. 1.19.

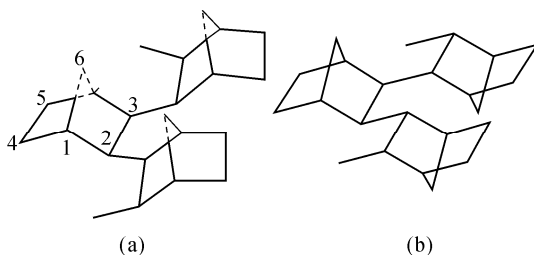


Fig.1.19. Representative structure of polynorbornene. The three disyndiotactic (a) and erythro diisotactic (b) trimmers are shown to illustrate possible stereochemical variation (Adapted from Ref. 116. Copyright (1998), with permission from the American Chemical Society)

This is unlike the commonly employed ring-opening metathesis polymerization (ROMP) mechanism which retains only a single ring in the polymer backbone. This polymer is currently being developed by the BFGoodrich Corp. under the trade name Avatrel dielectric polymer. Polynorbornene has excellent dielectric properties and a cost advantage over other materials currently being used as interlevel dielectrics.<sup>[117-122]</sup> Polynorbornene has been found to be an excellent binder for the preparation of solid fuel materials and solid propellants. Mixtures of polynorbornene with liquid fuel materials such as kerosene, gasoline, or advanced missile and aircraft liquid fuels such as JP-4, JP-5, JP-9, JP-10, RJ-4, and RJ-5, for example, can contain 80% or more of the liquid fuel material and still exist in the form of a tough rubbery polymer which has excellent burning characteristics as a solid fuel for a ramjet. Many of these materials can be tailored to have a combustion heat higher than the state-of-the-art solid ramjet fuel formulations. In

addition, self-sustaining gas-generating compositions which can be used for such various purposes as solid propellants or gas generators for ducted rockets and the like can be fabricated by inclusion in the polynorbornene, either alone or in conjunction with suitable liquid fuels and other additives of particulate oxidizer materials such as ammonium perchlorate or any of the other solid particulate oxidizers commonly used in the preparation of composite solid propellants. Suitable compositions can be prepared by admixture of the polynorbornene with the liquid fuel and suitable plasticizers and vulcanizing agents therefore. In the case in which a solid self-sustaining gas-generating composition is to be formulated, the suitable particulate oxidizing material and other solid ingredients can be mixed with the polynorbornene prior to the addition of the liquid ingredients, then curing the mixture into a tough rubbery polymeric structure. It is also possible to polymerize the norbornene monomer in situ in the presence of oxidizers, antioxidants, plasticizers and a suitable polymerization catalyst such as ruthenium chloride.

For the semi-conductor industry, it is required that the wavelength of exposure tools must shrink over time. At these extremely low wavelengths (such as 193 nm), the design of transparent polymers is a difficult problem due to the tendency for a wide variety of organic groups to absorb strongly in this ultraviolet wavelength range. Substituted polynorbornenes (PNBs) are one potential material solution for providing transparent photoresist polymer resins for photolithography at 193 nm.<sup>[122]</sup> The polynorbornene backbone provides a relatively transparent alicyclic polymer structure with suitable plasma etch resistance. For a 193 nm photoresist resin, the characteristics of a pendant side group include: solubility in the common aqueous alkaline developers used for resist processing, the ability to add acid-labile protecting groups to the polymer for producing chemically amplified resists with high contrasts, and reduction of the absorbance coefficient of the polymer due to the incorporation of fluorine.

## 1.7 Summary

High performance polymers which cover a wide range of applications are discussed in this chapter. We have given special emphasis to polyimides, both aliphatic and aromatic ones. Aliphatic polyimides, as a new field, are also reported as good candidates for applications in microelectronics and optoelectronics, owing to their excellent transparency, solubility and low dielectric constant. This chapter also dealt with the applications of the semi-conducting aromatic polyimides in organic electroluminescent devices and flexible substrates. Polyimide-based nanohybrids obtained from the polyimide/silica hybrid compositions by sol-gel process, their microstructure, interfacial interactions, properties and application studies conducted by our research group are also briefly discussed. Other high performance polymers are also the focus of this chapter. Polynorbornenes, which have attracted the researchers' attention due to their higher transparency and lower

dielectric constant, due to the aliphatic backbone together with high thermal resistance, are one of the best candidates for successful future applications. A short description of polynorbornenes together with other commercial engineering polymers like PEEK, PSU, PC, polysulphides and polyamides are also summarized in this chapter.

## References

- [1] Dohany, J. E., Humphry, J. S., Kroschwitz, J. I. *Encyclopedia of Polymer Science and Engineering*, 2nd ed. Mark, H. F., Bikales, N. M., Overberger, C. G., Menges, G., Eds. Wiley Interscience, New York, 1989.
- [2] Lynn, M. M., Worm, A. T. *Encyclopedia of Polymer Science Engineering*, Kroschwitz, J. I., Ed. Wiley Interscience, New York, 1987.
- [3] Feldman, D., Barbalata, A. *Synthetic Polymers: Technology, Properties, Applications*. Elsevier, USA, 1996.
- [4] Ferry, M. H., Becker, A. V., Bhatia, S. C. *Handbook of Polymer Technology and Applications*. Rapra Technology Limited, UK, 2006, vol. 1.
- [5] Throne, J. L. *Plastic Processing Engineering*. Noyes, UK, 1993.
- [6] Ferry, M. H., Becker, A. V., Bhatia, S. C. *Handbook of Polymer Technology and Applications*. Rapra Technology Limited, UK, 2006, vol. 2.
- [7] MacDermott, C. *Selecting Thermoplastics for Engineering Applications*. Marcel Dekker: Reinhold, USA, 1994.
- [8] Mathews, A. S., Kim, I., Ha, C. S. *Macromol. Res.*, 2007, 15: 114.
- [9] Mittal, K. L., Ed. *Polyimides: Synthesis, Characterization and Applications*. Plenum, New York, 1984.
- [10] Feger, C., Khojasteh, M. M., McGrath, J. E., Eds. *Polyimides: Materials, Chemistry and Characterization*. Elsevier, Amsterdam, 1989.
- [11] Polyimides, Wilson, D., Stenzenberger, H. D., Hergenrother, P. M., Eds. Blackie: Glasgow, UK, 1990.
- [12] Ghosh, M. K., Mittal, K. L., Eds. *Polyimides Fundamentals and Applications*. Marcel Decker, New York, 1996.
- [13] Faghihi, K., Hagibeygi, M. *Macromol. Res.*, 2005, 13: 14.
- [14] Ree, M. *Macromol. Res.*, 2006, 14(1): 1.
- [15] Cho, Y. H., Park, J. M., Park, Y. H. *Macromol. Res.*, 2004, 12: 38.
- [16] Ishida, H., Wellinghoff, S. T., Baer, E., Koenig, J. L. *Macromolecules*, 1980, 13: 826.
- [17] Wellinghoff, S. T., Ishida, H., Koenig, J. L., Baer, E. *Macromolecules*, 1980, 13: 834.
- [18] Li, X. D., Zhong, Z. X., Jin, G. *Macromol. Res.*, 2006, 14: 257.
- [19] Harris, F. W., Hsu, S. L.-C. *High Perform. Polym.*, 1989, 1: 3.
- [20] Lim, H., Cho, W. J., Ha, C. S., Ando, S., Kim, Y. K., Park, C. H., Lee, K. *Adv. Mat.*, 2002, 14: 1275.

- [21] Ha, C. S. *Curr. Trends in Polym. Sci.*, 2002, 7: 85.
- [22] Wahab, M. A., Kim, I., Ha, C. S. *Polymers*, 2003, 44: 4705.
- [23] Kim, Y., Kwan, H. B., Young, Y. J., Dong, K. C., Ha, C. S. *Chem. Mater.*, 2004, 24: 5051.
- [24] Kim, Y., Ree, M., Chang, T., Ha, C. S., Nunes, T. L., Lin, J. S. *J. Polym. Sci. Part B: Polym. Phys.*, 1995, 33: 2075.
- [25] Bessonov, M. I., Koton, M. M., Kudryavtsev, V. V., Laius, L. A. *Polyimides Thermally Stable Polymers*. Consultants Bureau, New York, 1987.
- [26] Edwards, W. M., Robinson, I. M. U.S. Patent 2867609, 1959.
- [27] Kreuz, J. A. U.S. Patent 3271366, 1966.
- [28] <http://en.wikipedia.org/wiki/kapton>
- [29] Rojstaczer, S., Ree, M., Yoon, D. Y., Volksen, W. J. *Polym. Sci., Part B: Polym. Phys.*, 1992, 30: 133.
- [30] Kochi, M., Isoda, S., Yokota, R., Kambe, H. J. *Polym. Sci., Part B: Polym. Phys.*, 1986, 24: 1619.
- [31] Wrasidlo, W. J. *Macromol. Sci. Phys.*, 1972, B3: 559.
- [32] Kim, Y., Goh, W. H., Chang, T., Ha, C. S., Ree, M. *Adv. Eng. Mater.*, 2004, 6: 39.
- [33] Chung, I. S., Park, C. E., Ree, M., Kim, S. Y. *Chem. Mater.*, 2001, 13: 2801.
- [34] Kim, Y., Kang, E., Kwon, Y. S., Cho, W. J., Chang, C., Ree, M., Chang, T., Ha, C. S. *Synth. Metals*, 1997, 85: 1399.
- [35] Kim, Y., Ree, M., Chang, T., Ha, C. S. *Polym. Bull.*, 1995, 34: 175.
- [36] Robertson, W. M., Arjavalingam, G., Hougham, G., Kopcsay, G. V., Edelstein, D., Ree, M., Chapple-Sokol, J. P. *Electronics Lett.*, 1992, 28: 62.
- [37] Shin, J. H., Park, J. W., Lee, W. K., Jo, N. J., Cho, W. J., Ha, C. S. *Synth. Metals*, 2003, 137: 1017.
- [38] Kim, Y., Lee, J. G., Choi, D. K., Jung, Y. Y., Park, B., Keum, J. H., Ha, C. S. *Synth. Met.*, 1997, 91: 329.
- [39] Ha, H. O., Cho, W. J., Ha, C. S. *Mol. Cryst. Liq. Cryst.*, 2000, 349: 443.
- [40] Sakai, Y., Ueda, M., Yahagi, A., Tanno, N. *Polymer*, 2002, 43: 3497.
- [41] Ha, C. S., Park, H. D., Frank, C. W. *Chem. Mater.*, 2000, 12: 839.
- [42] Carter, K. R., DiPietro, R. A., Sanchez, M. I., Swanson, S. A. *Chem. Mater.*, 2001, 13: 213.
- [43] Ha, C. S., Shin, J. H., Lim, H. T. *Mater. Sci. Eng. B-SOLID*, 2001, 85: 195.
- [44] Lee, S. J., Ha, C. S., Lee, J. K. *J. Appl. Poly. Sci.*, 2001, 82: 2365.
- [45] Mochizuki, A., Fukuoka, T., Kanada, M., Kinjou, N., Yamamoto, T. J. *Photopolym. Sci. Technol.*, 2002, 15: 159.
- [46] Lee, S. W., Kim, S. I., Lee, B., Choi, W., Chae, B., Kim, S. B., Ree, M. *Macromolecules*, 2003, 36: 6527.
- [47] Park, H. J., Park, J. W., Jeong, S. Y., Ha, C. S. *IEEE Proceedings*, 2005, 93: 1447.
- [48] Pyo, S. M., Kim, S. I., Shin, T. J., Ree, M., Park, K. H., Kang, J. S. *Macromolecules*, 1998, 31: 4777.
- [49] <http://www.pslc.ws/macrog/imide.htm>
- [50] Eliette, P., Barthe, M. F., Baerdemaeker, J. D., Mercier, R., Neyertz, S.,

- Alberola, N. D., Bas, C. J. *Polym. Sci. Part B: Polym. Phys.*, 2003, 41: 2998.
- [51] Chisso Corp. *Jpn. Kokai Tokkyo Koho*, JP 90 294330. *Chem. Abstr.*, 1990, 116: 42762u.
- [52] Mercer, F. W., McKenzie, M. T. *High Perform. Polym.*, 1993, 5: 97.
- [53] Jin, Q., Yamashita, T., Horie, K. *J. Polym. Sci., Part A: Polym. Chem.*, 1994, 32: 503.
- [54] Ando, S. *J. Photopolym. Sci. Technol.*, 2004, 17: 219.
- [55] Joly, C., Smaïhi, M., Porcar, L., Noble, R. D. *Chem. Mater.*, 1999, 11: 2331.
- [56] Mahoney, C. M., Gargella, Jr. J. A. *Macromolecules*, 2002, 35: 5256.
- [57] Furukawa, N., Yamada, Y., Furukawa, M., Yuasa, M. M., Kimura, Y. *J. Polym. Sci. Part A: Polym. Chem.*, 1997, 35: 2239.
- [58] Matsuura, T., Ishizawa, M., Hasuda, Y., Nishi, S. *Macromolecules*, 1992, 25: 3540.
- [59] Fort, R. C., and Schleyer, P. R. Jr. *Chem Rev.*, 1964, 64: 277.
- [60] Chern, Y. T., Shiue, H. C. *Chem. Mater.*, 1998, 10: 210.
- [61] Chern, Y. T., Chung, W. H. *J. Polym. Sci. Part A: Polym. Chem.*, 1996, 34: 117.
- [62] Chern, Y. T. *Macromolecules*, 1998, 31: 5837.
- [63] Watanabe, Y., Sakai, Y., Ueda, M., Oishi, Y., Mori, K. *Chem. Lett.*, 2000, 29: 450.
- [64] Watanabe, Y., Shibasaki, Y., Ando, S., Ueda, M. *J. Polym. Sci. Part A: Polym. Chem.*, 2004, 42: 144.
- [65] Watanabe, Y., Sakai, Y., Shibasaki, Y., Ando, S., Ueda, M. *Macromolecules*, 2002, 35: 2277.
- [66] Seino, H., Sasaki, T., Mochizuki, A., Ueda, M. *High Perform. Polym.*, 1999, 11: 255.
- [67] Seino, H., Mochizuki, A., Ueda, M. *J. Polym. Sci. Part A: Polym. Chem.*, 1999, 37: 3584.
- [68] Mathews, A. S., Kim, I., Ha, C. S. *J. Appl. Polym. Sci.*, 2006, 102: 3316.
- [69] Mathews, A. S., Kim, I., Ha, C. S. *J. Polym. Sci. Part A: Polym. Chem.*, 2006, 44: 5254.
- [70] Oishi, Y., Onodera, S., Oravec, J., Mori, K., Ando, S., Terui, Y., Maeda, K. *J. Photopolym. Sci. Technol.*, 2003, 16: 263.
- [71] Oishi, Y., Kikuchi, N., Mori, S., Ando, S., Maeda, K. *J. Photopolym. Sci. Technol.*, 2002, 15: 213.
- [72] Matsumoto, T. *High Perform. Polym.*, 2001, 13: S85.
- [73] Kaneda, T., Katsura, T., Nakagawa, K., Makino, H. *J. Appl. Polym. Sci.*, 1986, 32: 3133.
- [74] Jeon, J. Y., Tak, T. M. *J. Appl. Polym. Sci.*, 1996, 61: 371.
- [75] Volksen, W., Cha, H. J., Sanchez, M. I., Yoon, D. Y. *React. Funct. Polym.*, 1996, 30: 61.
- [76] Matsumoto, T. *Macromolecules*, 1999, 32: 4933.
- [77] Kim, Y., Ha, C. S. Semiconducting polyimide nanolayers for organic nanoelectronics: The first applications to hybrid organic light emitting devices” in “Nanotechnology at The Leading Edge. Dirote, E. V., Ed. Nova

- Science Publishers, Inc., New York, 2007.
- [78] Kim, Y. Ph.D. Thesis (molecular/nano composite thin films based on high performance rigid rodlike BPDA-PDA polyimide and organic electroluminescence devices). Pusan National University, Korea and references therein, 1996
- [79] Kim, Y., Goh, W. H., Chang, T., Ha, C. S., Ree, M. *Adv. Eng. Mater.*, 2004, 6: 39.
- [80] Kim, Y., Lee, J. G., Han, K., Hwang, H. K., Choi, D. K., Jung, Y. Y., Keum, J. H., Kim, S., Park, S. S., Im, W. B. *Thin Solid Film.*, 2000, 363: 263.
- [81] Kim, Y., Han, K., Ha, C. S. *Macromol.*, 2002, 35: 8759.
- [82] Kim, Y., Jeong, Y. Y., Choi, D. K. *IEEE J. Quantum Electron*, 2002, 38: 1039.
- [83] Kim, Y., Bae, K. H., Jeong, Y. Y., Choi, D. K., Ha, C. S. *Chem. Mater.*, 2004, 16: 5051.
- [84] Kim, Y., Lee, J. G. US Patent 2002, 6497969 B2.
- [85] Lee, J. G., Kim, Y. US Patent 2002, 6379743 B1.
- [86] Han, K., Kim, Y., Lee, J. G., Choi, D. K. US Patent, 2002, 6,337,404 B1 and 6,342,637 B1.
- [87] Kim, Y., Ha, C. S., Lim, H. *Advances in organic light-emitting devices*. Trans Tech Publishing Co., Switzerland, 2006.
- [88] Kim, Y., Cook, S., Sachtan, T. M., Choulis, S. A., Nelson, J., Durrant, J. R., Bradley, D. D. C., Ha, C. S., Ree, M. *Nature Mater.*, 2005, 5: 197.
- [89] Choulis, S. A., Kim, Y., Nelson, J., Bradley, D. D. C., Giles, M., Shkunov, M., McCulloch, I. *Appl. Phys. Lett.*, 2004, 85: 3890.
- [90] Kim, Y., Cook, S., Choulis, S. A., Nelson, J., Durrant, J. R., Bradley, D. D. C. *Chem. Mater.*, 2004, 16: 4812.
- [91] Kim, Y., Oh, E., Choi, D., Ha, C. S. *Nanotechnology*, 2004, 15: 149.
- [92] Lim, H. T., Lee, N. J., Lee, S. E., Jeong, H. I., Lee, K. H., Cha, M. S., Suh, H. S., Ha, C. S. *Thin Solids Films*, 2000, 363: 152.
- [93] Lim, H., Cho, W. J., Ha, C. S., Ando, S., Kim, Y., Park, C., Lee, K. *Adv. Mater.*, 2002, 14: 1275.
- [94] Wahab, M. A., Kim, I., Ha, C. S. *Silica- and Silsesquioxane-Containing Polymer Nanohybrids*, In: *Macromolecules Containing Metal and Metal-Like Elements*. Abd-El-Aziz, A. S., Carrahe, C. E. Jr., Pittman, C. U. Jr., Zeldin, M., Eds. Wiley Interscience, New York, 2005, vol. 4.
- [95] Ahn, J.H., Kim, I., Ha, C. S. *Polym. Sci. Technol.*, 2009, 20: 1.
- [96] <http://En.wikipedia.org/wiki/peek>
- [97] Ozden, S., Charayev, A. M., Shaov, A. H. *J. Mater. Sci.*, 1999, 34: 2741.
- [98] Lin, Y., Daghyani, H. R. *J. Mater. Sci. Letters*, 1996, 15: 1536.
- [99] Diffey, B. L. *Photodermatology*, 1984, 1: 151-157.
- [100] Casale, G. R., Borra, M., Colosimo, A., Colucci, M., Militello, A., Siani, A. M., Sisto, R. *Phys. Med. Biol.*, 2006, 51: 4413.
- [101] Parisi, A. V., Meldrum, L. R., Kimlin, M. G. *Protection Against the Hazards of UVR: Virtual Conf.* 18 Jan. – 5 Feb., 1999.
- [102] Rivaton, A., Gardette, J. L. *Polym. Degradation Stab.*, 1999, 66: 385.
- [103] Draganjac, M. E., Rauchfuss, T. B. *Angew. Chem. Int. Ed.*, 1985, 24: 742.



- [104] <http://en.wikipedia.org/wiki/Polysulfide>
- [105] Takeda, N., Tokitoh, N., Okazaki, R. *Top. Curr. Chem.*, 2003, 231: 153.
- [106] <http://www.pslc.ws/mactest/pc.htm>
- [107] Howdeshell, K. L., Peterman, P. H., Judy, B. M., Taylor, J. A., Orazio, C. E., Ruhlen, R. L., Vom Saal, F. S., Welshons, W. V. *Environ. Health Perspect*, 2003, 111: 1180.
- [108] <http://en.wikipedia.org/wiki/polycarbonate>
- [109] Vom Saal, F. S., Hughes, C. *Environ. Health Perspect*, 2005, 113: 926.
- [110] Rosato, D. V. *Polyamides*. Van Nostrand Reinhold, USA.
- [111] Zimmerman, J. *Polyamides*. In "Encyclopedia of Polymer Science and Engineering" (H. F. Mark, N. M. Bikales, C. G. Overberger and G. Menges, eds.), Wiley-Interscience, New York, 1988, 11: 340.
- [112] Gallini, J. *Polyamides-Aromatic*, Encyclopedia of Polymer Science and Technology. John Wiley & Sons, New York, 2005.
- [113] Kohan, M. *Nylon Plastics Handbook*, 1995. Hanser Publishers, New York, 1996.
- [114] [http://en.wikipedia.org/wiki/Polybutylene\\_terephthalate](http://en.wikipedia.org/wiki/Polybutylene_terephthalate)
- [115] Sahoo, N. G., Das, C. K., Jeong, H., Ha, C. S. *J. Elastomers Plast.*, 2004, 36: 77.
- [116] Ahmed, S., Bidstrup, S. A., Kohl, P. A., Ludovice, P. J. *J. Phys. Chem.*, B. 1998, 102: 9783.
- [117] Grove, N. R., Zhao, Q., Kohl, P. A., Bidstrup-Allen, S. A., Shick, R. A., Goodall, B. L., McIntosh, L. H., Jayaraman, S. *Adv. Microelectron*, 1996, 23: 16.
- [118] Grove, N. R., Zhao, Q., Kohl, P. A., Bidstrup-Allen, S. A., Shick, R. A., Goodall, B. L., McIntosh, L. H., Jayaraman, S. *IEEE Multichip Module Conf. Proc.*, 1997.
- [119] *HOECHST Magazin Future IV.*, 1995, 52.
- [120] *HOECHST Magazin Future IV Special Science 1*, 1995, 32.
- [121] Osan, F., Hatke, W., Helmer-Metzmann, F., Jacobs, A. L., Weller, H. T. *Cycloolefinic Copolymers*, Lecture Bayreuth Polymer Symposium, 1995.
- [122] Pierce, D. W., Realff, M. J. *Comput. Chem. Eng. Suppl Part B.*, 1996, 20: S1307.

---

## Advanced Biodegradable Organic Polymers

### Hong Li

Key laboratory of Functional Polymer Materials of Education Ministry, Institute of Polymer Chemistry, Nankai University, Tianjin, 300071, P. R. China

Tel.: +86-22-2350-8388; Fax: +86-22-2350-3510

E-mail: hongli@nankai.edu.cn

### 2.1 Introduction

In recent years, with the rapid development of pharmacology and biomedical science, the need for biodegradable polymers to possess excellent biocompatibility increases steeply. Among the variety of synthetic biodegradable polymers, linear aliphatic polyesters, polylactic acid (PLA), polyglycolic acid (PGA) and related copolymers are particularly attractive and most widely used. These polymers have found many significant applications in the field of biomedical science as drug-delivery carriers, resorbable sutures, artificial-tissue materials and so forth.<sup>[1-6]</sup>

Some biomedical devices made from synthetic polyesters are now commercially available<sup>[7]</sup>, as seen in Table 2.1. The incomparable advantage of the devices or implants made from biodegradable polymers is that they do not need to be removed surgically once they are no longer needed. Therefore they are of great value in short-term applications that require only the temporary presence of a device or implant. At the same time, the use of biodegradable devices/implants can circumvent some of the problems related to the long-term safety of permanently implanted devices/implants. As drug-carriers, the use of biodegradable polymers could increase drug-efficiency by controlling the release of the drug.

**Table 2.1** Commercially available medical devices made from biodegradable polymers

Application	Trade name	Composition*	Manufacturer
Suture anchors	Phantom Suture Anchor	PLLA	Du Puy
	SD Sorb	P(LLA-GA)	Surgical Dynamics
Fracture fixation	Smart Anchor	SR-PLLA	Bionx Implants
	Smart Pins, Smart Screw	SR-PLLA	Bionx Implants
		PDO	J&J. Orthopedics
Interference screws	Bio Screw	PLLA	Linvatec
		P(DLLA-GA)	Instrument Makar
Meniscus repair	Clearfix Meriscal Screw	PLLA	Innovasive Devices
	Menicus Arrow	SR-PLLA	Bionx Implants
	SD Sorb Meniscal Staple	P(LLA-GA)	Surgical Dynamics
ACL reconstruction	Biologically Quiet Staple	P(DLLA-GA)	Instrument Makar
Maxillofacial fixation	Lacto Sorb Screws and Plates	P(LLA-GA)	Biomet

\*LA: lactide; LLA: L-lactide; DLLA: D,L-lactide; GA: glycolide; PLLA: poly(L-lactide); PDO: poly(dioxanone); SR: self-reinforced

As is well-known, the properties of a biodegradable polymer (mechanical properties, degradation rate, hydrophilicity etc.) are largely dependent on its molecular weight (MW), MW distribution, chain stereochemistry, etc. Controlled synthesis of the biodegradable polymers with desired properties by means of living or stereospecific polymerizations is hence of significance. Great advances in polymer science in recent years have made it possible to design initiators and/or catalysts for the controlled synthesis of biodegradable polymers with desired MW and well-defined structures.

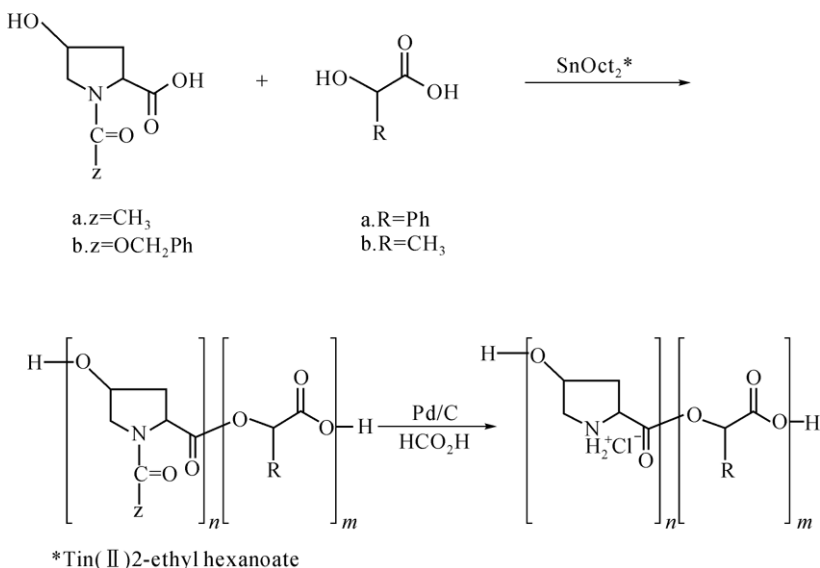
This article deals with recent developments in the controlled synthesis of biodegradable polymers, especially aliphatic polyesters based on lactic acid/lactide (LA). As one of the two synthetic approaches, the polycondensation technique has made great progress in the synthesis of high-MW biodegradable polymers. However, from the viewpoint of macromolecular design, it is not as useful as the ROP technique. In general, the catalysts or initiators suitable for the ring-opening polymerization (ROP) of lactides are also suitable for the polymerization of lactones and morpholinediones and other cyclic esters. The discussion is hence centered on the living and stereospecific or stereoselective ROP of LAs, particularly that which uses low-toxic/non-toxic metal compounds and metal-free organic compounds to initiate the controlled polymerization.

## 2.2 Synthesis of Biodegradable Polymers by Polycondensation

Two different approaches are used for biodegradable polymer synthesis: i.e., polycondensation and ring-opening polymerization (ROP). Each approach has its own advantages.

### 2.2.1 General Polycondensation Technique

Biodegradable polymers can be synthesized by polycondensation of: (i) a diol with a dicarboxylic acid (such as 1,3-propanediol and succinic acid); (ii) hydroxyacids. This is either by self-polycondensation of a hydroxyacid (e.g., lactic acid, glycolic acid) or by cross-polycondensation of two different hydroxyacids. In the latter case, careful selection of the reaction conditions is needed. Lee et al. synthesized a kind of pseudo poly(amino acid)s by the cross-polycondensation of *trans*-4-hydroxy-L-proline and  $\alpha$ -hydroxyacid (Scheme 2.1).<sup>[8]</sup>



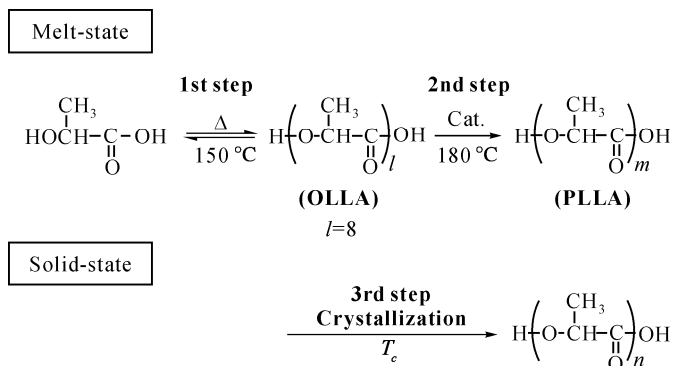
**Scheme 2.1.** A kind of pseudo poly(amino acid)s synthesized by the cross-polycondensation of *trans*-4-hydroxy-L-proline and  $\alpha$ -hydroxyacid (Adapted from Ref. 8. Copyright (2001), with permission from Wiley)

Pseudo poly(amino-acid)s are among the newest classes of biodegradable polymers, having the advantages of being amphiphilic, biocompatible and possessing pendant functional groups on the backbone.

The polycondensation technique is less expensive than ROP. It can be applicable for a variety of combinations of diols and diacids. However, it requires, in general, higher temperature and longer reaction time and usually hardly to obtain high-MW polymers. In addition, polymers made in this way do not have controlled lengths and stereostructures, because the polycondensation is neither living nor stereospecific. This approach is hence not suitable for the design and tailoring of biodegradable polymers.

## 2.2.2 Post Polycondensation Technique

Recently, a breakthrough in synthesizing high-MW biodegradable polymers by polycondensation was made by Kimura who developed a so-called post-polycondensation, i.e., melt/solid polycondensation technique to prepare poly(L-lactic acid) (PLLA) with high-MW.<sup>[9]</sup> It is a three-step polycondensation. In the first step, melt polycondensation of L-LA was conducted at 150 °C, and an oligomer with (degree of polymerization) DP of 8 on average was obtained. In the second step, the melt-state polycondensation was conducted at 180 °C and reduced pressure (10 mmHg) using the catalyst system of SnCl<sub>2</sub>·2H<sub>2</sub>O-TSA (*p*-toluene sulfonic acid), and a polymer with weight average MW ( $M_w$ ) of 13,000 (PDI = 1.9,  $T_m$  = 157 °C,  $T_g$  = 48 °C) was obtained. In the third step, the melt-polycondensate was firstly heat-treated at 105 °C for a couple of hours, then the solid-state post-polycondensation was conducted at 150 °C for 10 h, and a polymer with high MW ( $M_w$  = 3.2×10<sup>5</sup>) and higher crystallinity (≥85%) was obtained (Scheme 2.2).<sup>[9-11]</sup>



**Scheme 2.2.** A three-step polycondensation of synthesizing high-MW biodegradable polymers (Adapted from Ref. 9. Copyright (2000), with permission from Wiley)

According to the authors, in the 3rd step, the crystallization of the polymer chains could effectively cause the segregation and concentration of propagation active ends and the catalyst in the amorphous parts with the enhancing of the polycondensation. This accounts for the plausible mechanism of the solid-state post-polycondensation (Fig. 2.1).

By means of the post-polycondensation technique, PLLA with very high MW (>500,000 Da), high crystallinity (>85%) and good thermomechanical properties ( $T_m$ >179 °C) was prepared. However, one shortcoming of this process is that the catalyst SnCl<sub>2</sub> is cytotoxic. It was gratifying to know that using zinc acetate dihydrate Zn(OAc)<sub>2</sub>·2H<sub>2</sub>O, a non-toxic salt, as catalyst, poly(glycolic acid) (PGA) with higher MW ( $M_w$  = 44,000) and better molecular weight distribution (MWD) (polydispersity index (PDI) of 1.8) was prepared by this technique.<sup>[11]</sup>

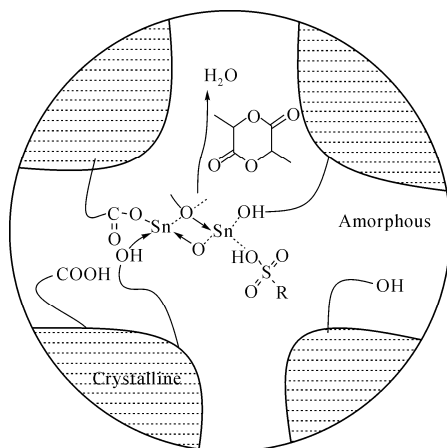
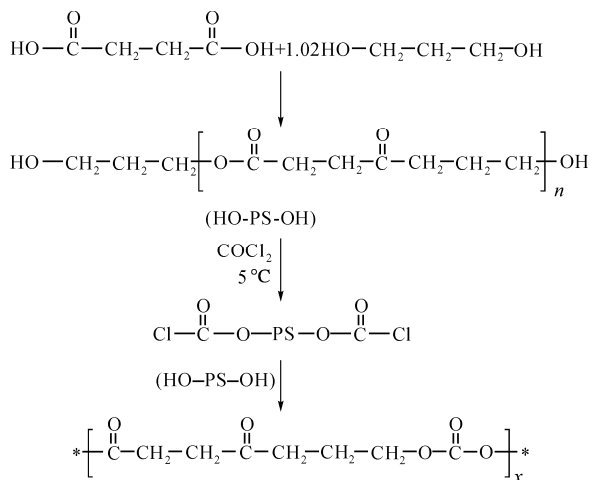


Fig. 2.1. Plausible mechanism of the solid-state post-polycondensation

### 2.2.3 Chain-Extension Technique

Another way to obtain high-MW biodegradable polymers via polycondensation is the so-called “Chain-extension” technique. Using this technique a higher MW poly(ester-carbonate) ( $M_w=48,000$ ,  $PDI=1.6$ ) was prepared (Scheme 2.3).<sup>[12]</sup> Thus, using a molar ratio of 1,3-propanediol to succinic acid of 1.02, an  $\alpha,\omega$ -bis-hydroxy-terminated oligomer (HO-PS-OH) having  $M_n$  of 2,200 and  $M_w$  of 3,000 was obtained. The oligomer was converted to an  $\alpha,\omega$ -bischloroformate by the reaction with phosgene. The final polymer was prepared by the polycondensation of the oligomer with the bischloroformate.



Scheme 2.3. High-MW biodegradable polymers synthesized by the so-called “Chain-extension” technique (Adapted from Ref. 12. Copyright (2000), with permission from Wiley)

Using diisocyanates as a chain-extension agent PLLA with higher MW ( $M_w = 57,000$ ) was produced from a pre-poly(L-lactic acid) with  $M_w = 9,800$ .<sup>[13]</sup>

### 2.2.4 *Enzyme-Catalyzed Polycondensation*

Enzyme-catalyzed polymerizations provide an environmentally friendly methodology for biodegradable polymer synthesis owing to the non-toxicity of the catalyst enzymes and the mild reaction conditions. Lipase catalyzed dehydration polycondensation of a diol and a diacid for biodegradable polyester synthesis has been intensively investigated. However, polyesters of low MW (<10,000) are usually obtained by this technique.<sup>[14]</sup>

By careful screening of different lipases and solvents, a polyester of higher MW ( $M_w = 77,000$ , PDI = 4.4) was prepared by the condensation polymerization of adipic acid and hexanediol in diphenyl ether at 37 °C for 7 d under reduced pressure (0.15 mmHg) using lipase M. michei.<sup>[15]</sup>

## 2.3 **Synthesis of Biodegradable Polymers by Ring-Opening Polymerization**

The ring-opening polymerization (ROP) of cyclic esters (e.g., lactides, lactones, morpholinediones) is an effective method for synthesizing biodegradable polyesters. It has some advantages over the polycondensation technique. Under rather mild conditions, high-MW polyesters of low dispersity can be prepared in short periods of time by this technique. Problems associated with polycondensation, such as the need for exact stoichiometry, high reaction temperatures and the removal of low MW by-products (e.g., water) are excluded in ROP. In recent years, quite a lot of catalysts and/or initiators were found to bring about living and/or stereospecific ROP of cyclic esters. This synthetic approach of ROP is hence becoming a useful tool for the design and tailoring of biodegradable polymers with desired properties and well-defined structures.

Depending on the initiators, ROP proceeds according to three different major reaction mechanisms, such as cationic, anionic and coordination mechanisms.

### 2.3.1 *Monomers*

The monomers that have been used for biodegradable polymer synthesis include lactides: L-lactide (LLA), D-lactide (DLA), D,L-lactide (DLLA or *rac*-LA), *meso*-lactide (*meso*-LA), glycolide (GA); lactones:  $\beta$ -propiolactone ( $\beta$ -PL),  $\gamma$ -butyrolactone

( $\gamma$ -BL),  $\beta$ -butyrolactone ( $\beta$ -BL),  $\delta$ -valerolactone ( $\delta$ -VL),  $\omega$ -caprolactone ( $\omega$ -CL), 1,5-dioxepan-2-one (DXO), etc. (Fig. 2.2).

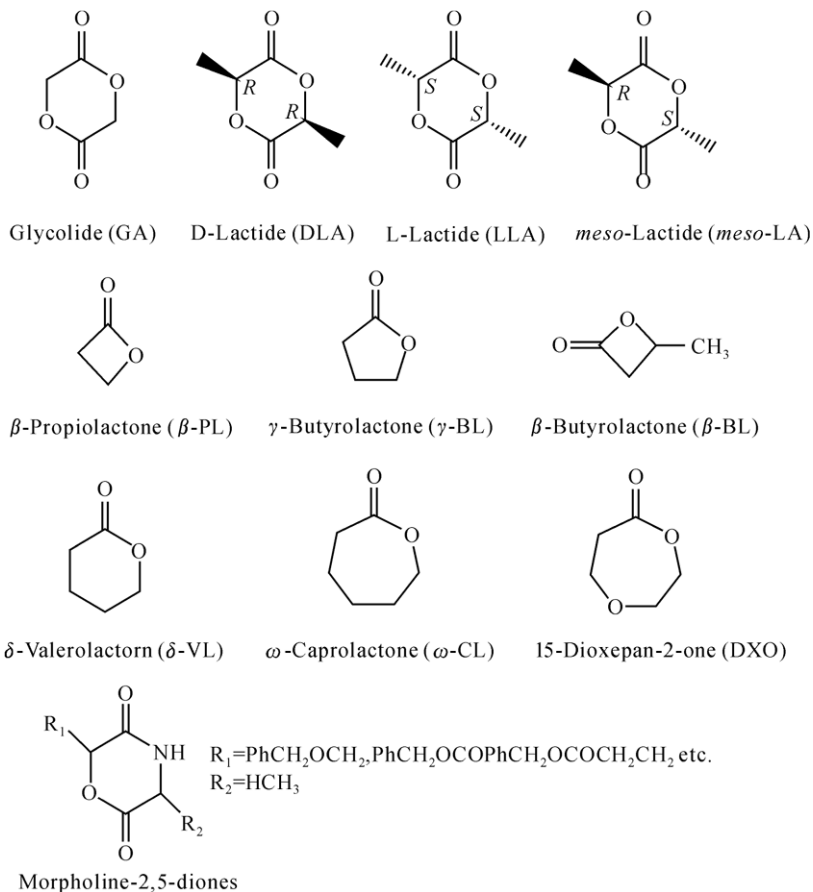


**Fig. 2.2.** Structures of different monomers used for biodegradable polymer synthesis

It is worth noting that polymer prepared from lactic acid by polycondensation is usually referred to as polylactic acid, while the same polymer prepared from lactide by ROP is referred to as poly(lactide). Both poly(lactide) and polylactic acid are usually abbreviated as PLA in references.

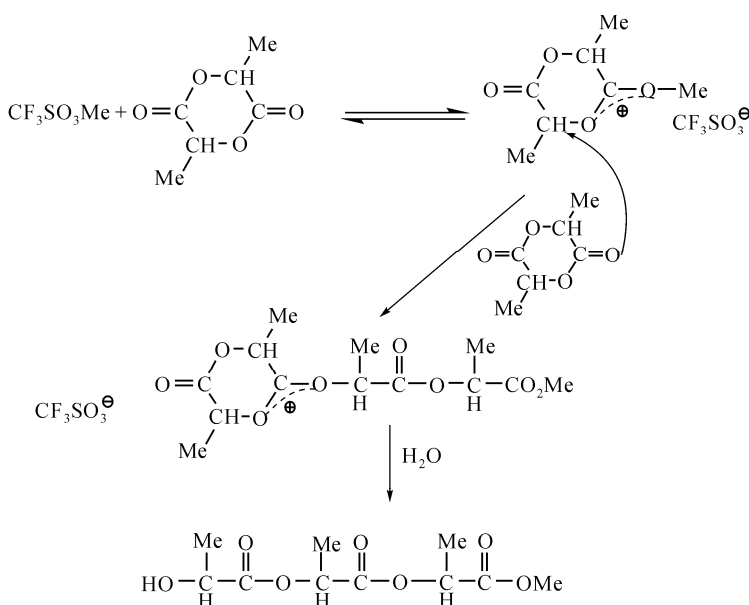
### 2.3.2 Polymerization with Metal Catalysts

Depending on the initiators, ROP proceeds according to three different major reaction mechanisms, such as cationic, anionic and coordination mechanisms. In this section, we will introduce them separately.



### 2.3.2.1 Cationic Ring-Opening Polymerization

Cationic ROP of cyclic esters is far less successful than the coordination ROP. Only a few extremely strong acids or carbenium ion donors are capable of initiating the cationic ROP. Among the numerous acidic compounds investigated, trifluoromethane sulfonic acid ( $\text{HOT}_f$ ) and methyl trifluoromethane sulfonate ( $\text{MeOT}_f$ ) have proved to be efficient initiators.<sup>[16-18]</sup> For ROP of LAs, the mechanism involves the protonation or alkylation of the carbonyl oxygen atom in the lactide molecule, with the consequence of an electrophilic activation of the  $\text{O}-\text{CH}$  bond. This bond is then cleaved by the nucleophilic attack of another monomer molecule, a process which is repeated in every propagation step (Scheme 2.4).

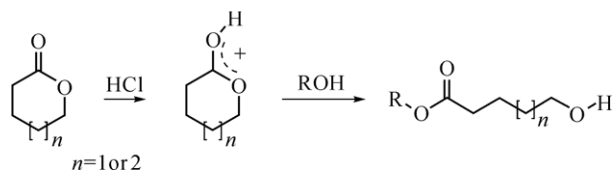


**Scheme 2.4.** Mechanism for ring-opening polymerization (ROP) of LAs

This mechanism involves a nucleophilic substitution at the chiral carbon, and it was found that at a lower temperature ( $\leq 50$  °C) optical pure PLLA can be prepared. At a higher temperature racemization occurs, which dramatically changes the properties (physical, mechanical) of the resulting polymer. Unfortunately, the polymerization is rather slow below 50 °C, and only yields low-MW polymers.

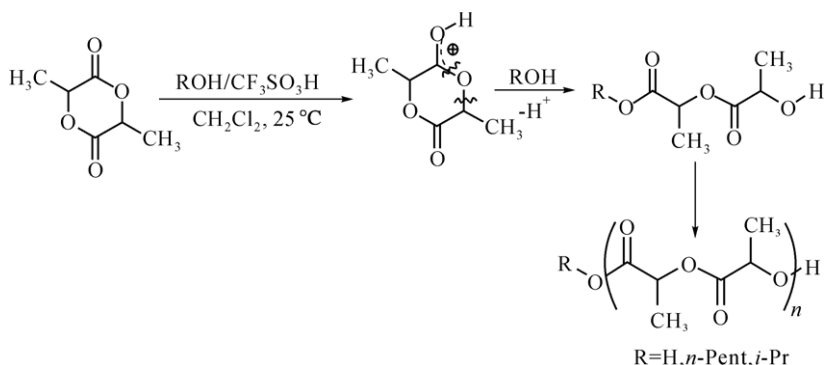
It was reported that a combination initiator system of an acid (such as  $\text{HCl}\cdot\text{Et}_2\text{O}$ ) and a protic agent (such as an alcohol) proved to effectively polymerize  $\omega$ -caprolactone and  $\delta$ -valerolactone smoothly in dichloro-methane solution at 0 °C.<sup>[19,20]</sup> The  $\text{HCl}$  acts as a transesterification catalyst, the alcohol is the actual initiator. The resulting polymer features the  $\alpha$ -chain ester end group. Moreover, the polymer MWs (3,000 – 14,000 Da) were found to increase linearly with the monomer to initiator ratio

with narrow polydispersity ( $PDI < 1.25$ ), which is in agreement with a living polymerization. All the experimental observations strongly support an “activated monomer cationic polymerization” (Scheme 2.5).



**Scheme 2.5.** Process of an “activated monomer cationic polymerization”

Recently, the controlled cationic ROP of LAs was realized with a combination initiation system of  $\text{HOTf-ROH}$  ( $\text{H}_2\text{O}$ ,  $^i\text{Pr}$ , 1-pentanol). Using the initiation system  $\text{HOTf-}^i\text{PrOH}$ , polymerization of DLLA at  $25^\circ\text{C}$  in  $\text{CH}_2\text{Cl}_2$  reached 96% conversion within 12 d ( $[\text{LA}]_0/[\text{ROH}]_0 = 76.5$ ) producing PLLA with narrow MWD ( $M_n = 11,300$ ,  $PDI = 1.15$ ). In case of ROP of LLA, the homonuclear decoupled  $^1\text{H}$  NMR spectroscopy of the produced polymer indicates that an isotactic PLLA was obtained. Investigation of the kinetics of the polymerization revealed the living feature of the polymerization. Based on the experimental observations, the polymerization was proposed to follow the activated-monomer mechanism: the acidic catalyst  $\text{HOTf}$  preferentially and selectively activates the monomer LA, the initiation and propagation involve the protonation of LA and its subsequent acyl-oxygen bond scission by the nucleophilic addition of either the initiation protic agent or the hydroxyl chain-end of the growing polymer (Scheme 2.6).<sup>[21]</sup>

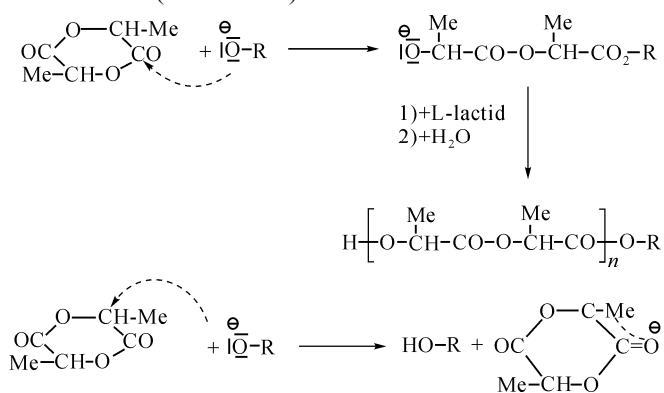


**Scheme 2.6.** Controlled cationic ROP of LAs with a combination initiation system of  $\text{HOTf-ROH}$  (Adapted from Ref. 21. Copyright (2005), with permission from ACS Publication)

### 2.3.2.2 Anionic Polymerization

The anionic ROP of cyclic esters has been much less investigated than the coordination-insertion approach. It is best initiated by some alkali metal alkoxides (such as  $\text{MeOK}$ ,  $^t\text{BuOK}$ ).<sup>[22-25]</sup> Potassium methoxide effectively initiates the

polymerization of L-lactide and D,L-lactide in THF at room temperature (20 °C). The polymerization proceeds very fast with good yield. Polymers with MW in good agreement with  $[M]_0/[I]_0$  ( $[M]_0, [I]_0$ : initial monomer and initiator concentration, respectively) and relatively narrow MW distribution (PDI=1.3 – 1.4) were obtained. Moreover, microstructural analysis by  $^{13}\text{C}$  NMR spectroscopy indicated a high degree of isotacticity for the resulting poly(L-lactide). The mechanism of anionic ROP was proposed to occur via acyl-oxygen bond cleavage based on the experimental results (Scheme 2.7).



**Scheme 2.7.** Mechanism of anionic ROP via acyl-oxygen bond cleavage

The alkoxide anion attacks the carbonyl atom in the monomer molecule with the cleavage of the acyl-oxygen bond and formation of the active propagating species bearing an alkyl ester dead-end group and the metal-alkoholate active end. The further propagation proceeds via the repeated attack of the polymeric anion onto the carbonyl group of the monomer, and formation of a new polymeric anion with a propagated chain.

A problem associated with the anionic ROP of the cyclic esters is the extensive side reactions. One possible way for the chain-transfer is the back-biting of the polymeric propagating anion. Another possible way is the reaction of the propagating anion with the  $\alpha$ -hydrogen of the monomer lactide. In this case the monomer lactide is deprotonated forming a monomer anion, which is capable of initiating a new chain, and at the same time a dead polymer bearing a hydroxyl end group was formed (Scheme 2.7). On the other hand, due to the planarity of the delocalized monomer anion, the rapid deprotonation-reprotonation reaction involves racemization. The racemization is an unavoidable side reaction of the anionic ROP. In case of the chiral monomer (such as L-lactide, D-lactide) the racemization leads to a decrease in stereoregularity and thermomechanical properties of the product polymers.

Recently it was reported that a hetero-bimetallic  $\text{Fe}(\text{II})$ -alkoxide complex  $[(\text{THF})\text{NaFe}(\text{O}^t\text{Bu})_2]_2$  (Fig. 2.3) is an effective initiator for the ROP of rac-lactide. At monomer conversion below 70%, a linear increase in polymer molecular weight with the monomer conversion was observed. The anionic  $\text{Fe}(\text{II})$ -alkoxide

rapidly initiates the polymerization at ambient temperature (60 min, conversion 81%). However, the molecular weight distribution of the synthesized polylactide is rather broad (PDI: 1.33 – 1.57).<sup>[26]</sup>

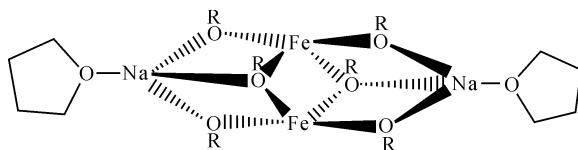


Fig. 2.3. Structure of a hetero-bimetallic Fe(II)-alkoxide complex  $[(\text{THF})\text{NaFe}(\text{O}^i\text{Bu})_2]_2$

### 2.3.2.3 Coordination-Insertion Ring-Opening Polymerization

As mentioned above, among all the polymerization techniques, the coordination-insertion ROP of cyclic esters is the most widely used and is the most popular one. Thus it has received scientists' attention in the past decade, and a lot of novel initiators/catalyst were developed. The encouraging recent advances in the controlled ROP have made it possible to design and tailor synthetic biodegradable polymers.

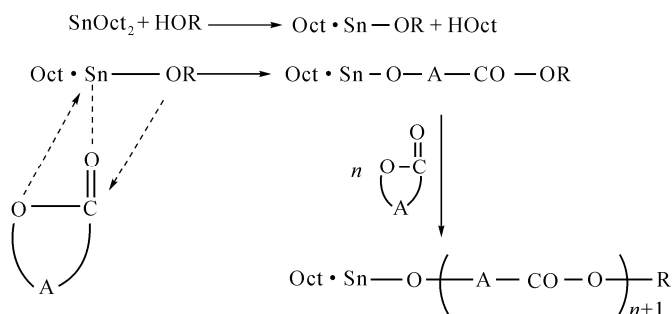
The term coordination-insertion implies that initiation and propagation reactions proceed via the coordination of the monomer to the active species, followed by the insertion of the ring-opened monomer into the active bond in the initiation and propagation species. It differs from the ionic ROP in that the active end of the propagating species is of a covalent bond, not an ion. This generally reduces the reactivity and the polymerization rate. However, the decreased reactivity also leads to fewer side reactions and narrow molecular weight distribution of the produced polymers, and even to a living ROP in some cases.

#### (1) Stannous Octoate Catalyst

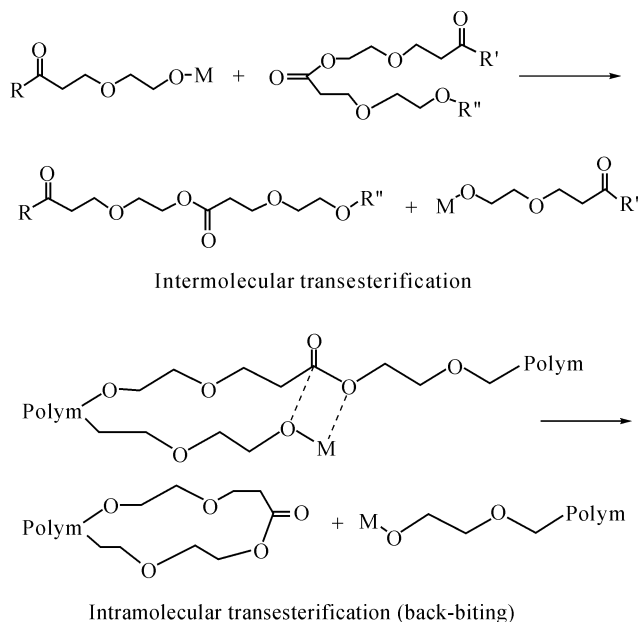
The most widely used catalyst for the industrial production of polylactides and poly(lactide-co-glycolide) is stannous 2-ethylhexanoate, which is usually referred to as stannous octoate and abbreviated as  $\text{SnOct}_2$ . It has several advantages: commercial availability, solubility both in common organic solvents and in melt monomers, convenience of handling, etc. It is of high catalytic activity and excellent versatility in general. However, in the case of separate use,  $\text{SnOct}_2$  shows only median activity. In the presence of an alcohol, a co-initiator, its activity increases greatly. Investigations into the initiation mechanism of the bi-component system  $\text{SnOct}_2\text{-ROH}$  revealed that the true initiation active species is  $\text{Oct-Sn-OR}$ , which was formed by partial alcoholysis of  $\text{SnOct}_2$ .<sup>[18,27]</sup> The ROP of LAs is well-accepted to follow the coordination-insertion mechanism (Scheme 2.8).

The propagation proceeds via the repeated insertion of the monomer into the  $\text{Sn-OR}$  bond in the activated Tin(II) initiator  $\text{OctSnOR}$  (Scheme 2.8). The  $\text{SnOct}_2$  catalyst is a strong transesterification agent at elevated temperature, and/or at long reaction times (Scheme 2.9). The intramolecular transesterification reactions, i.e.

back-biting chain transfers, cause degradation of the polymer chain and the formation of cyclic oligomers, while the intermolecular transesterifications change the sequences of the polyesters. Both types of transesterifications broaden the molecular weight distribution. Therefore, the ROPs of cyclic esters initiated by  $\text{SnOct}_2$  usually proceed via neither the living polymerization nor the stereospecific polymerization. Hence they are not suitable for the biomaterial design. It is worth noting that  $\text{SnOct}_2$  (with no exception for other tin compounds) is cytotoxic. This has recently aroused deep concern about the biosafety of materials made with  $\text{SnOct}_2$  and applied to pharmaceutical or biomedical applications. Seeking and designing catalysts and/or initiators possessing both high activity and biosafety are hence a new challenge in this field.



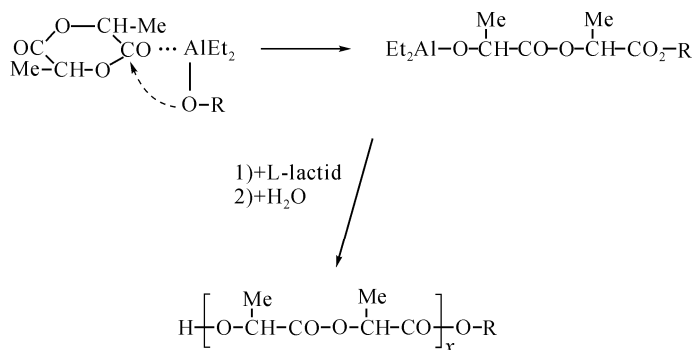
**Scheme 2.8.** ROP of LAs follows the coordination-insertion mechanism



**Scheme 2.9.** A strong transesterification agent of the  $\text{SnOct}_2$  catalyst

## (2) Aluminum Alkoxides Initiators

Catalysts based on aluminum are attractive with regard to the very low toxicity of aluminum<sup>[28-34]</sup>. Aluminum isopropoxide  $\text{Al}(\text{O}^i\text{Pr})_3$  was reported to be an effective initiator for ROP of lactides.<sup>[28-32]</sup> As was evidenced by the kinetic investigation, the polymerization of lactides in toluene at 70 °C is a perfect “living” process. However, since this linearity is no longer observed at the highest value of the monomer/initiator molar ratio ( $[\text{LA}]_0/[\text{Al}]_0 > 1,600$ ), the transesterification reaction could be responsible for the phenomenon. Aluminum alkoxides initiated ROP follows the coordination-insertion mechanism (Scheme 2.10). The monomer LA plays a temporal role of a ligand coordinated with the Al atom via the carbonyl O-atom. The coordination enhances the electrophilicity of the carbonyl group of the monomer and the nucleophilicity of the OR group in the initiator  $\text{Et}_2\text{AlOR}$ , so that the insertion of the monomer LA into the Al-O bond occurs.

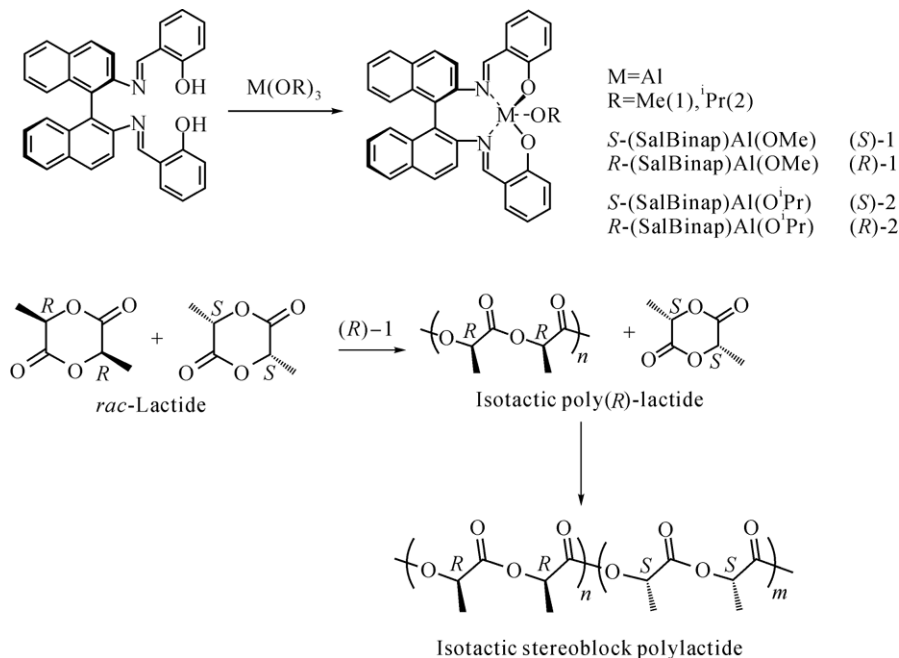


**Scheme 2.10.** Aluminum alkoxides initiated ROP following the coordination-insertion mechanism

## (3) Aluminum-Schiff Base Complex Initiators

The physical, mechanical and degrading properties of biodegradable polyesters are intimately dependent on the chain stereochemistry. For example, isotactic poly(L-lactide) is a high crystalline material ( $T_m \approx 170$  °C) possessing excellent mechanical properties and rather slow degradation rate, whereas atactic poly(D,L-lactide) is an amorphous polymer which degrades relatively fast in comparison with poly(L-lactide). However, most catalysts, including  $\text{SnOct}_2$  and  $\text{Al}(\text{O}^i\text{Pr})_3$ , mentioned above, do not show stereo-directive or stereo-selective effect towards a specific enantiomer (e.g., L-lactide) or enantiomer mixture (e.g., D,L-lactide). Designing and tailoring catalysts leading to stereospecific and/or stereoselective ROP of cyclic esters hence are of significance. One of the most important advances in the control of stereochemistry of polylactide was achieved by Spassky who found that the enantiometrically pure aluminum complex featuring the chiral Salen ligand (*R*-Sal Binap)Al(OMe) [(*R*)-1] derived from (*R,R*)-binaphthyl diamine (Scheme 2.11) preferentially polymerize D-lactide in the ROP of *rac*-lactide. The aluminum-Schiff base complex exhibited a 20:1 preference for the polymerization of D-lactide over L-lactide in the ROP of *rac*-lactide.<sup>[35]</sup> At conversion of less than 50%, the microstructure of the produced polymer was predominantly isotactic

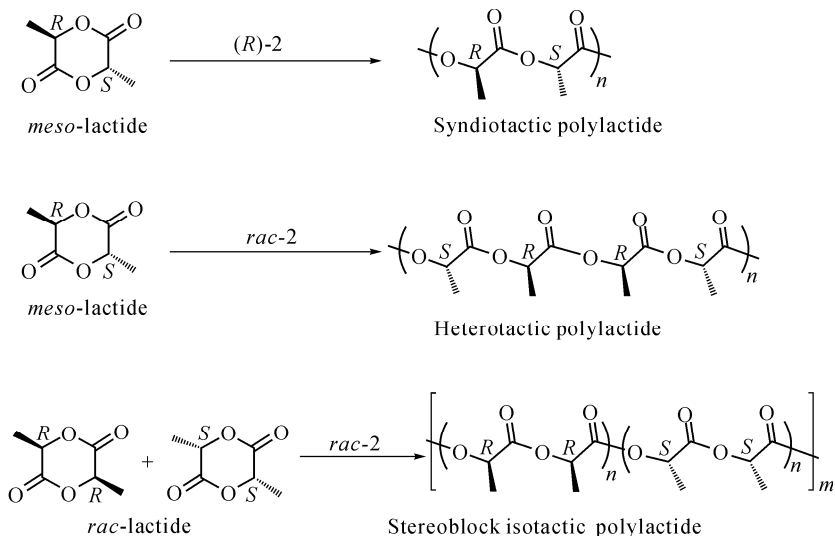
poly(D-lactide). At a conversion of over 60%, only L-lactide remained. The process is called the kinetic resolution of *rac*-lactide. Due to the kinetic preference for the *R,R*-enantiomer, the polymerization then slowly reached 97.5% monomer conversion. The polymer formed presumably had a stereoblock microstructure. The product polymer exhibited a high melting temperature (187 °C), this indicates that a stereocomplex between poly-L- and poly-D-lactide sequences is formed. It should be noted that the ROP initiated by the Al-Salen complex was also proceeded by the living mechanism, as evidenced by the good control of polymer molecular weight and very narrow polydispersity.



**Scheme 2.11.** Process of the enantiometrically pure aluminum complex featuring the chiral Salen ligand. (*R*-Sal Binap)Al(OMe) [(*R*)-1] derived from (*R,R*)-binaphthyl diamine preferentially polymerize D-lactide in the ROP of *rac*-lactide

The aluminum-Salen complex (SalBinap)Al(<sup>*i*</sup>Pr) [(*R*)-2] (Scheme 2.11) synthesized by Coates<sup>[36]</sup> also exhibits excellent stereo-control ability (Scheme 2.12). The enantiometrically pure complex *R*-(SalBinap)Al(<sup>*i*</sup>Pr) [(*R*)-2] polymerizes *meso*-lactide (70 °C in toluene), to syndiotactic polylactide, a crystalline polymer ( $M_n=15,440$ , PDI=1.06,  $T_m=149$  °C). Interestingly, the racemic complex *rac*-2 polymerizes *meso*- and *rac*-lactide to heterotactic polylactide ( $M_n=15,000$ , PDI=1.07,  $T_g=43.2$  °C) and stereoblock isotactic polylactide ( $M_w=22,600$ , PDI=1.09), respectively. The latter exhibited a  $T_m$  at 179 °C which was higher than that of isotactic poly(D-lactide) or poly(L-lactide). This is evidence that the stereoblock copolymer adopts a stereocomplex morphology in the solid state, but due to the shorter runs of enantiometrically pure blocks in the main chain, the melting point

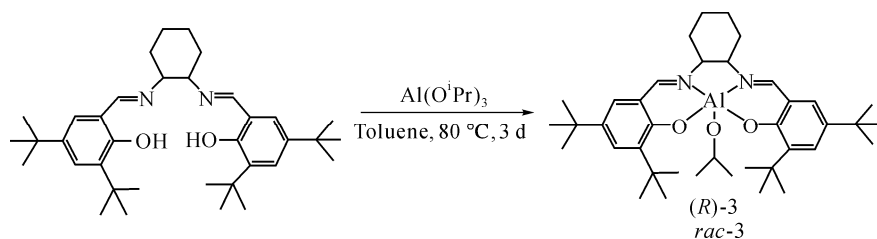
is lower than that of the 1:1 mixture of the enantiopure homopolymers.



**Scheme 2.12.** Stereoselective synthesis of PLA with aluminum-salen complex (SalBinap)Al(O<sup>i</sup>Pr)<sub>3</sub> [(R)-2] (Adapted from Ref. 36. Copyright (1999, 2002), with permission from the ACS Publication)

It worth mentioning that the mixture of PLLA and PDLA (1:1) is referred to as a stereocomplex of PLLA-PDLA (sc-PLA) which has a melting temperature  $T_m$  above 200 °C, being much higher than the  $T_m$  of PLLA or PDLA. The sc-PLA surpasses PLLA and PDLA, not only in thermal but also in mechanical properties. It may provide high performance materials possessing a bio-based nature.<sup>[37,38]</sup>

The Salen-Al complex Salen-Al-3 (Scheme 2.13) synthesized by Feijen also exhibited excellent stereoselectivity. Enantiometrically pure complex (R)-3 preferentially polymerizes LLA in the presence of *rac*-LA. Polymerization of *rac*-LA in toluene (70 °C, 2 d) at low conversion (21%) produced a polymer with an isotacticity of 92% while the racemic complex *rac*-3 polymerizes *rac*-LA, forming a hard crystalline polymer (isotacticity of 88%) with a high  $T_m$  of 183.5 °C (bulk polymerization at 130 °C for 2 d with  $[M]_0/[I]_0 = 200$ , 94.8% of conversion,  $M_n = 24,900$ , PDI = 1.37) which is significantly higher than that of optical pure PLLA ( $T_m = 168.4$  °C). It was attributed to the isotactic stereoblock poly(lactide) formation.<sup>[39]</sup>



**Scheme 2.13.** Salen-Al complex Salen-Al-3 synthesized by Feijen



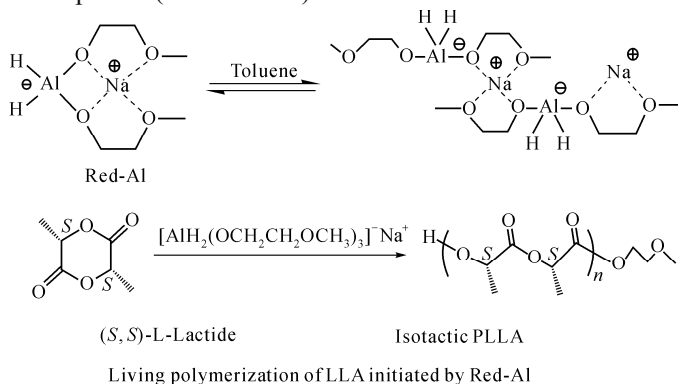
Great efforts have been made in the design and tailoring of molecular structures of Al-Salen type initiators in recent years, and quite a lot of this type of initiators were found to exhibit good stereocontrollability for the ROP of chiral cyclic esters. [40-50]

#### (4) Red-Al Initiators

The synthesis and optical resolution of the Salen-Al complexes is sometimes not only a time-consuming process, but also a low-yield process, and as a result the preparation cost of the initiators for the controlled biodegradable synthesis is usually far from cheap.

Recently Li, Woo and co-workers found that a commercially available aluminum complex Red-Al, i.e. sodium bis( $\alpha$ -methoxyethoxy) aluminum hydride  $\text{Na}[\text{AlH}_2(\text{OCH}_2\text{CH}_2\text{OCH}_3)]$  (Scheme 2.14) is an efficient initiator for the controlled ROP of lactides. [51,52] Polymerization of LAs in bulk at 110 °C reached 100% conversion within 48 h, producing a polymer with very narrow molecular weight distribution ( $[M]_0/[I]_0 = 150$ ,  $M_n = 2.30 \times 10^4$ ,  $\text{PDI} = 1.12$ ) (Table 2.2). [53]

The kinetic investigation into the ROP of D,L-lactide in toluene at 70 °C, revealed that the polymerization is living, as supported by the linear relationships of  $\ln [M]_0/[M]_w$  versus time and  $M_n$  versus conversion. Stereoregularity estimation based on the  $^{13}\text{C}$  NMR spectrum of the produced poly(L-lactide) indicates that the synthesized poly(L-lactide) is of very high isotacticity (>95.2%) (Fig. 2.4). Taking the optical purity of L-lactide (i.e., 96%) into account, it is reasonably concluded that the polymerization of L-lactide initiated by the aluminum complex (Red-Al) is highly stereospecific (Scheme 2.14). [53]



**Scheme 2.14.** Aluminum complex Red-Al initiated the controlled ROP of lactides (Adapted from Ref. 53. Copyright(2004), with permission from ACS Publications)

**Table 2.2** Bulk Polymerization of LLA Catalyzed by Red-Al<sup>a</sup> (Adapted from Ref. 53. Copyright (2004), with permission from ACS Publications)

No.	Temp (°C)	Time (h)	Yield (%)	$M_n \times (10^{-4})^b$	$\text{PDI}^c$
1	110	48	98.1	2.30	1.12
2	110	72	97.8	2.25	1.17

<sup>a</sup> $[M]_0/[I]_0=150$ ;  $[M]_0$ : initial molar number of LLA feed;  $[I]_0$ : initial molar number of Red-Al;

<sup>b</sup>Measured by GPC; <sup>c</sup>Polydispersity index, i.e.,  $M_w/M_n$  of the product polymer

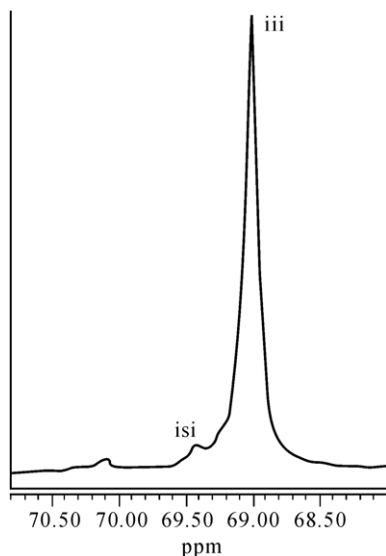
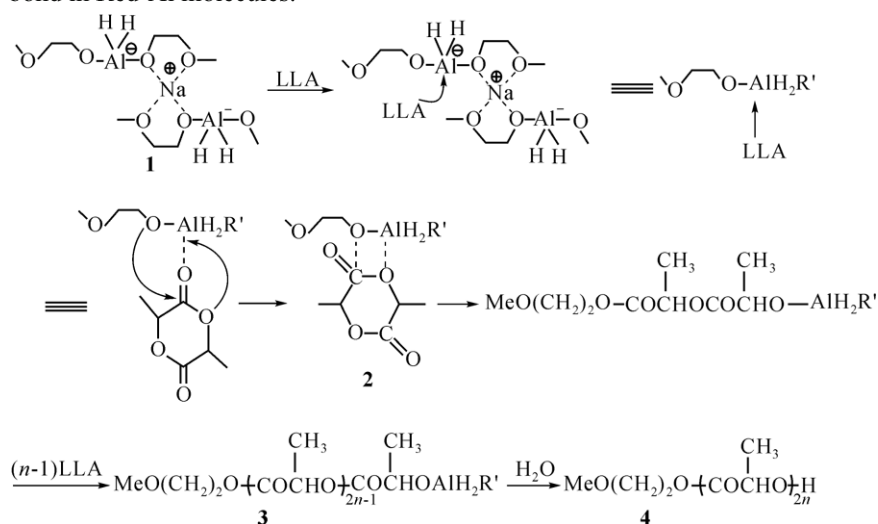


**Fig. 2.4.**  $^{13}\text{C}$  NMR spectrum of the methine carbon in PLLA (110 °C, 10 h,  $[\text{LLA}]_0/[\text{I}]_0=100$ , bulk polymerization)

Investigation into the nature of the active propagation species revealed the polymerization follows the coordination-insertion mechanism. Based on the  $^1\text{H}$  NMR monitoring the polymerization and characterizing the end-group, the polymerization mechanism is proposed (Scheme 2.15) to proceed via the fission of the acyl-oxygen bond in LLA and the insertion of the cleaved monomer residue into the Al-OR bond in Red-Al molecules.



**Scheme 2.15.** Polymerization mechanism via the fission of the acyl-oxygen bond in LLA and the insertion of the cleaved monomer residue into the Al-OR bond in Red-Al molecules

## (5) Other Catalysts Based on Non-toxic Metals

As mentioned above, catalysts based on aluminum are certainly less toxic than the  $\text{SnOct}_2$ . However, the aluminum ion does not belong to the human metabolism, and there is a suspicion that it causes Alzheimer's disease. Catalysts based on the metal ions (e.g.,  $\text{Mg}^{2+}$ ,  $\text{Zn}^{2+}$ ,  $\text{Ca}^{2+}$ ,  $\text{Fe}^{2+}$ ) involved in human metabolism are hence attractive.

The  $\text{Zn}(\text{II})$  complex featuring bidentate  $\beta$ -diketiminate ligands (Fig. 2.5) exhibits high activity and good control for the ROP of DLLA. The formed PLLA is highly heterotactic, i.e., the catalyst showed a preference for polymerizing D- and L-monomer in an alternate fashion. The polymerization proceeds in a "living" way. However, electrospray mass spectroscopy (ES-MS) showed a small amount of transesterification.<sup>[54-56]</sup>

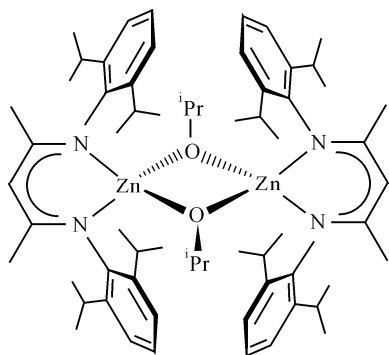
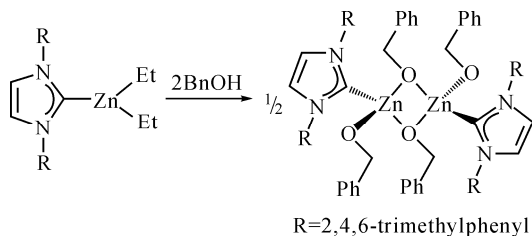


**Fig. 2.5.** Structure of the  $\text{Zn}(\text{II})$  complex featuring bidentate  $\beta$ -diketiminate ligands

The zinc complex of *N*-heterocyclic carbene, prepared by Tolman et al. (Scheme 2.16), was recently reported to be an efficient catalyst for the ROP of LA in  $\text{CH}_2\text{Cl}_2$  at 25 °C. Polymerization control was demonstrated by a linear relationship between  $M_n$  and conversion.  $^1\text{H}$  NMR analysis showed the heterotactic enrichment of the synthesized polymer.<sup>[57]</sup>



**Scheme 2.16.** An efficient catalyst for the ROP of LA in  $\text{CH}_2\text{Cl}_2$  at 25 °C by the zinc complex of *N*-heterocyclic carbene

In recent years, quite a number of zinc complexes, showing good controllability towards ROP of cyclic esters were reported.<sup>[58-63]</sup>

An oxo-bridged pentanuclear cluster  $\text{Fe}_5(\text{O})(\text{OEt})_{13}$  was found to be effective for the controlled ROP of LA. The polymerization proceeds at a high rate

( $[M]_0/[I]_0=450$ , at  $>0\text{ }^\circ\text{C}$ , in toluene, 21 min, 97% conversion), producing polymers with narrow MWD (PDI=1.17). No epimerization was observed in the polymerization of LLA with  $\text{Fe}_5(\text{O})(\text{OEt})_{13}$  initiator.<sup>[64, 65]</sup>

The Magnesium(II) complex of  $\beta$ -diketiminates were also designed and studied for the ROP of cyclic esters due to the attractive nature of their non-toxic components in the human metabolism. Both  $\text{Mg}(\text{II})$  complexes, shown in Fig. 2.6, exhibited highly active catalytic activity. However, the MWDs of produced polymers are broader. Moreover the polymerizations showed no steric controllability.<sup>[56,66]</sup>

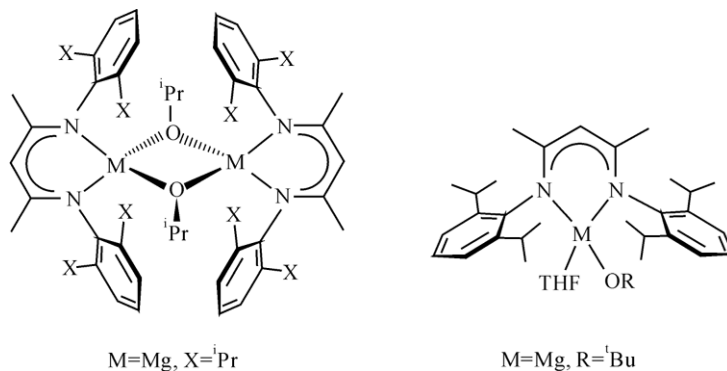


Fig. 2.6. Structures of both  $\text{Mg}(\text{II})$  complexes

### 2.3.3 Polymerization Using Metal-Free Organic Catalysts

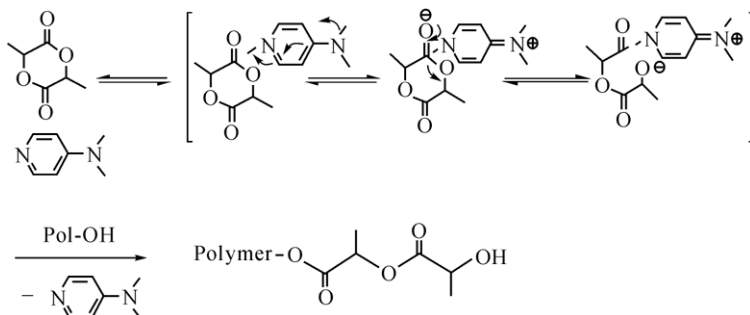
Over the past ten years, a great effort has been made in the development of non-stannous catalysts for the controlled synthesis of biodegradable polymers for biomedical applications. The application of metal-free organic catalysts to biodegradable polymer synthesis is of significance, because for applications in living systems the resulting polymers should be free of any metal residues. However, when metal-containing catalysts/initiators were applied to the polymer synthesis it was difficult to completely remove the metals bound to the polymer chains.

Here is the first organocatalytic approach to the living ROP of cyclic esters using strong basic amines, i.e., DMAP [4-(dimethylamino)pyridine], PPy (4-pyrrolidinopyridine), as transesterification catalysts (Fig. 2.7) and alcohols ( $\text{PhCH}_2\text{OH}$ ,  $\text{EtOH}$ ) as initiators.<sup>[67]</sup> Polymerization of LA in  $\text{CH}_2\text{Cl}_2$  at  $35\text{ }^\circ\text{C}$  with DMAP-EtOH initiation system ( $[\text{DMAP}]_0/[\text{EtOH}]_0 = 4$ ) reached 78% conversion in 64 h, producing a polymer with very narrow MWD (PDI = 1.10). The linear relationship between  $M_n$  and conversion indicated the polymerization proceeds in the “living” manner. Though the precise mode of action of the catalysts remains obscure, it would seem likely that the polymerization occurs through a “monomer-activated mechanism”. Initiation occurs when the nucleophilic initiator (ROH)

reacts with the monomer-catalyst complex (LA-DAMP), and PLA bears an ester group at the  $\alpha$ -chain end. A hydroxyl at the  $\omega$ -chain end was formed. The propagation proceeds when the terminal  $\omega$ -hydroxyl PLA acts as a nucleophile to facilitate further chain growth (Scheme 2.17).



Fig. 2.7. Structures of DMAP [4-(dimethylamino)pyridine] and PPy (4-pyrrolidinopyridine)



Scheme 2.17. Process of the propagation when the terminal  $\omega$ -hydroxyl PLA acts as a nucleophile to facilitate further chain growth

Other bicomponent nucleophilic catalyst-initiator systems reported of this type include  $R_3P$  (e.g.,  $Bu_3P$ ,  $PhPMe_2$ ,  $Ph_3P$ )-Ph/EtOH, *N*-heterocyclic carbene-ROH etc.<sup>[67-73]</sup> Tolman et al. reported that *N*-heterocyclic carbene (NHC) (Fig. 2.8) in the presence of BuOH can effectively initiate the ROP of LA producing PLA with isotactic enrichment.



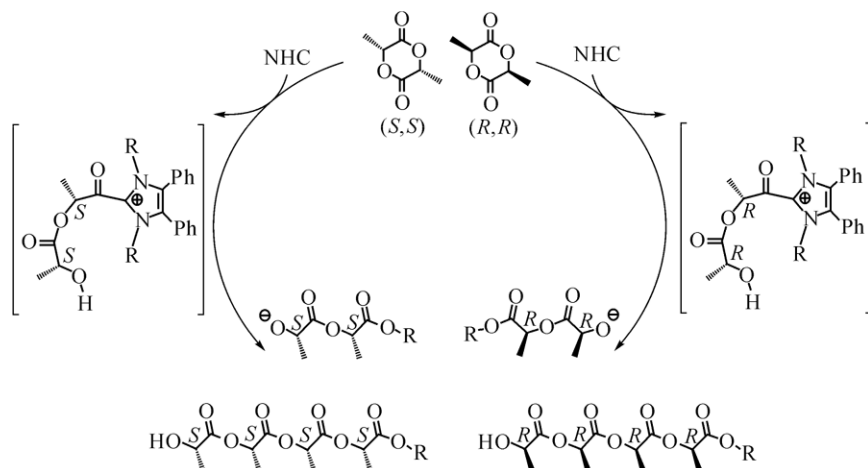
Fig. 2.8. Structure of *N*-heterocyclic carbene (NHC)

Polymerization of DLLA with the NHC ( $[LA]_0/[A]_0 = 50$ ) in  $CH_2Cl_2$  at  $-20\text{ }^\circ C$  reached 71% conversion within 20 min, producing a semi-crystalline, polymer ( $M_n = 1.59 \times 10^4$ ,  $P_m = 0.75$ ,  $PDI = 1.26$ ,  $T_m = 153\text{ }^\circ C$ ).<sup>[57]</sup>

Recently Hedrick et al. described that the *N*-heterocyclic carbene shows a pronounced higher selectivity for ROP of Las. *Rac*-LA was polymerized to PLA with high isotacticity ( $P_i = 0.9$ ,  $PDI = 1.20$ ,  $-70\text{ }^\circ C$ , 120 min, 91% conversion), while *meso*-LA yields heterotactic PLA ( $P_i = 0.83$ ,  $PDI = 1.25$ ,  $-40\text{ }^\circ C$ , 240 min).

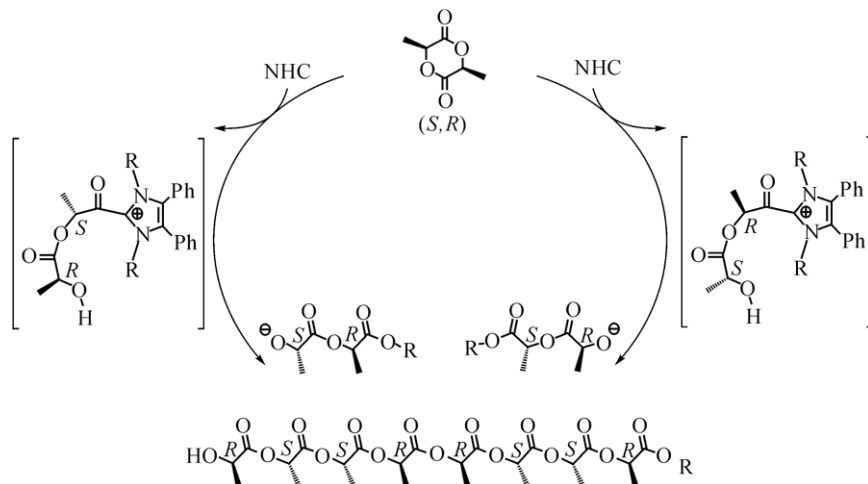
The polymerization was proposed to follow the chain-end control mechanism. For *rac*-LA, both D- and L-LA were equally activated and with stereoselective

attack by the terminal alkoxide of the last inserted monomer unit in the polymer chain, leading to isotactic enchainment (Scheme 2.18).<sup>[74]</sup>



**Scheme 2.18.** Structure of isotactic enchainment for *rac*-LA (Adapted from Ref. 74. Copyright (2006), with permission from RSC Publishing)

The formation of heterotactic-enriched PLA from *meso*-LA is due to the oxygen adjacent to the last stereogenic center of the polymer chain end (either *R* or *S*) preferentially attacking the activated monomer with the same stereogenic configuration adjacent to it. Repeating these steps, a heterotactic-enriched polymer-chain can thus be achieved (Scheme 2.19).



**Scheme 2.19.** Structure of a heterotactic-enriched polymer-chain

Guanidine is a natural organic base existing in some vegetables (e.g., beets, mushrooms, radishes) and some sea foods (such as oyster, scallop). Many guanidine derivatives are effective medicines (such as streptomycin, guanazde, guanothiazon, guanethidine). Some guanidine derivatives exist in the human body. Creatine and creatinine, for example, are guanidine derivatives participating in the arginine metabolism and energy-release process. Exploring the possibility of using these biogenic guanidines as catalysts for the biodegradable polymer synthesis is of interest and significance. Recently, Li and co-workers found that creatine effectively catalyzes the stereospecific ROP of LLA, producing PLA of high isotacticity ( $\geq 82.6\%$ ). Creatinine showed median catalytic activity, the ROP of LAs in bulk at 160 °C reached complete monomer conversion within 96 h, producing PLLA with relatively narrow dispersity ( $[M]_0/[I]_0=100$ ,  $M_n=1.56 \times 10^4$ ,  $PDI=1.20 - 1.28$ ). Investigation into the effect of additives on the polymerization revealed that the nature of the propagation-active species is neither radical nor ionic. The monitor of the polymerization and characterization of the propagating species by  $^1\text{H}$  NMR revealed that the active chain end of the propagating polymer bears a  $(\text{R}_2\text{N})_3\text{C-O}$  bond (Fig. 2.9).

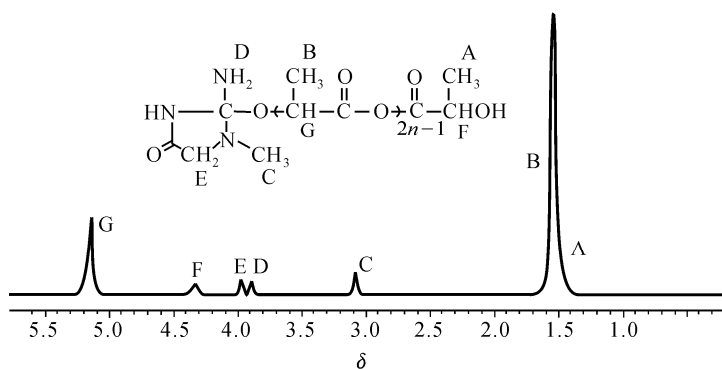
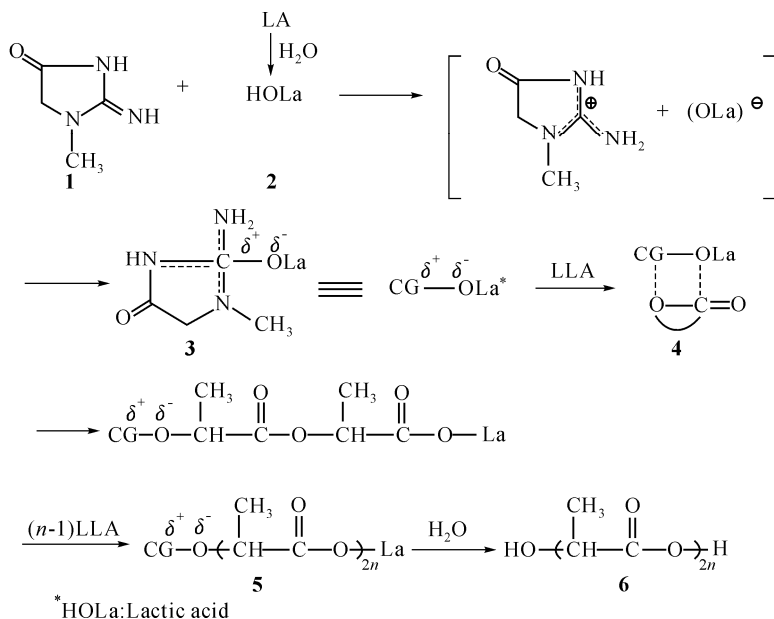


**Fig. 2.9.**  $^1\text{H}$  NMR spectrum of the propagation species in ROP of LLA initiated by creatinine (measured at 25 °C, 400 MHz,  $\text{CDCl}_3$  solvent; bulk polymerization at 120 °C,  $[\text{LLA}]_0/[\text{I}]_0=50$ )

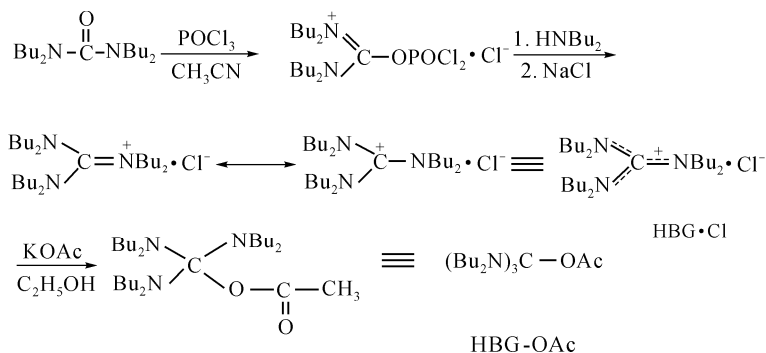
Thus, the active initiation species was deduced to be formed by the in-situ reaction of creatinine with lactic acid, which was either an impurity existing in the monomer or was formed in-situ due to the hydrolysis of the trace monomer. Polymerization proceeds via the cleavage of the acyl-oxygen bond in the coordinated LA molecules and the repeated insertion of the cloven LA residue into the active  $(\text{R}_2\text{N})_3\text{C-O}$  bond (CG-O bond, Scheme 2.20) of the propagating polymer species. The proposed mechanism is shown in Scheme 2.20, an investigation into the polymerization.



**Scheme 2.20.** Mechanism of polymerization proceeds via the cleavage of the acyl-oxygen bond in the coordinated LA molecules and the repeated insertion of the cloven LA residue into the active  $(R_2N)_3C-O$  bond (CG-O bond, Scheme 2.20) of the propagating polymer species

Kinetics revealed that creatinine-catalyzed ROP showed no controllability over the molecular weight of produced polymers.<sup>[75]</sup>

A guanidine carboxylate bearing the  $(R_2N)_3C-O$  bond which is of the same nature as the initiation active species 3 in Scheme 2.20, i.e. hexabutyl guanidinium acetate (HBG-OAc), was synthesized (Scheme 2.21) and successfully used as an initiator for ROP of LAs.<sup>[76]</sup>



**Scheme 2.21.** Process of synthesizing hexabutyl guanidinium acetate (HBG-OAc)

Experimental results indicated that HBG-OAc showed satisfactory catalytic behavior (Table 2.3).

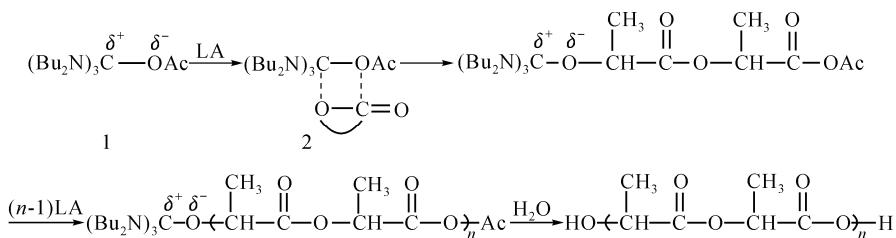


**Table 2.3** ROP of LAs in Bulk with HBG-OAc as on Initiator<sup>a</sup>

No.	Monomer	<i>T</i> (°C)	<i>t</i> (h)	Yield (%)	<i>M<sub>n</sub></i> (×10 <sup>-4</sup> ) <sup>b</sup>	PDI
1	110	48	98.1	2.30	1.12	1.12
2	110	72	97.8	2.25	1.17	1.17

<sup>a</sup> Bulk polymerization ( $[I]_0/[LA]_0=6.7 \times 10^{-3}$ ); <sup>b</sup> Measured by GPC

The polymerization of LAs is living as evidenced by the linear relationships of  $\ln[M]_0/[M]_c$  vs. time and  $M_n$  vs. conversion. Polymerization of LLA in bulk at 110 °C reached complete conversion within 24 h, producing PLLA with very narrow MWD (PDI = 1.09). The <sup>13</sup> C NMR analysis demonstrated that the synthesized PLLA is of high isotacticity (80%). The polymerization follows the coordination-insertion mechanism, as evidenced by the experimental investigation (Scheme 2.22).



**Scheme 2.22.** The coordination-insertion mechanism for the polymerization

### 2.3.4 Enzyme-Catalyzed Ring-Opening Polymerization

Enzyme-catalyzed ROP of lactides and lactones have been extensively investigated. Various cyclic esters, lactide and lactone (such as  $\delta$ -VL,  $\epsilon$ -CL), DXO etc., have been subjected to lipase-catalyzed ROP. Among various commercially available lipases, the *Candida Antarctica* lipase (lipase CA) was the most active toward the  $\epsilon$ -CL polymerization. Polymerization of  $\epsilon$ -CL in bulk produces a linear polymer with MW over  $4 \times 10^4$  under appropriate conditions, while polymerization in organic solvents forms mainly cyclic oligomers.<sup>[77]</sup> Lipase PS showed high catalytic activity for ROP of LA. Polymerization in bulk at 80 – 130 °C reached high conversion after several days, producing high MW polymers (up to  $2.7 \times 10^5$  Dalton) and narrow MWD (PDI = 1.1 – 1.3). However, the formation of cyclic oligomers in a fair amount and the existence of an induction period are common features of lipase-catalyzed polymerization.

Considerable progress has been made in the field of enzyme-promoted biodegradable synthesis over the last decade. A full exposition and detailed discussion on the research conducted in this field exceed the scope of this chapter. Readers wishing to know more information, please refer to the references.<sup>[78-85]</sup>

## 2.4 Concluding Remarks

Synthetic aliphatic polymers based on LA, GA,  $\epsilon$ -CL etc. have found some significant biomedical applications, such as bio-resorbable surgical sutures, prosthetics, bone screws, plates for temporary fracture fixation, dental implants, and long-term drug delivery carriers. Great progress in biodegradable polymer synthesis has been made over the last decade. Development of the controlled polymerization technique provides brilliant prospects for the practical use of these polymers in biomedical science engineering areas. Further improvements over the controlled ROP can be anticipated by the tailoring of the initiator structure and optimization of the polymerization technique. It can also be reasonably expected that the synthesis and practical applications of environmentally friendly LA-based polymers will keep increasing over a wider range and on an industrial scale as well.

## Acknowledgment

The persistent financial support of the author's project on "controlled synthesis of biodegradable polymers with guanidine-based organic initiators" by NSFC (No.21074057, No.20474030, No.20074016) is greatly acknowledged.

## References

- [1] Mainivarlet, P., Rahm, R., Gogolewski, S. *Biomaterials*, 1997, 18: 257.
- [2] Middleton, J. C., Tipton, A. J. *Biomaterials*, 2000, 21: 2335.
- [3] Perogo, G., Cella, G. D., Aldini, N. N., Fini, M., Giardino, R. *Biomaterials*, 1994, 15:189.
- [4] Kylma, J., Seppala, J. V. *Macromolecules*, 1997, 30: 2876.
- [5] Langer, R. *Nature*, 1998, 392: 5.
- [6] Kataoka, K., Harada, A., Nagasaki, Y. *Adv. Drug Delivery Rev.*, 2001, 7: 113.
- [7] Middleton, J. C., Tipton, A. J. *Biomaterial*, 2000, 21: 2335.
- [8] Lee, H. S., Yang, J. M. *J. Polym. Sci. Part A: Polym. Chem.*, 2001, 39: 724.
- [9] Moon, S. I., Lee, C. W., Miyamoto, M., Kimura, Y. *J. Polym. Sci., Part A: Polym. Chem.*, 2000, 38: 1673.
- [10] Moo, S. I., Lee, C. W., Taniuchi, I., Miyamoto, M., Kimura, Y. *Polymer*, 2001, 42: 5059.
- [11] Takahashi, K., Taniguchi, I., Miyamoto, M., Kimura, Y. *Polymer*, 2000, 41: 8725.
- [12] Ranucci, E., Liu, Y., Soderqvist, L. M., Albertsson, A. C. *Macromol. Rapid Commun.*, 2000, 21: 680.
- [13] Zhong, W., Ge, J., Gu, Z., Li, W., Chen, X., Zhang, Y., Yang, Y. *J. Appl.*

- Polym. Sci., 1999, 74: 2546.
- [14] Uyama, H., Inada, K., Kobayashi, S. *Chem. Lett.*, 1998, 1285.
- [15] Linko, Y. Y., Wang, Z. L., Seppala, J. *Enzymol. Technol.*, 1995, 17: 506.
- [16] Kricheldorf, H. R., Dunsing, R. *Makromol. Chem.*, 1986, 187: 1611.
- [17] Kricheldorf, H. R., Kreiser, I. *Makromol. Chem.*, 1987, 188: 1861.
- [18] Kricheldorf, H. R. *Chemosphere.*, 2001, 43: 49.
- [19] Luo, X., Detrembleur, C., Jerome, R. *Macromolecules.*, 2002, 35: 1190.
- [20] Shibasaki, Y., Sanda, F., Sanada, H., Yokoi, M., Endo, T. *Macromolecules.*, 2000, 33: 4316.
- [21] Bourissou, D., Vaca, B. M., Dumitresou, A., Graullier, M., Lacombe, F. *Macromolecules.*, 2005, 38: 9993.
- [22] Kricheldorf, H. R., Kreiser-Saunders, I. *Makromol. Chem.*, 1990, 191: 1057.
- [23] Jedlinski, Z., Walach, W., Kurcok, P., Adamus, G. *Makromol. Chem.*, 1991, 192: 2052.
- [24] Jedlinski, Z., Walach, W., Janeczek, H., Raddecka, J. *Makromol. Chem.*, 1993, 194: 1681.
- [25] Kricheldorf, H. R., Boettcher, C. *Makromol. Chem.*, 1993, 194: 1665.
- [26] McGuinness, D. S., Marshall, E. L., Gibson, V. C., Steed, J. W. *J. Polym. Sci. Part A: Polym. Chem.*, 2003, 41: 3798.
- [27] Penczek, S., Duda, A., Kowalski, A., Libiszowski, J., Majerska, K., Biela, T. *Macromol. Symp.*, 2000, 157: 61.
- [28] Dubois, P., Jacobs, C., Jerome, R., Teyssie, P. *Macromolecules*, 1991, 24: 2266.
- [29] Kricheldorf, H. R., Berl, M., Scharnagl, N. *Macromolecules*, 1988, 21: 286.
- [30] Degee, P., Dubois, P., Jerome, R., Jacobsen, S., Fritz, H. G. *Macromol. Symp.*, 1999, 144: 289.
- [31] Degee, P., Dubois, P., Jerome, R. *Macromol. Symp.*, 1997, 123: 67.
- [32] Degee, P., Dubois, P., Jerome, R. *Macromol. Chem. Phys.*, 1997, 198: 1973.
- [33] Von-Schenk, H., Ryner, M., Albertsson, A. C., Svensson, M. *Macromolecules*, 2002, 35: 1556.
- [34] Eguiburu, J. L., Fernandez-Berridi, M. J., Cossio, F. P., San-Roman, J. *Macromolecules*, 1999, 32: 8252.
- [35] Spassky, N., Wisniewski, M., Pluta, C., Le-Borgne, A. *Macromol. Chem. Phys.*, 1996, 197: 2627.
- [36] (a) Ovitt, T. M., Coats, G. W. *J. Am. Chem. Soc.* 2002, 124: 1316. (b) Tina, M., Coats, G. W. *Am. Chem. Soc.*, 1999, 121: 4072.
- [37] Ikada, Y., Jamshidi, K., Tsuji, H., Hyon, S. H. *Macromolecules.*, 1987, 20: 904.
- [38] Fukushima, K., Kimura, Y. *Polymer Int.*, 2006, 55: 626.
- [39] Zhong, Z., Dijkstra, P. J., Feijen, J. *Angew. Chem. Int. Ed.*, 2002, 41: 4510.
- [40] Zhong, Z., Dijkstra, P. J., Feijen, J. *J. Am. Chem. Soc.*, 2003, 125: 11291.
- [41] Tang, Z., Chen, X., Pang, X., Yang, Y., Zhang, X., Jing, X. *Biomacromolecules.*, 2004, 5: 965.
- [42] Pang, X., Du, H., Chen, X., Zhuang, X., Cui, D., Jing, X. *J. Polym. Sci. Part A: Polym. Chem.*, 2005, 43: 6605.
- [43] Tang, Z., Yang, Y., Pang, X., Hu, J., Chen, X., Hu, N., Jing, X. *J. App. Polym.*

- Sci., 2005, 98: 102.
- [44] Hormnirun, P., Marshall, E. L., Gibson, V. C., White, A. J. P., Williams, D. J. *J. Am. Chem. Soc.*, 2004, 126: 2688.
- [45] Taden, I., Kang, H., Massa, W., Okuda, J. *J. Organ. Metal. Chem.*, 1997, 540: 189.
- [46] Bhaw-Luximon, A., Jhurry, D., Spassky, N. *Polym. Bull.*, 2000, 44: 31.
- [47] Nomura, N., Ishii, R., Akakura, M., Aoi, K. *J. Am. Chem. Soc.*, 2002, 124: 5938.
- [48] Cameron, P. A., Jhurry, D., Gibson, V. C., White, A. J. P., Williams, D. J., Williams, S. *Macromol. Rapid Commun.*, 199, 20: 616.
- [49] Jhurry, D., Bhaw-Luximon, A., Spassky, N. *Macromol. Symp.*, 2001, 175: 67.
- [50] Radano, C. P., Baker, G. L., Smith, M. R. *J. Am. Chem. Soc.*, 2000, 122: 1552.
- [51] Cerny, Z., Fusek, J., Machacek, J., Kriz, O., Casensky, B. *J. Organomet. Chem.*, 1996, 516: 115.
- [52] Abe, T., Haga, T., Negi, S., Morita, Y., Takayanagi, K., Hamamura, K. *Tetrahedron.*, 2001, 57: 2701.
- [53] Li, H., Wang, C., Bai, F., Yue, J., Woo, H. *G. Organometallics*, 2004, 23: 1411.
- [54] Chen, M., Ovitt, T. M., Hustad, P. D., Coats, G. W. *Polym. Prepr. (Am. Chem. Soc., Div. Polym. Chem.)*, 1999, 40: 542.
- [55] Chen, M., Attygalle, A. B., Lobkovsky, E. B., Coats, G. W. *J. Am. Chem. Soc.*, 1999, 121: 11583.
- [56] Chamberlain, B. M. Cheng, M., Moore, D. R., Ovitt, T. M., Lobkovsky, E. B., Coats, G. W. *J. Am. Chem. Soc.*, 2001, 123: 3229.
- [57] Jensen, T. R., Breyfogle, L. E., Hillmyer, M. A., Tolman, W. B. *Chem. Commun.*, 2004, (21): 2504.
- [58] Williams, C. K., Breyfogle, L. E., Choi, S. K., Nam, W., Young, Jr. V. G., Hillmyer, M. A., Tolman, W. B. *J. Am. Chem. Soc.*, 2003, 125: 11350.
- [59] Yu, K., Jones, W. J. *Catal.*, 2004, 222: 558.
- [60] Chisholm, M. H., Eilerts, N. W., Huffman, J. C., Iyer, S. S., Pacold, M., Phomphrai, K. *J. Am. Chem. Soc.*, 2000, 122: 11845.
- [61] Cheng, M., Darling, N. A., Lobkovsky, E. B., Coats, G. W. *Chem. Commun.*, 2000, (20): 2007.
- [62] Coles, M. P., Hitchcock P. B. *Eur. J. Inorg. Chem.*, 2004, 13: 2662.
- [63] William, C. K., Brooks, N. R., Hillmyer, M. A., Tolman, W. B. *Chem. Commun.*, 2002, 2132.
- [64] O'Keefe, B. J., Monnier, S. M., Hillmyer, M. A., Tolman, W. B. *J. Am. Chem. Soc.*, 2001, 123: 339.
- [65] Baran, J., Duda, A., Kowalski, A., Penczek, S. *Macromol. Symp.*, 1998, 123: 93.
- [66] Chisholm, M. H., Huffman, J. C., Phomphrai, K. *J. Chem. Soc. Dalton Trans.*, 2001, 222.
- [67] Nederberg, F., Connor, E. F., Moller, M., Glauser, T., Hedrick, J. L. *Angew. Chem. Int. Ed.*, 2001, 40: 2712.

- [68] Myers, M., Connor, E. F., Glauser, T., Mock, A., Nyce, G., Hedrick, J. L. J. *Polym. Sci. Part A: Polym. Chem.*, 2002, 40: 844.
- [69] Coulembier, O., Lohmeijer, B. G. G., Dove, A. P., Pratt, R. C., Mespouille, L., Culkun, D. A., Benight, S. J., Dubois, P., Waymouth, R. M., Hedrick, J. L., *Macromolecules.*, 2006, 39: 5617.
- [70] Nyce, G. W., Glauser, T., Connor, E. F., Mock, A., Waymouth, R. M., Hedrick, J. L. J. *Am. Chem. Soc.*, 2003, 125: 3046.
- [71] Connor, E. F., Nyce, G. W., Myers, M., Mock, A., Hedrick, J. L. J. *Am. Chem. Soc.*, 2002, 124: 914.
- [72] Pratt, R. C., Lohmeijer, B. G. G., Long, D. A., Waymouth, R. M., Hedrick, J. L. J. *Am. Chem. Soc.*, 2006, 128: 4556.
- [73] Coulembier, O., Mespouille, L., Hedrick, J. L., Waymouth, R. M., Dubois, P. *Macromolecules*, 2006, 39: 4001.
- [74] Dove, A. P., Li, H., Pratt, R. C., Lohmeijer, B. G. G., Culkun, D. A., Waymouth, R. M., Hedrick, J. L. *Chem. Commun.*, 2006, 2881.
- [75] (a) Wang, C., Li, H., Zhao, X. *Biomaterials*, 2004, 25: 5797. (b) Li, H. *Proceedings of Int. Symp. of DIOPS (Oct. 28-30, 2004, Daegu, Korea)*. (c) Li, H. *Proceeding of Fifth National Conference on Functional Materials and Application (Sept. 12-16, Beijing, China, invited plenary lecture)*.
- [76] (a) Li, H., Wang, C., Yue, J., Zhao, X., Bai, F. J. *Polym. Sci. Part A: Polym. Chem.*, 2004, 42: 3775. (b) *Proceedings of 22nd Annual Meeting of the Polymer Processing Society (July 2-6, 2006, Yamagata, Japan, invited oral presentation)*.
- [77] Kobayashi, S., Uyama, H. *Current Organic Chemistry*, 2002, 6: 209.
- [78] Uyama, H., Wada, S., Fukui, T., Kobayashi, S. *Biochem. Eng. J.*, 2003, 16: 145.
- [79] Uyama, H., Kuwabara, M., Tsujimoto, T., Kobayashi, S. *Biomacromolecules*, 2003, 4: 211.
- [80] Kobayashi, S. J. *Polym. Sci. Part A: Polym. Chem.*, 1999, 37: 3041.
- [81] Loeker, F., Duxbury, C. J., Kumar, R., Gao, W., Gross, R. A., Howdle, S. M. *Macromolecules*, 2004, 37: 2450.
- [82] Matomura, S., Mabuchi, K., Toshima, K. *Macromol. Rapid Commun.*, 1997, 18: 477.
- [83] Matsumura, S., Tsukada, K., Toshima, K. *Int. J. Biol. Macromol.*, 1999, 25: 161.
- [84] Matsumura, S., Mabuchi, K., Toshima, K. *Macromol-Symp.*, 1998, 130: 285.
- [85] Kobayashi, S., Uyama, H., Namekawa, S., Hayakawa, H. *Macromolecules.*, 1998, 31: 5655.

---

## High Functional Inorganic Polymers Containing Main Group 13 – 16 Elements in the Polymer Backbone Chain

Myoung-Hee Kim<sup>2</sup>, Jun Lee<sup>2</sup>, Myong-Shik Cho<sup>1</sup> and Hee-Gweon Woo<sup>\*2</sup>

<sup>1</sup>Gwangju Regional Food & Drug Administration, Gwangju 500-480, the Republic of Korea

<sup>2</sup>Alan G. MacDiarmid Energy Research Institute (AMERI), Nanotechnology Research Center and Department of Chemistry, Chonnam National University, Gwangju 500-757, the Republic of Korea

Tel.: +82-62-530-3378; Fax: +82-62-530-3389

\*E-mail: hgwoo@chonnam.ac.kr

### 3.1 Introduction

Polymers can be largely divided into two categories: organic polymers and inorganic polymers. Organic polymers tend to lose their advantageous material properties (e.g., light weight, flexibility, fabricability, elasticity, mechanical strength, conductivity, optoelectricity) in the presence of oxygen, ozone, corrosion, ultraviolet radiation or at extreme high/low temperatures. Nonetheless, most organic polymers used heavily and widely in modern daily life, hardly decompose in the natural environment and burn releasing toxic chemicals as well, creating serious environmental pollution.<sup>[1]</sup> Furthermore, the availability of raw materials for organic polymers, whose backbone chains mainly consist of carbon atoms linked together or separated by heteroatoms, such as oxygen or nitrogen, is limited by the anticipated shortage of natural petroleum/coal resources. Therefore, research on the design, synthesis, characterization and applications of inorganic polymers, inorganic-organic hybrid polymers or organometallic polymers is needed to avoid

these problems.<sup>[2]</sup> Inorganic polymers have main group non-metallic or submetallic elements (e.g., Si, Ge, Sn, B, P, N, O, S), main group metals (e.g., Mg, Al) or transition metals (i.e., d-block or f-block elements) within the polymers. Main group metal-based and transition metal-containing inorganic polymers have been extensively reviewed by many authors<sup>[3]</sup> and are not covered here because they are beyond the scope of this article, due to the limit of space and interest. Main group non-metallic or sub-metallic inorganic polymers are composed of mainly boron (group 13 element; e.g., polyboranes, polyborazines, polycarboranes), silicon/germanium/tin (group 14 elements; e.g., polysilanes, poly(silane-*co*-germane), polycarbosilanes, polysiloxanes, polysilathianes, polysilazanes, polygermanes, polystannanes), phosphorous (group 15 element; e.g., polyphosphazenes) and sulfur (group 16 element; e.g., polysulfur, polysulfur nitrides) atoms, which do not originate from petroleum/coal resources.<sup>[1,2]</sup> Those main group non-metallic or submetallic inorganic polymers possess outstanding physicochemical/optoelectronic properties. In particular, silicon-based polymers are suitable for specialty materials applications because of quite unusual physical properties and because of the cheap price of natural-abundant silicon raw materials.<sup>[4]</sup>

For the heavier elements in group 14, the formation of A – A bonds to produce a long chain polymer has proven to be not easy because stable unsaturated A = A species, analogues of vinyl compounds, can be prepared only in combination with sterically demanding substituents, which will prevent their polymerization kinetically.<sup>[1,4-6]</sup> Wurtz-type coupling of group 14 dihalides using an alkali metal dispersion as a reagent has been used widely in industry, but it is very problematic because of the pyrophoric nature of sodium metal, hydrolysis of dichlorosilanes in damp air atmosphere, resulting in the formation of corrosive HCl gas. As an alternative to the Wurtz-type coupling of group 14 dihalide compounds, dehydrocatenation and redistributive catenation of group 14 hydrides to their corresponding polymers are useful synthetic routes to the formation of A – A bonds. Group 14 hydrides (hydrosilanes, hydrogermanes, hydrostannanes) possess an A – H bond (A = Si, bond energy of 320 kJ/mol; A = Ge, 289 kJ/mol; A = Sn, 263 kJ/mol) which is more reactive than the C-H bond of hydrocarbons (bond energy of 416 kJ/mol).<sup>[7]</sup> In the following sections, this article mainly accounts for some of the recent advances with respect to group 14 element-based advanced inorganic polymers prepared by dehydrocatenation, redistributive catenation and exhaustive multiple addition of group 14 hydrides. Some selective examples of recent research developments in specialty inorganic polymers (e.g., polyborazines, polyphosphazenes, polysulfur and poly(sulfur nitride)) containing groups 13, 15, and 16 elements are also included.

### **3.2 Group 14 Inorganic Polymers: Polysilanes, Polygermanes, Polystannanes, and their Copolymers**

Inorganic polymers have main group non-metallic or submetallic elements (e.g., Si,

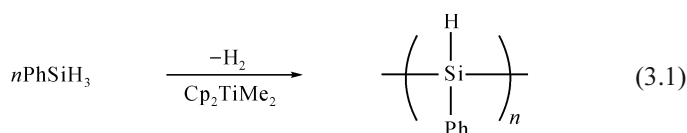
Ge, Sn, B, P, N, O, S), main group metals (e.g., Mg, Al) or transition metals (i.e., d-block or f-block elements) within the polymers. Main group metal-based and transition metal-containing inorganic polymers have been extensively reviewed by many authors and are not covered here because they are beyond the scope of this article, due to the limits of space and interest. In this part, we will introduce group 14 inorganic polymers: polysilanes, polygermanes, polystannanes and their copolymers.

### 3.2.1 Dehydrocatenation of Group 14 Hydrides to Polymers

Si-Si dehydrocatenation with high linear selectivity of hydrosilanes to polysilanes, dehydrocatenation of 1,1-dihydrotetraphenylsilole and 1,1-dihydrotetraphenylgermole to electroluminescent polymers for OLED application, Si-Si/Si-O dehydrocatenation of hydrosilane with alcohol to poly(alkoxysilane)s as sol-gel precursor, Si-N/B-N dehydrocatenation of poly(hydrosilane)s using polyborazine as cross-linking reagent, and dehydrocatenation of hydrogermanes and hydrostannanes to polymers will be introduced separately in this section.

#### 3.2.1.1 Si-Si Dehydrocatenation with High Linear Selectivity of Hydrosilanes to Polysilanes

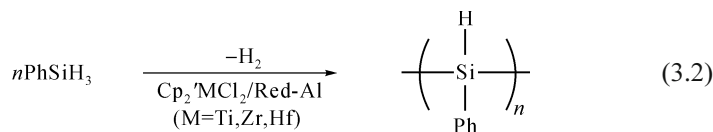
Polysilanes are an interesting type of inorganic polymer with many applications in ceramics/composites, photoelectronics, photoresistors and nonlinear optics.<sup>[8,9]</sup> The peculiar optical and electronic properties of polysilanes are due to the effective conjugation of sigma bond electrons among the silicon atoms in the polymer chain, varying with the molecular weight, conformation and substituents of the polymer.<sup>[10a]</sup> Wurtz-type reductive coupling of dihalosilanes with a hazardous alkali metal dispersion in a toluene-refluxing temperature has some critical disadvantages: (1) intolerance of reducible functional groups, (2) lack of reproducibility due to heterogeneous reaction condition, and (3) limitations for controlling stereochemistry and molecular weight distribution. Some improvements on the Wurtz-type coupling of dihalosilanes have been made by tuning several factors under ultrasonic activation conditions.<sup>[10b]</sup> As an alternative synthetic method, the dehydrocatenation of hydrosilanes, catalyzed by transition metal group 4 metallocene, such as dimethyltitanocene or dimethylzirconocene, was first reported by Harrod et al. (Eq. (3.1)).





However, the dehydrocatenation of hydrosilanes generally produces a mixture of linear polymers and cyclic oligomers, leading to a decrease in polymer molecular weights and improper molecular weight distribution. The following studies were intensively pursued with great efforts made by many researchers worldwide.<sup>[11-13]</sup> For the selective production of linear polymer, the careful design of new group 4 metallocene catalytic systems is important with proper tuning of other factors such as addition rate/order of reagents, and reaction temperature.<sup>[12a]</sup> Linear high molecular weight polysilanes can be used as precursors for preparing functional polysilanes by introducing functional groups upon the linear polysilane. The synthesis of high molecular weight polyphenylsilanes with number-average molecular weight ( $M_n$ ) of *ca.* 5,300 and 4,700  $\text{g}\cdot\text{mol}^{-1}$  was reported by careful control of dehydrocatenation conditions of phenylsilane using zirconocene-based catalysts.<sup>[12a,14]</sup> Tanaka<sup>[15]</sup> and Harrod<sup>[16]</sup> groups also prepared polyphenylsilanes with  $M_n$  of *ca.* 4,600 and 7,300  $\text{g}\cdot\text{mol}^{-1}$ , respectively, from the dehydrocatenation of phenylsilane by using the zirconocene-based combination catalysts of  $[\text{Me}_2\text{N}(\text{CH}_2)_3\text{-H}_4\text{C}_5](\text{Me}_5\text{C}_5)\text{ZrCl}_2/2\text{MeLi}$  and  $\text{Cp}(\text{Me}_5\text{C}_5)\text{ZrCl}_2/2n\text{-BuLi}/(\text{C}_6\text{F}_5)_3\text{B}$ , respectively. A recent survey of the catalytic dehydrocatenation of hydrosilanes under the influence of a wide range of early and late transition metal complexes was reported.<sup>[13b]</sup>

Woo and co-workers recently developed a facile, highly linear-selective dehydrocatenation catalytic system of phenylsilane:  $\text{Cp}'_2\text{MCl}_2/\text{Hydride}$  ( $\text{Cp}'=\text{C}_5\text{H}_5$  or  $\text{C}_5\text{Me}_5$ ;  $\text{M}=\text{Ti, Zr, Hf}$ ;  $\text{Hydride}=\text{Red-Al, Selectrides, super-hydride}$ ) combination catalysts are as shown in Eq. (3.2).<sup>[11,17]</sup>



Woo's combinative dehydrocatenating catalyst system of  $\text{Cp}'_2\text{MCl}_2/\text{Hydride}$  is different from the catalyst systems using  $\text{Cp}'_2\text{MCl}_2/2$  alkyllithiums of Corey, Tanaka, and Harrod. Real catalytic species in the dehydrocatenation of hydrosilanes could be a metallocene hydride based on a sigma-bond metathesis mechanism thru two four-centered transition states.<sup>[12,13b]</sup> Inorganic hydrides can produce a metallocene hydride rapidly whereas alkyllithium may produce a metallocene hydride via a complicated process (e.g., reductive elimination of metallocene alkyls or metathesis reaction with hydrosilane). Thus, an appreciable induction period is not found for the  $\text{Cp}'_2\text{MCl}_2/\text{Hydride}$  combination catalyst. The molecular weight distributions measured from the GPC traces were bimodal, indicating the presence of linear polysilanes and cyclic oligosilanes. The formation of cyclic oligosilanes can be determined by integrating the GPC peaks. The peaks corresponding to SiH in the  $^1\text{H}$  NMR spectrum can be visually separated as linear polysilane (in  $\delta$   $4.2\times 10^{-6}$  –  $4.8\times 10^{-6}$  range) and cyclic oligosilane (in  $\delta$   $4.9\times 10^{-6}$  –  $5.3\times 10^{-6}$  range). The cyclic oligosilane formation can be estimated by integration of the  $^1\text{H}$  NMR peaks, and is used as a means of cross-checking the cyclic/linear ratio. Woo et al. also screened the other group 4 metallocene-based combination

catalysts for the dehydrocatenation of phenylsilane under various reaction conditions. The dehydrocatenation of phenylsilane with  $\text{Cp}'_2\text{MCl}_2/\text{Red-Al}$  combination catalysts rapidly produces linear polyphenylsilanes. The linear selectivity increases in the order of  $\text{Cp}_2\text{Ti}$  (64%) <  $\text{Cp}_2\text{Zr}$  (92%) <  $\text{Cp}(\text{C}_5\text{Me}_5)\text{Zr}$  (95%) <  $\text{Cp}_2\text{Hf}$  (99%) <  $\text{Cp}(\text{C}_5\text{Me}_5)\text{Hf}$  (<99%).<sup>[17b]</sup> The higher linear-selectivity of hafnocene relative to zirconocene is likely due to the lower intrinsic dehydrocatenating activity (originating from stronger Hf—H and Hf—Si bond strengths). The lower linear-selectivity of titanocene relative to zirconocene and hafnocene is probably due to the combined effect of greater intrinsic dehydrocoupling activity (stemming from much weaker Ti—H and Ti—Si bond strengths) and much smaller atomic size (overriding steric crowding around the metal center) of Ti.<sup>[18]</sup> The change in linear selectivity is more pronounced than in other catalytic combination systems:  $\text{Cp}_2\text{TiCl}_2/2\text{MeLi}$  (55%) <  $\text{Cp}_2\text{ZrCl}_2/2\text{MeLi}$  (75%),  $\text{Cp}_2\text{TiCl}_2/2n\text{-BuLi}$  (75%) <  $\text{Cp}(\text{C}_5\text{Me}_5)\text{ZrCl}_2/2n\text{-BuLi}$  (80%) <  $\text{Cp}_2\text{HfCl}_2/2\text{MeLi}$  (85%).<sup>[16,18]</sup> The coordinating environment around the metal center of the  $\text{Cp}'_2\text{MCl}_2/\text{Red-Al}$  combination catalysts could be different from other catalytic systems such as  $\text{Cp}'_2\text{MCl}_2/2\text{R}'\text{Li}$ .<sup>[14,15,18,20]</sup> Red (or Vitride; sodium bis(2-methoxyethoxy)aluminum hydride;  $\text{Na}[\text{H}_2\text{Al}(\text{OCH}_2\text{CH}_2\text{OMe})_2]$ , soluble in toluene) will be quantitatively converted into  $\text{Na}[\text{Cl}_2\text{Al}(\text{OCH}_2\text{CH}_2\text{OMe})_2]$  after reacting with dichlorometallocene. The coordinating structure of the present catalytic system could be similar to the zwitterionic structure of the  $\text{Cp}_2\text{ZrCl}_2/2n\text{-BuLi}/(\text{C}_6\text{F}_5)_3\text{B}$  catalytic system.<sup>[16,19]</sup> The  $\text{Na}[\text{Cl}_2\text{Al}(\text{OCH}_2\text{CH}_2\text{OMe})_2]$  moiety is assumed to be affected by simply coordinating to the metal through an H, Cl-bridge or H, OMe-bridge between the group 4 metal and Al metal. The favorable steric demands imposed by the Cp ring and cocatalyst moiety could prevent the formation of the inactive dimer of metallocene hydride and could suppress the cyclic oligomer formation by chain cleavage reaction as well, leading to greater chain elongation.<sup>[15,16]</sup> However, an overriding steric demand should result in low dehydrocatenating activity. The order of dehydrocatenating activity for the various zirconocenes was found to be the same as the sequence of Tilley<sup>[12]</sup> and Harrod<sup>[16]</sup>:  $(\text{C}_5\text{Me}_5)_2\text{Zr} \ll \text{Cp}_2\text{Zr} < \text{Cp}(\text{C}_5\text{Me}_5)\text{Zr}$ . The  $(\text{C}_5\text{Me}_5)_2\text{ZrCl}_2/\text{Red-Al}$  combination catalyst thus slowly produces a mixture of dimer, trimer, tetramer, and so on. In addition, the order of linear-selectivity for the dehydrocatenating of phenylsilane catalyzed by hydrides with  $\text{Cp}_2\text{ZrCl}_2$  was found to be super-hydride (82%) < *N*-selectride (88%) < Red-Al (92%).<sup>[17c]</sup> The dehydrocatenating of  $\text{PhCH}_2\text{SiH}_3$  yields only low-molecular weight oligomers because an alkylsilane is generally less reactive than an arylsilane.<sup>[20]</sup> The increase in molecular weight of the polymer is made using higher catalyst concentration, but it is affected little by longer reaction times (1 day *versus* 5 days).<sup>[17b]</sup> As expected, linear selectivity and molecular weights decrease with the addition of solvent and with heating, which was similarly observed in other catalytic systems.<sup>[12a,16]</sup> This is because dilution and heating could hamper the proper coordination of the  $\text{Na}[\text{Cl}_2\text{Al}(\text{OCH}_2\text{CH}_2\text{OMe})_2]$  moiety to the metal center. Interestingly, linear selectivity and molecular weights decrease drastically by adding 4 Å molecular sieve (MS 4 Å). The interaction of  $\text{Na}[\text{Cl}_2\text{Al}(\text{OCH}_2\text{CH}_2\text{OMe})_2]$  moiety with MS 4 Å might prevent the close

coordination of  $\text{Na}[\text{Cl}_2\text{Al}(\text{OCH}_2\text{CH}_2\text{OMe})_2]$  moiety to the metal center.<sup>[17b]</sup> An exact molar ratio of Red-Al to dichlorometalocene is necessary to replace both chlorines in order to attain high reactivity. The inactivity observed for higher molar ratios of Red-Al to dichlorometalocene could be attributed to over-complexation of Red-Al moieties to the metal, blocking the empty coordination site necessary for the dehydrocoupling of silane.<sup>[18]</sup> Poor activity is observed for lower molar ratios of Red-Al to dichlorometalocene. All the experimental results described above strongly suggest that better catalysts affording higher linear-selectivity and higher-molecular-weight polymer can be properly designed by tuning the steric and electronic factors of the catalyst environment carefully, including metal, ligand and co-catalyst moieties.

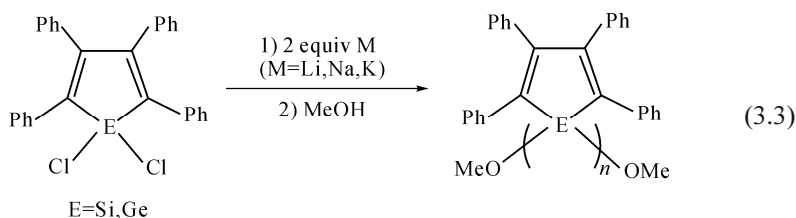
It is interesting to note that the dehydrocatenating of *p*-fluorophenylsilane using  $\text{Cp}_2\text{ZrCl}_2/\text{Red-Al}$  produced soluble amorphous polysilane (*ca.* 75%) and sparingly-soluble crystalline polysilane (*ca.* 25%) in toluene and chloroform. The two polysilanes are soluble in THF and pyridine. In comparison, the dehydrocatenating of *p*-fluorophenylsilane using  $\text{Cp}_2\text{TiCl}_2/\text{Red-Al}$  gives soluble polysilane only.<sup>[17c]</sup> The crystalline polysilane may have interactions<sup>[17b]</sup> in the polymer molecules either with high possibility between Si and F or with low possibility between F and the phenyl ring according to the medium level of MO calculation.

Linear high molecular weight polysilanes can be used as precursors for making functional polysilanes by introducing functional groups on the linear polysilane. The Si-H bonds in the backbone chain of poly(hydrophenylsilane) are transformed to Si-Cl bonds using a mild chlorinating reagent,  $\text{CCl}_4$ . The Si-Cl bonds in the poly(chlorophenylsilane) can be replaced by various nucleophiles such as cyclopropyl, epoxy, aziridinyl, pyridyl, bipyridyl, phosphinyl, poly(ethylene oxide), and thiol. to give new functional polymers which can be used for versatile materials applications in sensors, ion-exchange resins, batteries, drug delivery, nanometal particles preparation, etc.<sup>[17c]</sup>

### 3.2.1.2 Dehydrocatenation of 1,1-Dihydrotetraphenylsilole and 1,1-Dihydrotetraphenylgermole to Electroluminescent Polymers for OLED Application

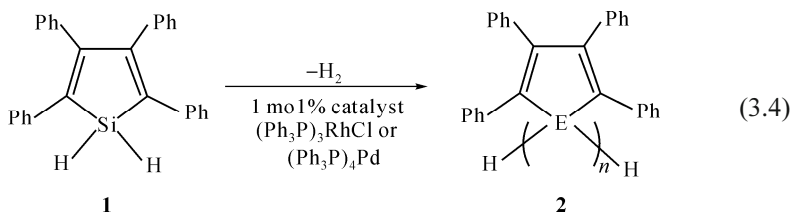
Polysilanes<sup>[21-23]</sup> having low oxidation potentials and a high-lying HOMO exhibit interesting optoelectronic properties, due to sigma bond-conjugation along the silicon backbone chain in the polymer.<sup>[10,24]</sup> Siloles (i.e., silacyclopentadienes), having low reduction potential and low-lying LUMO's, have drawn considerable attention because of their useful electronic properties.<sup>[25,26]</sup> They may be used for electron-transporting materials in devices such as OLED (organic light emitting diode).<sup>[27]</sup> A silole itself does not luminesce in diluted solution but does luminesce in concentrated solution, implying that polysiloles could exhibit different luminescent behavior from that of monomeric siloles.<sup>[25]</sup> Polysiloles, which are expected to have hybrid properties of polysilane and silole by nature in the structure, can be

prepared by 1,1- or 2,5-coupling reactions of siloles using various synthetic catenation methods.<sup>[28]</sup> Electroluminescent poly(silole-*co*-silane)s have also been synthesized in several laboratories worldwide.<sup>[29]</sup> West et al. reported recently the synthesis of polysiloles and polygermole ( $M_w$  ca. 5,200 – 5,700 g·mol<sup>-1</sup>) that have methoxy end groups in 30% – 37% yield by heterogeneous Wurtz 1,1-dehydrocoupling of 1,1-dichlorotetraphenylsilole with 2.0 equivalents of Li, Na, K metal in refluxing THF for 3 days as shown in Eq. (3.3).<sup>[28a]</sup>



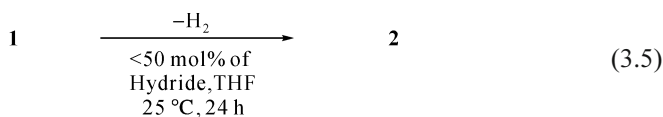
Tamao and collaborators had earlier reported the Wurtz coupling synthesis of polysiloles.<sup>[28d]</sup> The research group also reported the increase of the synthetic yield using Grignard reagent in the Wurtz catenation.

As an alternative to the Wurtz coupling of 1,1-dichlorosilole, the homogeneous dehydrocatenating methodology was demonstrated in Tanaka's earlier report of the dehydrocatenating synthesis of poly(dibenzosilole).<sup>[30a]</sup> Trogler and co-workers recently reported the 1,1-dehydrocatenating of 1,1-dihydro-tetraphenylsilole (**1**) to an electroluminescent polysilole (**2**) ( $M_w$  ca. 4,000 – 6,000 g·mol<sup>-1</sup>), having hydrogen end groups, in high yield 80% – 90% using 1 mol% of the late transition metal complexes [(Ph<sub>3</sub>P)<sub>3</sub>RhCl and ((Ph<sub>3</sub>P)<sub>4</sub>Pd)] as catalysts.<sup>[29b,30b]</sup> Woo et al. prepared **2** ( $M_w$  ca. 5,500 – 6,200 g·mol<sup>-1</sup>) in > 95% yield by the dehydrocatenating of **1** using [RhCl(COD)<sub>2</sub>]<sub>2</sub> and Pt(PMe<sub>3</sub>)<sub>4</sub> as catalyst (Eq. (3.4)).<sup>[31a]</sup>

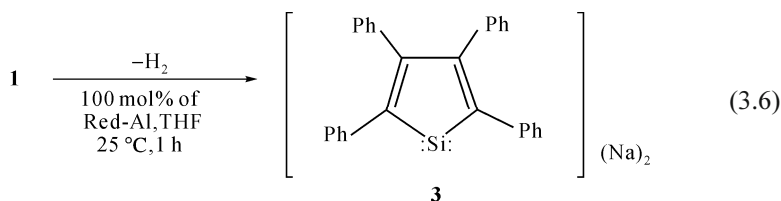


The same authors also reported the synthesis of poly(tetraphenylgermole) ( $M_w$  ca. 5,800 – 6,500 g·mol<sup>-1</sup>) in > 92% yield by dehydrocatenating of 1,1-dihydro-tetraphenylgermole using the same catalysts. The UV-vis spectrum of poly(tetraphenylgermole) shows an absorption at 377 nm, which is assignable to both the  $\sigma$ - $\sigma^*$  transition of the Ge-Ge backbone chain and  $\pi$ - $\pi^*$  transition of the germole ring. The polygermole is intensively photoluminescent, emitting green light at 487 nm.<sup>[31a]</sup> The hydrogen end groups of the polysiloles and polygermoles are then transformed to other useful functional groups by various chemical reactions.<sup>[31a]</sup> Interestingly, the dehydrocatenating of **1** using AgNO<sub>3</sub> in air atmosphere produced polysiloloxane instead of polysilole.<sup>[31c]</sup>

As an alternative to the heterogeneous Wurtz reductive coupling of dichlorosilole and the homogeneous late-transition-metal-complex-catalyzed dehydrocatenating of **1**, Woo et al. also synthesized **2** in high yield by anionic homogeneous dehydrocatenating of **1** under mild conditions, catalyzed with inorganic hydrides such as Selectrides {MB[CH(CH<sub>3</sub>)C<sub>2</sub>H<sub>5</sub>]<sub>3</sub>H; M = Li, Na, K}, Red-Al {Na[H<sub>2</sub>Al(OCH<sub>2</sub>CH<sub>2</sub>OCH<sub>3</sub>)<sub>2</sub>]}, and super-hydride [LiB(C<sub>2</sub>H<sub>5</sub>)<sub>3</sub>H] as shown in Eq. (3.5).<sup>[32a,b]</sup>



Dehydrocatenating of **1** catalyzed by < 50 mol% (i.e., M-H/Si-H ≤ 0.5) of Red-Al produced **2** as light yellow powders. Polymers with molecular weights (*M<sub>w</sub>*) of 4,600 and 4,100 g·mol<sup>-1</sup> were obtained in 86% and 78% yields when 15 mol% and 50 mol% of Red-Al were used, respectively. Polymer yields and molecular weights with 15 mol% of Red-Al were higher compared to polymers obtained with 50 mol% of Red-Al. Products from the reaction of **1** with 15 mol%, 25 mol%, and 50 mol% Red-Al were isolated by preparative GPC and were characterized by NMR spectroscopy. Shorter oligosiloles, such as silole dimer or trimer, were not found in products. However, when 100 mol% of Red-Al (i.e., M-H/Si-H = 1) was used, the formation of silole dianion **3**<sup>[33a]</sup> was observed without forming **2** as shown in Eq. (3.6).



Similarly, the dehydrocatenating of **1** using 15 mol% of Selectrides and super-hydride at 25 °C for 24 h produced **2** in 77% – 78% isolated yield. The molecular weight (*M<sub>w</sub>*) and polydispersity index (PDI) of all the polysiloles were in the range of 4,300 – 5,800 g·mol<sup>-1</sup> and 1.1 – 1.2, respectively. Polymerization yield and polymer molecular weight increase in the order: *L*-selectride < *N*-selectride < *K*-selectride. This trend appears to be closely related to the ionic character of the selectrides. The polymerization yields were almost the same for Red-Al, *K*-selectride and super-hydride, but the molecular weight increases in the order: Red-Al < *K*-selectride < super-hydride. Like the polysiloles prepared by West and co-workers,<sup>[28a]</sup> these polysiloles have a characteristic UV absorption around 300 nm, assigned to the σ-σ\* transition of the Si-Si polymer backbone chain. They are photoluminescent, emitting green light at 520 nm when the excitation is at 330 nm. These polysiloles are strongly electroluminescent around 520 nm. The similar dehydrocatenating of 1,1-dihydrotetraphenylgermole with the hydrides produced

polygermole in high yield. Furthermore the co-dehydrocatenating of **1** and 1,1-dihydrotetraphenylgermole (varying the mixing mole ratio) with the hydrides yielded poly(silole-*co*-germole)s in high yield.<sup>[31]</sup> The attempts at synthesizing other copolymers such as poly(silole-*co*-stannole) and poly(germole-*co*-stannole) were unsuccessful.<sup>[31c]</sup>

For the dehydrocatenating of **1** to **2**, K-Selectride and super-hydride were the most active catalysts examined. **2** was prepared in high yield directly from the reaction of 1,1-dichlorotetraphenylsilole (instead of **1**) using < 1.5 equiv of Red-Al (instead of < 0.5 equiv).<sup>[32c]</sup> Unlike in the case of late-transition-metal-complex-catalyzed dehydrocatenating (which is generally proceeded by oxidative addition/reductive elimination processes),<sup>[30,31a,b]</sup> catalysis for the conversion of **1** to **2** by early transition metal complexes, Cp<sub>2</sub>MCl<sub>2</sub>/Red-Al (M = Ti, Zr, Hf)<sup>[17]</sup> is ineffective in the dehydrocatenating of **1** because **1** is sterically demanding, considering the four-centered transition state in the sigma-bond metathesis mechanism.<sup>[12]</sup> Woo suggested a plausible mechanism involving the preferential attack of a hydride ion on either the silicon atom or silole ring of **1** to form an activated anionic intermediate such as a pentacoordinated  $\sigma$ -complex or  $\pi$ -complex.<sup>[32]</sup>

The activated anionic intermediate may release both a dihydrogen molecule and a hydride ion (This hydride may participate again in the catalytic cycle) sequentially to form a silylene type of silole. If the activated anionic intermediate accepts another hydride ion, a silole dianion **3** will be formed after releasing two dihydrogen molecules. The silylene type of silole will then either self-couple or keep inserting into the Si-H bond of **1**, forming **2** (Fig. 3.1). For the homo dehydrocatenating of 1,1-dihydrogermole to polygermole or *co*-dehydrocatenating of 1,1-dihydrogermole with 1,1-dihydrosilole to poly(silole-*co*-germole)s the same mechanism depicted in Fig. 3.1 should be used.

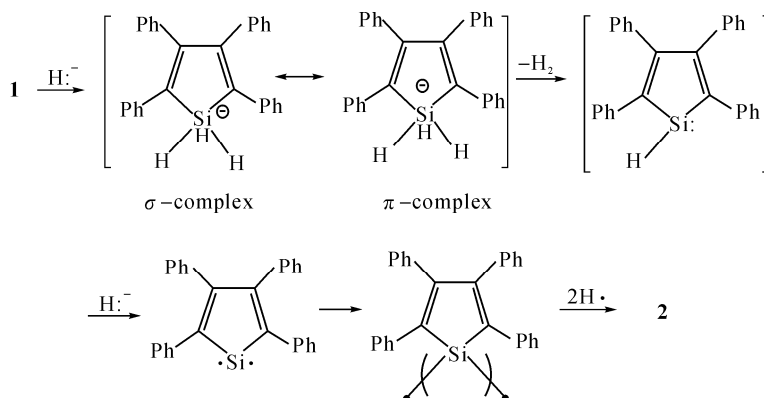
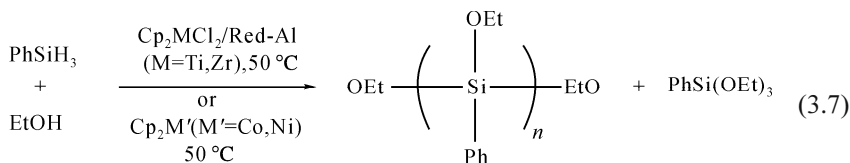


Fig. 3.1. Possible mechanism for the formation of polysilole **2** from the dehydrocatenation of **1**

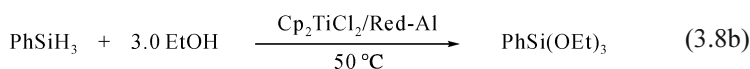
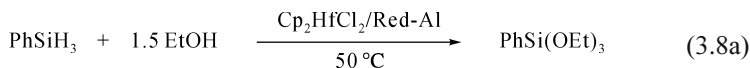
### 3.2.1.3 Si-Si/Si-O Dehydrocatenation of Hydrosilane with Alcohol to Poly(alkoxysilane)s as Sol-Gel Precursor

A wide range of catalysts (e.g., acids, bases, and homogeneous/heterogeneous transition metal catalysts) have been used for the Si-O dehydrocatenation of alcohols with silanes.<sup>[13a,34,35a]</sup> The Si-O dehydrocatenation of bis-hydrosilanes with diols, catalyzed by rhodium complex, yielding polysiloxanes was reported.<sup>[35b,c]</sup> The Si-S dehydrocatenation of hydrosilanes with dithiols to produce polysilathianes was also reported.<sup>[35d]</sup> The polysiloxanes and polysilathianes are beyond the scope and interest of this account and thus are not covered here. Si-Si dehydrocatenation of hydrosilanes with late transition metal complex catalysts produces a mixture of oligomers along with significant amounts of proportionated by-products.<sup>[13b]</sup> Harrod et al. surveyed the recent dehydrocatenation of hydrosilanes with alcohols.<sup>[11]</sup> The transition metal complexes of group VIII (Ni, Co, Rh, Pd, Ir, Pt, etc.) have been extensively used in the catalytic dehydrocatenation of hydrosilanes with various nucleophilic reagents.<sup>[36]</sup> A recent review described the catalytic dehydrocatenation of hydrosilanes under the influence of a range of early and late transition metal complexes.<sup>[13b]</sup>

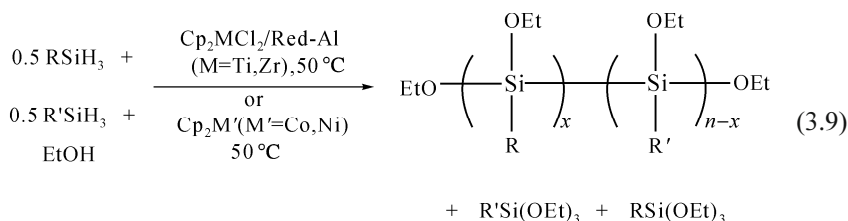
Numerous studies were performed either on the alcoholysis of hydrosilanes (i.e., Si-O catenation) or on the dehydropolymerization of silanes (i.e., Si-Si catenation) in the presence of various transition metal complex catalysts.<sup>[13,34,35a-c,36]</sup> Poly(alkoxysilane)s can be used as important precursors for preparing interesting polysilane-siloxane hybrids by sol-gel methods with an acid/base catalyst in the reverse micellar environment.<sup>[37a]</sup> The Woo group first described the combinative Si-Si/Si-O dehydrocatenation of hydrosilanes with alcohols (hydrosilane:alcohol = 1:1.5 mole ratio) at 50 °C, catalyzed by Cp<sub>2</sub>MCl<sub>2</sub>/Red-Al (M = Ti, Zr) and Cp<sub>2</sub>M' (M = Co, Ni), producing poly(alkoxysilane)s in one-pot in high yield (Eq. (3.7)).



The hydrosilanes include *p*-C<sub>6</sub>H<sub>4</sub>SiX<sub>3</sub> (X = H, CH<sub>3</sub>, OCH<sub>3</sub>, F), PhCH<sub>2</sub>SiH<sub>3</sub> and (PhSiH<sub>2</sub>)<sub>2</sub>. The alcohols are MeOH, EtOH, *i*-PrOH, PhOH and CF<sub>3</sub>(CF<sub>2</sub>)<sub>2</sub>CH<sub>2</sub>OH. The weight average molecular weights (*M<sub>w</sub>*) of the poly(alkoxysilane)s are in the range of 600 – 8,000 g·mol<sup>-1</sup>. However, Cp<sub>2</sub>M' (M' = Co, Ni) has no catalytic activity toward Si-Si dehydrocatenation of primary hydrosilanes in inert atmosphere.<sup>[37b]</sup> Interestingly, the dehydrocoupling reactions of phenylsilane with ethanol (1:1.5 mole ratio) using Cp<sub>2</sub>HfCl<sub>2</sub>/Red-Al, and phenylsilane with ethanol (1:3 mole ratio) using Cp<sub>2</sub>TiCl<sub>2</sub>/Red-Al, produced only triethoxyphenylsilane PhSi(OEt)<sub>3</sub> as product (Eq. (3.8a)) and (Eq. (3.8b)).<sup>[38]</sup>



Similarly, the combinative Si-Si/Si-O dehydrocatenation of mixed hydrosilanes with alcohols at 50 °C, catalyzed by Cp<sub>2</sub>MCl<sub>2</sub>/Red-Al (M = Ti, Zr) and Cp<sub>2</sub>M' (M' = Co, Ni), giving copoly(alkoxysilane)s in one-pot in high yield were reported (Eq. (3.9)).<sup>[37a]</sup>



In a similar manner, Woo and co-workers performed the combinative Si-Si/Si-O dehydrocoupling reactions of hydrosilanes with mixed alcohols (two different alcohols were used in the same mole ratio; 1:0.75:0.75 mole ratio) at 50 °C, catalyzed by Cp<sub>2</sub>MCl<sub>2</sub>/Red-Al (M = Ti, Zr) and Cp<sub>2</sub>M' (M'=Co, Ni), producing copoly(alkoxysilane)s in one-pot in high yield.<sup>[37a]</sup> The bonding characters [mixing interaction between σ (silicon) orbital and n (oxygen) orbital] of Si-O bonds in poly(dialkoxysilylene)s were studied in detail using various levels of molecular orbital calculations.<sup>[37c]</sup> The poly(alkoxysilane)s were used as precursor for sol-gel reaction to synthesize the polysilane-polysiloxane hybrid in high yield.<sup>[37d]</sup>

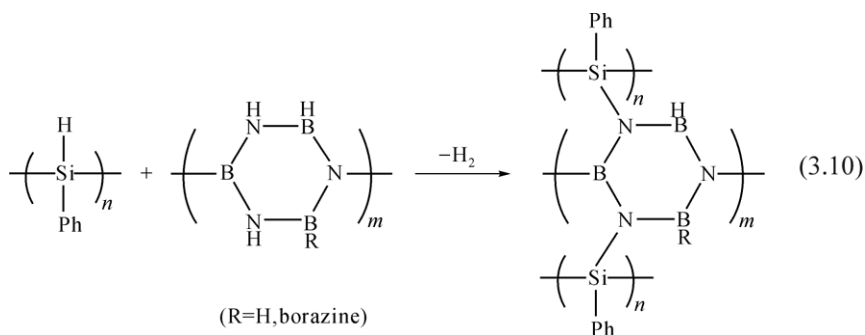
### 3.2.1.4 Si-N/B-N Dehydrocatenation of Poly(hydrosilane)s using Polyborazine as Cross-Linking Reagent

An extensive review on the Si-N dehydrocatenation of hydrosilanes with various amines (including ammonia, alkyl amines and aromatic amines, hydrazines), catalyzed by early and late transition metal complexes, has appeared.<sup>[11]</sup> Eisen and co-workers reported the Si-N dehydrocatenation of phenylsilane with various amines with [(Et<sub>2</sub>N)<sub>3</sub>U[BPh<sub>4</sub>]].<sup>[39a]</sup> The B-N dehydrocatenation of borazine and poly(vinylborazine) was reported by Sneddon et al.<sup>[39b]</sup> No Si-B dehydrocatenation of hydrosilane with borazine has been reported up to date although it may possibly occur.

Since silicon-based polymers are generally used for preparing non-oxide ceramics, various polymeric precursors with different structures and compositions have been designed and synthesized.<sup>[39c]</sup> Preceramic polycarbosilane (PCS), used for preparing commercial Nicalon fiber, is synthesized by the poorly efficient pyrolysis of polydimethylsilane (PDMS) because of the formation of



hazardous gaseous compounds (resulting in low yield) and irregularity of the composition of the resulting PCS<sup>[39d]</sup>, although some modifications were made by adding additives such as polyborodimethylsiloxane and zeolite ZSM-5.<sup>[39e,f]</sup> As an alternative precursor for SiC ceramics, the Woo group investigated polyphenylsilane (PPS,  $\text{-(Si(Ph)H)}_n$ ) and polyvinylsilane (PVS,  $\text{-(CH}_2\text{CH(SiH}_3\text{))}_n$ ). An ideal preceramic precursor for Si-C ceramics should show: (1) high ceramic residue yield, to minimize the cost and volume change associated with pyrolytic conversion to ceramics and consequently maximize the control of porosity and densification, and (2) a suitable processability (i.e., viscosity) allowing it to be shaped into the needed forms prior to pyrolysis. In this context, it is disadvantageous that the low viscosity PPS and PVS undergo drastic mass loss during pyrolysis, which leads to low ceramic residue yields (20 wt% – 40 wt%).<sup>[39g,40a]</sup> To improve the ceramic residue yields and processabilities of PPS and PVS, the Seyferth group tried to use many efficient additives including early and late transition metal complex catalysts, urea and decaborane.<sup>[39g,h]</sup> Woo and collaborators also reported an increase in thermal stability (i.e., an increase of TGA ceramic residue yield) of PCS and oligocarborasilane (OCS) by dehydrocatenation of Si-H bonds in the PCS and OCS using groups **4** and **6** transition metal complex catalysts.<sup>[40b,c]</sup> Woo, Kim et al. described the additive effect of polyborazine (PBN) on the improvement of the ceramic residue yield of the polysilane, as depicted in Eq. (3.10).<sup>[41]</sup>



The ceramic residue yield of PPS increases from an original 39 wt% to 65 wt%, and PVS from an original 26 wt% to 64 wt%, by simply heating with 1 wt% PBN at 70 °C for < 6 h. Furthermore, the low viscosity PPS and PVS are transformed into highly viscous polymers, which are suitable for hand drawing into green fibers. Analysis using NMR spectroscopy suggests that Si-N/B-N dehydrocatenation of SiH<sub>3</sub> in PVS and Si-H in PPS with PBN is responsible for the improved ceramic residue yields.<sup>[41a]</sup> When the concentration of PBN increases, the B, N-incorporated SiC ceramic composites, which can be used for advanced materials applications, are produced. Similarly, poly(hydrosilane)s can be also used for a crosslinking agent for PBN. When the addition of poly(hydrosilane) increases, the SiC-incorporated BN ceramic composites are effectively formed.<sup>[41b]</sup>

### 3.2.1.5 Dehydrocatenation of Hydrogermanes and Hydrostannanes to Polymers

Recent reviews have appeared on the catalytic dehydrocoupling of hydrogermanes and hydrostannanes to polygermanes and polystannanes mediated by transition metal complex catalysts.<sup>[11,42]</sup> As in the case of polysilanes, polygermanes and polystannanes have been conventionally synthesized by the Wurtz-type dehalocatenation of halogermanes and halostannanes using alkali metals (e.g., Li, Na, K) or alkaline earth metal (Mg).<sup>[43]</sup> The catalytic dehydrocatenation of  $\text{PhGeH}_3$  to a cross-linked gel type of polygermane using  $\text{Cp}_2\text{TiMe}_2$  catalyst was first reported.<sup>[44a]</sup> The formation of the highly cross-linked insoluble gel product might be caused by further dehydrocatenation of backbone Ge-H bonds or by partial redistribution of  $\text{-(Ph-GeH)}_n$  moiety to  $\text{-(Ph}_2\text{Ge)}_x\text{-(GeH}_2)_{n-x}$ , followed by further dehydrocatenation of  $\text{-(GeH)}_{n-x}$  moiety. The first one seems to occur with a higher possibility because the catalytic dehydrocatenation of  $\text{Ph}_2\text{GeH}_2$  gives a mixture of oligomer and  $(\text{Ph}_2\text{GeH})_2$  using  $\text{Cp}_2\text{TiMe}_2$  catalyst.<sup>[44a]</sup> Tanaka et al. synthesized partially cross-linked soluble poly(phenylgermane) in 67% isolated yield by the catalytic dehydrocatenation of  $\text{PhGeH}_3$  using  $\text{CpCp}^*\text{ZrCl}_2/2n\text{-BuLi}$  ( $\text{Cp}=\text{Cp}$  or  $\text{Cp}^*$ ) combination catalyst, followed by precipitation of the polymer solution in THF with pentane.<sup>[44b]</sup> Similarly, Woo and co-worker reported the preparation of soluble poly(phenylgermane) and insoluble poly(phenylgermane) by the catalytic dehydrocatenation of  $\text{PhGeH}_3$  using  $\text{Cp}_2\text{MCl}_2/\text{Red-Al}$  ( $\text{M}=\text{Ti, Zr, Hf}$ ) combination catalyst.<sup>[44c]</sup> From the catalytic reaction, the percentage of the soluble poly(phenylgermane) decreased in the order of  $\text{Hf (89\%)} > \text{Zr (82\%)} > \text{Ti (25\%)}$  probably because the larger size of zirconium and hafnium could provide better coordinating space for polygermane chains than the smaller size of titanium.

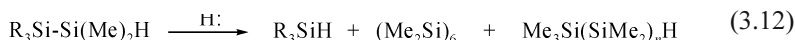
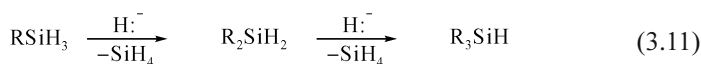
Tilley et al. prepared linear polystannanes ( $M_w$ , ca. 70,000  $\text{g}\cdot\text{mol}^{-1}$ ) by dehydrocatenation of  $\text{R}_2\text{SnH}_2$  ( $\text{R} = n\text{-Bu, } n\text{-Hex, } n\text{-Oct}$ ) using  $\text{CpCp}^*\text{Zr}[\text{Si}(\text{SiMe}_3)_3]\text{Me}$  catalyst.<sup>[45]</sup> The authors investigated the properties of  $\sigma$ -conjugated polystannanes such as low band gap,<sup>[46a]</sup>  $\sigma$ - $\sigma^*$  transition energy,<sup>[46b]</sup> and order-disorder phase transition.<sup>[46c]</sup> The dimerization of  $\text{R}_3\text{SnH}$  ( $\text{R} = \text{Ph, } n\text{-Bu}$ ) by a Fe-Pd heterobimetallic alkoxysilyl and siloxysilyl complex was reported.<sup>[47]</sup> The mechanism for the dehydrocatenation of hydrogermanes and hydrostannanes by the group 4 metallocene catalysts could be similar to the mechanism for dehydrocatenation of hydrosilanes by those catalysts.<sup>[11,12]</sup> Tilley and Neale recently proposed a modified mechanism comprising steps of  $\sigma$ -elimination and  $\sigma$ -bond metathesis based on their kinetic study of hafnium hydrostannyl complexes by  $^1\text{H}$  NMR spectroscopy.<sup>[48]</sup>

### 3.2.2 Redistributive Catenation of Group 14 Hydrides to Polymers

This section mainly accounts the recent advances with respect to group 14 element-based advanced inorganic polymers prepared by redistributive catenation.

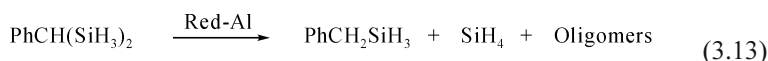
## 3.2.2.1 Desilanative Catenation of Multisilylmethanes to Oligomers

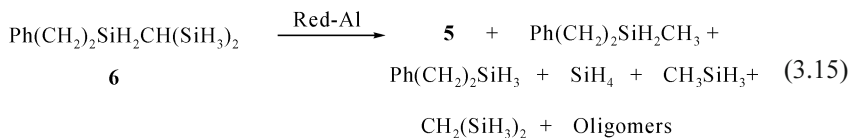
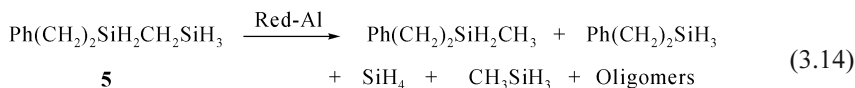
There are many types of hydrides which have Lewis basicity. Inorganic hydrides are generally soluble in polar solvent (e.g., THF) because of their ionic or polar nature. Nonetheless, the toluene solution of Red-Al (or vitride; sodium bis(2-methoxyethoxy)aluminum hydride) commercially available efficiently catalyzes the polymerization of lactams and olefins and the trimerization of isocyanates.<sup>[49]</sup> Corriu and co-workers reported the desilanative proportionation reactions of di- and trihydrosilanes to both the more substituted silanes and the less substituted silanes<sup>[50a]</sup> and the desilanative oligomerization of disilanes<sup>[50b]</sup> by exchanging their substituents Eqs. (3.11) and (3.12), catalyzed by inorganic hydrides (e.g., NaH, KH in THF).



The authors proposed a mechanism involving a reactive pentacoordinated hydrosilyl anion,<sup>[50c]</sup> which is formed by the addition of hydride ( $\text{H}^-$ ) on the silanes, for the redistribution reactions. They suggested that the reactivity increases in the order: hexa-coordinated silicon > penta-coordinated silicon > tetra-coordinated silicon.

Similarly Riviere and collaborators reported the preparation of oligophenylgermane ( $\text{PhHGe}$ )<sub>n</sub> by redistributive coupling of ( $\text{PhH}_2\text{Ge}$ )<sub>2</sub> under the influence of a Lewis base  $\text{PhH}_2\text{GeLi}$ .<sup>[51]</sup> The strong Lewis acid  $\text{AlCl}_3$  also catalyzes a redistribution reaction of hydroarylsilane to quaternary arysilane with evolving pyrophoric  $\text{SiH}_4$ .<sup>[52]</sup> Woo et al. reported the intriguing desilanative catenation of bis- and tris(silyl)methanes to oligomers, catalyzed by Red-Al.<sup>[53]</sup> The bis- and tris(silyl)methanes are multisilylmethanes which have reactive Si-C-Si linkages. Thus, 2-phenyl-1,3-disilapropane (**4**) undergoes desilanative coupling at ambient temperature with 1 mole% Red-Al (3.4 mol·L<sup>-1</sup> solution in toluene) within 1 h to produce benzylsilane as the major product and as yet uncharacterized high-boiling oligomers as minor products with  $\text{SiH}_4$  gas, as shown in Eq. (3.13). In a similar manner, the bis(silyl)methane, 1-phenyl-3,5-disilapentane **5**, is quantitatively converted to methylphenethylsilane and phenethylsilane (7:3 ratio, identified by GC/MS analysis) as the major product and uncharacterized high-boiling oligomers as minor products with  $\text{SiH}_4$  and  $\text{MeSiH}_3$  gases (Eq. (3.14)). Likewise, the tris(silyl)methane, 1-phenyl-4-silyl-3,5-disilapentane **6**, is quantitatively transformed to **5**, methylphenethylsilane, and phenethylsilane (3:12:4 ratio identified by GC/MS analysis) as major products and uncharacterized high-boiling oligomers as minor products along with the formation of  $\text{SiH}_4$ ,  $\text{MeSiH}_3$ , and  $\text{CH}_2(\text{SiH}_3)_2$  molecules (Eq. (3.15)).<sup>[53]</sup>



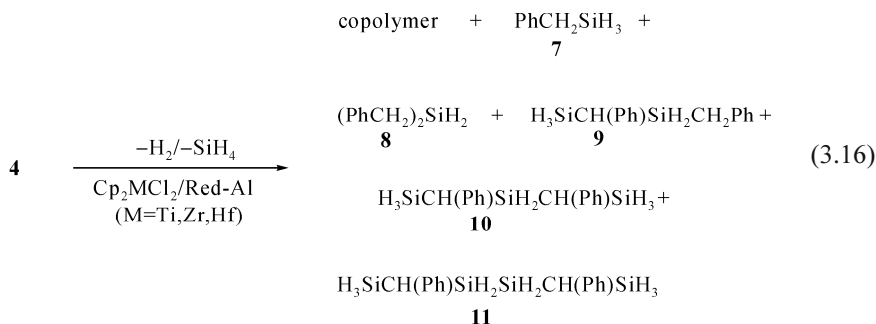


Benzylsilane does not undergo further appreciable redistribution (i.e., to dibenzylsilane and tribenzylsilane; such redistribution should be possible at high temperature because the cleavage of less reactive Si-C bond needs higher energy than that of more reactive Si-C-Si bonds) under the mild redistribution conditions. Methylene bridges between two silicon atoms are more readily deprotonated by strong organometallic bases than are methyl groups bonded to a single silicon atom because two silicon centers jointly can stabilize the resulting anion better than one silicon center via  $\pi\pi$ - $d\pi$  interaction between p-orbital of carbon and d-orbital of silicon<sup>[54]</sup> (but another explanation based on some molecular orbital calculation may be possible.<sup>[37c]</sup>). However, cleavage of the Si-C bond takes place normally under extremely harsh conditions.<sup>[55]</sup> Methylphenethylsilane can be obtained via Si-C bond cleavage of **4**, evolving SiH<sub>4</sub> gas in the redistribution reaction of **5**. However, phenethylsilane cannot be obtained via the direct Si-C bond cleavage of methylphenethylsilane, but via the direct Si-C bond cleavage of **5** with CH<sub>3</sub>SiH<sub>3</sub> gas evolution. Methylphenethylsilane was obtained in a higher yield than phenethylsilane, implying that SiH<sub>4</sub> formation is easier than CH<sub>3</sub>SiH<sub>3</sub> formation, likely due to less steric hindrance exerted upon adding hydride to the silanes. On the other hand, methylphenethylsilane can be formed via consecutive Si-C bond scissions of **6**, giving off SiH<sub>4</sub> gas in the redistribution reaction of **6**. However, phenethylsilane cannot be obtained by the direct Si-C bond cleavage of methylphenethylsilane, but can be obtained either by the direct Si-C bond cleavage of **5** with release of CH<sub>3</sub>SiH<sub>3</sub> or by the direct Si-C bond cleavage of **6** with the formation of CH<sub>2</sub>(SiH<sub>3</sub>)<sub>2</sub>. The yield for methylphenethylsilane was higher than that for phenethylsilane, which suggests that SiH<sub>4</sub> formation is easier than CH<sub>2</sub>(SiH<sub>3</sub>)<sub>2</sub>, because of a different steric demand upon the addition of hydride to the silane. The as yet uncharacterized high-boiling oligomers could be obtained only during the redistribution process because the reactions of benzylsilane, methylphenethylsilane and phenethylsilane with Red-Al do not yield an oligomeric mixture of silanes under the reaction conditions. The oligomers might be oligocarbosilanes or a mixture of oligocarbosilanes and oligosilanes.

Based on the experimental results described above, Woo et al. proposed a likely mechanism involving the preferential addition of the hydride to the silicon at the less hindered site, forming an active intermediate and SiH<sub>4</sub> gas.<sup>[53]</sup> The  $\alpha$ -silyl carbanion of pentacoordinated anionic species then collapses to give an  $\alpha$ -silyl carbanion. The  $\alpha$ -silyl carbanion may then take up a hydrogen from a hydrogen source that is around (e.g., silane or solvent) to form a silane or may lose a hydride to produce a

silene, associating to produce some oligo(carbosilane)s, or isomerizing to a silyl anion. The silyl anion may lose a hydride to give an unstable silylene, which can add to silane or an associate, producing some linear or cyclic oligosilanes. The regenerated hydride may add to **4** to participate again in the catalytic cycle.

Very interestingly, the catalytic reactions of **4** with Red-Al, Cp<sub>2</sub>MCl<sub>2</sub>/Red-Al, and Cp<sub>2</sub>MCl<sub>2</sub>/2*n*-BuLi (M = Ti, Zr, Hf) give different results. The redistribution-dehydrocoupling of **4** catalyzed by Cp<sub>2</sub>MCl<sub>2</sub>/Red-Al gives polymer (*M<sub>w</sub>* = 550 for Ti; 750 for Zr; 2040 for Hf) with low TGA ceramic residue yield (*ca.* 3% at 800 °C for Ti, Zr, Hf) in moderate yield (20% for Ti; 25% for Zr; 28% for Hf)<sup>[56,57]</sup> as shown in Eq. (3.16) whereas the redistributive catenation, as shown in Eq. (3.13), of **4** catalyzed by Red-Al gives oligomer (*M<sub>w</sub>* < 500) in very low yield (less than 3%).<sup>[53]</sup>



A plausible mechanism for the redistribution-dehydrocoupling of **4** with Cp<sub>2</sub>ZrCl<sub>2</sub>/Red-Al is depicted in Fig. 3.2.<sup>[57]</sup>

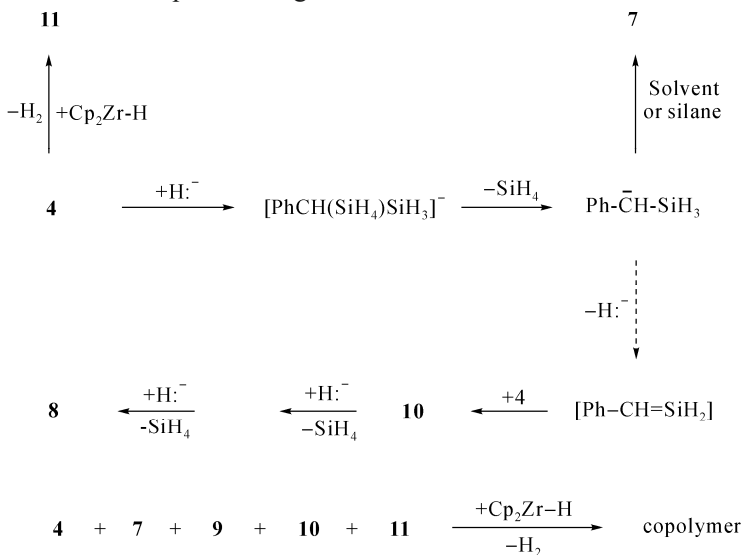
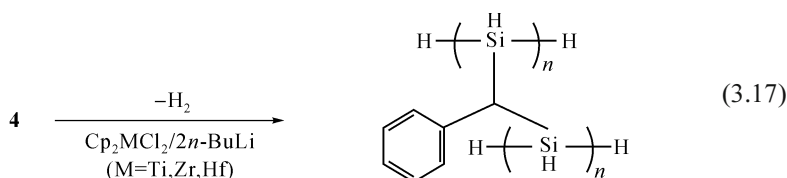


**Fig. 3.2.** Plausible mechanism for the redistribution-dehydrocatenation of **4** catalyzed by Cp<sub>2</sub>ZrCl<sub>2</sub>/Red-Al (Adapted from Ref. 57. Copyright (1996), with permission from the Korean Chemical Society)

The mechanism involves the preferential attack of the hydride on the less hindered silicon with the formation of a penta-coordinated anionic species which collapses to give an  $\alpha$ -silyl carbanion intermediate and  $\text{SiH}_4$  gas. The  $\alpha$ -silyl carbanion may then take up a hydrogen from the hydrogen source (e.g., silane or solvent) to yield **7** or may lose a hydride, participating again in the catalytic cycle to produce phenylsilane. All attempts at trapping the transient intermediate silene are unsuccessful. The reason could be probably due to the active Si-H bonds abundant in the reaction mixture. Compound **4** may add to phenylsilane to give **10**, which will become **8** and **9** by sequentially losing  $\text{SiH}_4$  gas. The silanes might then undergo catalytic dehydrocoupling to produce a copolymer.<sup>[56,57]</sup>

By comparison with the reactions as shown in Eqs. (3.15) and (3.16), dehydrocoupling (without redistribution) of **4** catalyzed by  $\text{Cp}_2\text{MCl}_2/2n\text{-BuLi}$  gives mostly highly crosslinked polysilanes along with soluble oily polymers as minor products (Eq. (3.17)).<sup>[56-58]</sup>

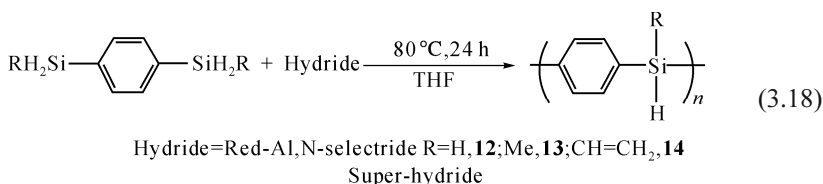


Insoluble polymers are isolated in 82% yield for Ti, 95% yield for Zr, and 80% yield for Hf. TGA ceramic residue yields are measured to be 72% for Ti, 73% for Zr, and 74% for Hf. The weight average molecular weights of the oily polymers are 4,120 for Ti, 9,020 for Zr and 5,010 for Hf. The TGA ceramic residue yields of the soluble oily polymers are *ca.* 14%. The dehydrocatenation mechanism of **4** could be similar to the sigma-bond metathesis for the dehydrocatenation of phenylsilane.<sup>[11,12]</sup>

### 3.2.2.2 Redistributive Catenation of Bis(silyl)phenylenes to Hyperbranched Polymers

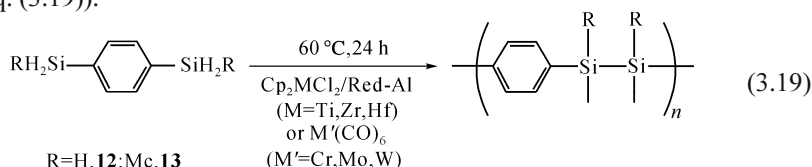
As described in detail in the above section, the desilanative coupling and desilanative-dehydrocatenation of **4** possessing a Si-C-Si connection (i.e., 1,1-bissilyl connection) in the molecule, catalyzed by Red-Al and  $\text{Cp}_2\text{MCl}_2/\text{Red-Al}$  (M = Ti, Zr, Hf), produce oligomers and polymers Eqs. (3.13) and (3.16), respectively.<sup>[53,56-58]</sup> In comparison, redistributive catenation of 1,4- $\text{C}_6\text{H}_4(\text{SiH}_3)_2$  **12** using 2 mol% Red-Al gave 33% of soluble polysilane ( $M_w$ : 2,800;  $M_w/M_n = 1.2$ ) and hyperbranched polysilane (TGA ceramic residue yield: 63%) which is insoluble in organic solvents because of the high extent of crosslinking.<sup>[59]</sup> Similarly, redistributive catenation of **12** in the presence of 2 mol% inorganic hydride (*N*-selectride, super-hydride) afforded soluble polysilane in moderate yield (30%,  $M_w = 3,100$  for *N*-selectride; 27%,  $M_w=3,500$  for super-hydride) and hyperbranched polysilane (TGA ceramic residue yield=83% for *N*-selectride; 67%

for super-hydride) as shown in Eq. (3.18).



The redistributive catenation of 1,4-C<sub>6</sub>H<sub>4</sub>(SiH<sub>2</sub>Me)<sub>2</sub> **13** using 2 mol% Red-Al gave 70% of soluble polysilane ( $M_w$ : 1,500;  $M_w/M_n = 1.5$ ) and hyperbranched polysilane (TGA ceramic residue yield: 70%).<sup>[59]</sup> Similarly, redistributive coupling of **13** under the influence of 2 mol% inorganic hydride (*N*-selectride, super-hydride) afforded soluble polysilane in moderate yield (58%,  $M_w = 2,100$  for *N*-selectride; 40%,  $M_w = 2,500$  for super-hydride) and hyperbranched polysilane (TGA ceramic residue yield: 75% for *N*-selectride; 80% for super-hydride). The redistributive coupling of 1,4-C<sub>6</sub>H<sub>4</sub>(SiH<sub>2</sub>CH=CH<sub>2</sub>)<sub>2</sub> **14** with 2 mol% Red-Al yielded 70% of soluble polysilane ( $M_w$ : 1,500,  $M_w/M_n = 1.5$ ) and hyperbranched polysilane (TGA ceramic residue yield: 63%).<sup>[59]</sup> Similarly, redistributive catenation of **14** in the presence of 2 mol% inorganic hydride (*N*-selectride, super-hydride) afforded soluble polysilane in moderate yield (58%,  $M_w = 2100$  for *N*-selectride; 40%,  $M_w = 2,500$  for super-hydride) and hyperbranched polysilane (TGA ceramic residue yield: 75% for *N*-selectride; 80% for super-hydride). Thus, steric bulkiness on the silicon center increases the portion of soluble polymer as expected, because it will retard the extensive redistributive coupling to form hyperbranched polysilane.

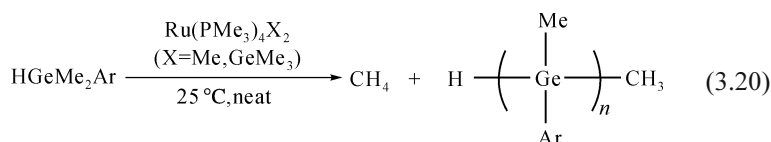
The dehydrocatenation of **12** using 1 mol% by Cp<sub>2</sub>MCl<sub>2</sub>/Red-Al (M = Ti, Zr, Hf) catalyst produces soluble polysilane (in 25%,  $M_w = 2,600$ ,  $M_w/M_n = 1.1$  for Ti; in 15%,  $M_w = 3,300$ ,  $M_w/M_n = 1.2$  for Zr; in 15%,  $M_w = 3,600$ ,  $M_w/M_n = 1.1$  for Hf) and hyperbranched polysilane (TGA ceramic residue yield: ca. 60% for all Ti, Zr, Hf) which is insoluble in organic solvents because of the high extent of crosslinking.<sup>[60]</sup> The dehydrocatenation of **12** with 1 mol% M'(CO)<sub>6</sub> (M'=Cr, Mo, W) catalyst also yields soluble polysilane (in 65%,  $M_w = 4,100$ ,  $M_w/M_n = 2.1$  for Cr; in 53%,  $M_w = 5,100$ ,  $M_w/M_n = 2.4$  for Mo; in 40%,  $M_w = 5,900$ ,  $M_w/M_n = 2.0$  for W) and hyperbranched polysilane (TGA ceramic residue yield: ca. 70% for Cr, Mo, W).<sup>[60]</sup> The dehydrocatenation of **13** in the presence of 1 mol% Cp<sub>2</sub>MCl<sub>2</sub>/Red-Al (M = Ti, Zr, Hf) catalyst gives soluble polysilane (in 95%,  $M_w = 1,300$ ,  $M_w/M_n = 1.4$  for Ti; in 90%,  $M_w = 1,400$ ,  $M_w/M_n = 1.1$  for Zr; in 93%,  $M_w = 2,400$ ,  $M_w/M_n = 1.1$  for Hf).<sup>[60]</sup> The dehydrocatenation of **13** with 1 mol% M'(CO)<sub>6</sub> (M'=Cr, Mo, W) catalyst affords soluble polysilane (in 75%,  $M_w = 2,500$ ,  $M_w/M_n = 1.3$  for Cr; in 80%,  $M_w = 2,700$ ,  $M_w/M_n = 1.1$  for Mo; in 50%,  $M_w = 2,720$ ,  $M_w/M_n = 1.1$  for W) (Eq. (3.19)).<sup>[60]</sup>



In a similar manner, other disilanes such as bis(1-sila-3-butyl)benzene,<sup>[57,58]</sup> 2,5-disilaoct-7-ene, 2,5-disilahexane<sup>[61]</sup> undergo dehydrocatenation using group 4 metallocene combination catalysts such as Cp<sub>2</sub>MCl<sub>2</sub>/Red-Al (M = Ti, Zr, Hf) and Cp<sub>2</sub>ZrCl<sub>2</sub>/2*n*-BuLi. Thus, types of substituent on silane and catalyst can make a pronounced difference in the coupling processes.

### 3.2.2.3 Demethanative Catenation of Tertiary Germanes to Polygermanes

As described in Subsections 3.2.1.5 and 3.2.2.1, polygermanes can be prepared: (1) by the Wurtz coupling of chlorogermanes with alkali metal dispersions in toluene-refluxing temperature, (2) by the dehydrocatenation of hydrogermanes, and (3) by redistributive coupling of (PhH<sub>2</sub>Ge)<sub>2</sub> mediated by a Lewis base PhH<sub>2</sub>GeLi.<sup>[51]</sup> Berry et al. reported an extraordinary demethanative catenation of tertiary germanes to polygermanes (*M<sub>w</sub>* = 5,000 – 10,000 determined by light scattering measurements), catalyzed by Ru(PMe<sub>3</sub>)<sub>4</sub>X<sub>2</sub> (M = GeMe<sub>3</sub>, Me) as shown in Eq. (3.20).<sup>[62]</sup>



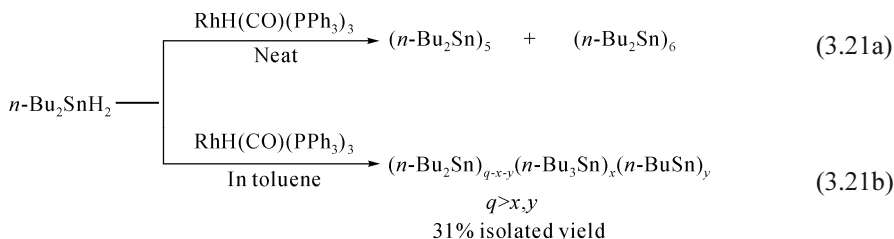
The hydrogermanes should have at least one CH<sub>3</sub> group in the molecule for demethanative catenation: HGeMe<sub>2</sub>Ar (Ar = methyl, phenyl, *p*-tolyl, *p*-fluoro, *p*-trifluorotolyl, *p*-anisyl, *m*-xylyl). The properties of polygermanes prepared by catalytic demethanative coupling and Wurtz coupling of MeArGeCl<sub>2</sub> with sodium are practically the same. Furthermore, in principle, the demethanative catenation (i.e., removal of CH<sub>4</sub> gas) is similar to dehydrocatenation (i.e., removal of H<sub>2</sub> gas). According to the sigma-bond metathesis mechanism thru four-center transition states, the dehydrocatenation of a tertiary germane should produce a digermane if the tertiary germane is not sterically demanding. If the tertiary germane is sterically demanding, dehydrocatenation cannot take place.<sup>[11,12]</sup> The authors suggested a mechanism for demethanative catenation where Ge-C bond scission and Ge-Ge bond formation are attained by sequential α-CH<sub>3</sub> and germyl to germylene migration steps *via* an intermediacy of metal-germylene species.<sup>[62b]</sup> Polygermanes have the characteristics of both polysilanes and polystannanes.

### 3.2.2.4 Redistributive Catenation of Hydrostannanes to Highly Branched Polystannanes

As described in Subsection 3.2.1.5, polystannanes, prepared by the Wurtz coupling of chlorostannanes with alkali metal dispersion and by the dehydrocatenation of hydrostannanes, exhibit intriguing physical properties. Sita et al. studied a usual

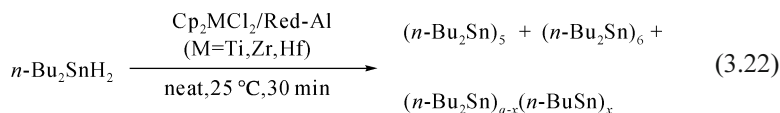


polymerization of  $n\text{-Bu}_2\text{SnH}_2$  with a  $\text{RhH}(\text{CO})(\text{PPh}_3)_3$  catalyst neat or in toluene (Eqs. (3.21a) and (3.21b)).<sup>[63]</sup>



Normal dehydrocatenation reaction occurs to give only the cyclic oligomers ( $\text{Sn}_5$  and  $\text{Sn}_6$ ) when the reaction is carried out in neat hydrostannane with fast addition of the catalyst Eq. (21a). However, redistributive dehydrocatenation takes place to yield high molecular weight, moderately branched polystannane  $[(n\text{-Bu}_2\text{Sn})_{q-x-y}(n\text{-Bu}_3\text{Sn})_x(n\text{-BuSn})_y]$ ,  $q > x, y$ ;  $M_w = 50,240 \text{ g}\cdot\text{mol}^{-1}$ ,  $M_w/M_n = 1.43$ , measured by GPC in 31% yield without appreciable formation of cyclic oligomers when the reaction is carried out in toluene with slow addition of the catalyst Eq. (21b). The high molecular weight branched polystannane prepared by Sita group is different from the high molecular weight linear polystannane  $[\text{H}(n\text{-Bu}_2\text{Sn})_m\text{H}]$ ;  $M_w = 33,430$ ,  $M_w/M_n = 2.26$ ] of Tilley that was produced by dehydropolymerization of  $n\text{-Bu}_2\text{SnH}_2$  using  $\text{Cp}_2\text{ZrMe}_2$  catalyst,<sup>[43c,45]</sup> judged by  $^{119}\text{Sn}$  NMR, UV-vis, and GPC analytical techniques. The redistribution could occur via a well-known process with intermediacy of metal-stannylenes species.

Woo and collaborators also described such unusual redistributive dehydrocatenation of  $n\text{-Bu}_2\text{SnH}_2$  with  $\text{Cp}_2\text{MCl}_2/\text{Red-Al}$  ( $M = \text{Ti, Zr, Hf}$ ) combination catalyst.<sup>[64a]</sup> The redistributive dehydrocatenation is performed at ambient temperature for 30 min, producing soluble cyclic oligomers ( $\text{Sn}_5$  and  $\text{Sn}_6$ ) and insoluble hyperbranched polystannane  $[(n\text{-Bu}_2\text{Sn})_{p-x}(n\text{-BuSn})_x]$  as depicted in Eq. (3.22).



The insoluble products (TGA ceramic residue yield: *ca.* 33%) are obtained in moderate yield (for Ti, 39%; for Zr, 27%; for Hf, 26%) as a yellow solid. In the same manner, the redistributive dehydrocatenation of  $\text{Bu}_2\text{SnH}_2$  with  $\text{M}'(\text{CO})_6/\text{Red-Al}$  ( $M' = \text{Cr, Mo, W}$ ) at ambient temperature for 16 h affords soluble oligostannanes and insoluble hyperbranched polystannanes. The insoluble product (TGA ceramic residue yield: *ca.* 33%) is obtained in moderate yield (for Cr, 40%; for Mo, 48%; for W, 39%) as a yellow solid. The same authors also describe the redistributive dehydrocatenation of  $\text{Bu}_3\text{SnH}$  with  $\text{Cp}_2\text{MCl}_2/\text{Red-Al}$  ( $M = \text{Ti, Zr, Hf}$ ) and  $\text{M}'(\text{CO})_6/\text{Red-Al}$  ( $M' = \text{Cr, Mo, W}$ ) at 70 °C (for group 4 catalyst) or 90 °C (for group 6 catalyst) for 3 d, to give soluble oligomer (mainly, dimer  $\text{Sn}_2$ ) and insoluble hyperbranched polystannane (TGA ceramic residue yield = *ca.* 33%; for

Ti, 17%; for Zr, 14%; for Hf, 13%; for Cr, 23%; for Mo, 23%; for W, 7%).<sup>[64b]</sup>

### 3.2.3 Exhaustive Hydrosilylation, Hydrogermylation and Hydrostannylation of Group 14 Hydrides on Vinyl Derivatives

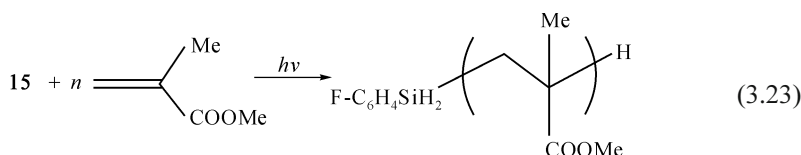
The addition of Si-H bond to unsaturated bonds such as alkenes (including C=C, C=O, C=N, C=metal, etc.) and alkynes (including C≡C, C≡N, C≡metal, etc.) is termed hydrosilylation (or hydrosilylation) and is promoted by many homogeneous transition-metal complex catalysts and heterogeneous supported metal catalysts.<sup>[65-78]</sup> Catalytic hydrosilylation is a complex process and the overall mechanism is not well understood. Chalk and Harrod proposed a simplified mechanism for transition metal complex-catalyzed hydrosilylation involving coordination of alkenes to a coordinatively unsaturated transition metal hydride residue, followed by metal-hydride insertion, oxidative addition of the silane to the metal alkyl, then reductive elimination of the alkylsilane to regenerate the metal-hydride.<sup>[68]</sup> Nonetheless, some experimental observations (including an induction period for many precatalysts and the formation of vinylsilanes) cannot be explained well by the Chalk-Harrod mechanism.<sup>[69]</sup> An alternative mechanism to the Chalk-Harrod mechanism involves insertion of the alkene into the M-Si bond instead of insertion of the alkene into the M-H bond.<sup>[70]</sup> Alternative mechanisms were also proposed by several researchers on the basis of their studies with their own catalytic systems.<sup>[71]</sup>

The common hydrosilylation of olefins is the single addition of Si-H bond to vinyl derivatives in the presence of organic or inorganic catalysts by adding more excess hydrosilanes than olefins. Versatile silicon-containing polymers can be prepared by continuous multiple hydrosilylation: (1) hydrosilylation of  $\text{CH}_2=\text{CH}(\text{CH}_2)_x\text{SiR}_2\text{H}$  ( $x = 0 - 2$ ; R = H, Me, OMe, Cl), (2) hydrosilylation of  $[\text{CH}_2=\text{CH}(\text{CH}_2)_x]_2\text{Y}$  ( $x = 0 - 2$ ; Y =  $\text{CH}_2$ ,  $\text{CMe}_2$ ,  $\text{SiMe}_2$ ,  $\text{GeMe}_2$ , phenylene, etc.) with  $\text{R}_2\text{SiH}_2$  or  $\text{HSiMe}_2\text{-X-SiMe}_2\text{H}$  [X =  $(\text{SiMe}_2\text{-O})_n$ ,  $\text{CH}_2$ ,  $\text{CMe}_2$ ,  $\text{SiMe}_2$ ,  $\text{GeMe}_2$ , phenylene, etc.], (3) hydrosilylation of olefin with  $(\text{RSiH})_n$ , and (4) hydrosilyl copolymerization of vinyl monomer with hydrosilane or  $(\text{RSiH})_n$ . For example, a series of new 3,3,3-trifluoropropyl substituted copoly(carbosiloxane)s were prepared by step-growth hydrosilylation copolymerization of 1,9-dihydro-1,1,3,5,7,9,9-heptamethyl-3,5,7-tris(3',3',3'-trifluoropropyl) pentasiloxane with various  $\alpha,\omega$ -divinylsilanes and siloxanes using Karstedt's catalyst, Pt-divinyltetramethyldisiloxane<sup>[79a]</sup> Poly(arylene-1,2-dioxy-co-oligodimethylsiloxanylene)s were synthesized by dehydrosilylation condensation copolymerization of o-quinones with  $\alpha,\omega$ -dihydro-oligodimethylsiloxanes catalyzed by  $\text{H}_2(\text{CO})\text{Ru}(\text{PPh}_3)_3$ .<sup>[79b]</sup> Woo and co-workers prepared novel preceramic polymers (for making SiC ceramics) such as a copolymer of polycarbosilane-dichloromethylvinylsilane and a copolymer of polycarbosilane- $\gamma$ -methacryloxypropyltrimethoxysilane by hydrosilylation copolymerization promoted by Pt-based catalyst.<sup>[79c,d]</sup>

Green technology is very important to maintain a pollution-free environment.

Clean photopolymerization technology is used commercially in surface coatings, photoresists, adhesives and holography.<sup>[81]</sup> Woo and co-workers reported a novel exhaustive multiple addition (i.e., hydrosilapolymerization) of vinyl monomers to hydrosilanes thermally and photochemically, to produce the first organic polymers with reactive hydrosilyl end groups by the addition of excess olefin with respect to hydrosilane.<sup>[80a - m]</sup>

Only a few vinyl monomers, including methyl methacrylate (MMA) and styrene, absorb the most convenient wavelength of light (250 – 500 nm) for common experimental work of photopolymerization. The bulk photopolymerization of MMA with *para*-substituted phenylsilanes such as *p*-F-C<sub>6</sub>H<sub>4</sub>SiH<sub>3</sub> (**15**), *p*-H<sub>3</sub>C-C<sub>6</sub>H<sub>4</sub>SiH<sub>3</sub> (**16**), and *p*-H<sub>3</sub>CO-C<sub>6</sub>H<sub>4</sub>SiH<sub>3</sub> (**17**) produces poly(MMA)s containing the respective silyl moiety as an end group.<sup>[80]</sup> Poly(MMA)s possessing the *p*-F-C<sub>6</sub>H<sub>4</sub>SiH<sub>2</sub> moiety as an end group with weight average molecular weight ( $M_w$ ) of 6,200 – 22,020 and TGA residue yields of 12% – 73% were prepared in 24% – 85% yields by 300 nm UV light-initiated bulk polymerization of MMA with different molar ratios of 15 (MMA : 15 = 9:1 through 3:7) as shown in Eq. (3.23).



Similarly, poly(MMA)s possessing *p*-H<sub>3</sub>C-C<sub>6</sub>H<sub>4</sub>SiH<sub>2</sub> end groups with weight average molecular weights ( $M_w$ ) of 8,130 – 28,090 and TGA residue yields of 12% – 67% were prepared in 30% – 93% yields by the bulk polymerization of MMA with different molar ratios of 16. For the hydrosilanes, the polymerization yields and the polymer molecular weights decrease, while the TGA residue yields and the relative intensities of Si-H IR stretching bands increase as the relative silane concentration with respect to MMA increases. The highest polymerization yield and polymer molecular weight were obtained in the case of MMA: hydrosilane = 9:1, but the highest TGA residue yield was obtained for MMA: hydrosilane = 3:7. The polymerization yields and polymer molecular weights of MMA with 15 – 17 increased in the order: 17 < 15 < 16.

The hydrosilapolymerization mechanism (Fig. 3.3) for the photopolymerization of MMA with 15 – 17 could be similar to that with other hydrosilanes. Light absorption of an MMA molecule is well known to produce an excited singlet state of MMA which may then either fluoresce with a return to the ground state of MMA or may be converted to a long-lived triplet excited state, the diradical of the MMA monomer.<sup>[82]</sup> Addition of another MMA by this diradical gives a new diradical of MMA dimer which either reverts to the ground state or continues attacking other MMAs to produce poly(MMA)s. Under neat conditions, the latter will be a predominant process to produce poly(MMA) radicals. At high [MMA]/[silane] ratios, chain propagation will be able to compete with chain transfer over the poly(MMA) radicals. However, chain transfer will eventually

rule over chain propagation with increasing silane concentration. Chain transfer could produce a silyl radical which, in turn, leads to chain initiation, resulting in the production of poly(MMA) containing silyl end groups. Higher concentrations of hydrosilane over MMA will produce shorter chain lengths of poly(MMA), which contributes to the increase in thermal stability of poly(MMA).

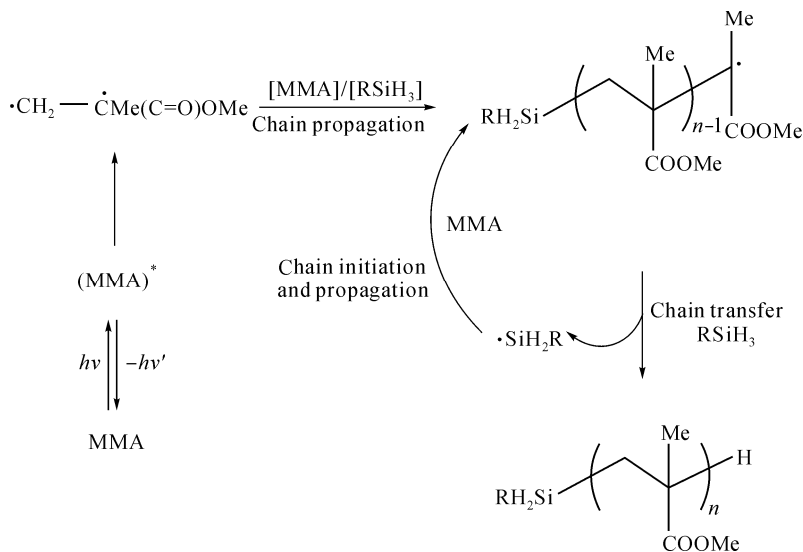
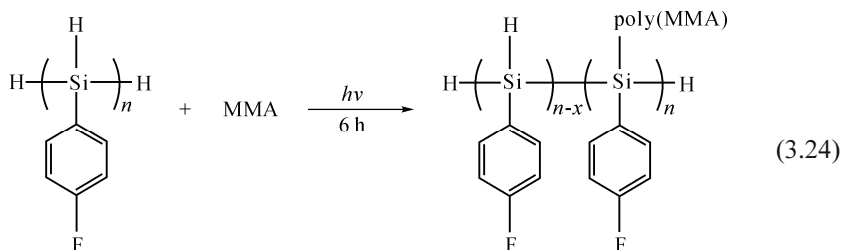


**Fig. 3.3.** Postulated mechanism for the exhaustive hydrosilylation of MMA on  $\text{RSiH}_3$  under the influence of UV light

The increase of Si-H contents with respect to poly(MMA) moiety will result in the higher possibility of high temperature cross-linking hydrosilylation with C=O groups in poly(MMA), which will give higher thermal stability (i.e., higher TGA ceramic residue yield). The reported hydrosilanes include  $\text{PhSiH}_3$ ,  $\text{PhCH}_2\text{SiH}_3$ ,  $\text{PhMeSiH}_2$ ,  $\text{Ph}_2\text{SiH}_2$ ,  $\text{PhSiH}_2\text{SiH}_2\text{Ph}$ ,  $\text{PhCH}(\text{SiH}_3)_2$  and  $1,4\text{-C}_6\text{H}_4(\text{SiH}_{3-x}\text{Me}_x)_2$ . The reported monomers include MMA, AA (acrylic acid), MA (methacrylic acid), HEMA (2-hydroxyethyl methacrylate) and styrene. The hydrosilapolymerization yield of styrene was lower than that of MMA, MA and HEMA. No appreciable thermal and photopolymerizations of the vinyl monomers with  $\text{CH}_2(\text{CH}_2)_5\text{SiH}_3$ ,  $\text{Ph}(\text{CH}_2)_2\text{SiH}_3$ ,  $\text{Ph}_3\text{SiH}$ , and (mesityl) $_2\text{SiH}_2$  were observed, probably because of their steric and/or electronic effects. Therefore, the types of vinyl monomer and hydrosilane appear to be important for successful hydrosilapolymerization.

Chatgililoglu and co-workers reported the reactivity study of alkyl peroxy radicals toward poly(hydrosilane)s.<sup>[83]</sup> The Woo group extended the above hydrosilapolymerization methodology to poly(hydrophenylsilane)s instead of monomeric hydrosilanes for first making novel inorganic-organic hybrid copolymers. Such inorganic-organic hybrid graft copolymers can be used for many applications in contact lens, paints, etc. Poly(*p*-fluoro-substituted phenylsilane),  $\text{H}[(p\text{-F-C}_6\text{H}_4)\text{SiH}]_n\text{H}$  ( $M_w = 3300$ ;  $M_w/M_n = 1.83$ ) was prepared by

dehydropolymerization of  $p$ -F-C<sub>6</sub>H<sub>4</sub>SiH<sub>3</sub> using the Cp<sub>2</sub>ZrCl<sub>2</sub>/Red-Al combination catalyst. In a typical photopolymerization experiment, a quartz tube (15 mm×120 mm) charged with MMA, poly( $p$ -fluoro-substituted phenylsilane) and toluene (1 mL) was degassed, sealed and irradiated with UV-light (280 nm) for 6 h. Precipitation with  $n$ -hexane and drying in vacuo gives poly( $p$ -fluoro-substituted phenylsilane)- $g$ -poly(MMA), which is an inorganic-organic hybrid graft copolymer Eq. (3.24).<sup>[84a]</sup>



In this photopolymerization, various molar ratios of polysilane:MMA are used: 1:1, 1:5, 1:10, 1:20, 1:50. Similarly, in the graft photopolymerization, while the polymer molecular weights and the polymerization yields decrease, the relative intensities of Si-H IR stretching bands and the TGA residue yields increase with the increase in the hydrosilane molar ratio over MMA. The higher contents of Si-H moieties remaining in the graft copolymer backbone will result in the higher possibility of high temperature cross-linking hydrosilation with C=O groups in the graft chain of poly(MMA), which will give higher thermal stability (i.e., higher TGA ceramic residue yield). For the other vinyl monomers, such as MA and styrene, similar trends are observed.<sup>[84b]</sup> Similar trends are also observed for the copolymerization of MMA-MA, MMA-styrene and MA-styrene.<sup>[84c]</sup> Furthermore, for various other poly(hydroarylsilane)s prepared by Cp<sub>2</sub>MCl<sub>2</sub>/Red-Al (M = Ti, Zr, Hf) combination catalyst, similar trends are found.<sup>[84c]</sup> The hydrosilapolymerization mechanism of vinyl monomers on poly(hydrosilane)s could be similar to that of vinyl monomers on hydrosilanes in Fig. 3.3.

The addition of Ge-H bond and Sn-H bond to unsaturated bonds is termed *hydrogermation* (or *hydrogermylation*) and *hydrostannation* (or *hydrostannylation*), respectively, and is promoted by many homogeneous transition-metal complex catalysts and heterogeneous supported metal catalysts.<sup>[85-88]</sup> (Germyl)stannanes and digermanes may be used for germylstannation and double germation, respectively.<sup>[87]</sup> Catalytic hydrogermation and hydrostannation could be complex processes and the overall mechanisms are not well understood, although plausible mechanisms could be similar to the Chalk and Harrod mechanism or modified Chalk-Harrod mechanism.<sup>[68-70]</sup> Hydrogermapolymerization (and hydrostannapolymerization) of hydrogermanes (and hydrostannanes) on MMA and MA gave similar trends as the hydrosilapolymerization of MMA and MA.<sup>[89a]</sup> The reactivity increases in the order of Si-H < Ge-H < Sn-H, which is the reverse order of bond strength if their steric bulkiness is the same. Nonetheless, the hydrogermapolymerization/hydrostannapolymerization mechanisms of vinyl monomers on poly(hydrosilane)s should be

similar to that of vinyl monomers on hydrosilanes depicted in Fig. 3.3.

### 3.2.4 Formation of Polysilane-Metal Nanoparticle Composites

In an inert atmosphere, hydrosilanes and poly(hydrosilane)s reduce metal cations such as Ni(II), Ag(I), Au(III), and Pt(IV) complexes to form the composite of a polysilane-metal nanoparticle composite.<sup>[89b]</sup> In comparison, in an air atmosphere hydrosilanes reduce the metal cations to form the composite of a silica-metal nanoparticle composite.<sup>[89c]</sup>

## 3.3 Group 13 Inorganic Polymers: Polyborazines

Boron nitride (BN) is one of the technologically important non-oxide ceramics (e.g., aluminum nitride AlN, silicon nitride Si<sub>3</sub>N<sub>4</sub>, silicon carbide SiC) whose synthesis and properties have been intensively investigated.<sup>[90]</sup> Boron nitride has different polymorphic forms: hexagonal (h-BN), cubic (c-BN), rhombohedral (r-BN), or würtzite (w-BN). In particular, the graphite-like anisotropic structure of h-BN provides unique electrooptical and thermomechanical properties such as low thermal expansion coefficient, great resistance toward thermal shocks/oxidation, and high tensile strength/Young's modulus.<sup>[91]</sup> Thus, h-BN has been used for many specialty applications.<sup>[92]</sup> These advanced properties are heavily dependent on their preparation method, purity, crystallinity and microstructure. BN ceramic powders were traditionally prepared by *co*-pyrolysis of cheap boric acid and urea. Most of the commercially available BN ceramic goods are prepared by hot-pressing technique of BN powder or CVD process. For the purpose of reinforced composite preparation, BN ceramic fiber is needed. The BN ceramic fiber can be prepared by the polymer-derived ceramic route.<sup>[91]</sup> Polyborazines are frequently used as preceramic polymer precursors for the preparation of boron nitride fiber or composites.<sup>[93]</sup>

Polyborazines can be prepared from the homodehydrocoupling of borazine derivatives or hetrodehydrocoupling of borazine derivatives with ammonia or coupling of aminoboranes with ammonia.<sup>[91,92,94]</sup> A simple borazine ring, a cyclic trimer [BH=NH]<sub>3</sub>, has a formula of B<sub>3</sub>N<sub>3</sub>H<sub>6</sub> whose structure is similar to the delocalized benzene. Borazine has polarity compared to benzene (which is composed of carbon atoms with the same electronegativity) because nitrogen (boron) is more (less) electronegative than carbon.<sup>[95]</sup> Thus, borazine should be more reactive than benzene toward dehydropolymerization. Polyborazine (B<sub>3</sub>N<sub>3</sub>H<sub>x</sub>)<sub>n</sub> can be made by intermolecular dehydrocoupling between N-H and B-H bonds in borazines (Eq. (3.25)).



### 3.4 Group 15 Inorganic Polymers: Polyphosphazenes

Polyphosphazenes with  $[-N=PR_2-]$  repeating units attract much interest in materials science.<sup>[97]</sup> Polyphosphazenes can be prepared by (1) the thermal ring-opening polymerization of cyclic trimer  $[N=PR_2]_3$  over 200 °C, (2) the substitution reactions with diverse nucleophiles on poly(dichlorophosphazene)  $[N=PCl_2]_n$ , and (3) the condensation reactions of phosphazene derivatives with good leaving groups ( $(CH_3)_3Si-$  and  $-Cl$  or  $-OCH_2CF_3$ ) such as  $(CH_3)_3Si-N=PR_2(OCH_2CF_3)$  and  $Cl_3P=NSi(CH_3)_3$ .<sup>[1b,102,103]</sup> Oligomeric  $[N=PCl_2]_x$  ( $x = 3, 4, \dots$ ) with various ring sizes are classically prepared from the reaction of phosphorus pentachloride with ammonium chloride. The main product is white crystalline hexachlorocyclotriphosphazene  $[N=PCl_2]_3$ , which melts at 114 °C and is a useful precursor for ring-opening polymerization to polyphosphazene, unlike borazine which is known to undergo B-N dehydrocoupling to polyborazine. Hexafluorocyclotriphosphazene or partially substituted cyclotriphosphazenes can also be used instead of hexachlorocyclotriphosphazene as a precursor for ring-opening polymerization. The ring-opening polymerization mechanism of hexachlorocyclotriphosphazene is not fully clear. Experimental evidence highly suggests that an ionic mechanism is more possible than a radical mechanism. The catalytic species could be (pentachlorocyclotriphosphazene)<sup>+</sup>Cl<sup>-</sup> formed from the ionization of a P-Cl bond of hexachlorocyclotriphosphazene. The phosphonitrilic cation could then keep attacking the nitrogen atoms of other hexachlorocyclotriphosphazene monomers to produce polyphosphazene.<sup>[1b]</sup>

Polyphosphazenes exhibit low  $T_g$  values and elasticity because of large bond angles and substitution-free nitrogen leading to a high degree of chain movement, which is similar to the case of polysiloxanes. The property scope of polyphosphazene greatly counts on the type of side groups (R) from hydrophilic, hydrophobic, electroredox, coordinative to elastomeric character. Thus, polyphosphazene can be used as electrode mediator, polymeric drugs, hydrogels, liquid crystalline materials, non-burning fibers, biomaterials, low-temperature elastomers, semiconductors, composites, etc. Allcock and co-workers reported the synthesis and applications of oligoalkoxy-substituted polyphosphazenes,  $[N=P(OC_6H_5)(OCH_2CH_2)_xOCH_3]_n$  and  $\{N=P[OC_6H_4(OCH_2CH_2)_xOCH_3]_2\}_n$ , as solid polymer electrolytes to be used for rechargeable batteries.<sup>[98]</sup> The phenoxy group improves mechanical strength and the oligoethyleneoxy group promotes lithium ion transport. Qin et al. synthesized polyphosphazenes with the indole-based chromophore (nitro-indole or sulfonyl indole) and charge-transporting carbazoyl side groups. These polyphosphazenes possess the second-order nonlinear optical property.<sup>[99]</sup> Sohn and collaborators described that polyphosphazene-platinum conjugates  $[N=P(MPEG)_x(GlyGluPt(dach))_{2-x}]_n$  (MPEG = methoxy-poly(ethylene glycol); GlyGlu = glycyl-L-glutamic dipeptide; dach=*trans*-(±)-1,2-diaminocyclohexane) have selective targeting antitumor activity by attaining a favorable pharmacokinetic profile and a longer blood circulation time.<sup>[100]</sup> Polyphosphazenes with coordinating ligands such as nitrile,



pyridine or phosphine can be used as a supporting material for a transition metal complex. For example, phosphazene copolymers  $\{[N=P(O_2C_{12}H_8)]_{0.5}[N=P(O-C_6H_4-CO_2Pr^i)(O-C_6H_4-L)]_{0.5}\}_n$  ( $L = CN, PPh_2$ ) and  $\{[N=P(O_2C_{12}H_8)]_{0.6}[N=P(O-C_6H_4-CO_2Pr^i)(O-C_5H_4N)]_{0.4}\}_n$  react with  $W(HOMe)(CO)_5$  to give  $W(CO)_5$ -coordinated complexes.<sup>[101a]</sup> Similarly, phosphazene copolymers coordinated to  $CpMn(CO)_2$  moiety have been reported.<sup>[101b]</sup> These metal complex-coordinated phosphazene copolymers show high glass transitions and are quite stable. Polyphosphazenes with sulfonamide side groups showing good proton conductivity have been developed for fuel cell applications. Thus,  $[N=P(OC_6H_4CH_3)(OC_6H_4-SO_2-NNa-SO_2CF_3)]_{0.34n}[N=P(OC_6H_4CH_3)_2]_{1.66n}$  can be employed for application in fuel cells.<sup>[102]</sup> Amphiphilic biodegradable polyphosphazene block copolymers forming spherical micellar aggregates with 100 – 120 nm diameters have been reported.<sup>[103]</sup> The amphiphilic polyphosphazenes such as poly[bis(ethylglycinat-*N*-yl)phosphazene]-*b*-poly(ethylene oxide) and poly[bis(trifluoroethoxy)phosphazene]-*b*-poly(ethylene oxide) are prepared by the cationic polymerization of  $Cl_3P=NSi(CH_3)_3$  at room temperature. Therefore, in principle, any interesting functional group (e.g., proteins, poly nucleic acids, antibodies, organometallic complex, nanometallic materials, carbon nanotubes) can be introduced to the polyphosphazene backbone by using the synthetic methods described in this section.

### 3.5 Group 16 Inorganic Polymers: Polysulfur and Poly(sulfur nitride)

Cyclooctasulfur ( $S_8$ ) is the W-shape of crystalline rhombic sulfur stable in a normal condition. Upon being heated at 95 °C, the rhombic sulfur transforms into the different crystalline cyclooctasulfur of monoclinic sulfur which melts at 119 °C. The cyclooctasulfur undergoes radical ring-opening polymerization in the temperature range of 150 – 180 °C, to give elastomeric polysulfur. The unstable polysulfur slowly reverts to rhombic sulfur while unperturbed at room temperature. Interestingly, the reversal back-biting process cannot be prevented even in the presence of an end-capping agent such as alkenes. Nonetheless, we know the vulcanization of 1,4-polyisoprene or 1,4-poly(1,3-butadiene) with sulfur to make the polymer elastomeric.<sup>[104]</sup> Selenium and tellurium could undergo similar ring-opening polymerization as sulfur. The reaction of polyphenylsilanes,  $[Si(H)Ph]_x$ , with sulfur is unsuccessful, but the reaction with selenium and tellurium produces the insertion products,  $[Si(SeH)Ph]_x$  and  $[Si(TeH)Ph]_x$ .<sup>[105]</sup>

Disulfur dinitride ( $S=N)_2$ , which is prepared by sublimation of  $(S=N)_4$ , undergoes solid-state ring-opening polymerization to give poly(sulfur nitride),  $(S=N)_{2m}$ , at a temperature of 0 °C or higher. The poly(sulfur nitride) shows metallic behaviour. Poly(sulfur nitride) has a good electrical/thermal conductivity like mercury and exhibits superconductivity around 0 °C. Poly(sulfur nitride), which is insoluble and infusible, has high light reflectivity and is shock-sensitive.<sup>[104]</sup>

### 3.6 Summary

Main group metalloid-based inorganic polymers, which are composed of boron (group 13: polyborazines), silicon/germanium/tin (group 14: polysilanes, polygermanes and polystannanes), phosphorous (group 15: polyphosphazenes) and sulfur (group 16: polysulfur and poly(sulfur nitride)) atoms, are reviewed as advanced speciality materials. In particular, silicon-based polymers with outstanding properties are described with main emphasis in this account. Group 14 hydrides possessing reactive A-H (A = Si, Ge, Sn) bonds can be used in synthesizing novel functional materials with interesting properties in the presence of various promoters such as organometallic complexes, inorganic hydrides, heat and UV-irradiation. Catalytic catenation of hydrosilanes with molecules having active A'-H bonds (A' = Si, O, N) or vinylic bonds thru Si-Si/Si-O/Si-N dehydrocatenation, redistributive catenation and exhaustive addition processes are described in this review as chosen examples of our recent research developments. However, due to limits of space and interest, other types of inorganic polymers such as main group metal-based polymers (e.g., polyaluminoxanes) and transition metal-containing inorganic polymers are not described in this account. For the same reason, some main group metalloid-containing inorganic polymers (e.g., polycarbosilanes, polysiloxane, polysilazane, polysilathianes, polyboranes, polycarboranes, polyborxanes) are not included.

### Acknowledgment

This research was supported by Nano R&D program through the National Research Foundation of Korea, funded by the Ministry of Education, Science and Technology. (Grant No. 2009-0082745). H.G.W. is grateful to the KICOS (Grant No. K20602000009-09E0200-00910) through a grant provided by the MEST.

### References

- [1] (a) Odian, G. Principles of Polymerization, 3rd ed. John Wiley & Sons, New York, 1991. (b) Allcock, H. R., Lampe, F. W. Contemporary Polymer Chemistry, 2nd ed. Prentice-Hall Inc., New York, 1990, Chap. 9.
- [2] (a) Inorganic and Organometallic Polymers II. Wisian-Neilson, P., Allcock, Wynne, K. J., Eds. ACS Symposium Series 572, American Chemical Society, Washington, D.C., 1994. (b) Design, Activation and Transformation of Organometallics into Common and Exotic Materials. Laine, R. M., Ed., NATO ASI Series E, no. 141, Martinus Nijhof: Amsterdam, 1988. (c) Gates,

- D. P. Annu. Rep. Prog. Chem., Sect. A, 2003, 99: 453.
- [3] (a) Ciardelli, F., Tsuchida, E., Wohrle, D. *Macromolecule-Metal Complexes*. Springer-Verlag: Berlin, 1996. (b) Pittman, Jr., C. U., Carraher, Jr., C. E., Zeldin, M., Sheats, J., Culbertson, B. M. *Metal-Containing Polymeric Materials*. Plenum Press: New York, 1996.
- [4] (a) *Silicon in Polymer Synthesis*, Kricheldorf, E. R., Ed. Springer-Verlag: Berlin, 1996. (b) *Silicon-containing Polymers*, Jones, R. G., Ed. The Royal Society of Chemistry: Cambridge, 1995.
- [5] (a) Regitz, M., Binger, P. *Angew. Chem. Int. Ed.*, 1988, 27: 1484. (b) West, R. *Angew. Chem. Int. Ed.*, 1987, 26: 1201.
- [6] Sakamoto, K., Yoshida, M., Sakurai, H. *Macromolecules*, 1990, 23: 4494.
- [7] (a) Walsh, R. *Acc. Chem. Res.*, 1981, 14: 246. (b) Dewar, M. J. S. *Organometallics*, 1986, 5: 375. (c) Jackson, R. A. *J. Organomet. Chem.*, 1979, 166: 17.
- [8] West, R. *J. Organomet. Chem.*, 1986, 300: 327.
- [9] *Silicon-Based Polymer Science*, Ziegler, J. M., Fearon, F. W. G., Eds. *Advances in Chemistry Series 224*, American Chemical Society: Washington, D. C., 1990.
- [10] (a) Miller, R. D., Michl, J. *Chem. Rev.*, 1989, 89: 1359 and references cited therein. (b) Matyjaszewski, K., Chen, Y. L., Kim, H. K. in *Inorganic and Organometallic Polymers*. Zeldin, M., Wynne, K. J., Allcock, H. R., Eds. *ACS Symposium Series 360*, American Chemical Society: Washington D. C., 1988, p 78.
- [11] Gauvin, F., Harrod, J. F., Woo, H. G. *Adv. Organomet. Chem.*, 1998, 42: 363 and references cited therein.
- [12] (a) Tilley, T. D. *Acc. Chem. Res.*, 1993, 26: 22 and references cited therein. (b) Tilley, T. D. *Comments Inorg. Chem.*, 1990, 10: 37.
- [13] (a) Corey, J. Y. *Adv. Silicon Chem.*, 1991, 1: 327 and references cited therein. (b) Corey, J. Y. *Adv. Organomet. Chem.*, 2004, 51: 1 and references cited therein.
- [14] Banovetz, J. P., Stein, R. M., Waymouth, R. M. *Organometallics*, 1991, 10: 3430.
- [15] Choi, N., Onozawa, S. Y., Sakakura, T., Tanaka, M. *Organometallics*, 1997, 16: 2765.
- [16] Dioumaev, V. K., Harrod, J. F. *Organometallics*, 1994, 13: 1548.
- [17] (a) Woo, H. G., Kim, S. Y., Han, M. K., Cho, E. J., Jung, I. N. *Organometallics*, 1995, 14: 2415. (b) Woo, H. G., Song, S. J. *Chem. Lett.*, 1999, p 457. (c) Woo, H. G., Kim, B. H. manuscript in preparation. (d) Resel, R., Leising, G., Lunzer, F., Marschner, C. *Polymer*, 1998, 39: 5257. (e) Woo, H. G., Kim, B. H. manuscript in preparation.
- [18] Li, H., Gauvin, F., Harrod, J. F. *Organometallics*, 1993, 12: 575.
- [19] Dioumaev, V. K., Harrod, J. F. *Organometallics*, 1996, 15: 3859.
- [20] Campbell, W. H., Hilty, T. K., Yurga, L. *Organometallics*, 1989, 8: 2615.
- [21] (a) Aitken, C., Harrod, J. F., Gill, U. S. *Can. J. Chem.*, 1987, 65: 1804. (b) Harrod, J.

- F., Yun, S. S. *Organometallics*, 1987, 6: 1381. (c) Aitken, C., Barry, J.-P., Gauvin, F., Harrod, J. F., Malek, A., Rousseau, D. *Organometallics*, 1989, 8: 1732. (d) Harrod, J. F., Ziegler, T., Tschinke, V. *Organometallics*, 1990, 9: 897. (e) Woo, H. G., Harrod, J. F., Henique, J., Samuel, E. *Organometallics*, 1993, 12: 2883. (f) Britten, J., Mu, Y., Harrod, J. F., Polowin, J., Baird, M. C., Samuel, E. *Organometallics*, 1993, 12: 2672.
- [22] (a) Woo, H. G., Tilley, T. D. *J. Am. Chem. Soc.*, 1989, 111: 3757. (b) H. G. Woo, H. G., Tilley, T. D. *J. Am. Chem. Soc.*, 1989, 111: 8043. (c) Woo, H. G., Walzer, J. F., Tilley, T. D. *Macromolecules*, 1991, 24: 6863. (d) Woo, H. G., Heyn, R. H., Tilley, T. D. *J. Am. Chem. Soc.*, 1992, 114: 5698. (e) Woo, H. G., Walzer, J. F., Tilley, T. D. *J. Am. Chem. Soc.*, 1992, 114: 7047. (f) Banovetz, J. P., Suzuki, H., Waymouth, R. M. *Organometallics*, 1993, 12: 4700. (g) Imori, T., Woo, H. G., Walzer, J. F., Tilley, T. D. *Chem. Mater.*, 1993, 5: 1487. (h) Corey, J. Y., Huhmann, J. L., Zhu, X. H. *Organometallics*, 1993, 12: 1121.
- [23] (a) Woo, H. G., Kim, S. Y., Kim, W. G., Cho, E. J., Yeon, S. H., Jung, I. N. *Bull. Korean Chem. Soc.*, 1995, 16: 1109. (b) Woo, H. G., Song, S. J., Han, M. K., Cho, E. J., Jung, I. N. *Bull. Korean Chem. Soc.*, 1995, 16: 1242. (c) Woo, H. G., Song, S. J. *Bull. Korean Chem. Soc.*, 1996, 17: 494. (d) Woo, H. G., Song, S. J. *Bull. Korean Chem. Soc.*, 1996, 17: 1040. (e) Woo, H. G., Kim, B. H., Song, S. J., Han, M. K., Kim, S. Y., Kim, J. H., Lee, J. S. *Bull. Korean Chem. Soc.*, 2000, 21: 935.
- [24] West, R. in *Comprehensive Organometallic Chemistry II*. Davis, A. G., Ed. Pergamon Press: Oxford, 1995, pp 77-110.
- [25] Luo, J., Xie, Z., Lam, J. W. Y., Cheng, L., Chen, H., Qiu, C., Kwok, H. S., Zhan, X., Liu, Y., Zhu, D., Tang, B. Z. *J. Chem. Soc. Chem. Commun.*, 2001, p 1740.
- [26] (a) Sohn, H., Woo, H. G., Powell, D. R. *J. Chem. Soc. Chem. Commun.*, 2000, p697. (b) Woo, H. G., Kim, B. H., Sohn, H. *Chem. Lett.*, 2000, p 544.
- [27] Tamao, K., Uchida, M., Izumizawa, T., Furukawa, K., Yamaguchi, S. *J. Am. Chem. Soc.*, 1996, 118: 11974.
- [28] (a) Sohn, H., Huddleston, R. R., Powell, D. R., West, R. *J. Am. Chem. Soc.*, 1999, 121: 2935. (b) Tamao, K., Yamaguchi, S. *Pure Appl. Chem.*, 1996, 68: 139. (c) Yamaguchi, S., Tamao, K. *J. Chem. Soc. Dalton Trans.*, 1998, p 3693. (d) Yamaguchi, S., Jin, R. Z., Tamao, K. *J. Am. Chem. Soc.*, 1999, 121: 2937. (e) Kanno, K., Ichinohe, M., Kabuto, C., Kira, M. *Chem. Lett.*, 1998, p 99.
- [29] (a) Sanji, T., Sakai, T., Kabuto, C., Sakurai, H. *J. Am. Chem. Soc.*, 1998, 120: 4552. (b) Sohn, H., Sailor, M. J., Magde, D., Trogler, W. C. *J. Am. Chem. Soc.*, 2003, 125: 3821. (c) Woo, H. G., Kim, B. H., Song, S. J. manuscript in preparation.
- [30] (a) Chauhan, B. P. S., Shimizu, T., Tanaka, M. *Chem. Lett.*, 1997, 785. (b) Trogler, W. C., Sohn, H., Liu, S., Toal, S. Abstracts of Papers (225th ACS National Meeting, New Orleans, March 23-27, 2003), INOR-746.
- [31] (a) Kim, B. H., Cho, M. S., Woo, H. G. manuscript in preparation. (b) Kim, M.

- H., Cho, M. S., Woo, H. G. manuscript in preparation.
- [32] Kim, B. H., Woo, H. G. *Organometallics*, 2002, 21: 2796. (b) Woo, H. G., Song, S. J., Kim, B. H., Yun, S. S. *Mol. Cryst. Liq. Cryst.*, 2000, 349: 87. (c) Kim, B. H., Cho, M. S., Kong, J. I., Woo, H. G., Lee, S. W., Lee, C. J. *Mol. Cryst. Liq. Cryst.*, 2004, 425: 243.
- [33] (a) Hong, J. H., Boudjouk, P. J. *Am. Chem. Soc.*, 1993, 115: 5883. (b) Hong, J. H., Boudjouk, P., Castellino, S. *Organometallics*, 1994, 13: 3387. (c) West, R., Sohn, H., Bankwitz, U., Calabrese, J., Apeloig, Y., Mueller, T. J. *Am. Chem. Soc.*, 1995, 117: 11608.
- [34] (a) Lukevics, E., Dzintara, M. J. *Organomet. Chem.*, 1985, 295: 265. (b) Pitt, C. G. *Homoatomic Rings, Chains, and Macromolecules of Main-Group Elements*. Rheingold, A. L., Ed., Elsevier Scientific Publishing Company: Amsterdam, 1977, p 203.
- [35] (a) Bedard, T. C., Corey, J. Y. *J. Organomet. Chem.*, 1992, 428: 315. (b) Li, Y., Kawakami, Y. *Macromolecules.*, 1999, 32: 6871. (c) Zhang, R., Mark, J. E., Pinhas, A. R. *Macromolecules.*, 2000, 33: 3508. (d) Baruah, J. B., Osakada, K., Yamamoto, T. *Organometallics*, 1996, 15: 456.
- [36] (a) Sommer, L. H., Lyons, J. E. *J. Organomet. Chem.*, 1967, 89: 1521. (b) Corriu, R. J. P., Moreau, J. J. *J. Chem. Soc., Chem. Commun.*, 1973, p 38. (c) Ojima, I., Kogure, T., Nihonyanagi, M., Kono, H., Inaba, S., Nagai, Y. *Chem. Lett.*, 1973, p 501.
- [37] (a) Kim, B.H., Park, S.H., Kim, M.S., Woo, H.G. manuscript in preparation. (b) Kim, B. H., Woo, H. G., manuscript in preparation. (c) Koe, J. R., Motonaga, M., Fujiki, M., West, R. *Macromolecules*, 2001, 34: 706. (d) Kim, B.H., Woo, H. G. unpublished results.
- [38] Kim, B.H., Cho, M. S., Kim, M. A., Woo, H. G. *J. Organomet. Chem.*, 2003, 685: 93.
- [39] (a) Wang, J. X., Dash, A. K., Berthet, J. C., Ephritikhine, M., Eisen, M. S. *J. Organomet. Chem.*, 2000, 610: 49. (b) Sneddon, L. G., Kai, Fazen, P., Lynch, A. T., Remsen, E. E., Beck, J. S. S., *Inorganic and Organometallic Polymers and Oligomers*. Harrod, J. F., R.M. Laine, R. M., Eds. Kluwer Academic Publishers, Dordrecht, The Netherlands, 1991, p 199. (c) Roewer, G., Herzog, U., Trommer, K., Müller, E., Frühauf, S. *Structure and Bonding*. 2002, 101: 59. (d) Laine, R. M., Babonneau, F. *Chem. Mater.*, 1993, 5: 260. (e) Yajima, S., Hasegawa, Y., Okamura, K., Matsuzawa, T. *Nature.*, 1978, 273: 525. (f) Riu, D. H., Kim, S. J., Shin, D. G., Kim, H. R., Kim, Y. H. *J. Am. Ceram. Soc.*, 2004, 112: 5432. (g) Woo, H.G. Research Report, Massachusetts Institute of Technology, M. A., U. S. A., 1991. (h) Seyferth, D., Tasi, M., Woo, H. G. *Chem. Mater.*, 1995, 7: 236.
- [40] (a) Cho, M. S., Kim, B. H., Kong, J. I., Woo, H. G. *J. Organomet. Chem.*, 2003, 685: 99. (b) Yang, S. Y., Park, J. M., Woo, H.G., Kim, W. G., Kim, I. S., Kim, D. P., Hwang, T. S. *Bull. Korean Chem. Soc.*, 1997, 18: 1264. (c) Woo, H. G., Yang, S. Y., Hwang, T. S., Kim, D. P. *Bull. Korean Chem. Soc.*, 1998, 19: 1310.

- [41] (a) Hong, L. Y., Cao, F., Kim, D. J., Woo, H. G., Kim, B. H., Cho, M. S., Li, X. D., Kim, D. P. *J. Organomet. Chem.*, 2003, 687: 27. (b) Woo, H. G., Kim, B. H., Cho, M. S., Hong, L. Y., Kim, D. P. unpublished results.
- [42] Braunstein, P., Morise, X. *Chem. Rev.*, 2000, 100: 3541.
- [43] (a) Trefonas, P., West, R. J. *Polym. Sci., Polym. Chem. Ed.*, 1985, 23: 2099. (b) Szymanski, W. J., Visscher, G. T., Bianconi, P. A. *Macromolecules*, 1993, 26: 869. (c) Imori, T., Lu, V., Cai, H., Tilley, T. D. *J. Am. Chem. Soc.*, 1995, 117: 9931. (d) Kashimura, S., Ishifune, M., Yamashita, N., Bu, H. B., Takebayashi, M., Kitajima, S., Yoshiwara, D., Kataoka, Y., Nishida, R., Kawasaki, S.I., Murase, H., Shono, T. *J. Org. Chem.*, 1999, 64: 6615.
- [44] (a) Aitken, C., Harrod, J. F., Malek, A. J. *J. Organomet. Chem.*, 1988, 249: 285. (b) Choi, N., Tanaka, M. *J. Organomet. Chem.*, 1998, 564: 81. (c) Kim, B. H., Woo, H. G. manuscript in preparation.
- [45] Imori, T., Tilley, T. D. *J. Chem. Soc. Chem. Commun.*, 1993, p 1607.
- [46] (a) Lu, V., Tilley, T. D. *Macromolecules*, 1996, 29: 5763. (b) Lu, V., Tilley, T. D. *Macromolecules*, 2000, 33: 2403. (c) Bukalov, S. S., Leites, L. A., Lu, V., Tilley, T. D. *Macromolecules*, 2002, 35: 1757.
- [47] Braunstein, P., Morise, X. *Organometallics*, 1998, 17: 540.
- [48] Neale, N. R., Tilley, T. D. *J. Am. Chem. Soc.*, 2002, 124: 3802.
- [49] (a) Kralicek, J., Kubanek, V., Kondelikova, J. German Patent, 1973, 2: 301,784. (b) Kralicek, J., Kubanek, V., Kondelikova, J., Casensky, B., Machacek, J. German Patent, 1976, 2: 445,647. (c) Bukac, Z., Sebenda, J. U. S. Patent, 1976, 3: 962,239.
- [50] (a) Becker, B., Corriu, R. J. P., Guérin, C., Henner, B. J. L. *J. Organomet. Chem.*, 1989, 369: 147. (b) Becker, B., Corriu, R., Guérin, C., Henner, B. *Polym. Prepr. (Am. Chem. Soc., Div. Polym. Chem.)*, 1987, 281: 409. (c) Corriu, R. J. P. *J. Organomet. Chem.*, 1990, 400: 81.
- [51] Riviere, P., Satge, J., Soula, D. *J. Organomet. Chem.*, 1974, 72: 329.
- [52] Speier, J. L., Zimmerman, R. E. *J. Am. Chem. Soc.*, 1955, 77: 6395.
- [53] Woo, H. G., Song, S. J., Cho, E. J., Jung, I. N. *Bull. Korean Chem. Soc.*, 1996, 17: 123.
- [54] Seyferth, D., Lang, H. *Organometallics*, 1991, 10: 551.
- [55] Armitage, A. D. in *Comprehensive Organometallic Chemistry*. Wilkinson, G., Stone, F. G. A., Abel, E. W., Eds. Pergamon Press: Oxford, 1982, vol. 2, chap. 1.
- [56] Woo, H. G., Song, S. J., You, H., Cho, E. J., Jung, I. N. *Bull. Korean Chem. Soc.*, 1996, 17: 475.
- [57] Woo, H. G., Song, S. J. *Bull. Korean Chem. Soc.*, 1996, 17: 1040.
- [58] Woo, H. G., Kim, S. Y., Kim, W.G., Yeon, S. H., Cho, E. J., Jung, I. N. *Bull. Korean Chem. Soc.*, 1995, 16: 1109.
- [59] Woo, H.G., Kim, B. H., Cho, M.S., Hwang, T. S. *Proceedings of International Symposium on Silicon-containing Polymers and Applications*, 2001, p 49.
- [60] Woo, H. G., Kim, B. H., Cho, M. S. *Proceedings of International Symposium on Silicon-containing Polymers and Applications*, 2001, p 53.
- [61] (a) Woo, H. G., Song, S. J., Han, M. K., Cho, E. J., Jung, I. N. *Bull. Korean*

- Chem. Soc., 1995, 16: 1242. (b) Woo, H.G., Kim, B.H., Cho, M. S., Song, S.J., Han, M. K., Kim, S. Y., Sung, A. Y., Kim, J. H., Lee, J. S. Bull. Korean Chem. Soc., 2000, 21: 935. (c) Shaltout, R. M., Corey, J. Y. Organometallics, 1996, 15: 2866.
- [62] (a) Reichl, J. A., Popoff, C. M., Gallagher, L. A., Remsen, E. E., Berry, D. H. J. Am. Chem. Soc., 1996, 118: 9430. (b) Katz, S. M., Reichl, J. A., Berry, D. H. J. Am. Chem. Soc., 1998, 120: 9844.
- [63] Babcock, J. R., Sita, L. R. J. Am. Chem. Soc., 1996, 118: 12481.
- [64] (a) Woo, H. G., Park, J. M., Song, S. J., Yang, S. Y., Kim, I. S., Kim, W. G. Bull. Korean Chem. Soc., 1997, 18: 1291. (b) Woo, H. G., Song, S. J., Kim, B. H. Bull. Korean Chem. Soc., 1998, 19: 1161.
- [65] (a) Speier, J. L. Adv. Organomet. Chem., 1978, 17: 407. (b) Pesek, J. J., Matyska, M. T., Pan, X. J. Chromatography A, 2003, 992: 57.
- [66] (a) Harrod, J. F., Chalk, A. J. In: Organic Synthesis via Metal Carbonyls, Wender, I., Pino, P., Eds., Wiley: New York, 1977, p 673. (b) Ojima, I. In: The Chemistry of Organic Silicon Compounds, Patai, S., Z. Rappoport, Z., Eds., Wiley, New York, 1989, p 1479. (c) Marciniac, B. Comprehensive Handbook on Hydrosilylation, Pergamon Press, Oxford, England, 1992.
- [67] Collman, J. P., Hegedus, L. S., Norton, J. R., Finke, R. G. In: Principles and Applications of Organotransition Metal Chemistry, University Science Books: Mill Valley, 1987, p 564.
- [68] Chalk, A. J., Harrod, J. F. J. Am. Chem. Soc., 1965, 87: 16.
- [69] Roy, A. K., Taylor, R. B. J. Am. Chem. Soc., 2002, 124: 9510.
- [70] (a) Seitz, F., Wrighton, M. S. Angew. Chem. Int. Ed., 1989, 28: 762. (b) Tanke, R. S., Crabtree, R. H. Organometallics, 1991, 10: 415. (c) Bergens, S. H., Whelan, P. N. J. Am. Chem. Soc., 1992, 114: 2128. (d) Yasue, T. R. Organometallics, 1996, 15: 2098. (e) LaPointe, A. M., Rix, F. C., Boorkhart, M. J. Am. Chem. Soc., 1997, 119: 906.
- [71] Marciniac, B. Appl. Organomet. Chem., 2000, 14: 527 and references cited therein.
- [72] Rubin, M., Schwier, T., Gevorgyan, V. J. Org. Chem., 2002, 67: 1936.
- [73] (a) Oertle, K., Wetter, H. Tetrahedron Lett., 1985, 26: 5511. (b) Asao, N., Sudo, T., Yamamoto, Y. J. Org. Chem., 1996, 61: 7654. (c) Lambert, J. B., Zhao, Y., Wu, H. J. Org. Chem., 1999, 64: 2729.
- [74] (a) Dash, A. K., Wang, J. Q., Eisen, M. S. Organometallics, 1999, 18: 4724. (b) Kawanami, Y., Sonoda, Y., Mori, T., Yamamoto, K. Org. Lett., 2002, 4: 2825. (c) Faller, J. W., D'Alliessi, D. G. Organometallics, 2002, 21: 1743.
- [75] Takahashi, T., Bao, F., Gao, G., Ogasawara, M. Org. Lett., 2003, 5: 3479.
- [76] (a) Jensen, J. F., Svendsen, B. Y., la Cour, T. V., Pedersen, H. L., Johannsen, M. J. Am. Chem. Soc., 2002, 124: 4558. (b) Shimada, T., Mukaide, K., Shinohara, A., Han, J. W., Hayashi, T. J. Am. Chem. Soc., 2002, 124: 1584.
- [77] Itami, K., Mitsudo, K., Nishino, A., Yoshida, J. I. J. Org. Chem., 2002, 67: 2645.

- [78] (a) Hao, L., Harrod, J. F., Lehuis, A. M., Mu, Y., Shu, R., Samuel, E., Woo, H. G. *Angew. Chem. Int. Ed.*, 1998, 37: 3126. (b) Harrod, J. F., Shu, R., Woo, H. G., Samuel, E. *Can. J. Chem.* 2001, 79: 1075.
- [79] (a) Grunlan, M. A., Mabry, J. M., Weber, W. P. *Polymer*, 2003, 44: 981. (b) Mabry, J. M., Runyon, M. K., Weber, W. P. *Macromolecules*, 2001, 34: 7264. (c) Hwang, T. S., Lim, J. T., Woo, H. G. *Polymer (Korea)*, 1999, 23: 197. (d) Hwang, T. S., Lim, J. H., Woo, H. G. *Polymer (Korea)*, 1998, 22: 194.
- [80] (a) Hong, L. Y., Woo, H. G., Ham, H. S. *Bull. Korean Chem. Soc.*, 1995, 16: 360. (b) Woo, H. G., Hong, L. Y., Kim, S. Y., Park, S. H., Song, S. J., Ham, H. S. *Bull. Korean Chem. Soc.*, 1995, 16: 774. (c) Woo, H. G., Hong, L. Y., Yang, S. Y., Park, S. H., Song, S. J., Ham, H. S. *Bull. Korean Chem. Soc.*, 1995, 16: 1056. (d) Woo, H. G., Hong, L. Y., Park, J. Y., Jeong, Y. T., Park, H. R., Ham, H. S. *Bull. Korean Chem. Soc.*, 1996, 17: 16. (e) Woo, H. G., Park, S. H., Park, J. Y., Yang, S. Y., Ham, H. S. *Bull. Korean Chem. Soc.*, 1996, 17: 373. (f) Woo, H. G., Park, S. H., Hong, L. Y., Kang, H. G., Song, S. J., Ham, H. S. *Bull. Korean Chem. Soc.*, 1996, 17: 376. (g) Woo, H. G., Park, S. H., Hong, L. Y., Yang, S. Y., Kang, H. G., Ham, H. S. *Bull. Korean Chem. Soc.*, 1996, 17: 532. (h) Woo, H. G., Park, J. Y., Hong, L. Y., Song, S. J., Ham, H. S., Kim, W. G. *Bull. Korean Chem. Soc.*, 1996, 17: 560. (i) Woo, H. G., Oh, E. M., Park, J. H., Kim, B. H., Kim, Y. N., Yoon, C. H., Ham, H. S. *Bull. Korean Chem. Soc.*, 2000, 21: 291. (j) Woo, H. G., Lee, M. S., Kim, Y. J., Kim, B. H., Kim, Y. S. *Proceedings of International Symposium on Silicon-containing Polymers and Applications*, 2001, p 81. (k) Woo, H. G., Lee, M. S., Kim, Y. J., Kim, B. H., Kim, Y. S. *Proceedings of International Symposium on Silicon-containing Polymers and Applications*, 2001, p 85. (l) Woo, H. G., Kim, B. H., Cho, M. S., Kim, D. Y., Choi, Y. S., Kwak, Y. C., Ham, H. S., Sung, A. Y., Kim, D. P., Hwang, T. S. *Bull. Korean Chem. Soc.*, 2001, 22: 1337. (m) Woo, H. G., Kim, B. H. manuscript in preparation.
- [81] (a) Odian, G. *Principles of Polymerization*, 3rd ed. Wiley, New York, 1991, pp 222-223. (b) Mimura, S., Naito, H., Kanemitsu, Y., Matsukawa, K., Inoue, H. *J. Organomet. Chem.*, 2000, 611: 40. (c) Peinado, C., Alonso, A., Catalina, F., Schnabel, W. J. *Photochem. & Photobiol. A.: Chemistry*, 2001, 141: 85.
- [82] Norrish, R. G., Simons, J. P. *Proc. Roy. Soc. (London)*, 1959, A251: 4.
- [83] Chatgililoglu, C., Timokhin, V. I., Zaborovskiy, A. B., Lutsyk, D. S., Prystansky, R. E. *J. Chem. Soc., Perkin Trans.*, 2000, 2: 577.
- [84] (a) Woo, H. G., Cho, M. S., Lee, M. S., Jun, M. J. *Proceedings of International Symposium on Silicon-containing Polymers and Applications*, 2001, 97. (b) Woo, H. G., Lee, S. E., Kwak, Y. C., Kim, B. H., Ham, H. S. *Proceedings of International Symposium on Silicon-containing Polymers and Applications*, 2001, 69. (c) Woo, H. G., Kim, B. H. manuscript in preparation.
- [85] (a) Tanaka, S., Nakamura, T., Yorimitsu, H., Shinokubo, H., Oshima, K. *Org. Lett.*, 2000, 2: 1911. (b) Faller, J. W., Kultyshev, R. G. *Organometallics*, 2003,



- 22: 199. (c) Kadib, A. E., Castel, A., Delpéch, F., Riviere, P., Riviere-Baudet, M., Gornitzka, H., Aguirre, P., Manriquez, J. M., Chavez, I., Abril, D. *Inorg. Chem. Acta*, 2004, 357: 1256. (d) Choi, K., Buriak, J. M. *Langmuir*, 2000, 16: 7737.
- [86] Kinoshita, H., Nakamura, T., Kakiya, H., Shinokubo, H., Matsubara, S., Oshima, K. *Org. Lett.*, 2001, 3: 2521.
- [87] (a) Nakano, T., Ono, K., Senda, Y., Migita, T. *J. Organomet. Chem.*, 2001, 619: 313. (b) Komoriya, H., Kako, M., Nakadaira, Y., Mochida, K. *J. Organomet. Chem.*, 2000, 611: 420.
- [88] Miura, K., Wang, D., Matsumoto, Y., Fujisawa, N., Hosomi, A. *J. Org. Chem.*, 2003, 68: 8730.
- [89] (a) Kim, B. H., Woo, H. G. unpublished results. (b) Kim, B. H., Kim, S. Y., Kim, M. H., Woo, H. G., Kim, D. H., Jun, J., Sohn, H. J. *Nanosci. and Nanotech*, 2008, 8: 5311. (c) Kim, B. H., Cho, M. S., Kim, S. Y., Kim, Y. J., Woo, H. G., Kim, D. H., Sohn, H., Li, H. J. *Nanosci. and Nanotech*, 2007, 7: 3964.
- [90] (a) *Ultrastructure Processing of Advanced Ceramics*, Mackenzie, J. D., Ulrich, D. R., Eds. John Wiley & Sons, New York, 1988. (b) Dou, D., Ketchum, D. R., Hamilton, E. J. M., Florian, P. A., Vermillion, K. E., Gradinetti, P. J., Shore, S. G. *Chem. Mater.*, 1996, 8: 2839.
- [91] (a) Kim, D. P., Economy, J. *Chem. Mater.*, 1993, 5: 1216. (b) Cornu, D., Bernard, S., Duperrier, S., Toury, B., Miele, P. J. *Eur. Ceram. Soc.*, 2005, 25: 111.
- [92] Guillhon, F., Bonnetot, B., Cornu, D., Mongeot, H. *Polyhedron*, 1996, 15: 851.
- [93] (a) Moon, K. T., Min, D. S. Kim, D. P. *Bull. Korean Chem. Soc.*, 1998, 19: 222. (b) Moon, K. T., Jeon, J. K., Kim, Y. J., Kim, D. P. *Scripta Mater.*, 2001, 44: 2111. (c) Kho, J. G., Moon, K. T., Nouet, G., Ruterana, P., Kim, D. P. *Thin Solid Films*, 2001, 389: 78. (d) Bernard, S., Cornu, D., Miele, P., Vincent, H., Bouix, J. J. *J. Organomet. Chem.*, 2002, 657: 91. (e) Bernard, S., Chassagneux, F., Berthet, M. P., Vincent, H., Bouix, J. J. *Eur. Ceram. Soc.*, 2002, 22: 2047. (f) Perdigon-Melon, J. A., Auroux, A., Guimon, C., Bonnetot, B. *J. Solid State Chem.*, 2004, 177: 609.
- [94] (a) Miele, P., Toury, B., Cornu, D., Bernard, S. J. *J. Organomet. Chem.*, 2005, 690: 2809. (b) Toury, B., Cornu, D., Chassagneux, F., Miele, P. J. *Eur. Ceram. Soc.*, 2005, 25: 137.
- [95] Butler, I., Harrod, J. F. *Inorganic Chemistry*, The Benjamin/Cummings Publishing Co., Inc., Redwood City, CA, 1989, Chap. 16.
- [96] (a) Paine, R. T., Sneddon, L. G. *Chemtech.*, 1994, 24: 29. (b) Narula, C. K., Lindquist, D. A., Fan, M. M., Borek, T. T., Duesler E. N., Datye, A. K., Schaeffer, R., Paine, R. T. *Chem. Mater.*, 1990, 2: 377.
- [97] (a) *Phosphazenes: A World Wide Insight*, Gleria, M., De Jaeger, R., Eds. Nova Science Publishers, New York, 2004. (b) Neilson, R. H., Neilson, P. W. *Chem. Rev.*, 1988, 88: 541. (c) Rojo, G., Martin, G., Lopez, F., Carriedo, G. A., Alonso, F. J. G., Martinez, J. I. F. *Chem. Mater.*, 2000, 12: 3603.

- [98] Allcock, H. R., Kellam, E. C. *Solid State Ionics*, 2003, 156: 401.
- [99] Li, Z., Gong, W., Qin, J., Yang, Z., Ye, C. *Polymer*, 2005, 46: 4971.
- [100] Jun, Y. J., Kim, J. I., Jun, M. J., Sohn, Y. S. *J. Inorg. Biochem.*, 2005, 99: 1593.
- [101] (a) Carriedo, G. A., Alonso, F. J. G., Valenzuela, C. D., Valenzuela, M. L. *Polyhedron*, 2006, 25: 105. (b) Carriedo, G. A., Alonso, F. J. G., Gonzalez, P. A., Valenzuela, C. D., Saez, N. Y. *Polyhedron*, 2002, 21: 2579.
- [102] Hofmann, M. A., Ambler, C. M., Maher, A. E., Chalkova, E., Zhou, Y., Lvov, S. N., Allcock, H. R. *Macromolecules*, 2002, 35: 6490.
- [103] (a) Chang, Y., Bender, J. D., Phelps, M. V. B., Allcock, H. R. *Biomacromolecules*, 2002, 3: 1364. (b) Chang, Y., Prange, R., Allcock, H. R., Lee, S. C., Kim, C. *Macromolecules*, 2002, 35: 8556.
- [104] Odian, G. *Principles of Polymerization*, 3rd ed. John Wiley & Sons, New York, 1991, pp 586-587, 701-703.
- [105] Kim, B. H., Woo, H. G. unpublished results.



---

# Preparation and Applications of Ceramic Composite Phases from Inorganic Polymers

**Tae-Ho Yoon, Lan-Young Hong and Dong-Pyo Kim\***

School of Applied Chemistry and Biological Engineering, Chungnam National University, Daejeon 305-764, the Republic of Korea

Tel.: +82-42-821-6695; Fax: +82-42-823-6665

\*E-mail: dpkim@cnu.ac.kr

## 4.1 Introduction

Silicon-based polymers containing nitrogen, carbon and boron have been considered as precursors for various non-oxide ceramics such as silicon carbide (SiC), SiCN and SiBCN.<sup>[1]</sup> These ceramics can be easily shaped using various forming processes and then cross-linked by exposure to heat or radiation to form an infusible solid. The consolidated preceramic polymers are finally pyrolyzed at high temperature to transform into the dense ceramic phases. These materials can be used for high temperature applications in areas such as electronic devices and structural composites.<sup>[2]</sup> Table 4.1 shows some selected important preceramic polymers that have been studied in various aspects. The polymers such as polysilanes, polycarbosilanes, polysilanzane, polysiloxanes are good candidates for ceramic phases due to their high ceramic yields on account of the combination of cross-linking and pyrolysis. Commercially available polysilazane (VL-20, KiON Corp., USA) and two types of polycarbosilane (Starfire System, USA and Nippon Carbon Co., Ltd., Japan) are readily used as preceramic polymers for SiCN and SiC ceramics, respectively.

**Table 4.1** A list of typical preceramic polymers

Preceramic polymers	Polymeric unit	Ceramic	Ceramic yield (%)
Polycarbosilane	$(-R_2SiCH_2-)_n$	SiC	65
Polysiloxane	$(-R_2SiO-)_n$	Si-O-C	30 – 60
Polysilazane	$(-R_2SiNR-)_n$	Si <sub>3</sub> N <sub>4</sub>	20 – 90
Aluminum amide	$(=AlNR-)_n$	AlN	20 – 50
Polyborazine	$(-B_3N_3H_3-)_n$	BN	85
Polytitanium imide	$(=Ti(NR)_2-)_n$	TiN	50 – 70

It has been demonstrated that the use of preceramic polymers is beneficial for controlling the chemical compositions of ceramics. Thus, significant research efforts have been expanded to design novel ceramics with ultra high temperature stability or extraordinary hardness. Different synthetic pathways have been reported for the synthesis of the polymeric precursors from various starting materials. The composite phase of ceramics with some specialties has been involved in various elemental combinations including nitrogen and carbon in addition to main group elements (E=B, P, O, Al, Si).<sup>[3]</sup> Alternatively, the composite phases can be fabricated by combined techniques between ceramics and some kinds of metals to achieve better performance. With respect to composite production, physical properties such as adhesion force, thermal expansion coefficients, shrinkage and mechanical strength are very important. For example, titanium boride (TiB<sub>2</sub>) has high chemical and thermal stability, high thermal conductivity, low electrical resistance and strong hardness, and has been used for structural and electrical applications.<sup>[4]</sup> So it is considered that a Ti-B-N composite phase may adapt the synergistic advantages of the two phases and exhibit a better performance than either of the single phases made by titanium nitride or boron nitride alone. Therefore, it is meaningful to study the feasibility of versatile ceramic composite systems synthesized from different combinations, including preceramic polymers.

On the other hand, the excellent processability of the preceramic polymers facilitates the fabrication of complex shapes and structures, and conversion into ceramics at a lower temperature, compared to the power sintering process. Therefore, polymeric precursors are being studied as an efficient approach to the synthesis of ceramic structured materials, as the polycarbosilanes have demonstrated definite advantages in the commercialization of SiC fibers.<sup>[5]</sup> These oligomers can be obtained over a relatively wide viscosity range and are relatively easy to manufacture and are of commercial interest, such as fiber-reinforced composites, nanocomposites and protective coatings on various bodies.<sup>[6]</sup> Generally, ceramic films are prepared by dry processes, such as sputtering and chemical vapor deposit techniques, or wet processes, such as the sol-gel method.<sup>[7]</sup> However, for economic reasons, non-oxide ceramic films are commonly obtained only by a spin-coating process using preceramic polymers. Moreover, low viscosity oligomers with high ceramic yield would facilitate impregnation of a carbon fiber layup, which would permit a greatly simplified process for composite fabrication.<sup>[8]</sup>

Eventually, this chapter covers the preparation of various ceramic composites using various hybrid preceramic polymeric precursors, including super-resistant

Si-C-B-N, electrically conducting MoSi<sub>2</sub>/SiC, superhard Ti-B-N and highly thermally conducting Al-B-N nanocomposites, thermally insulating Al-Cr-Phosphates. Moreover, some application examples of preceramic polymers are introduced to demonstrate their utility in structural ceramic materials as an alternative preparative route to the conventional powder sintering process, such as ceramic matrix composites and ceramic film. In addition, we summarize the recent development of porous SiC materials from templated preceramic polymers and the fabrication of small and complicated ceramic features using near net shape processing techniques, such as lithography. It is obvious that one of the challenging strategies in ceramic applications is the integration of preceramic polymers into existing manufacturing processes to achieve nano-level process control and the ability to produce useful architectures.

## 4.2 Preparation of Composite Phases from Inorganic Polymers

We know that composite phases can be fabricated by combined techniques using ceramics and some kinds of metals to achieve better performance. In the view of composite production, physical properties such as adhesion force, thermal expansion coefficients, shrinkage and mechanical strength are very important. This section covers the preparation of various ceramic composites using various hybrid preceramic polymeric precursors.

### 4.2.1 *Si-C-B-N Ceramics via Hydroboration from Borazine Derivatives and Trivinylcyclotrisilazane*

Recently, Si-C-B-N ceramics from organosilanes, organosilazanes and borane compounds have been reported and the amorphous phases of these materials have shown excellent thermal stability up to 2,000 °C without mass loss or oxidative damage, although the reasons for these remarkable properties are not completely understood.<sup>[9]</sup> Takamizawa et al. reported first, on the high temperature stability of Si-C-B-N ceramics.<sup>[10]</sup> Soon after, Seyferth et al. made silazanes react with borane methyl sulfide to obtain silazane-substituted borazines as a Si-C-B-N precursor.<sup>[11]</sup> Sneddon and co-workers obtained Si-C-B-N preceramics that are also based on borazine by dehydrogenation and dehydrosilylation of hydridosilazane with borazine.<sup>[12]</sup> However, it is disadvantageous that most of the preceramic polymers for Si-C-B-N ceramics are extremely pyrophoric and insoluble in most solvents, which makes them difficult to handle and limits their processability.

In this section, we describe the synthesis of a soluble polymeric precursor for Si-C-B-N ceramics, without catalyst or byproducts, which involves reaction between the vinyl groups of organosilazane and the B-H groups of borazine via

hydroboration. In addition, the polymer produced was investigated in an attempt to understand the conversion chemistry to the ceramic and the thermal stability of pyrolyzed specimens at high temperatures.

The hydroboration of unsaturated groups has been investigated using various organoboranes. However, little has been published on the preparation of processable polymers by hydroboration using cyclic boron hydrides, except transition metal catalyzed alkylation of borazine via hydroboration.<sup>[13]</sup> In our experiments, 2,4,6-trimethyl-2,4,6-trivinylcyclotrisilazane (VSZ) was found to react smoothly with liquid borazine at moderate temperatures to produce borazine copolymer. The product was isolated as a moisture-sensitive colorless gel by the removal of solvent at reduced pressure, which is soluble in common organic solvents, including benzene and tetrahydrofuran. The molecular weight distribution of the as-synthesized polymer was found to be the number-average molecular weight ( $M_n$ ) = 1,155 and the weight-average molecular weight ( $M_w$ ) = 2,915 with a polydispersity  $M_w/M_n = 2.52$ . Elemental analysis produced 29.07 (26) for Si, 23.59 (30) for C, 12.29 (10) for B, 25.83 (26) for N and 7.68 (8) for H, which are relatively consistent with theoretical values in parentheses. When cured at elevated temperature, the color of the polymer changed from colorless to white then yellow, and finally to a blackish ceramic when subsequently pyrolyzed.

Fig. 4.1 shows Fourier transform infrared spectra of the polymeric products obtained at various temperatures up to 900 °C. A comparison of the as-synthesized polymer with two starting materials of VSZ and borazine revealed that the band intensities of the vinyl group at 3,047  $\text{cm}^{-1}$ , 1,594  $\text{cm}^{-1}$  and B-H group at 2,500  $\text{cm}^{-1}$  slightly decreased, and that absorption bands of N-H group at 3,420  $\text{cm}^{-1}$  and of the B-N group at 1,442  $\text{cm}^{-1}$  broaden on polymerization. Moreover, a weak and broad absorption band appeared in the range 2,800 – 3,000  $\text{cm}^{-1}$ . It is believed that this new band correlates with aliphatic C-H stretching, i.e.,  $\nu_{\text{as}}(\text{CH}_3) = \nu_{\text{as}}(\text{CH}_2) = 2,956 \text{ cm}^{-1}$  and  $\nu_{\text{as}}(\text{CH}) = 2,900 \text{ cm}^{-1}$ , which could be formed from both an  $\alpha$ - and  $\beta$ -addition reaction in the vinyl and borane groups.<sup>[14]</sup> When the synthesized polymer was cured at 200 °C, the intensities of the absorption bands assigned to vinyl groups and B-H groups decreased, and completely disappeared when the polymer was cured at 300 °C. For polymers treated at 400 °C and 600 °C, the IR vibration bands of the  $\text{CH}_x$  ( $x = 1, 2, 3$ ) units almost disappeared, indicating the transformation of the original polymeric phase into the ceramic intermediate phase. In the amorphous ceramic at 900 °C, the band at about 3,400  $\text{cm}^{-1}$  due to N-H bonds almost disappeared. It was interesting to observe that the N-H bonds displayed high thermal stability, and they reportedly survived up to 800 °C in the recent literature.<sup>[15]</sup>

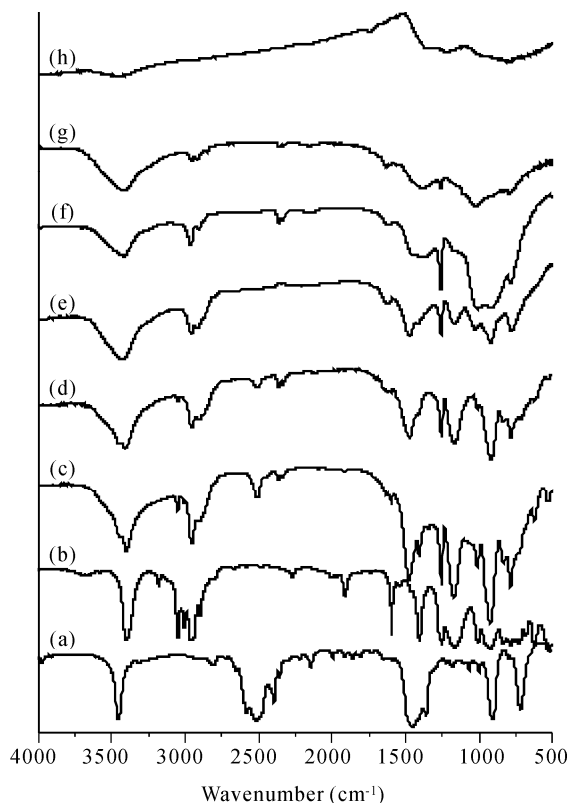


**Fig. 4.1.** IR spectra of the starting materials (a) borazine, (b) 2,4,6-trimethyl-2,4,6-trivinyldisilazane, and of copolymers pyrolyzed at various temperatures, (c) as-synthesized, (d) 200 °C, (e) 300 °C, (f) 400 °C, (g) 600 °C and (h) 900 °C

Fig. 4.2 shows the  $^1\text{H}$  NMR spectrum of the soluble polymeric product. The as-synthesized polymer showed the vinylic hydrogen of the VSZ monomer at around  $5.9 \times 10^{-6}$  as a multiplet is significantly reduced, which becomes clearer on decreasing the relative intensity ratio of  $-\text{CH}=\text{CH}_2/\text{CH}_3\text{-Si}$  from *ca.* 0.26 to *ca.* 0.15. Moreover, new peaks appeared in the range  $0.8 \times 10^{-6} - 1.5 \times 10^{-6}$ , which are attributed to the formation of an alkyl bridge via two possible routes of hydroboration.<sup>[16]</sup> Broad peaks at  $0.9 \times 10^{-6} - 1.2 \times 10^{-6}$  can be assigned to  $\text{BCH}_2$  protons and the peaks at around  $0.4 \times 10^{-6}$  can be assigned to  $\text{SiCH}_2$  protons due to  $\beta$ -addition of the borazine ring, and the others at  $1.07 \times 10^{-6}$  and  $1.4 \times 10^{-6}$  can be attributed to  $\text{CHCH}_3$  and  $\text{CHCH}_3$  protons due to the  $\alpha$ -addition, respectively. The B-H quartet of borazine around  $3.75 \times 10^{-6} - 4.75 \times 10^{-6}$  almost disappeared due to the partial formation of B-C bonds, which is consistent with a report in the literature.



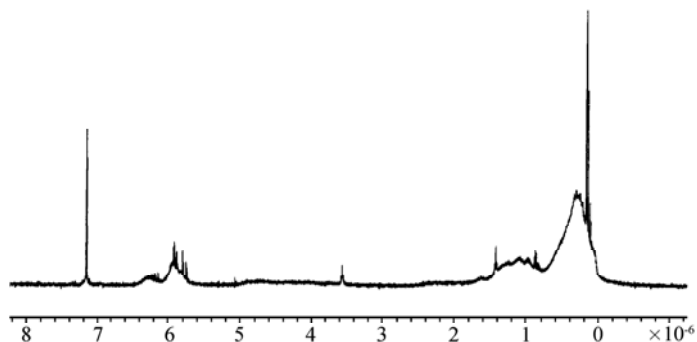
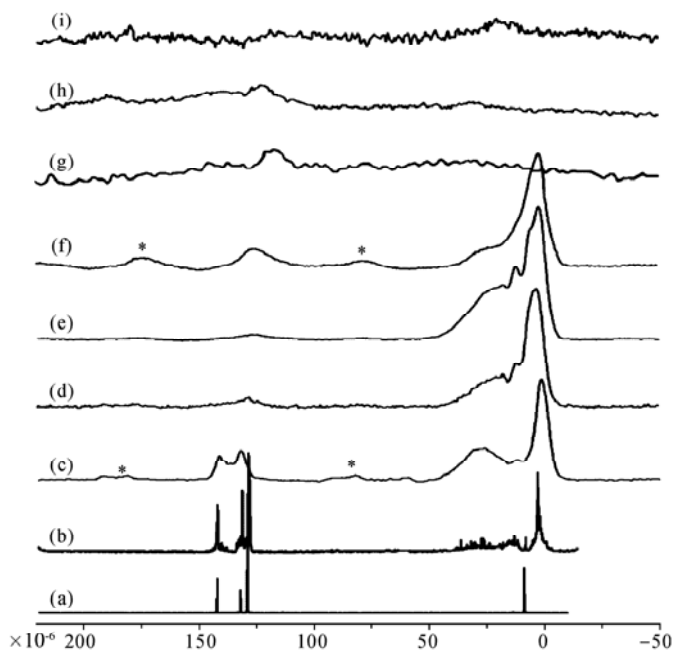
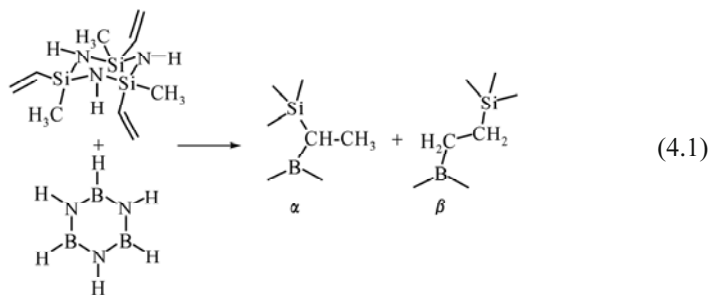


Fig. 4.2.  $^1\text{H}$  NMR spectrum of as-synthesized copolymer in  $\text{C}_6\text{H}_6$

The hydroboration reaction between VSZ and borazine was confirmed by  $^{13}\text{C}$  NMR spectroscopy. By comparing the as-synthesized polymer with VSZ, as shown in Fig. 4.3, new weak peaks were found at  $12.4 \times 10^{-6} - 13.7 \times 10^{-6}$  and at  $29.2 \times 10^{-6} - 29.5 \times 10^{-6}$  due to the formation of methyl and methylene groups from vinyl groups reacting with borane groups of borazine ring via  $\alpha$ - or  $\beta$ -addition.<sup>[17]</sup> The peak centered at  $2.3 \times 10^{-6}$  was assigned to  $\text{Si-CH}_3$ , and the peaks at  $131.9$  and  $142.0 \times 10^{-6}$  to unreacted vinyl groups. As the polymers became insoluble upon curing at intermediate temperatures, solid-state NMR spectroscopy is the only way to investigate the chemical structural changes at the molecular level. In Fig. 4.3b, the sample annealed at  $200^\circ\text{C}$  generally showed signals that were identical with those of the as-synthesized polymer;  $1.6 \times 10^{-6}$  assigned to  $\text{Si-CH}_3$  sites, the broad overlapping peaks in the  $11 \times 10^{-6} - 28 \times 10^{-6}$  range to two types of aliphatic carbon bridge, and the doublet at  $125 \times 10^{-6} - 150 \times 10^{-6}$  to  $\text{C=C}$  sites.<sup>[18]</sup> In particular, the peak at around  $28 \times 10^{-6}$  in the aliphatic region was attributed to the  $\text{CH}_3\text{CHBSi}$  unit, whereas the  $\text{SiCH}_2\text{CH}_2\text{B}$  group was assigned to the resonance at *ca.*  $12 \times 10^{-6}$ . These can be explained by the addition of the borazine ring to the  $\alpha$ - and  $\beta$ -vinyl carbon atoms as shown by Eq. (4.1).<sup>[19]</sup> When heated at  $300^\circ\text{C}$ , the signals at  $125 \times 10^{-6} - 150 \times 10^{-6}$  vanished completely, which is consistent with the IR result, whereas the hydroborated aliphatic carbon peaks at  $27.7 \times 10^{-6}$  and  $11.6 \times 10^{-6}$  substantially increased.

Upon heating to  $400^\circ\text{C}$ , the intensity of the signals of the hydroborated carbons decreased, and almost disappeared at  $600^\circ\text{C}$ , due to the thermal decomposition of the organic structures. The transformation of the polymeric phase into the ceramic phase was indicated by a new broad spectral component at *ca.*  $125 \times 10^{-6}$ , which was assigned to amorphous carbon.<sup>[20]</sup> In the amorphous ceramic at  $1,100^\circ\text{C}$ , the carbon is found to exist in one main fraction, namely as graphite like domains, given by the resonance centered at  $122 \times 10^{-6}$ , as well as  $\text{CH}_x\text{Si}_{4-x}$  units ( $x = 0, 1$  or  $2$ ). As total loss of aliphatic carbons had occurred in the  $1400^\circ\text{C}$  specimen, only graphitic carbon was clearly identifiable at  $123.16 \times 10^{-6}$ .<sup>[21]</sup> In the crystalline ceramic at  $1800^\circ\text{C}$ , the presence of carbidic carbon is not confirmed in the  $^{13}\text{C}$  MAS NMR spectra, but this does not preclude the existence of  $\text{SiC}$  in these samples; others have noted a similar difficulty due to the extremely

long relaxation of  $^{13}\text{C}$  in SiC.<sup>[21]</sup> In summary, the most drastic changes in  $^{13}\text{C}$  NMR spectra are observed from 400 to 600 °C, and the disintegration of the polymeric precursors and formation of an amorphous preceramic network were found.



**Fig. 4.3.**  $^{13}\text{C}$  NMR spectra of (a) monomer VSZ, (b) soluble as-synthesized polymer in  $\text{C}_6\text{D}_6$  and the solid-state NMR spectra of insoluble polymers treated at various temperatures under MAS conditions: (c) 200 °C, (d) 300 °C, (e) 400 °C, (f) 600 °C, (g) 1,100 °C, (h) 1,400 °C and (i) 1,800 °C. \* spinning side bands

The  $^{29}\text{Si}$  NMR spectra of the monomer and of the hydroborated products annealed at different temperatures are shown in Fig. 4.4. The spectrum of the as-synthesized polymer shows two major peaks at  $-3.16 \times 10^{-6}$  and  $-14.99 \times 10^{-6}$ , and a minor peak at  $16.3 \times 10^{-6}$ . Since the  $-14.99 \times 10^{-6}$  chemical shift is seen in the

solution  $^{29}\text{Si}$  NMR spectrum of VSZ, it can be assigned to silicon atoms in intact silazane rings with vinyl groups within the polymer. The new peak centered at  $-3.16 \times 10^{-6}$  was generated by the saturation of the vinyl groups on the Si atoms in the ring, and the peak at  $16.3 \times 10^{-6}$  suggests B-N bonding with the silazane ring, resulting in a silicon environment.<sup>[21]</sup>

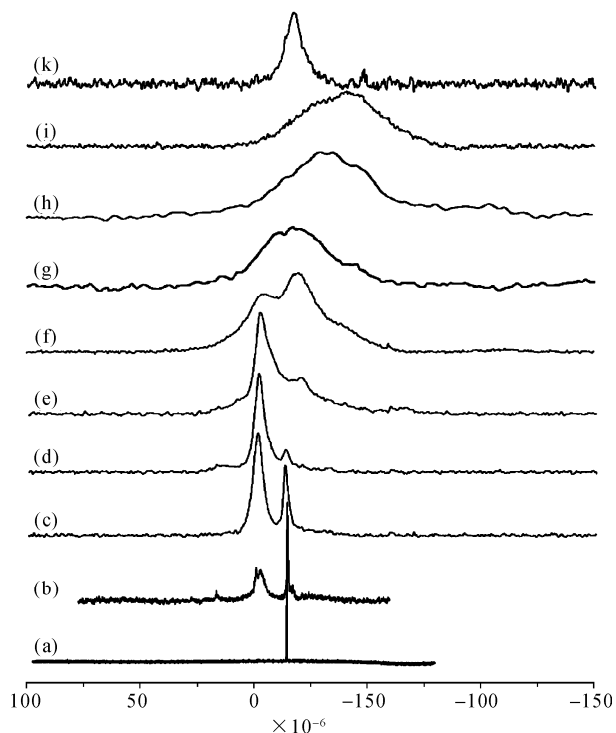


**Fig. 4.4.**  $^{29}\text{Si}$  NMR spectra of (a) monomer VSZ, (b) soluble as-synthesized polymer in  $\text{C}_6\text{D}_6$  and the solid state NMR spectra of insoluble products treated at various temperatures under MAS conditions: (c) 200 °C, (d) 300 °C, (e) 400 °C, (f) 600 °C, (g) 900 °C, (h) 1,100 °C, (i) 1,400 °C and (k) 1,800 °C

Upon heating to 300 °C, the peak at  $-14.99 \times 10^{-6}$  showed only a weak intensity while the peak at  $-3.16 \times 10^{-6}$  became broader, and the peak at  $16.3 \times 10^{-6}$  almost disappeared. After heating at 400 °C, the peak at  $-14.99 \times 10^{-6}$  essentially disappeared, indicating that hydroboration was nearly completed at this temperature, with a consequent increase in the relative intensity of the peak at  $-3.16 \times 10^{-6}$ . It is reasonably consistent with results of  $^{13}\text{C}$  NMR. At 600 °C, two peaks were observed at  $-6.62 \times 10^{-6}$  and  $-21.6 \times 10^{-6}$ , which could be assigned to  $\text{Si}(\text{Csp}^3)_2\text{N}_2$  sites and  $\text{Si}(\text{Csp}^3)\text{N}_3$  sites, respectively.<sup>[22]</sup> It has also been reported that observation of broadened signals and signals shifted to higher fields was possibly caused by a decrease in the number of protons as a consequence of thermal decomposition.<sup>[22]</sup> At 900 °C and 1,400 °C, only a signal with greater width peak

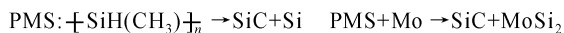
was observed, thus representing a superposition of the NMR line due to three main structural components, namely  $\text{SiC}_x\text{N}_{4-x}$  units with  $x = 0, 1$  or  $2$ . This indicates the heterogeneity of the local environment around the Si atoms in the amorphous material, regardless of the distribution of bond lengths and angles.<sup>[23]</sup> Finally, after heating to  $1,800\text{ }^\circ\text{C}$ , a major peak at  $-18.95 \times 10^{-6}$  and a minor peak at  $-49 \times 10^{-6}$  were observed. These peaks were attributed to the formation of  $\text{Si}_3\text{N}_4$  ( $-49 \times 10^{-6}$ ) and SiC ( $-19 \times 10^{-6}$ ) crystallites.<sup>[14]</sup> We conclude that the conversion of  $\text{SiC}_x\text{N}_{4-x}$  units to SiC between  $1,400\text{ }^\circ\text{C}$  and  $1,800\text{ }^\circ\text{C}$  in an argon atmosphere can be explained by the redistribution reaction of different silicon sites, as shown by the reaction between SiCN and the free carbon phase  $2\text{SiCN} + 2\text{C} \rightarrow 2\text{SiC} + 2\text{C} + \text{N}_2$ , which is consistent with a report that  $\text{Si}_3\text{N}_4$  reacts with free carbon at over  $1,450\text{ }^\circ\text{C}$ , according to the reaction:  $\text{Si}_3\text{N}_4 + 3\text{C} \rightarrow 3\text{SiC} + 2\text{N}_2$ .<sup>[22]</sup>

#### 4.2.2 SiC/MoSi<sub>2</sub> Ceramic Composites Prepared by Polymer Pyrolysis

The polymeric route to nonoxide ceramics offers a unique opportunity for manufacturing ceramic components such as fibers, coatings and composites by liquid fabrication and subsequent pyrolysis.<sup>[24]</sup> SiC compounds derived from various polysilanes have been studied for a variety of advanced applications. It is well known that the composition of pyrolytic products depends primarily on the chemical nature of their polymeric precursors. For example, SiC ceramics are produced with an excess of silicon by polymethylsilane (PMS) or with an excess of carbon by polycarbosilane (PCS).<sup>[25]</sup> Most researches have concentrated upon the development of polysilanes as stoichiometric SiC precursors because of their high-temperature stability. On the other hand, ceramic or metal fillers can be incorporated into the preceramic polymer matrix to overcome intrinsic volume shrinkage and porosity formation during polymer-ceramic conversion.<sup>[26]</sup> Results to date suggest that one might be able to develop functional high-density composites by designed reaction between excess components in the polymers and incorporated metal components.

It has been well known that the SiC/MoSi<sub>2</sub> composite phase has not only high creep and high oxidation resistance at elevated temperatures, but also high heat conductivity and electrical conductivity.<sup>[27]</sup> These properties can be utilized for both high-temperature structural materials and functional materials. In particular, commercial applications obviously exist as evidenced by the fact that MoSi<sub>2</sub> composite phases have been used for heating element materials in the high-temperature industries as well as in ceramic glow plugs of diesel engines.<sup>[28]</sup> However, powder processing technologies are commonly used to produce large articles with simple design, which involve high costs owing to the high-temperature sintering procedure. Therefore, a new approach with a versatile processibility such as paste types, is being demanded for applications where electrically conductive components or small precision parts with complex geometries are applied, for example, electrodes, sensors, or precision parts in micromechanical and electronic devices.

In this section, formation of electrically conducting SiC/MoSi<sub>2</sub> composite phases by the pyrolytic reaction between excess Si in PMS and Mo sources, such as metal powder, or MoCl<sub>5</sub> at temperatures over 1,000 °C, will be explained. This preliminary study demonstrates the potential of hybrid pastes as precursors of SiC/MoSi<sub>2</sub> composites for developing electrically resisting micro devices. The reaction is designed to be represented as shown in Scheme 4.1.



**Scheme 4.1.** Reaction of synthesizing the SiC/MoSi<sub>2</sub> composites

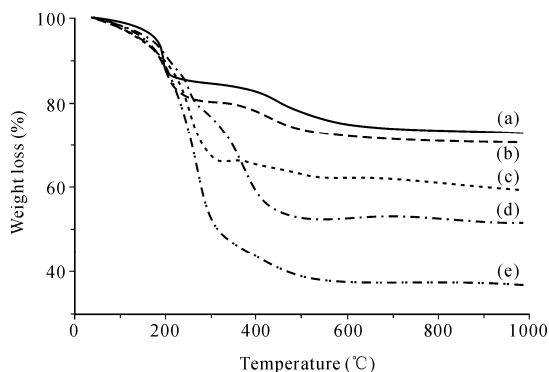
#### 4.2.2.1 Preparation of Samples

PMS was synthesized by the polycondensation of dichloromethylsilane (50.21 mL) with sodium (15 g) in a tetrahydrofuran (THF)/*n*-hexane solvent mixture of 1:6 (500 mL) under a dry nitrogen atmosphere.<sup>[29]</sup> After a reaction time of 16 h, the synthesized polymer solution was transferred to a round-bottomed flask in vacuum through a cannular equipped with a filter tip. An oily white liquid was obtained with a yield of 60% – 70% after evaporating the solvent. Borazine monomer B<sub>3</sub>N<sub>3</sub>H<sub>6</sub>, and the polymeric product  $\text{-(B}_3\text{N}_3\text{H}_x\text{)}_n\text{-}$  were prepared as described in the literature.<sup>[30]</sup> A Schlenk flask equipped with a magnetic stirrer and a thermometer was charged with 5 g of liquid PMS by the addition of 1 wt% polyborazine and 10 or 15 wt% of Mo powder with 325 mesh in THF solution. The PMS mixture was ultrasonicated for 5 h to activate the surface of metal powder in a nitrogen atmosphere. After curing at 200 °C for 2 h in the flask, the vacuum-dried solid mixture was pelletized by uniaxial pressing in a stainless steel die under programmed control up to 20 ksi and 400 °C. The consolidated sample was followed by pyrolysis to 1,400 °C in an inert atmosphere in a high-temperature furnace. For a spin-coating of solution, PMS was also mixed with 5, 10 or 15 wt% MoCl<sub>5</sub> and 1 wt% polyborazine in THF. The mixture was heated in an oil bath at 70 °C for 5 h with nitrogen purging to increase the molecular weight, and the diluted solutions to 20 wt% – 30 wt% in THF spun at 3,000 r/min on a silicon wafer. The coated samples were pyrolyzed up to 900 °C in the same manner, as was done for the pelletized specimens.

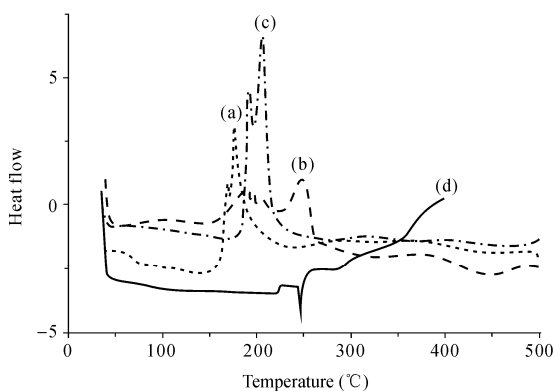
#### 4.2.2.2 Characterization of Specimens

It has been reported that PMS was converted into a ceramic in 30% yield.<sup>[25a]</sup> Such a low yield is attributed to rapid mass loss below 300 °C due to the decomposition and evaporation of the low molecular weight fraction in the PMS. We previously reported that the addition of 1 wt% polyborazine to PMS post-treated at 70 °C for 10 h dramatically increased the ceramic yield to 70%, with a lower weight loss below 300 °C.<sup>[31]</sup> In Fig. 4.5, similar behavior was also observed in the thermal properties of PMS and metal mixtures, as determined by TGA. PMS mixed with

two types of Mo sources, which were significantly improved to 80% from about 55% – 65% of ceramic yields with the addition of polyborazine.<sup>[32]</sup> It is interesting that the PMS/MoCl<sub>5</sub> mixtures showed a nearly identical level of ceramic yield as the PMS/Mo mixtures, despite the pyrolytic decomposition of the former that involved a significant mass loss as Cl<sub>2</sub> gas. In connection with the achievement of high ceramic yield, the precursor system must be beneficial at minimizing volume shrinkage on pyrolysis.<sup>[33]</sup> As shown in Fig. 4.6, the highly improved ceramic yield was ascribed to exothermic peaks at 150 – 250 °C, which might be due to dehydrocoupling between the Si–H groups remaining on the PMS. It is a contrast to pyrolytic behavior of the PMS only, which showed drastic weight loss with no exothermic reaction.



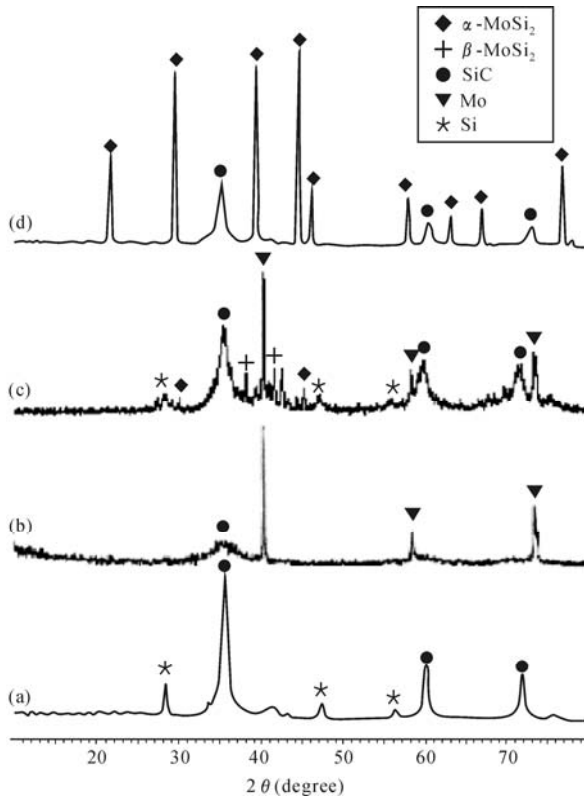
**Fig. 4.5.** TGA curves of various precursors. (a) Polyborazine added PMS/15 wt% Mo metal; (b) Polyborazine added PMS/15 wt% MoCl<sub>5</sub>; (c) PMS/15 wt% Mo metal only; (d) PMS/15 wt% MoCl<sub>5</sub> only; (e) PMS only



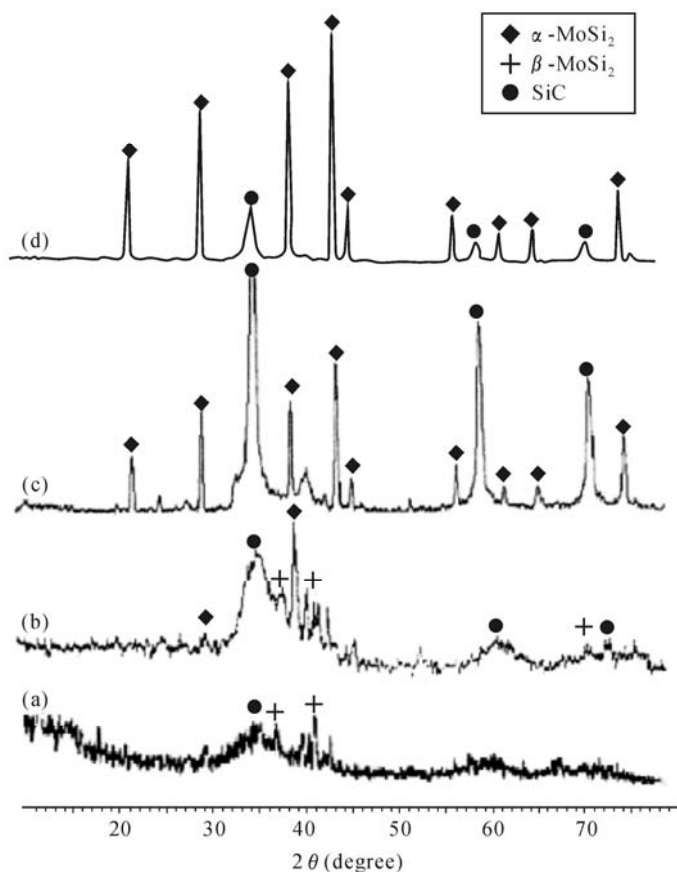
**Fig. 4.6.** DSC curves of various precursors. (a) Polyborazine added PMS/15 wt% Mo metal; (b) Polyborazine added PMS/15 wt% MoCl<sub>5</sub>; (c) Polyborazine added PMS; (d) PMS only

Figs. 4.7 and 4.8 show the XRD patterns of the pyrolyzed PMS mixtures with Mo metal or MoCl<sub>5</sub> sources at various temperatures in a nitrogen atmosphere. It has been repeatedly reported that the PMS converts  $\alpha$ -SiC ceramics with an excess

of Si (C/Si ratio 0.6).<sup>[25a]</sup> This work suggested that one might be able to develop SiC/MoSi<sub>2</sub> composites by reaction between the excess Si and Mo components. Therefore, as the mixtures were heated to 1,000 °C in nitrogen, the MoCl<sub>5</sub> mixture began to develop  $\beta$ -MoSi<sub>2</sub> (hexagonal) phase with diffused SiC peaks, while the Mo metal mixture did not initiate the reaction with excess Si in PMS. As heated to 1,200 °C, the MoCl<sub>5</sub> mixture converted the mixtures of  $\beta$ -MoSi<sub>2</sub> phase and new  $\alpha$ -MoSi<sub>2</sub> (tetragonal) phase with the crystallization of SiC. However, the Mo mixture only began to produce silicide phases by reaction between Mo and Si. It could be expected that molecularly dispersed Mo species in the MoCl<sub>5</sub> mixture must have better intimate contact to promote the intermetallic reactions at lower temperature than Mo powder in a few tenth's of a micrometer order of size. Both types of mixtures when pyrolyzed at 1,400 °C for 3 h were clearly consistent with the characteristic peak pattern of  $\alpha$ -MoSi<sub>2</sub> and SiC.<sup>[34]</sup> The intensity of the MoSi<sub>2</sub> phase was increased relative to SiC at higher mixing MoCl<sub>5</sub> ratios, as shown in Figs. 4.8c and 4.8d, which qualitatively indicated the comparative composition of the SiC/MoSi<sub>2</sub> composite. Presumably, it could be interpreted that the MoSi<sub>2</sub> phase dispersed in the SiC phase was formed by diffusion of the more mobile Si from PMS into the Mo particle as added or as decomposed from MoCl<sub>5</sub>.



**Fig. 4.7.** XRD patterns of PMS/15 wt% Mo metal mixture treated at various temperatures: (a) PMS only at 1,400 °C, the mixture annealed at (b) 1,000 °C, (c) 1,200 °C and (d) 1,400 °C



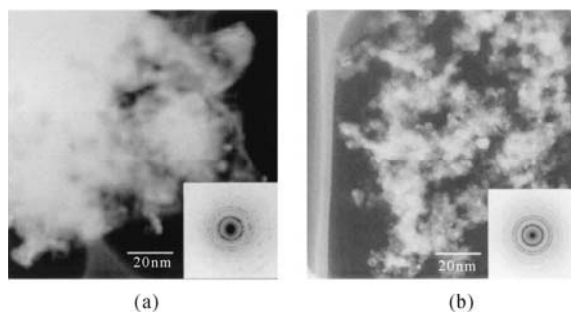
**Fig. 4.8.** XRD patterns of PMS/MoCl<sub>5</sub> mixtures treated at various temperatures. (a) 15 wt% MoCl<sub>5</sub> at 1,000 °C; (b) 15 wt% MoCl<sub>5</sub> 1,200 °C; (c) 5 wt% MoCl<sub>5</sub> at 1,400 °C and (d) 15 wt% MoCl<sub>5</sub> at 1,400 °C

Fig. 4.9 shows TEM image and selected area electron diffraction (SAED) for the composites treated at 1,400 °C. Electron diffraction of both products consisted of several rings corresponding to the (002), (101), (110) and (103) planes of  $\beta$ -MoSi<sub>2</sub>, and the (111) and (200) planes of SiC.<sup>[34b]</sup> The diffraction patterns of both MoSi<sub>2</sub>/SiC composites similarly displayed the multiple order reflections, indicating the presence of a homogeneously distributed composite phase on the nanometer scale. However, the grain sizes of the composite products depended on their precursors. The Mo metal containing a precursor resulted in coarse grains, due to an Mo grain size of about 20  $\mu$ m. In the case of the MoCl<sub>5</sub> precursor, the grains were very fine because Mo nuclei, presumably produced from thermal decomposition of MoCl<sub>5</sub>, reacted with PMS at the molecular level.

Fig. 4.10 shows various morphology of composite pellets and spin-coated ceramic films. The pellet types of the PMS mixtures were converted into



homogeneously dense composites of SiC/MoSi<sub>2</sub> with no cracks and only small pin holes at 1,400 °C, and of density *ca.* 1.7 g·cm<sup>-2</sup>, which is somewhat higher than 1.5 g·cm<sup>-2</sup>, of the commercial heating element. On other hand, composite films treated at 900 °C with a 5 wt% MoCl<sub>5</sub> mixture had rough surface morphologies with many pin holes due to the evaporation of Cl<sub>2</sub> gas from decomposed MoCl<sub>5</sub> at temperatures exceeding 250 °C.<sup>[34c]</sup> However, SiC film of about 1 μm thickness, produced by the spin-coating process of PMS, displayed a smooth surface and dense structure with no appreciable defects. Thus, it is promising to develop the paste types of precursors for functional composite phases, which can be controlled over a relatively wide viscosity range with versatile processibility.



**Fig. 4.9.** TEM image and SAED patterns for composites prepared with PMS and different Mo sources at various temperatures. (a) 15 wt% Mo at 1,400 °C; (b) 15 wt% MoCl<sub>5</sub> 1,400 °C

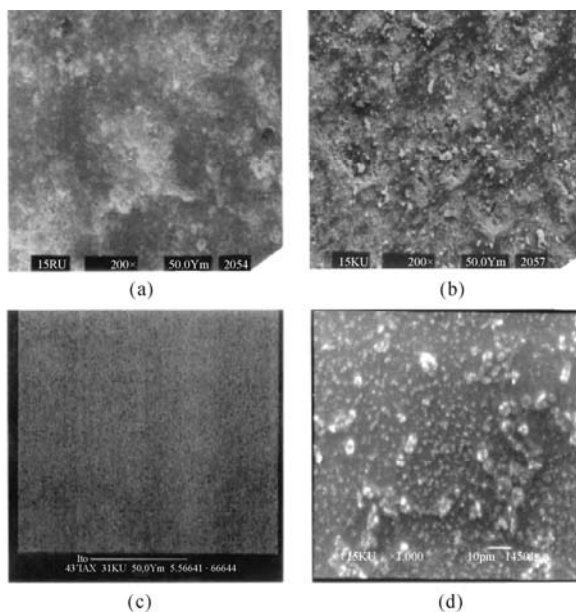


**Fig. 4.10.** SEM image of ceramic specimens prepared from various precursors; cross section of pellet (a) from PMS/10 wt% Mo mixture at 1,400 °C, (b) from PMS/10 wt MoCl<sub>5</sub> mixture at 1,400 °C, surface of spin-coated film annealed at 900 °C, (c) from PMS only, (d) PMS/5 wt% MoCl<sub>5</sub> mixture

The electrical conductivity of a pellet specimen obtained from PMS/Mo mixture and a commercial SILICONIT<sup>®</sup> heating element are shown in Fig. 4.11, and the electrical conductivity of the composite pellet increased from  $1.5 \times 10^{-2}$  to  $7 \times 10^{-2} \text{ S} \cdot \text{cm}^{-1}$  with increasing temperatures up to 520 °C. The values are about 1/50 those of the commercial heating element, but exhibit the same positive temperature coefficient. These results suggest that mixtures of preceramic precursor offer versatile processibility, and may be suitable as high-temperature heating elements after adequate optimization of the process of raw materials.

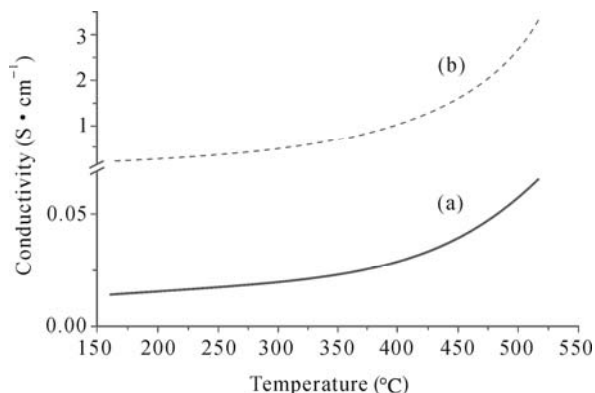
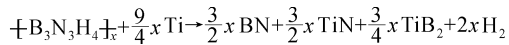


**Fig. 4.11.** Electrical conductivity of (a) SiC/MoSi<sub>2</sub> composite pellet formed from PMS/15 wt% Mo mixture at 1400 °C and (b) commercial SILICONIT<sup>®</sup>

### 4.2.3 Ti-B-N Composite from a Hybrid Precursor of Polyborazine and TiH<sub>2</sub>

Metal nitrides and borides have many desirable properties, such as high melting points and high Vicker hardness and strength at high temperatures.<sup>[4]</sup> In particular, titanium nitride (TiN) has some remarkable properties, such as extreme hardness, excellent electrical conductivity and valuable optical properties.<sup>[35]</sup> These properties have led to its use in a wide range of industrial applications in microelectronics, high-quality optical coatings and as material for cutting tools. Titanium boride (TiB<sub>2</sub>) has high chemical and thermal stability, high thermal conductivity, low electrical resistance and strong hardness, and has been used for structural and electrical applications.<sup>[4]</sup> So it is considered that a Ti-B-N composite phase may adapt the combined advantages of the two phases and exhibit a better performance than either that of the single phase made by titanium nitride or by boron alone. Recently, dry gas-phase processes have become commonly used to produce such non-oxide ceramic films. For example, Ti-B-N systems are prepared by chemical vapor deposition, plasma-assisted CVD, arc plasma vapor deposition and sputtering.<sup>[36]</sup> In this context, the performance of preceramic polymers with various metals came

to people's attention in terms of their ability to form a nanocomposite at low temperature in economic wet processes.<sup>[37]</sup> In addition, it has been reported that the introduction of a metal into preceramic polymers significantly improved the dimensional stability of the shaped body because of the reduced shrinkage. In this section, the use of a chemically reactive Ti source that is less prone to oxidation would permit a more-simplified low temperature process. So we propose a simple route to a BN/TiN/TiB<sub>2</sub> composite, using a hybrid precursor that involves thermally decomposable titanium hydride in a polyborazine, as represented in Scheme 4.2.



**Scheme 4.2.** Process of synthesizing a BN/TiN/TiB<sub>2</sub> composite

#### 4.2.3.1 Preparation of Samples

Titanium hydride powder was used as the titanium metal source. The borazine monomer was synthesized using a modified version of Sneddon's method.<sup>[30]</sup> For the polymerization reaction, the synthesized borazine was heated up to 70 °C in a pressure reaction vessel. Polymerization was continued with periodic H<sub>2</sub> degassing, to obtain a viscous product.<sup>[6]</sup>

To prepare a typical precursor of the BN/TiN/TiB<sub>2</sub> ceramic, TiH<sub>2</sub> powder and synthesized polyborazine were dispersed homogeneously in tetrahydrofuran as a solvent. And the hybrid precursor was subjected to vacuum drying to evaporate the THF. The highly viscous hybrid was cured at 70 °C until it became a black solid. The ground powder obtained was placed at 400 °C for 2 h under 60 ksi. The prepared pellet or powder was heated in inert gas at 500 – 1,300 °C over 6 h. To evaluate thermal properties of materials obtained, differential thermal analysis and thermogravimetric analysis was performed in the range of 100 °C to 800 °C. Powder X-ray diffraction was used to study ceramic conversion during the pyrolysis.

#### 4.2.3.2 Characteristics of Preceramic Composites

Fig. 4.12 shows the thermal properties of the hybrid precursor cured at 100 °C. The slight weight loss observed at up to 200 °C is due to the volatile low-molecular weight fraction of polyborazine; approximately 8% of its weight was lost at 800 °C.<sup>[38]</sup> This ceramic yields over 90% and this is relatively high compared to the 30% – 65% observed for other preceramic polymers. DTA curves show endothermic peaks at around 450 – 500 °C and 550 – 600 °C that are due to polythermic decomposition of TiH<sub>2</sub> to Ti over two steps.<sup>[39]</sup>

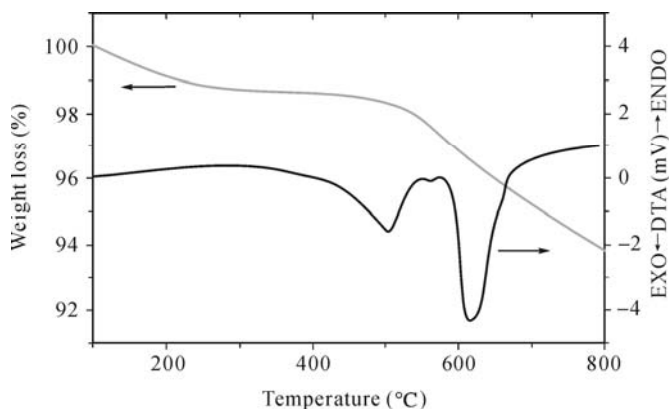


Fig. 4.12. TG-DTA curves for the mixture of  $\text{TiH}_2$  and polyborazine

Fig. 4.13 shows the change in chemical composition during the pyrolysis of the hybrid precursor. The precursor gradually converts to the ceramic composition phase via an intermetallic phase upon increasing the treatment temperature. At first, samples heated up to  $500\text{ }^\circ\text{C}$  displayed mixed patterns for  $\text{TiH}_2$  and Ti, indicating an intermediate state in which  $\text{TiH}_2$  decomposed to Ti. When heated up to  $900\text{ }^\circ\text{C}$ , all of the Ti was consumed to form a composite phase that was composed of a main  $\text{Ti}_2\text{N}$  phase, a minor amount of TiN and the slight presence of  $\text{TiB}_2$  in an amorphous BN matrix. At this point, Ti metal facilitates the transition to TiN rather than  $\text{TiB}_2$  because of similarity in the crystal structure. As the composite phase was annealed at higher temperatures, the crystallinity of the TiN and  $\text{TiB}_2$  phases became significant with the appearance of well-developed X-ray diffraction patterns, which means formation of the  $\text{TiB}_2$  phase began only at  $900\text{ }^\circ\text{C}$  when using the  $\text{TiH}_2$  reactant. This result clearly contrasts with that of the solid state reaction between titanium metal and BN powder, which formed the composite phase at  $1,450\text{ }^\circ\text{C}$ , and the wet chemical process between a polymeric precursor and Ti metal at  $1,200\text{ }^\circ\text{C}$ .<sup>[37,40]</sup> On the other hand, the amorphous BN phase that derived from the excess pyrolyzed polyborazine remained after reaction with Ti metal, as indicated by a balanced chemical equation.

Here, a simple low-temperature route to the production of a BN/TiN/ $\text{TiB}_2$  composite phase was developed using a hybrid precursor, which indicates both oxidatively stable  $\text{TiH}_2$  and polyborazine (a BN precursor). Based on the XRD results, the TiN and  $\text{TiB}_2$  phases were formed only at  $100\text{ }^\circ\text{C}$ , and commenced at  $900\text{ }^\circ\text{C}$  as a gradual inter-diffusion reaction. When heated to  $1,300\text{ }^\circ\text{C}$ , elements Ti, B and N displayed well-diffused chemical profiles that were similar to the nanocomposite phase. In particular, it was interesting to observe the development of a foam-like porous ceramic structure that presumably was caused by liberated hydrogen.

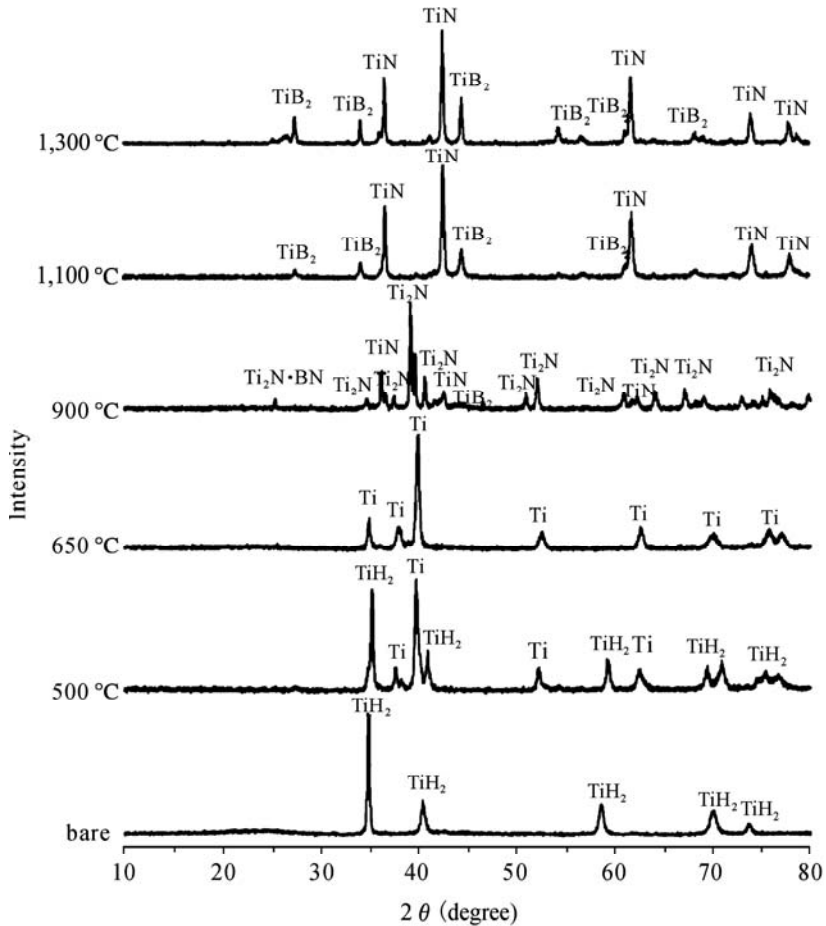


Fig. 4.13. XRD patterns of pyrolyzed  $\text{TiH}_2$ /Polyborazine samples

#### 4.2.4 Al-B-N Nanocomposite from Polyborazine and Al Metal

Hexagonal boron nitride (h-BN) and aluminum nitride (AlN) are two important non-oxide ceramics whose synthesis and properties have been extensively studied.<sup>[41]</sup> h-BN is a well known non-oxide ceramic, which can be prepared by the thermal decomposition of polymeric precursors such as polyborazine. It has high thermal conductivity, a low thermal expansion coefficient ( $1.7 \times 10^{-3}$  mm/mm at 1,100 °C) and an electrical insulator with wide band gap of 5.2 eV. Therefore, BN has been studied for many possible applications such as in types of fiber, coatings and composites.<sup>[6]</sup> On the other hand, AlN also has good thermal conductivity and a thermal expansion coefficient that matches silicon, low electric conductivity and

unique optical properties.<sup>[41]</sup> Combined they offer the promise of improved fracture toughness and resistance to wear and erosion, by the incorporation of the soft lubricating properties of BN with the hard and wear resistant AlN phase.<sup>[42]</sup> Furthermore, the above properties suggest that a homogeneous mixture of BN and AlN might be a strong candidate for use in electronic applications such as electronic heat sinks and others.

These materials are usually prepared by conventional carbothermal reduction and by solid state reaction between BN and AlN ceramics at high temperatures.<sup>[43]</sup> This section reports that the addition of active metal components into a preceramic polymer provides an efficient route with feasible processibility to obtain the homogeneous BN/AlN composite phase by a pyrolysis process using alternatively low temperatures, as shown in Scheme 4.3.



**Scheme 4.3.** Process of synthesizing the homogeneous BN/AlN composite phase

#### 4.2.4.1 Preparation of Samples

The synthesis of borazine as monomeric precursor and its polymerization to produce soluble polyborazine, were performed as reported in our previous report.<sup>[30]</sup> And 325 mesh of aluminum was added into polyborazine with a 2:1 or 1:1 molar ratio with tetrahydrofuran for the dispersion of aluminum powder under sonication. Cross-linkage of polymer was performed on polymer at 70 °C for 3 h. The polymeric mixture was further cured and dried at 100 °C for 1 h in inert gas conditions. Pelletized specimens were prepared by gradual heating in a vacuum press up to 400 °C at 20 ksi. The released mold pellet was pyrolyzed up to 1,400 °C for 3 h in an inert gas atmosphere. Alternatively, polyborazine was mixed with 10% by weight of AlCl<sub>3</sub> in tetrahydrofuran. This mixed sample was spun coated on a silicon wafer, and pyrolyzed at 900 °C for 2 h in an inert gas atmosphere.

#### 4.2.4.2 Characterization of Metal Preceramic Composite

Fig. 4.14 shows the thermal behavior of the various precursors. The DSC thermogram of polyborazine shows broad endothermic peaks at 90 – 120 °C, which may indicate the evaporation of low molecular weight volatiles. The TGA curve shows most weight loss occurs up to the corresponding temperature.<sup>[6]</sup> The exothermic phenomenon in the temperature range of 160 – 200 °C is believed to indicate a cross-linking reaction. An exotherm corresponding to a further condensation rearrangement occurs at above 400 °C and involves a 5 wt% loss, which is due to the transition of BN from the polymeric to the amorphous phase. It should be pointed out that the ceramic yield of up to 83% for BN from borazine polymer is very high compared to that of polymeric precursors for SiC and carbon.<sup>[44]</sup> The DTA

curve of the Al mixed precursor displays a strong endotherm at 660 °C due to melting of the Al metal. The diffused pattern of the thermogram below 400 °C was partially attributed to a curing process at 100 °C prior to measurement. The ceramic yield, of over 90%, is significantly higher due to the presence of the Al metal filler. However, the  $\text{AlCl}_3$  mixtures showed a 60% weight loss in the temperature range 100 °C to 300 °C caused either by the evaporation of  $\text{AlCl}_3$  or its thermal decomposition into byproducts such as  $\text{Cl}_2$ . On the other hand, lower weight loss was promisingly observed by ultrasonic treatment of the metal solutions. It should be noted that metal colloids have been previously synthesized using a sonochemical process on metal salt solutions.<sup>[45]</sup>

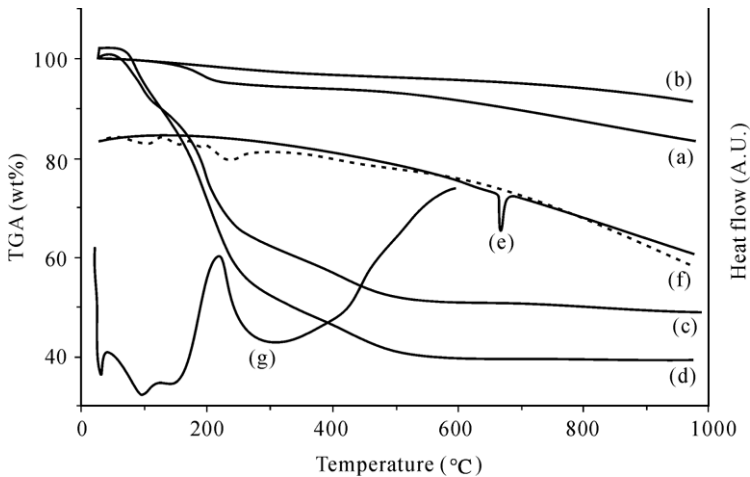


**Fig. 4.14.** TGA curves of (a) polyborazine, (b) Al metal/polyborazine (2:1 ratio) mixture, (c)  $\text{AlCl}_3$ /polyborazine (2:1 ratio) mixture with sonication, (d)  $\text{AlCl}_3$ /polyborazine (2:1 ratio) mixture with no sonication, DTA curves of (e) Al metal/polyborazine mixture, (f)  $\text{AlCl}_3$  as-mixed precursor, and DSC curve of (g) polyborazine

Fig. 4.15 shows the SEM micrograph of a pellet and spin-coated specimens prepared from Al/polyborazine and  $\text{AlCl}_3$ /polyborazine, respectively. The pellet type specimens are of a relatively dense structure ( $2.6 \text{ g}\cdot\text{cm}^{-3}$ ) and show no cracks. However, more detailed observation demonstrated that the sample consisted of an agglomerated structure of particles which were less than  $1 \mu\text{m}$  in diameter. In particular, hollow spheres were found by cross sectioning the pellet. This indicated that intimate contact between Al melt and pyrolyzed polyborazine must form the AlN phase, preferentially at the surface of the Al melt bubble, while the unreacted internal Al might then gradually evaporate at above 660 °C. Conversely, spin-coated specimens displayed thin films with randomly dispersed needle shaped AlN crystals on the substrate.

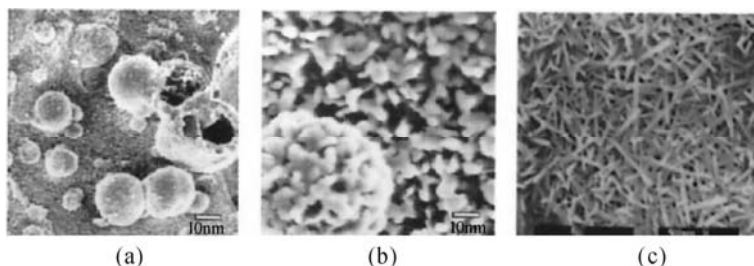


**Fig. 4.15.** SEM image of a cross-section of (a) Al metal/polyborazine (2:1 ratio) pellet pyrolyzed at 1400 °C, (b) the detailed observation of (a), and (c) spin-coated AlCl<sub>3</sub>/polyborazine (0.1:1 ratio) mixture pyrolyzed at 900 °C

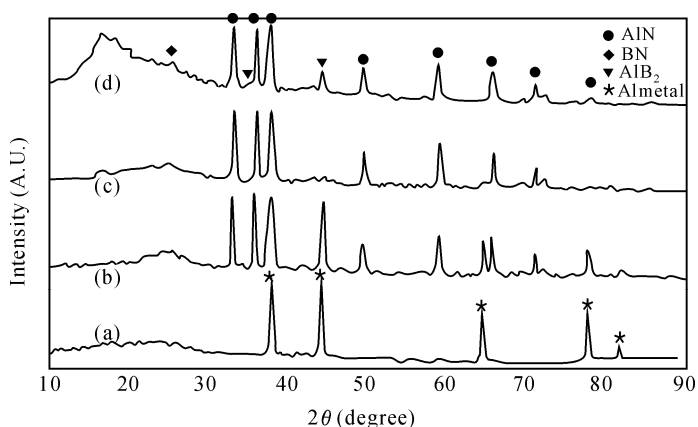


**Fig. 4.16.** XRD pattern of Al metal/polyborazine (2:1 ratio) mixture pyrolyzed at (a) 600 °C, (b) 1000 °C, (c) 1200 °C and (d) 1400 °C

XRD patterns of the products obtained from Al powder mixed precursors are shown in Fig. 4.16. Al metal began to react with the pyrolyzed polyborazine at 1,000 °C to form the AlN phase, while no reaction was observed at 600 °C.<sup>[41,46]</sup> This might indicate that the Al liquid above the melting point of 660 °C must readily contact the pyrolytic intermediate phase converted from polyborazine to form AlN only at the interface between the reactive phases. The formation temperature is definitely lower than the 1,650 °C required by the carbon reduction route, and comparable to that of the organometallic vapor-phase route, in which AlBN layers were formed at 1,100 °C. As the specimens were annealed at higher temperatures, Al metal converted into the crystalline AlN phase with a weak turbostratic BN peak. At 1,400 °C, the Al peak pattern was no longer observed with additional (100) and (101) AlB<sub>2</sub> peaks, which were observed at 35° and 45° (2θ), respectively. The minor intensity of AlB<sub>2</sub> might be related to a half coefficient of AlN at the balanced reaction equation, as suggested in the introduction. In the phase diagram of Al-B, the AlB<sub>12</sub> phase, which is thermodynamically stable over 980 °C, is converted to the AlB<sub>2</sub> phase on cooling.<sup>[47]</sup> The amorphous peak at 16° (2θ)



must be attributed to the glass slide as substrate. The spin-coated product obtained from the pyrolysis of a polyborazine and  $\text{AlCl}_3$  mixture at  $900^\circ\text{C}$  showed only (002) and weak (100) reflections of the characteristic BN and AlN peak, respectively. In addition, the XPS spectra of the Al/polyborazine pyrolyzed at  $1,200^\circ\text{C}$  was consistent with the above XRD results. The BN phase was evidenced by both the strong peak binding energy at 190.5 eV of B 1s and the 398.0 eV of N 1s, and similarly for AlN by the 73.5 eV of Al 2p,  $\text{TiB}_2$  from the 188.3 eV of B 1s.<sup>[48]</sup>

Fig. 4.17 shows EF-TEM images of Al/polyborazine derived ceramics at a  $1,400^\circ\text{C}$  processing temperature. It is known that light elements such as boron and nitrogen may be effectively detected by an energy filtering technique in TEM analysis. Through elemental mapping, it was noticed that Al-B-N were commonly distributed over the whole region to different extents. However, aluminum and nitrogen were localized at identical regions, whereas boron was present in isolated islands. This indicates that the Al melt readily infiltrated into the pyrolyzed polyborazine matrix to form 300 nm AlN grains, and that the low level of oxygen impurity from the aluminum was trapped at the boundary between the AlN grains without any other oxide formation. In order to interpret the isolation of boron, based on the phase diagram of Al-B, it is likely that the  $\text{AlB}_{12}$  as a high temperature stable phase might partially remain even at room temperature, due to phase conversion kinetics on cooling.<sup>[47]</sup> However, the mechanism of boron isolation remains unclear. On the basis of these preliminary investigations, the reaction of polyborazine with Al sources offers a potential precursor for AlN/BN ceramics prepared below  $1,000^\circ\text{C}$ . There is a definite benefit in having a ceramic composition pre-determined on a molecular level since this would ensure uniform properties.

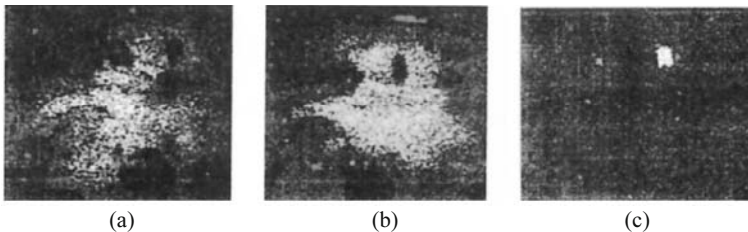


**Fig. 4.17.** EF-TEM of Al metal/polyborazine (2:1 ratio) mixture pyrolyzed at  $1400^\circ\text{C}$ : (a) nitrogen, (b) aluminum and (c) boron

#### 4.2.5 Al-Cr-Phosphates as Low Temperature Curable Binders

Phosphate materials have been used as binders in refractory ceramics for 60 years. Phosphoric acid and aluminum phosphate are used the most because phosphate-bonded refractory materials have good strength, high-temperature stability and abrasion resistance.<sup>[49]</sup> Furthermore, consolidation at low temperatures facilitates

various processes under conditions that are generally applied to organic resins.<sup>[50]</sup> It is well known that a curing reaction at low temperatures is caused by a substitutional reaction of basic or neutral metal ions to hydrogen in phosphoric acid to form an irregular structure.<sup>[51]</sup> Recently, thermally insulating glass fiber/Al-Cr-phosphate composites were prepared by a low temperature hardening process under 200 °C on prepregs impregnated with an aqueous matrix solution which was homogeneous mixture binders of aluminum phosphate and chromium phosphate containing Al<sub>2</sub>O<sub>3</sub> and Cr<sub>2</sub>O<sub>3</sub> powders as a filler. Interestingly, the composites with an amorphous matrix can achieve excellent rehydration resistance with a low thermal conductivity only by curing at low temperature. It seems that properties of the metal phosphates depend on the chemical compositions, curing temperature and pressure, and various additives such as different types of fillers. Despite the industrial importance of phosphate binders, their chemical nature has attracted little interest. In this section, the hardening chemistry of an aluminum chromium phosphate binder to form an amorphous phase at low temperatures was examined using sophisticated instrumental analysis such as solid-state nuclear magnetic resonance (NMR). As a preliminary step toward tailoring the process and properties of composites, the effect of the chromium species as a component of the binder and filler on the curing and crystallization behaviors was investigated.

#### 4.2.5.1 Preparation of Samples

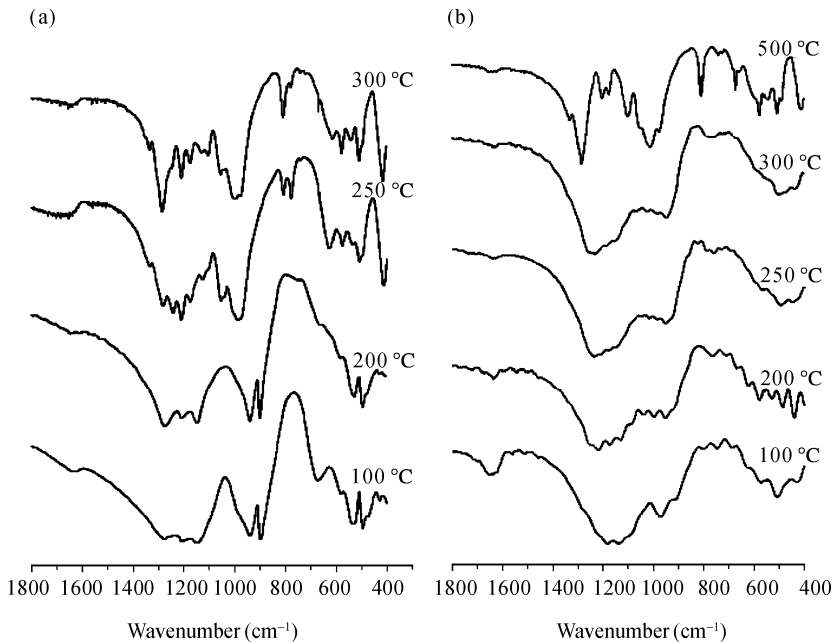
Highly viscous Al<sub>3</sub>Cr(H<sub>2</sub>PO<sub>4</sub>)<sub>x=9,12</sub> binder solutions were prepared by dissolving Al(OH)<sub>3</sub> and either CrO<sub>3</sub> in H<sub>3</sub>PO<sub>4</sub> using two mixing ratios, as shown in Table 4.2, based on the stoichiometric ratio of the two metals and the phosphate.<sup>[52]</sup> In a typical reaction, Al(OH)<sub>3</sub> was dissolved in aqueous phosphoric acid, which was permitted to react at 80 °C for 20 min until it became optically clear. Subsequently, CrO<sub>3</sub> was added to the solution, which was quickly dissolved by adding several drops of methanol. The vigorous evolution of gas and foam was controlled by the drop-wise addition of methanol.<sup>[53]</sup> The binders obtained are described as the ACP binder, while the aluminum phosphate solution denoted as the AP binder was prepared by dissolving Al(OH)<sub>3</sub> in H<sub>3</sub>PO<sub>4</sub>. The chromium phosphate binder, which is denoted as the CP binder, was prepared by dissolving CrO<sub>3</sub> in H<sub>3</sub>PO<sub>4</sub> at a mole ratio 1:3. The AP and CP binders were used as the reference specimens. The binders were mixed with two kinds of fillers such as Al<sub>2</sub>O<sub>3</sub> and Cr<sub>2</sub>O<sub>3</sub> powders at a ratio of binder:Al<sub>2</sub>O<sub>3</sub>:Cr<sub>2</sub>O<sub>3</sub> = 48:41:11 wt% by stirring at 80 °C for 30 min, which is described as the matrix solution. The binder solutions were dried at 100 °C for 24 h. The specimens were cured in an autoclave below 300 °C under a pressure of 10 atm at a heating rate of 10 °C·h<sup>-1</sup> then held at the desired temperature for 12 h. During the cooling stage, the pressurized air containing water as a byproduct was released to prevent rehydration. However, annealing over 300 °C was conducted using a muffle furnace in air.

**Table 4.2** Mixing ratios of the reactants to prepare the binder solution (Adapted from Ref. 52. Copyright (1995), with permission from the Springer)

Sample name	Chemical formula	Mixing ratio (mol%)
ACP-319	$\text{Al}_3\text{Cr}(\text{H}_2\text{PO}_4)_9$	Al:Cr:H <sub>3</sub> PO <sub>4</sub> = 3:1:9
ACP-3112	$\text{Al}_3\text{Cr}(\text{H}_2\text{PO}_4)_{12}$	Al:Cr:H <sub>3</sub> PO <sub>4</sub> = 3:1:12

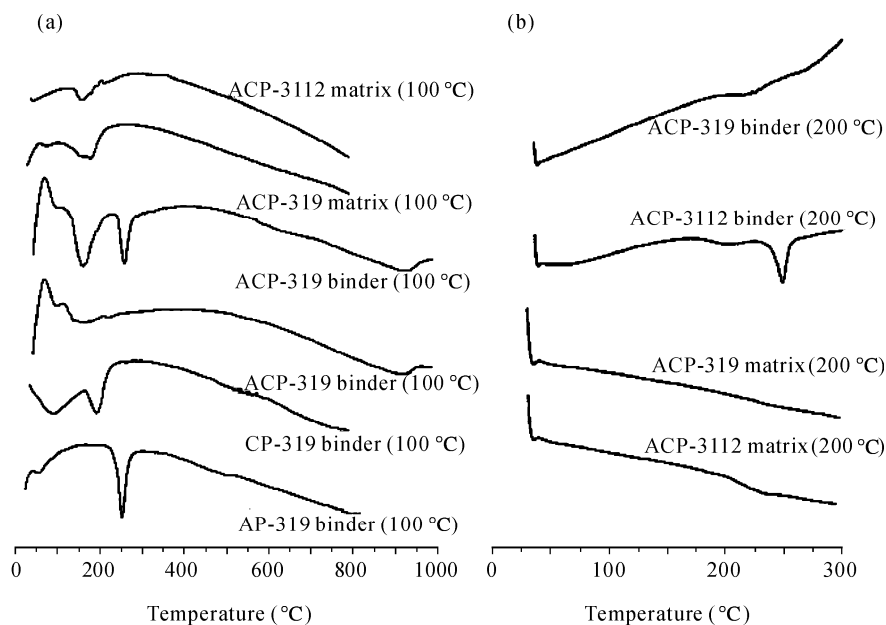
#### 4.2.5.2 Characteristics of Specimens

Fig. 4.18 shows the IR spectrum for the chemical evolution of the binders heated at various temperatures. Generally, several characteristic IR absorptions gradually changed with higher heat-treatment. A broad absorption band in the range  $1,100 - 1,400 \text{ cm}^{-1}$  converted to a strong peak at  $1,295 \text{ cm}^{-1}$  and was assigned to the asymmetric stretch of the P=O group, and a weak  $1,205 \text{ cm}^{-1}$  peak to the symmetric stretch of the P=O group. In addition, the band at  $950 \text{ cm}^{-1}$ , which was assigned to the asymmetric stretch of the linear P-O-P chain, was slightly shifted to  $1,000 \text{ cm}^{-1}$  with decreasing intensity of the hydroxyl group, P-OH, at  $890 \text{ cm}^{-1}$ . This was presumably due to a phase transformation from monoaluminum phosphate ( $\text{Al}(\text{H}_2\text{PO}_4)_3$ ), to aluminum hydrogen phosphate hydrate ( $\text{AlH}_2\text{P}_3\text{O}_{10} \cdot 2.5\text{H}_2\text{O}$ ). Furthermore, the appearance of a  $1,050 \text{ cm}^{-1}$  band, which was assigned to the asymmetric stretch of the P-O-P rings, suggests that the nature of the P-O-P bond began to change from a linear structure at low temperatures to a small

**Fig. 4.18.** IR spectra of (a) AP binders and (b) ACP-319 binders at various temperatures

metaphosphate  $\text{Al}(\text{PO}_3)_3$  ring structure even at 250 °C. This was confirmed by a newly generated band at  $800\text{ cm}^{-1}$  that was assigned to the symmetric stretch of P-O-P groups of the small metaphosphate ring.<sup>[54]</sup> The IR spectrum of ACP-319 in Fig. 4.18(b) showed basically a similar pattern to that of the AP binder, but with a slower evolution rate. The spectrum of the ACP-319 binder treated at 500 °C is nearly identical to that of the AP binder treated at 300 °C. Typically, the ACP-319 annealed at 300 °C does not evolve in chemical behavior to transform from a linear P-O-P into cyclic phosphates, which was confirmed by the absence of the  $1,050\text{ cm}^{-1}$  band. In addition, the IR spectrum of the ACP-3112 binder was also similar to those of the ACP-319, but with a slightly stronger intensity of hydroxyl group at  $890\text{ cm}^{-1}$  due to excess phosphoric acid.

Fig. 4.19 shows DTA and DSC curves of various binders and matrices pretreated at 100 or 200 °C to evaluate the effect of the chemical composition and fillers on the curing behavior. For the binders pretreated at 100 °C, the AP binder shows a large endothermic peak at 250 °C due to dehydrolytic condensation, while the CP binder shows an endotherm at 180 °C. For the ACP binders dried at 100 °C, the ACP-3112 binder shows two large endothermic peaks at 170 °C and 250 °C, which is similar in a simple mixture of the CP and AP binders. In contrast, the ACP-319 binder shows a small endotherm at 170 °C. When fillers were added to the binders, both the matrices displayed a single peak at 170 °C with a smaller peak area. Furthermore, as the binders were pre-treated at 200 °C, the endotherm became much weaker due to the dehydration that proceeded during pre-treatment. In particular, the matrices pre-treated at 200 °C showed no peak due to completion



**Fig. 4.19.** Curves of the various binders and matrices (pre-treated at 100 or 200 °C). (a) DTA; (b) DSC

of the curing reaction. This indicates that dehydrolytic condensation must be promoted by the presence of filler or the Cr compound to form a consolidated network. It is similar to the previous report in which the addition of  $\text{Al}_2\text{O}_3$  increased the cross-link density between phosphate chains to result in high aqueous durability.<sup>[54]</sup> It is believed that the processing conditions would significantly affect the overall physical properties of the products such as the thermal stability, rehydration resistance and the material strength. Crystalline structures tend to be rigid as a result of crystalline interlocking, while the lack of residual forces in a well-ordered crystal leads to poor bonding characteristics. However, amorphous structures may also possess three-dimensional continuity that is more flexible and is more able to accommodate internal stresses and strains, which is beneficial in composite applications.

Fig. 4.20 shows crystallization behavior of the various binders when heated up to 1200 °C. From XRD analysis of the AP binders, it was observed that monoaluminum phosphate  $\text{Al}(\text{H}_2\text{PO}_4)_3$  as JCPDS 44-0724 mainly transformed to aluminum hydrogen phosphate  $\text{AlH}_3(\text{PO}_4)_2$  at 200 °C. It undergoes a transition to type B aluminum metaphosphate  $\text{Al}(\text{PO}_3)_3$  at 300 °C. The transition to type A aluminum metaphosphate as JCPDS 13-0430 begins at 500 °C and is complete at 700 °C, which occurred 200 °C lower than the reported transition.<sup>[55]</sup> It is known that type B aluminum metaphosphate has a chain structure where the  $\text{PO}_4$  tetrahedra are linked together to form infinite  $(\text{PO}_3^-)_n$  chains while the type A, as a high temperature phase, has a ring structure. The XRD patterns of the ACP-319 binders show an identical crystalline structure with a slower evolution rate than the AP binders. In contrast to the AP binders, significant crystallization does not occur up to 500 °C but a small single peak at  $21.6^\circ$  ( $2\theta$ ), corresponding to the structural type of aluminum hydrogen phosphate, begins to form. It then starts to transform to the type B aluminum metaphosphate at 700 °C and finally to the type A aluminum metaphosphate, beginning at 1,000 °C. In comparison with the IR results for the ACP-319 binder, it appears that the presence of Cr species may greatly reduce the kinetics of crystallization compared to that of the AP binder, although the ACP-319 binder microscopically developed the P-O-P ring type structure for the metaphosphate even at 500 °C. Furthermore, when the relative mole ratio of the Cr species in the AP binder increased, the evolution of the crystalline phases at each annealing temperature became weak. Previous reports showed that the formation of disordered structures is related to the cationic size in phosphate systems. Larger metal cations formed regular structures with a high coordination number. In contrast, smaller cations increased the degree of randomness in polymers. Thus, it can be concluded that chromium addition, with a relatively small cationic radius, increases the bonding power of the phosphate binder that promotes dehydrolytic condensation and the formation of an amorphous structure.

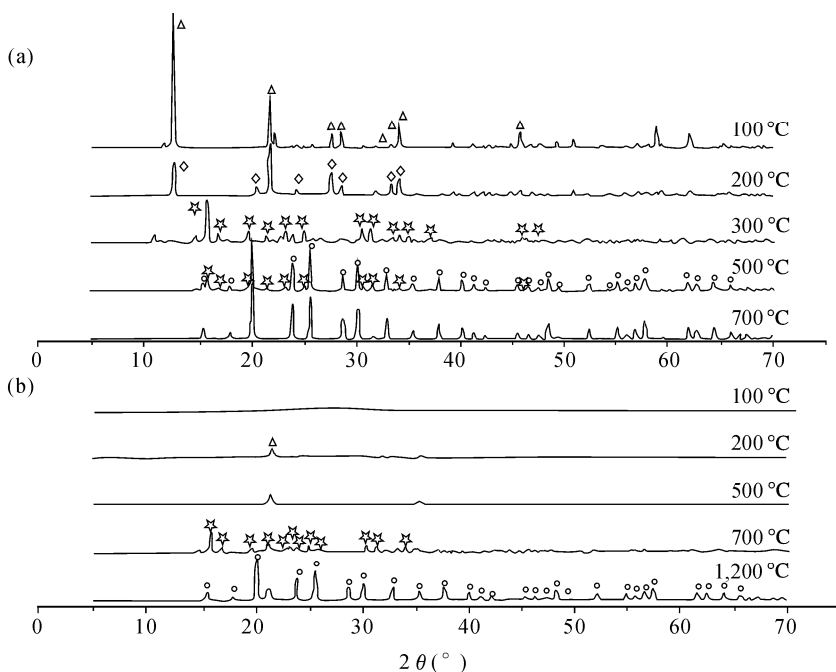


**Fig. 4.20.** XRD patterns of (a) AP and (b) ACP-319 binders heated at various temperatures.  $\Delta$   $\text{Al}(\text{H}_2\text{PO}_4)_3$ ,  $\diamond$   $\text{AlH}_3(\text{PO}_4)_2$ ,  $\star$   $\text{Al}(\text{PO}_3)_3$  (B) and  $\circ$   $\text{Al}(\text{PO}_3)_3$  (A)

Fig. 4.21 shows the  $^{31}\text{P}$ -MAS-NMR spectra of the AP and ACP-319 binders treated at various temperatures. The AP solution without heat treatment shows monomeric peak patterns in the range  $-20 \times 10^{-6} - 0 \times 10^{-6}$ , which is similar to that observed in the ACP solution. As the reaction proceeds at higher temperatures, the spectrum becomes complicated with peak patterns for the mixed phases over a broad  $-50 \times 10^{-6} - 0 \times 10^{-6}$  range since polymeric phosphates containing more than one phosphate consisted of 3 type of units (end, middle, branch). Thus, the extent of condensation increases as the structure changes from  $\text{Al}(\text{H}_2\text{PO}_4)_3$  to  $\text{Al}(\text{PO}_3)_3$  through to the  $\text{AlH}_3(\text{PO}_4)_2$  phase with the gradual formation of a cured network with P branching having 3 functionalities. Therefore, the chemical shifts primarily depend on the number of bridging oxygens linked to the P atom and on the electrostatic field strength of the metal cation bonded to the non-bridging oxygens. Eventually, at 700 °C a group of scattered peaks consistently converges to a single peak at  $-50.6 \times 10^{-6}$ , which corresponds to circular P-O-P metaphosphate. However, ACP binders show a consistent single broad peak at each step, and similar pattern of peak shift observed at AP binders with slightly different evolution, as shown in the IR spectrum. The strong dipolar coupling with the unpaired electron of the  $\text{Cr}^{3+}$  paramagnetic species in the vicinity of the P nuclei thus causes a broadening of the NMR signal. Moreover, at over 500 °C a peak begins to split slightly with crystallization as indicated by XRD. This should be investigated further to

understand fully the relationship between properties and chemical structures in various phosphate systems.

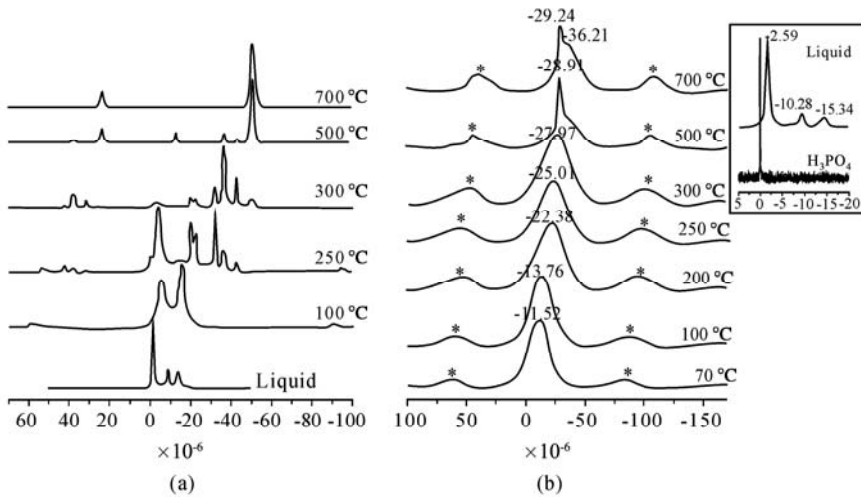


**Fig. 4.21.** Liquid and solid state  $^{31}\text{P}$ -NMR of the (a) AP and (b) ACP-319 binders heated at various temperatures

### 4.3 Applications of Preceramic Polymers

In this section, some application examples of preceramic polymers are introduced to demonstrate their utility in structural ceramic materials as an alternative preparative route compared with the conventional powder sintering process, such as ceramic matrix composite and ceramic film.

#### 4.3.1 Preparation of Carbon Fiber Reinforced BN Matrix Composite

Carbon fiber/carbon matrix (C/C) composites are attractive materials for use in high-temperature applications requiring strength, light weight and toughness.<sup>[56]</sup> However, their high temperature use in air is limited to about 425 °C. To prevent cracks generating at temperatures up to 1,300 °C, thick CVD coatings of SiC are currently used.<sup>[57]</sup> Micro-cracks in such coatings may develop with thermal cycling due to a mismatch of the thermal expansion coefficient. In this case, micro-cracks can lead to severe failure since penetration of oxygen through the crack will result in rapid oxidation of the C/C composite to CO and CO<sub>2</sub>. To defeat these problems, adoption of the BN matrix composite makes it possible to increase oxidation resistance from 425 °C to 850 °C.<sup>[58]</sup> If micro-cracks developed in the

SiC coating, the BN matrix would oxidize to  $B_2O_3$ , which only begins to evaporate at temperatures above 1,500 °C. According to the literature, it came to our attention that several types of borazine oligomers had been prepared and polymerized starting at relatively low temperatures and, on further heating to 1200 °C, produced a boron nitride-like material.<sup>[59]</sup> In this section, we report the successful preparation of carbon fiber BN (C/BN) matrix composite using either a one or two step impregnation. From preliminary tests, these composites display outstanding mechanical properties and excellent resistance to oxidation up to 850 °C.<sup>[6]</sup>

#### 4.3.1.1 Preparation of BN Precursor Oligomers

In the early 1960s, the reaction of borazine with itself to form a borazine like polymer had been reported by several researchers and shown to form a BN-like material.<sup>[60]</sup> Heating of borazine at relatively low reaction temperatures produces intermediates that correspond to biphenyl and naphthalene, such as pyrolysis of benzene. The reactions presumably continue on heating to 700 – 1,000 °C to form polynuclear, layered structures which resemble disordered carbon structures. This kind of BN is known to be very sensitive to moisture and is typically characterized by relatively large interlayer spacing larger than 3.5 Å.<sup>[61]</sup> The reaction of borazine was performed under viscous melt suitable for impregnating the carbon fiber layer.

In our study following this procedure developed by Sneddon, we deliberately carried out the reaction of borazine with itself to produce a viscous melt suitable for impregnating the carbon fiber layup. In Fig. 4.22 are shown the DSC and TGA patterns for the conversion of borazine polymer into BN. The broad endothermic peak at 60 – 120 °C may indicate the evaporation of low molecular weight volatiles. The TGA shows a small weight loss up to the corresponding temperature. The exotherm in the temperature range 160 – 270 °C is believed to be a cross linking reaction involving a weight loss of 5%, followed by further condensation above 400 °C.<sup>[62]</sup> It should be pointed out that the ceramic yield of up to 85% of BN from borazine polymer is very high compared to those of other polymeric precursors used to prepare SiC and carbon. From the elemental analyses in Table 4.3, one can infer a partially branched-chain and cross-linked structure at reaction temperatures of 70 and 300 °C, respectively.

**Table 4.3** Effect of heat treatment on the structure of bulk BN and properties of composites

Heat treatment	Interlayer spacing of bulk BN (Å)	Density of composite ( $g\cdot cm^{-3}$ )
1200 °C (30 min)	3.50	1.4 (1.5 – 1.6) <sup>a</sup>
1200 °C (3 h)	3.56	
1500 °C (20 h)	3.34	

<sup>a</sup> The value of densified composites in parentheses



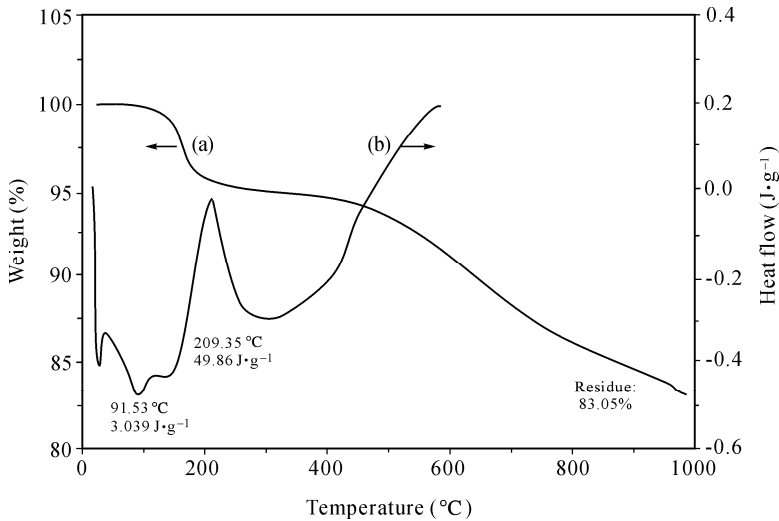


Fig. 4.22. (a) DSC and (b) TGA patterns of borazine polymer

#### 4.3.1.2 Fabrication of Composite

C/BN composites were prepared using PAN- or pitch-based carbon fibers. The impregnated prepreps were gently heated at 40 – 70 °C for 2 d to solidify the matrix through further polymerization, as shown in Fig. 4.23. At this point the composite was heated up to 400 °C under pressure. Subsequent heating to 1200–1,500 °C produced specimens with outstanding mechanical properties, even though the average apparent density of the various specimens was about 1.4 g·cm<sup>-3</sup>. These composites could be further densified to a density of 1.6 g·cm<sup>-3</sup> by the second impregnation. After 3 h at 1,200 °C the interlayer spacing is down to 3.36 Å, which is indicative of a BN structure which is stable against moisture. The very high mechanical properties of all of the specimens suggested optimal bonding at the interface. This is illustrated in Fig. 4.24, where a fracture surface shows good bonding between the fiber and matrix. The borazine oligomer was found to easily wet the fiber layups, permitting excellent infiltration into the interstices between fibers.

It has been known that the flexural test is useful in simulating actual behavior during service.<sup>[63]</sup> In these tests, with high ratio of span to thickness, failure involved buckling of the fibers and fragmentation of the matrix on the compressive side of the specimen and cracking along the neutral planes where the shear stresses were highest, as seen in Fig. 4.25. The load deflection curves for these tests are shown in Fig. 4.26. Those samples which were tested without a second impregnation displayed a much tougher behavior consistent with porosity in the structure.<sup>[64]</sup>

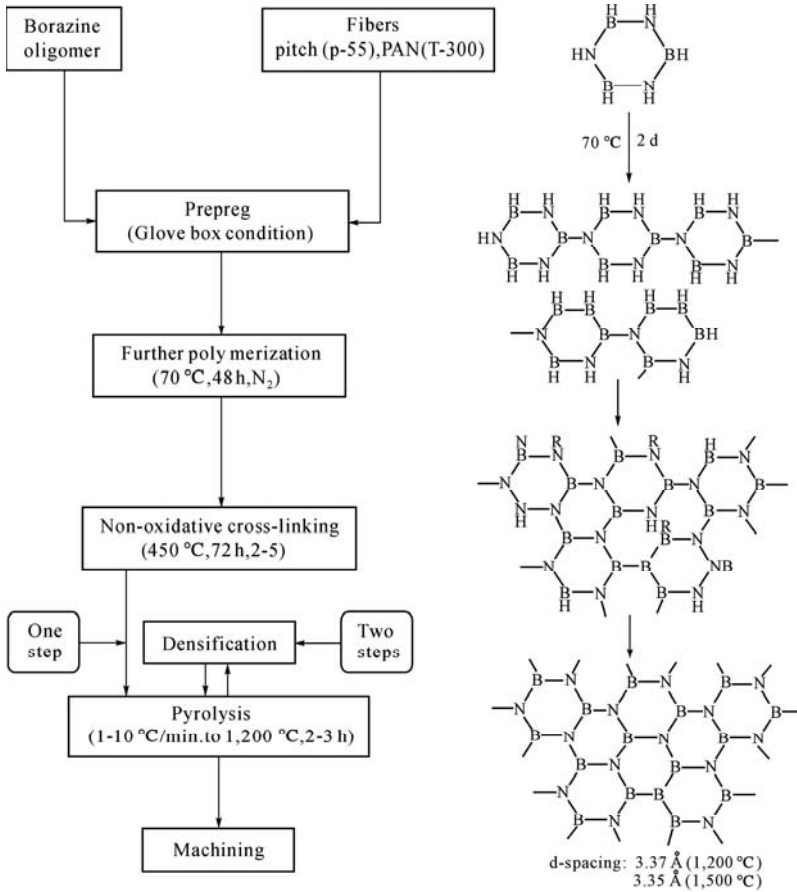


Fig. 4.23. Flow chart of process for making C/BN composite materials using borazine polymer

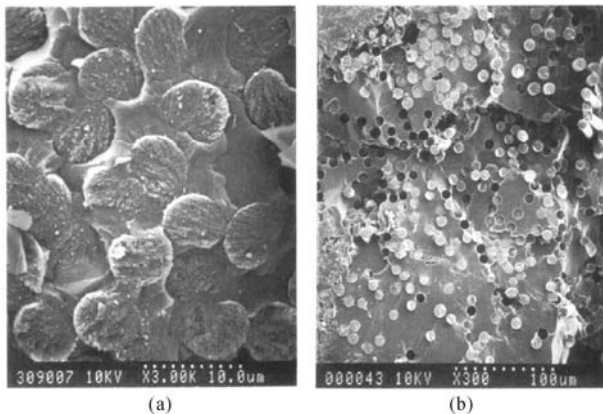
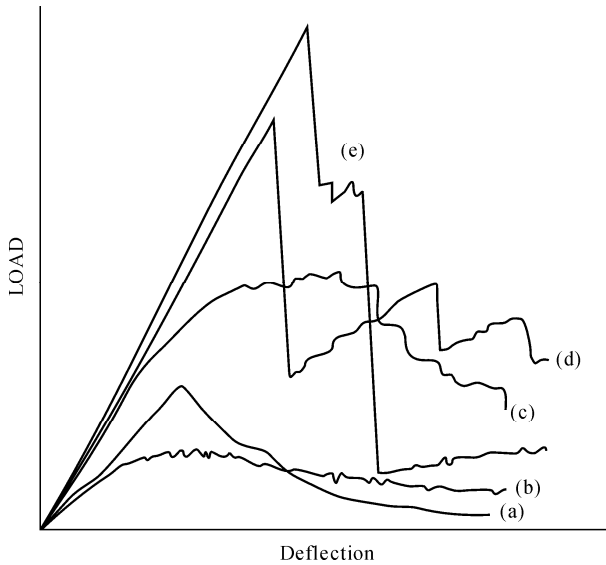


Fig. 4.24. SEM micrographs of a fractured surface. (a) Fracture surface of 60 wt% of PAN/BN annealed at 1,200 °C for 3 h; (b) Fracture surface of 20 wt% of pitch/BN annealed at 1,200 °C for 30 min



**Fig. 4.25.** SEM image of fracture side view for 60 wt% of pitch/BN composite annealed at 1,200 °C for 3 h



**Fig. 4.26.** Load-deflection curves from the three-point flexural test. (a) Densified 20 wt% of pitch/BN; (b) 20 wt% of pitch/BN; (c) 60 wt% of pitch/BN; (d) 60 wt% of PAN/BN; (e) densified 60 wt% of PAN/BN annealed at 1,200 °C for 3 h

In Fig. 4.27 is shown the dependence of the strength and modulus of these composites on heat treatment. Surprisingly, heating the pitch-based carbon fiber composites to 1,500 °C led to a further increase in mechanical properties, while the composites based on PAN-based carbon fiber decreased with higher heat treatment.<sup>[65]</sup> This decrease with the PAN-based fiber may be caused by the

elimination of nitrogen from the fiber. The strength of the composite based on pitch was somewhat higher than predicted from the rule of mixtures, suggesting some kind of beneficial role for the BN matrix. This is surprising considering the large mismatch in the coefficient of thermal expansion between the anisotropic fiber and the isotropic matrix.<sup>[66]</sup> On the other hand, samples which were reimpregnated to increase the density showed significantly improved flexural strength, with a failure strain of 1%.

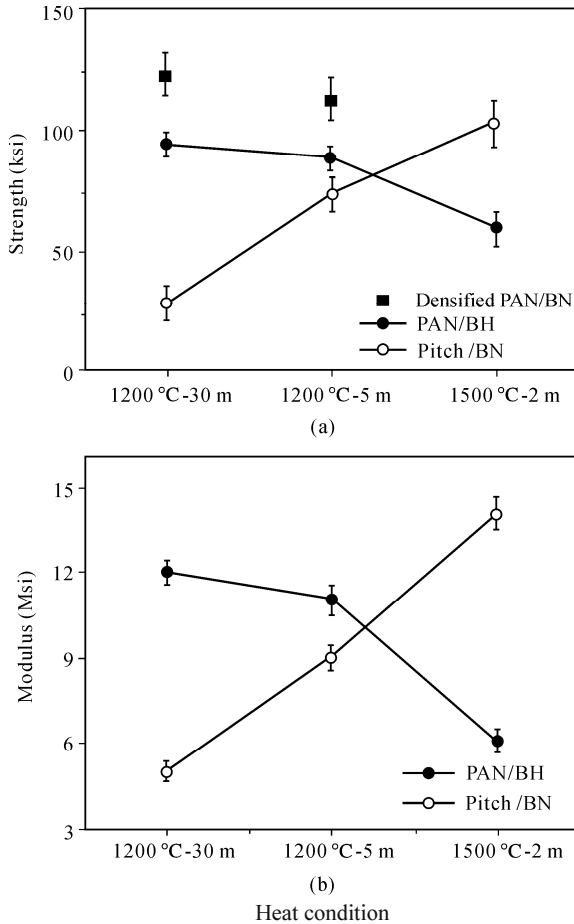


**Fig. 4.27.** Dependence of (a) flexural strength and (b) modulus of 60 wt% of pitch/BN and PAN/BN composites on heat treatment

One of the most exciting aspects of this study is that the boron nitride matrix does indeed provide oxidative protection for the carbon fibers up to 850 °C. As shown in Fig. 4.28, C/C composites begin to oxidize at 425 °C while the C/BN composite begins to oxidize at 850 °C. C/BN composites were not completely burned away even with isothermal oxidation at 1,000 °C for 20 min as shown in

Fig. 4.29. It is somewhat surprising that in the C/BN case we do not observe an initial weight increase at 850 °C consistent with conversion of BN to B<sub>2</sub>O<sub>3</sub>. Rather a rapid weight loss occurs suggesting that at these temperatures oxygen can readily diffuse through the B<sub>2</sub>O<sub>3</sub> to react with the carbon fibers. This area requires further study especially to evaluate the effect of Sic coatings.

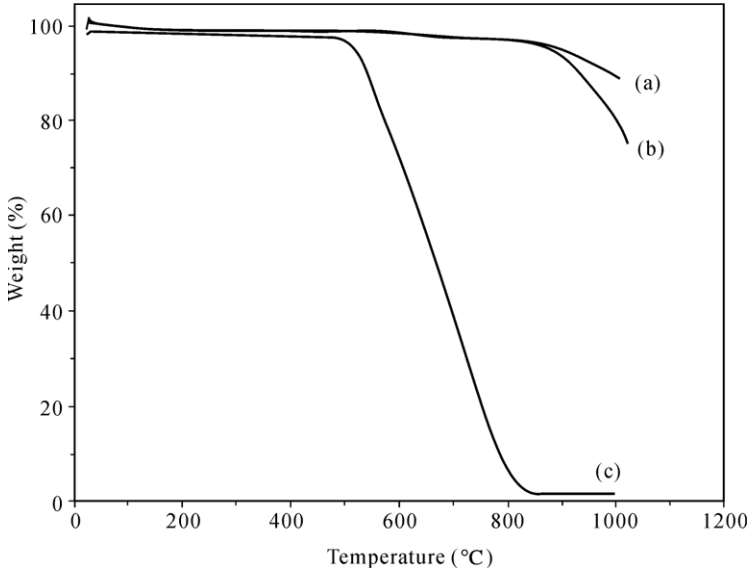


**Fig. 4.28.** Comparison of oxidation resistance among (a) pitch/BN, (b) PAN/BN composite annealed at 1,200 °C for 3 h and (c) C/C composite

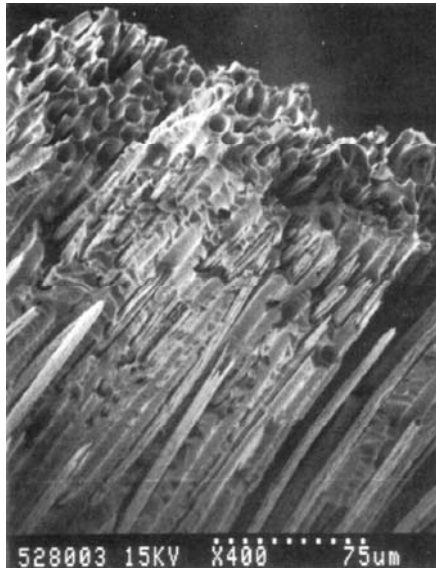


**Fig. 4.29.** Surface of C/BN composite after isothermal oxidation at 1,000 °C for 20 min

### 4.3.2 BN Film by Spin-Coating Process of a Polymeric Precursor

The interesting properties of BN are low density, high thermal conductivity, strength and high chemical inertness even at very high temperatures.<sup>[4,67]</sup> CVD processes are commonly used to produce BN films for buffer layering of multi-layer ceramic packaging, semiconductor applications and fiber coatings. These techniques in general involve high preparation costs owing to the relatively expensive equipment and the time-consuming procedures.<sup>[35,68]</sup> Recently, Chan et al. reported a quick and simple route for producing reliable spin-coated BN films ( $\sim 0.1 \mu\text{m}$ ) from polyborazine, although their study was limited to the feasibility of BN film formation and its composition.<sup>[69]</sup> However, properties of BN films obtained by the spin-coating method have not been subjected to a comparison with those produced by gas-phase techniques. Furthermore, it is important that such a comparison be made to establish the relative merits of the liquid-film-forming process as a suitable technique for the preparation of BN films for their various applications. In this section, thermal conductivities, hardness and dielectric constants of spin-coated BN films prepared on Si, SiO<sub>2</sub>/Si, and Pt/Ti/SiO<sub>2</sub>/Si substrates from a polyborazine precursor were characterized using the methods detailed herein.

#### 4.3.2.1 Preparation of Samples

Borazine (B<sub>3</sub>N<sub>3</sub>H<sub>6</sub>) used as a monomeric precursor, which provides the boron and nitrogen sources for BN synthesis, was prepared by the reaction between NaBH<sub>4</sub> and (NH<sub>4</sub>)<sub>2</sub>SO<sub>4</sub> using Sneddon's synthetic route.<sup>[30,70]</sup> Polyborazine films were produced using a spin-coating technique on 1 inch $\times$ 1 inch in substrates of Si(100), Si covered with *ca.* 0.1  $\mu\text{m}$  thick layer of SiO<sub>2</sub>, and Pt/Ti/SiO<sub>2</sub>/Si. The substrates were flooded with the solution and then spun at 2,500 r/min for 1 min using a spinner. The spin-coating process used the deposition method previously reported by Chan et al.<sup>[69]</sup> Samples were heated to 200 °C with a holding time of about 1 h to minimize mass loss, and subsequently heated at a rate of 5 °C $\cdot$ min<sup>-1</sup> to the operating temperature, which was in the range of 900 to 1,100 °C and maintained for *ca.* 2 h before being allowed to cool slowly to room temperature.<sup>[30]</sup> The pyrolysis of polyborazine films was conducted under reduced pressure.

#### 4.3.2.2 Characterization of Boron-Nitride Films

The film thickness measured after pyrolysis varied with polyborazine concentration and polymerization time for the borazine. The coating solution could be adjusted to obtain a desirable thickness as shown in Table 4.4. Therefore, the coating solutions were diluted to 20 wt% – 30 wt% in THF using polyborazine reacted for 50 h. Films in the thickness range of 0.15 – 2.0  $\mu\text{m}$  were mainly crack-free, but

those over 2  $\mu\text{m}$  cracked because of shrinkage associated with pyrolysis. It should be pointed out that films up to 2 mm thick were obtained by a single spin-coating process while other liquid-film forming processes such as sol-gel only gave a maximum thickness of  $\sim 0.1 \mu\text{m}$ . One other group recently reported that spin-coated SiC films of about 1  $\mu\text{m}$  thickness could be prepared from polycarbosilane precursor.<sup>[71]</sup>

**Table 4.4** Dependence of pyrolyzed BN film thickness on the polymerization period of borazine at 70 °C and on the polyborazine concentration in THF

	Polymerization period (h)	Concentration in THF (wt%)	Thickness ( $\mu\text{m}$ )
Polyborazine concentration: 20 wt%	50		0.4
	60		0.9
	65		1.2
	70		2.3
Polymerization period : 50 h		10	0.15
		20	0.4
		25	0.7
		30	0.9

Fig. 4.30 shows the morphology of BN films pyrolyzed at 900 °C under vacuum. The films on  $\text{SiO}_2/\text{Si}$  or Si substrates showed smooth surfaces and dense structures with no appreciable defects. Slight roughness of the film may be caused by the more vigorous evaporation of volatile species, such as  $\text{H}_2$  during the pyrolysis. However, it turned out that the hydrogen was not completely removed under the pyrolytic conditions, since N—H bonds with weak intensity were still present in the FT-IR spectra. It has been reported that CVD films prepared from a borazine precursor showed a stronger N—H intensity, depending on both deposition temperature and film thickness.<sup>[72]</sup>

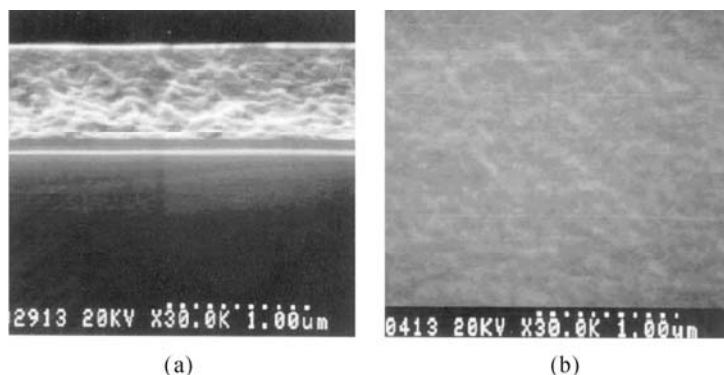


**Fig. 4.30.** SEM images of spin-coated BN films pyrolyzed at 900 °C on  $\text{SiO}_2/\text{Si}$  substrate under vacuum. (a) Cross section; (b) Surface morphology

For measuring the depth concentration, a polyborazine spin-coated film pyrolyzed at 900 °C ( $\sim 0.4 \mu\text{m}$ ) on  $\text{SiO}_2/\text{Si}$  substrate was examined by AES. In Fig. 4.31, the AES analysis revealed that the composition of the analyzed film was homogeneous with 0.75 N/B ratio which was similar to the RBS analysis reported by Chan et al. (0.73 N/B ratio) and consistent with the compositional results of RF magnetron sputtering and ion-beam-assisted deposition.<sup>[69,73]</sup> In addition, it appeared that a high oxygen level (25 wt%) in the BN film originated from the diffusion of oxygen out of the  $\text{SiO}_2$  buffer layer and high moisture sensitivity at the polymeric stage of the precursor.<sup>[74]</sup> To characterize the microstructure, a cross section of the prepared film was analyzed by high-resolution transmission electron spectroscopy (HR-TEM).

In Fig. 4.32 of the interfacial region, SAD (selected area diffraction) is shown with (002), (100), (101), (102), and (004) rings corresponding to the characteristic pattern of turbostratic BN.<sup>[75]</sup> The film showed locally preferred but discontinuous orientation in a direction parallel to the substrate surface, presumably because of the high shear rate generated by the spin-coating process. This orientation trend was due to the planar polyborazine with layers lying parallel to the planar substrate. It is noteworthy that BN crystallized epitaxially to the carbon fiber surfaces in the C/BN composite fabricated from the same polymer.<sup>[76]</sup> It has also been reported that the BN films prepared by gas-phase techniques mostly showed similar fringes due to stacking and orientation effects of the lamella structure.<sup>[77]</sup>

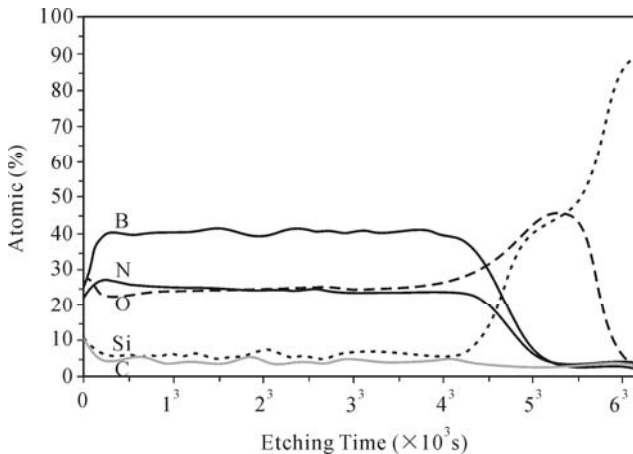


**Fig. 4.31.** AES depth profile of 0.2  $\mu\text{m}$  thick BN film vacuum-pyrolyzed on  $\text{SiO}_2/\text{Si}$  substrate at 900 °C (Adapted from Ref. 69. Copyright (1996), with permission from the MRS)

The hardness and the elastic modulus of the films on the Si substrate were measured by nanoindentation. The hardness and elastic modulus increased to 1.6 GPa and 50 GPa with increasing loading depths. It has been reported that the film strength strongly depends on the composition of the BN film, with a minimum hardness and modulus at  $\sim 0.7$  N/B ratio.<sup>[73]</sup> The thermal conductivity



of the boron-rich *h*-BN film with 0.9  $\mu\text{m}$  thickness was also measured at 296.5 K. The observed value was relatively low at  $134 \text{ W}\cdot\text{m}^{-1}\cdot\text{k}^{-1}$  as compared with 220 and  $250 \text{ W}\cdot\text{m}^{-1}\cdot\text{k}^{-1}$  for highly oriented pyrolytic BN and mixed cubic and hexagonal BN films prepared by CVD, respectively.<sup>[78]</sup> Dielectric properties of the 0.3 and 0.9  $\mu\text{m}$ -thick films, vacuum-pyrolyzed on a Pt/Ti/SiO<sub>2</sub>/Si substrate at 900 °C, were examined. The dielectric constant varied between 5 and 7 in the range of  $1\times 10^3$  to  $3\times 10^6$  Hz and the loss factor ( $\tan \theta$ ) was typically between 0.01 and 0.47. The dielectric constant is seen to decrease with decreased film thickness, which suggests the possibility of orientational effects. A similar phenomenon has been previously reported where the dielectric constants were 2.9 – 3.3 in a direction perpendicular to the basal planes of highly aligned BN and 5.0 – 5.2 in a direction parallel to these planes.<sup>[67]</sup> From the results of our measurements, a higher dielectric constant and a lower thermal conductivity could be due to the discontinuous orientation of the nanocrystallized BN and, in addition, the incomplete conversion to BN at 900 °C.

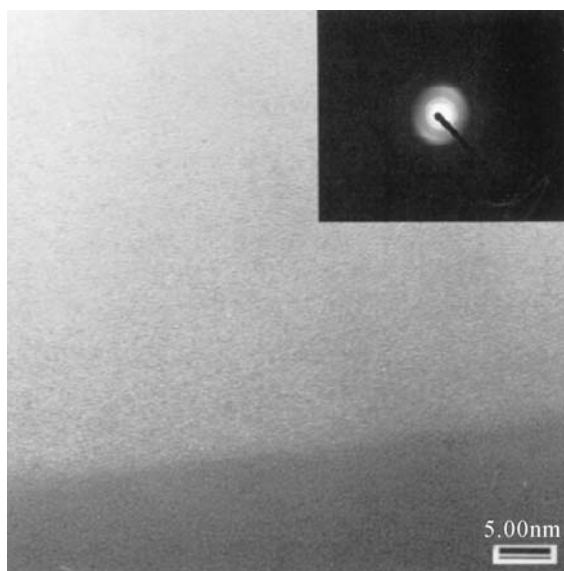


**Fig. 4.32.** High-resolution TE micrograph of interfacial BN film on SiO<sub>2</sub>/Si substrate vacuum-pyrolyzed at 900 °C (Adapted from Ref. 75. Copyright (1994), with permission from the ACS publications)

### 4.3.3 Fabrication of SiC-Based Ceramic Microstructures

A variety of synthetic approaches have been proposed for the development of porous materials with a high surface area and a controlled pore size distribution due to their many potential applications. There are many reports on the variety of

porous carbon, oxides, sulfides and metals prepared from various hard and soft templates. Moreover, porous ceramics with a different porous morphology and size distribution have been fabricated via different routes, such as burning out a polymeric sponge impregnated with a ceramic slurry, solid-state sintering, sol-gel process, replica of a polymer foam by impregnation and gel casting methods.<sup>[79]</sup> Because of the low oxidation resistance of carbon and the poor hydrothermal stability of porous silica materials, SiC with a high surface area has attracted considerable attention as a support material in the catalysis. Therefore, several attempts have been made to prepare various SiC macroporous and mesoporous materials. In this section, the recent development of porous SiC materials from templated preceramic polymers and the fabrication of small and complicated SiC ceramic features using near net shape processing techniques such as soft lithography will be explained.

#### 4.3.3.1 Macroporous SiC-Based Ceramics

There have been many studies on macroporous structures using oxide and carbon materials, but there are only a few on SiC for making macroporous structures. The macroporous structure has the advantage of a lower pressure drop than that of a mesoporous structure when used as a catalyst support. Table 4.5 shows the various precursors and templates used to prepare macroporous SiC, SiCN ceramic materials.<sup>[80]</sup> According to Quin et al., a SiC-based macropore structure ‘wood ceramic’ was prepared from carbonized wood powder and phenol resin via a direct reaction with Si powder.<sup>[81]</sup> However, the wood ceramic product showed disordered porosity with broad range of pore size distribution. Accordingly, the sacrificial template method has been used in the manufacture of highly ordered macroporous materials with a narrow pore size distribution. Firstly, homogeneous colloidal silica spheres ranging in size from 112 to 700 nm, as shown in Fig. 4.33, were gently precipitated to form a closed packed crystal template.<sup>[80a]</sup> A low molecular weight polymer precursor, polymethylsilane (PMS), was then infiltrated into the sacrificial colloidal silica crystalline arrays, which were subsequently etched with HF after pyrolysis in an argon atmosphere.<sup>[82]</sup> Pore sizes of approximately 84 – 658 nm and a BET surface of approximately 585 – 300 m<sup>2</sup>·g<sup>-1</sup> of the obtained porous products in proportion to the sizes of the sacrificial templates were obtained. It is believed that the high surface area was due to the interfacial area between the sphere and the infiltrated polymer as well as to the formation of micropores at the ceramic wall during pyrolysis. In addition, 3-dimensionally ordered macroporous (3DOM) SiCN ceramics were prepared using polysilazane and silica spheres, ranging in size from 112 to 650 nm.

**Table 4.5** Summarized characteristics of the macropores originating from different precursors and templates (Adapted from Ref. 80. Copyright (2002), with permission from the RSC Publishing)

Precursor	Template	Final product	Pore sizes and types	BET surface area ( $\text{m}^2 \cdot \text{g}^{-1}$ )
phenol resin, Si	Wood powder	SiC	10 – 30 $\mu\text{m}$ Irregular channel	–
PMS PCS	Monolayered silica sphere (500 nm)	SiC	340 nm Ordered macropore	150 – 172
PMS, polysilazane	macroporous carbon (150 – 1,000 nm)	SiC SiCN	135 – 896 nm Hollow spheres	50.8 – 5.0
PMS, PCS PMS&PCS hybrid	Alumina membrane (100 – 400 nm)	SiC	200 nm Hollowed tube	339
polysilazane	Silica spheres (112 – 650 nm)	SiCN	98 – 578 nm Ordered macropore	455.6 – 250.3

PMS: polymethylsilane; PCS: polycarbosilane

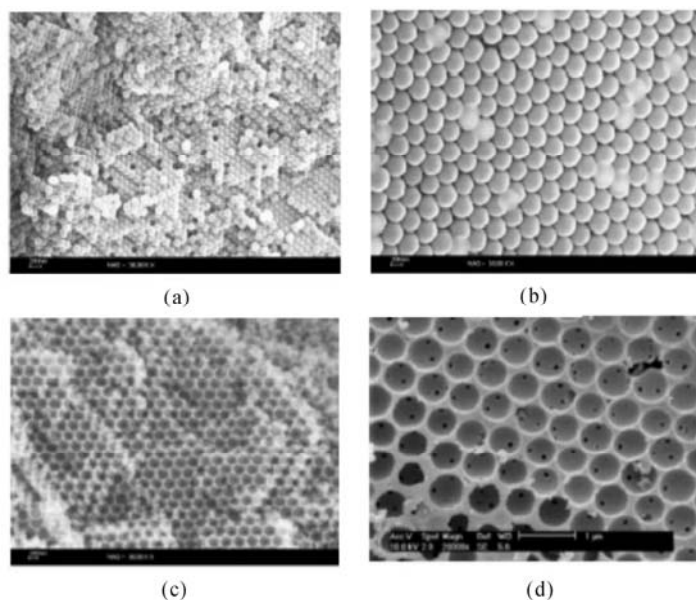


**Fig. 4.33.** SEM images of a representative silica template and porous SiC with different diameters. (a) 137 nm silica template; (b) 300 nm silica template; (c) Porous SiC from 192 nm template; (d) Porous SiC from 700 nm silica template (Adapted from Ref. 80. Copyright (2002), with permission from the RSC Publishing)

This was followed by a thermal curing step, pyrolysis at 1,250 °C in a N<sub>2</sub> atmosphere, and an identical etching process.<sup>[80d]</sup> Table 4.6 summarizes the comparative pore characteristics using silica sphere templates with various sizes (112 – 500 nm) and different types of preceramic polymers.

**Table 4.6** Summarized pore characteristics of various ordered macroporous ceramics obtained from silica sphere templates and different preceramic polymers

Precursor	SiO <sub>2</sub> sphere (nm)	BET Surface area (m <sup>2</sup> ·g <sup>-1</sup> )	Average pore size (nm)	Pore volume (cm <sup>3</sup> ·g <sup>-1</sup> )
SiC	112	584.6	4.9	0.68
	300	387.1	4.9	0.35
	500	362.3	2.8	0.26
SiCN	112	455.6	4.5	0.31
	243	367.7	3.8	0.23
	500	316.4	3.1	0.18
BCN	145	412.9	2.5	0.40
	300	387.1	2.4	0.35
	500	315.3	4.9	0.27
SiBCN	145	220.5	2.5	0.14
	300	211.7	3.9	0.12
	500	203.2	5.0	0.11
SiC-MoSi <sub>2</sub>	500	232.4	3 – 5	0.46

On the other hand, porous carbon was used as an alternative sacrificial template to prepare a different type of macroporous SiC ceramic with a unique morphology. A 3DOM carbon template was prepared by infiltrating sugar or phenolic resin into a closed and packed silica sphere assembly, followed by an oxidation or curing step and subsequent carbonization at 900 °C.<sup>[80b]</sup> The 3DOM carbon, as a sacrificial template, was gently infiltrated by low molecular weight preceramic polymers. In order to obtain the hollow nanosphere assembly, a polymeric precursor diluted to 25 mass% in THF was used to induce polymer adsorption on the inner wall of the carbon template during solvent evaporation. The carbon-precursor composites were cured at 160 °C for 6 h, and then pyrolyzed at 1,250 °C. Finally, the carbon was oxidized at 650 °C in air atmosphere to obtain an interconnected SiC sphere assembly, as shown in Fig. 4.34(a). The TEM image (Fig. 4.34(b)) clearly shows a regular ordered array of hollow spheres with dense shells.<sup>[80c]</sup> It should be noted that a hollow nanosphere with an empty core and inter-connections might have applications in capsules for drug delivery systems (DDS), pigment stabilizers in paints, photonic materials, chemical and biological sensors and catalysts.<sup>[83]</sup> On the other hand, an ordered assembly of SiCN ceramic spheres with filled cores was produced when low viscous polysilazane with no dilution was inserted into a carbon template, as shown in the SEM and TEM image in Fig. 4.34(c) and Fig. 4.34(d), respectively.<sup>[80c]</sup> The filled SiCN sphere

nanostructures with diameters ranging from 142 to 944 nm were proportional to the initial pore sizes of the sacrificial carbon templates used (approx. 150 – 1,000 nm).

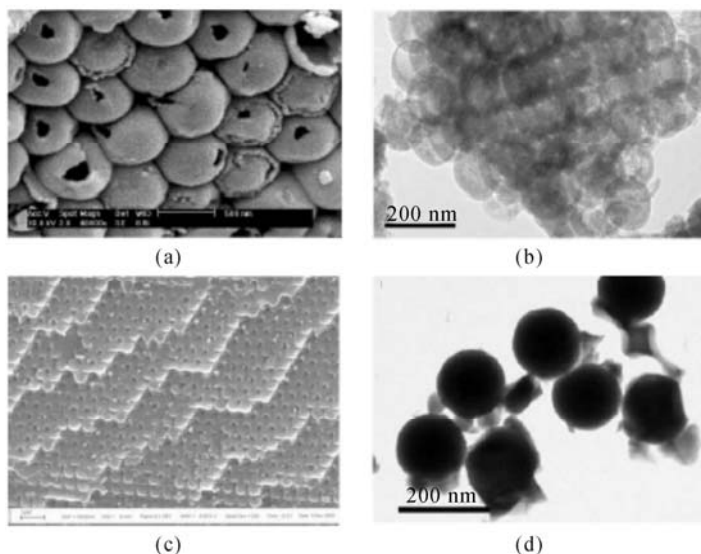


**Fig. 4.34.** Three representative SEM (a) and TEM (b) images of 500 nm and 135 nm hollow SiC sphere assemblies, and SEM (c) and TEM (d) images of 613 nm and 142 nm filled SiCN sphere assemblies, respectively (Adapted from Ref. 80c. Copyright (2005), with permission from the AIP)

#### 4.3.3.2 Mesoporous SiC-Based Ceramics

Since mesoporous silicates (M41S) were first discovered in the early 1990s, many efforts have been devoted to producing various mesostructure materials including mesoporous carbon CMK-*i*, oxides and metal. The use of a hard sacrificial template for the replication of nanoscale structures using a direct-templating process has sparked excellent contributions in this field. According to this strategy, some disordered mesoporous SiC materials were originally prepared using gas-phase infiltration techniques. For example, Ledoux et al. prepared high surface area SiC by a reaction between SiO vapor and active charcoal at temperatures ranging from 1,200 to 1,500 °C, which is known as the shape-memory synthesis method.<sup>[84]</sup> Parmentier et al. synthesized mesoporous SiC with a surface area of 120 m<sup>2</sup>·g<sup>-1</sup> via a carbothermal reduction reaction between mesoporous MCM-48 silica with pyrolytic carbon filled using chemical vapor infiltration (CVI) with propylene as the carbon precursor at temperatures ranging from 1,250 to 1,450 °C.<sup>[85]</sup> Krawiec et al. produced disordered mesoporous SiC with a high surface area (508 m<sup>2</sup>·g<sup>-1</sup>) using a CVI process involving the introduction of a gaseous SiC precursor, dimethyldichlorosilane, into nanoporous SBA-15 silica as summarized in Table 4.7.<sup>[86]</sup>

**Table 4.7** Comparative summary of the reported mesoporous SiC products and corresponding templates (Adapted from Ref. 86. Copyright (2004), with permission from the ACS Publications)

Template	Structure	SiC precursor	Space group	$S_{\text{BET}}$ ( $\text{m}^2 \cdot \text{g}^{-1}$ )
Active Charcoal	Disordered	SiO vapor, Carbon	-	~100
MCM-48	Disordered	C, SiO <sub>2</sub>	-	120
SBA-15	Disordered	DDS vapor	-	508
Silica nanosphere	Disordered	AHPCS	-	612
SBA-15	Ordered	AHPCS	<i>P6mm</i>	260
MCF	Ordered	AHPCS	Unknown	250
SBA-15	Ordered	PCS	<i>P6mm</i>	720
KIT-6	Ordered	PCS	<i>Ia3d</i>	590

DDS: dimethyldichlorosilane; AHPCS: allylhydridopolycarbosilane; PCS: polycarbosilane

The first report on the production of mesoporous SiC using a preceramic polymer showed a simple method, similar to that used to produce macroporous SiC, involving the infiltration of low viscous allylhydridopolycarbosilane (AHPCS, SP matrix) into a randomly packed silica colloidal sphere template with a diameter of 20 – 30 nm. The disordered mesoporous SiC exhibited an amorphous foam-like SiC with a high surface area of  $612 \text{ m}^2 \cdot \text{g}^{-1}$  and a total pore volume of  $0.81 \text{ cm}^3 \cdot \text{g}^{-1}$ .<sup>[87]</sup> The above mesoporous SiC showed no long-range order of porosity because the silica nanosphere used could not be precipitated into a closed-packed mode as a result of the strong electrostatic interactions between spheres. Because ordered mesoporous carbon such as CMK-3 has been formed from the use of ordered mesoporous silica templates, highly ordered mesoporous SiC materials were also prepared using trimethylsilylated SBA-15 and mesocellular siliceous foam as sacrificial hard templates. It is well known that SBA-15, which is prepared using triblock copolymers as a structure directing agent, is a two-dimensional hexagonally ordered mesoporous silica with channel-interconnecting micropores (6.5 nm) within the wall.<sup>[88]</sup> Mesocellular siliceous foam was also composed of uniform and large spherical cells ( $\sim 20$  nm) and connecting windows.<sup>[89]</sup> The diluted allylhydridopolycarbosilane was infiltrated into two types of surface modified nanoporous silica templates. The silica templates were subsequently etched off after pyrolysis at 1,000 °C in a nitrogen atmosphere to leave an ordered mesoporous structure. Both synthesized mesoporous SiC materials had a high BET surface area in the range of 250 – 260  $\text{m}^2 \cdot \text{g}^{-1}$  with a pore size of 3.4 – 3.6 nm. The mesoporous SiC materials prepared from the two types of silica templates were exact inverse replicas of their templates, as shown in Fig. 4.35.<sup>[90]</sup>

A similar study was also carried out by Zhao's group, as listed in Table 4.6. Highly ordered mesoporous SiC ceramics were synthesized via a one-step nanocasting process using commercial polycarbosilane as a precursor and mesoporous silica materials, SBA-15 and KIT-6, as hard templates.<sup>[91]</sup> The obtained mesoporous SiC ceramics with 12% excess of carbon were amorphous below 1,200 °C, and were composed of randomly oriented  $\beta$ -SiC crystallites after

being heated to 1,400 °C. These ordered mesoporous SiC ceramics had very high BET specific surface areas up to 720 m<sup>2</sup>·g<sup>-1</sup>, large pore volumes (about 0.8 cm<sup>3</sup>·g<sup>-1</sup>) and a narrow pore-size distribution (2.0 – 3.7 nm). It is expected that these novel techniques will be suitable for synthesizing many other types of ordered mesoporous non-oxide ceramic materials with interesting pore topologies.

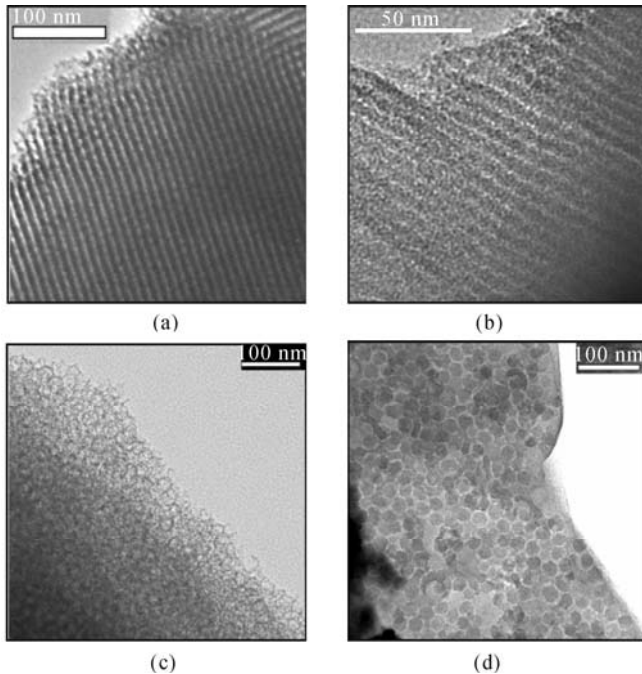


**Fig. 4.35.** TEM images of the mesoporous SiC products and corresponding nanoporous silica templates. (a) SBA-15 template; (b) SiC product from SBA-15; (c) MCF template; (d) SiC product from MCF (Adapted from Ref. 90. Copyright (2006), with permission from the ACS Publications)

It should be noted that the porous SiC products prepared from silica templates had severe oxygen contamination as a result of oxygen diffusion at the interface during the pyrolysis of the infiltrated preceramic polymers. The mesoporous SiC obtained had a surface severely contaminated with SiC<sub>x</sub>O<sub>y</sub> impurities, which is detrimental to high temperature applications. Therefore, it is desirable to use a sacrificial template containing no oxygen, which can avoid the formation of silicon oxycarbide species in the produced mesoporous SiC. In this context, it is worthy of note that mesoporous BN with a specific surface area of 540 m<sup>2</sup>·g<sup>-1</sup>, a mesoporous volume of 0.27 cm<sup>3</sup>·g<sup>-1</sup>, and a narrow pore size distribution (4.4 nm), was obtained from tri(methylamino)borazine as a precursor using CMK-3 mesoporous carbon as a non-oxygen template.<sup>[92]</sup> The mesoporous carbon template route appears to be a promising method for fabricating mesoporous ceramics from polymeric precursors. BN and BCN nanostructures were alternatively prepared via

a substitution reaction using carbon templates.<sup>[93]</sup>

#### 4.3.3.3 SiC Nanotube Structure

Since the discovery of carbon nanotubes in 1991, there has been considerable interest in fabricating one-dimensional tubular structures for their potential applications as electric devices and sensors.<sup>[94]</sup> Recently, many types of organic materials (peptide, polypyrrole) and inorganic materials (nitride, sulfide, oxide, carbide) have been considered in the preparation of tubular structures.<sup>[95]</sup> Different types of tubular SiC nanostructures were synthesized since Dai et al. first reported the preparation of SiC nanotubes using a shape memory synthesis method.<sup>[96]</sup> Most preparation methods are based on a carbothermal reduction and/or chemical vapor deposition, resulting in randomly dispersed nanotube structures. An alumina ( $\text{Al}_2\text{O}_3$ ) membrane with a 200 nm diameter was used as a template for making SiC arrays with a well-aligned tubular structure and a tailored diameter and wall thickness. A polymethylsilane solution was infiltrated into the dried alumina membrane at room temperature under a nitrogen atmosphere. After vacuum evaporation, the infiltrated polymer was cured and the polymer was heated to 1,250 °C in an argon atmosphere. Fig. 4.36 shows SEM and TEM images of a well-aligned array of SiC tubes with a uniform wall thickness of 35 nm. The SiC nanotube had an electrical resistance of  $6.9 \times 10^3$  to  $4.85 \times 10^3 \Omega\text{m}$  at temperatures ranging from 20 to 300 K with a negative temperature dependence, which is similar to a semiconductor-like behavior.<sup>[80c]</sup> In addition, Pt/Ru alloy nanoparticles could be selectively deposited on the inner wall of the nanotube. This material might be useful in the fields of heat-resistant nanodevices, fuel cells and nanofluidic devices.

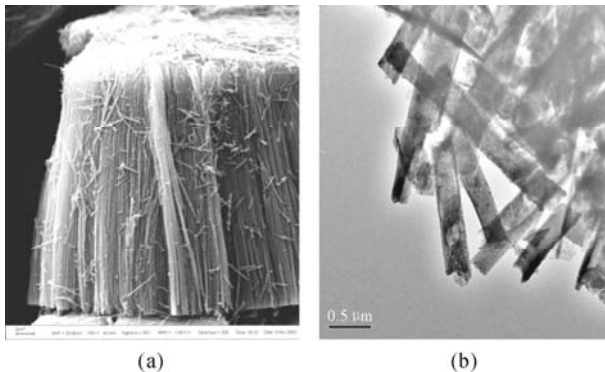


Fig. 4.36. Image of 100 nm tubular SiC derived from PMS. (a) SEM; (b) TEM

#### 4.3.3.4 Non-porous Ceramic Patterning via Soft Lithography

Most currently used MEMS devices in the silicon semiconductor industry are



fabricated using photolithography coupled with surface machining, which is the most common method for obtaining the micrometer sized surface features needed for sensors and actuators. Recently, the use of preceramic polymers offers a simple route for fabricating 2- or 3-dimensional ceramic microstructures using soft lithography techniques. SiC ceramic line patterns on the micron scale were fabricated using the MIMIC method, which involved filling PDMS channels that had been formed by conformal contact of a low viscosity preceramic polymer to a silicon wafer, followed by curing and pyrolysis at 800 °C.<sup>[97]</sup> Moreover, fine ceramic line patterns were also made by applying PDMS mold transfer techniques. Fig. 4.37 shows SEM images of the dense SiC ceramic line patterns, which were exact replicas of the CD and DVD relief structure as an economic master, respectively.<sup>[98]</sup> This suggests that preceramic polymers have excellent patterning processibility even on the nanoscale level by efficiently filling a narrow gap. This preliminary study highlights the feasibility of developing high temperature resistant nanoscale ceramic components, including MEMS, as well as NEMS (nano electromechanical system).

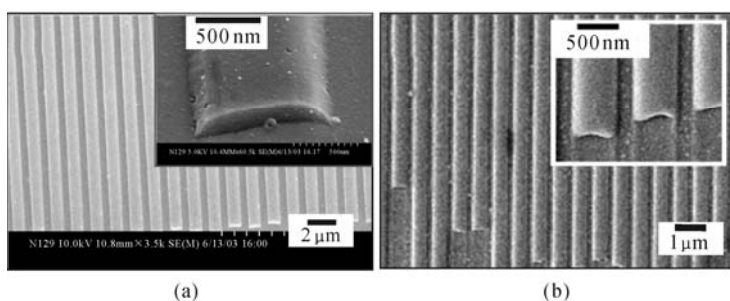


**Fig. 4.37.** SEM images of the imprinted SiC ceramic precursor pyrolyzed at 800 °C in an argon atmosphere. (a) SiC line pattern from CD master; (b) SiCN line pattern from DVD master (Adapted from Ref. 98. Copyright (2006), with permission from the TTP)

R. Raj group reported a very meaningful achievement by preparing SiCN ceramic MEMS devices using polyureamethylvinylsilazane as a precursor.<sup>[99]</sup> Even primitive types of high-temperature MEMS, i.e., electrostatic actuators, pressure transducers and combustion chambers were developed mainly using preceramic polymers that form SiCN ceramics by pyrolysis via a temperature or radiation induced transformation of a processable liquid state to an infusible solid state (cured polymer). This suggests that multi-layered ceramic MEMS can be fabricated by adding and curing successive layers of liquid polymers on top of each other using multi-level photopolymerization.

#### 4.3.3.5 Porous SiC-Based Ceramic Channels for Microreactor

The previous section summarized the preparation of tailored, highly uniform SiC

and SiCN porous structures by filling the void space in packed beds of silica spheres with a low viscous preceramic polymer. However, these products are a powdery type, which limits their utility in existing applications. Recently, we reported that the integration of templated preceramic polymers into a new fabrication technique such as soft lithography can produce useful products with new architectures. For the fabrication of tailored porous SiC and SiCN microchannels, as shown in Fig. 4.38, a PDMS mold was placed onto the flat surface of a silicon wafer, forming open channels at both ends. A solution-containing colloidal silica or polystyrene spheres was allowed to flow slowly into the channels from one end via capillary forces. The void space between the spheres was filled with the preceramic polymer through capillary action. After curing the preceramic polymer, the colloidal polystyrene spheres were decomposed during the early stages of the pyrolysis process, as shown in Fig. 4.39.<sup>[100]</sup> The inverted beaded SiC porous monoliths showed a crack-free ceramic microchannel replica with 150 – 200 nm of interconnecting windows for the 1 $\mu$ m spheres used. The pore size could be tailored independently according to the bead size, allowing for the easy integration of porous monoliths into a microreactor. The SiC ceramic monoliths obtained were used in the decomposition of ammonia after depositing a ruthenium catalyst via wet impregnation and calcinations. The efficient conversion of NH<sub>3</sub> to H<sub>2</sub> with increasing reaction temperature demonstrated its successful performance as a hydrogen reformer for fuel cells, as shown in Fig. 4.40. These novel porous materials show great promise for use in high temperature micro-reactors, possibly for the on-demand reforming of higher hydrocarbons into hydrogen for portable power sources.

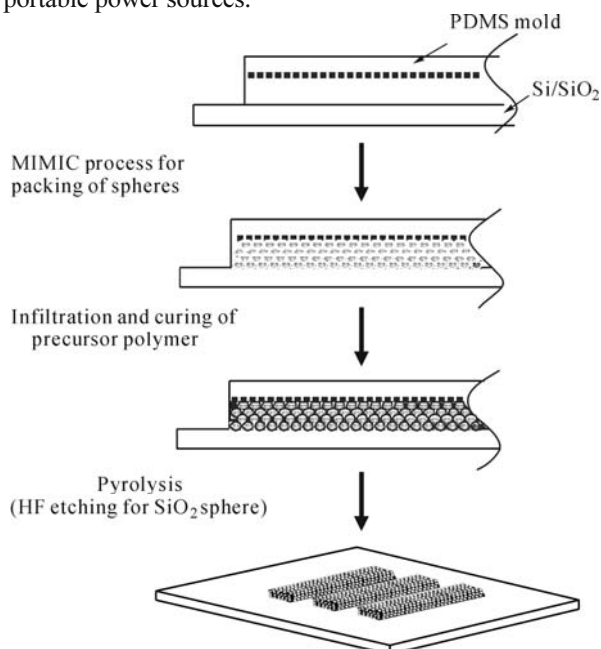


**Fig. 4.38.** Schematic diagram of the fabrication steps used to prepare microchannels

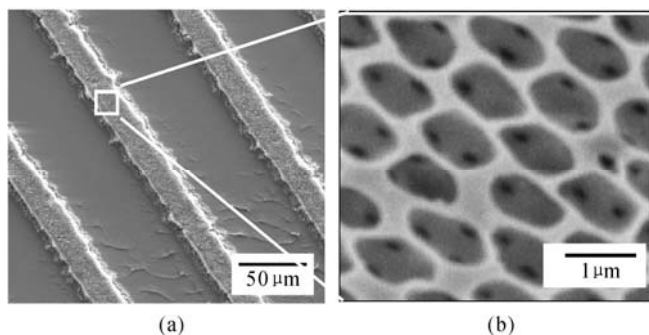


**Fig. 4.39.** SEM micrographs of (a) SiCN microchannel replica and (b) its 3-dimensional interconnected pore structure containing 1  $\mu\text{m}$  pores formed by pyrolysis (Adapted from Ref. 100. Copyright (2005), with permission from Wiley)

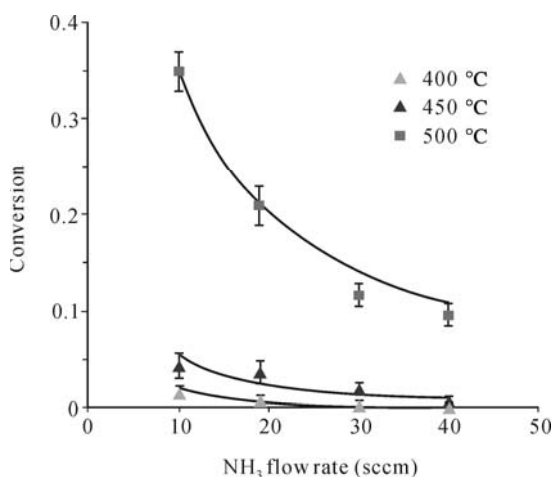


**Fig. 4.40.** Ammonia ( $\text{NH}_3$ ) conversion as a function of temperature for different flow rates measured at different temperatures

## 4.4 Summary

In this chapter, various hybrid preceramic polymers were easily prepared to form unique composite phases. Such ceramic composite phases can be excellent potential candidates for high-temperature functional applications. At first, a soluble gel polymeric precursor of SiC<sub>3</sub>N<sub>4</sub> ceramic was synthesized using a hydroboration reaction between borazine, a cyclic boron hydride, and organosilazane containing vinyl groups, in THF solvent without a catalyst or byproducts. Crystalline composite phases of SiC, Si<sub>3</sub>N<sub>4</sub> and BN were formed at 1,800 °C. A polymer derived Si-C-B-N ceramic product obtained at 1,000 – 1,400 °C exhibited excellent

oxidation resistance in air, and it was demonstrated in dense and smooth ceramic films. Secondly, SiC/MoSi<sub>2</sub> composites were prepared from mixtures of polymethylsilane (PMS) with Mo metal filler or MoCl<sub>5</sub> at 5 – 15 wt%. Pelletized specimens were formed by uniaxially pressing the Mo mixtures into a mold at temperatures up to 400 °C and 20 ksi, while films were obtained by spin-coating the MoCl<sub>5</sub> mixture solution on an Si wafer. Both types of samples were pyrolyzed at 900 – 1,400 °C to induce the transformation into the SiC/MoSi<sub>2</sub> composite phase. It appeared that the formation of the composite phases was initiated by reaction between excess Si, from the pyrolyzed polymer, and Mo metal or MoCl<sub>5</sub> at over 1,000 °C. The electrical conductivity of a pellet from the Mo mixture exhibited 10<sup>-2</sup> S·cm<sup>-1</sup> with positive temperature dependence, which is about 1/50 that of a commercial heating element. Thirdly, the Al-B-N composite phase was prepared by the pyrolysis of the mixed polyborazine, [B<sub>3</sub>N<sub>3</sub>H<sub>x</sub>]<sub>n</sub>, with Al bulk powder or AlCl<sub>3</sub>. The mixtures were spin-coated or pelletized at 400 °C using a uniaxial press, and then heat-treated to 1,400 °C in an inert atmosphere. It was also shown that the Al-B-N nanocomposite phase homogeneously consisted of AlN, BN and AlB<sub>2</sub>, presumably containing AlB<sub>12</sub>, at the nanoscale level when annealed at 1400 °C. Fourthly, a TiN/TiB<sub>2</sub>/BN nanocomposite has been prepared by pyrolyzing a hybrid precursor, which contained less oxidative titanium hydride dispersed in a viscous polyborazine polymer as a BN precursor. The hybrid precursor showed a step-wise pyrolytic conversion starting from the decomposition of TiH<sub>2</sub> to pure Ti at 450 °C without vulnerable oxidation. This process was followed by the formation of a non-oxide composite phase that was composed of Ti<sub>2</sub>N, TiN and TiB<sub>2</sub> in amorphous BN at 900 °C; finally, crystalline TiN and TiB<sub>2</sub> phases developed at 1,100 °C. When heated to 1,300 °C, the titanium-based phase adopted the nanocomposite state by what appeared to be an interdiffusion-type mechanism. Of particular interest is that a foam-like porous ceramic structure was formed by the liberation of H<sub>2</sub> from TiH<sub>2</sub>.

For some example of the applications of preceramic polymers, the C/BN composite was fabricated from polyborazine. Although C/C composites begin to oxidize at 425 °C, the C/BN composite exhibits no initial weight increase even at 850 °C, indicating that the BN matrix does indeed provide oxidative protection for the carbon fibers up to 850 °C. Alternatively, boron-rich BN films were prepared from a spin-coating process using polyborazine precursor on Si substrates and subsequent vacuum pyrolysis at 900 °C. The spin-coated films up to 2 μm thick converted turbostratic BN characteristics with an N/B ratio of 0.75 and a locally preferred orientation. It is important that such a comparison with the CVD process for the preparation of BN films be made to establish the relative merits of the liquid film-forming process for their varied applications. Finally, several ceramic nano- and micro-structures with a high degree of order were also fabricated by nanocasting of preceramic polymers into the sacrificial templates. Macroporous and mesoporous SiC ceramic structures have been fabricated using various templates including a packed silica sphere assembly, a porous carbon template, nanoporous silica structures. In addition, SiC nanotubes were also obtained from an alumina membrane as a template. These structures were generally produced by

a series of infiltration, curing and pyrolysis, chemical or oxidative etching steps. In particular, the porous channel monolith shows great promise for use in high temperature micro-reactors such as a hydrogen reformer from ammonia.

As written in this chapter, ceramic composites originating from inorganic polymers are promising candidates for use in the specialized chemical industry with high mechanical strength and chemical inertness in harsh conditions. By optimization of their synthesis route, curing and pyrolysis conditions, their application will be expanded widely into the field of Lab-On-a-Chip.

## References

- [1] (a) Madou, M. J. *Fundamentals of Microfabrication - The Science of Miniaturization*, 2nd ed. CRC Press, Boca Raton, 2002. (b) Nguyen, N. T., Wereley, S. T. *Fundamentals and Applications of Microfluidics*. Artech House, Boston, 2002. (c) Liew, L., Bright, V. M., Raj, R. *Sensor Actuat. A*, 2003, 104: 246.
- [2] (a) Xia, Y., Whitesides, G. M. *Annu. Rev. Mater. Sci.*, 1998, 28: 153. (b) Kim, E., Xia, Y., Whitesides, G. M. *J. Am. Chem. Soc.*, 1996, 118: 5722.
- [3] (a) Bill, J., Aldinger, F. *Adv. Mater.*, 1995, 7: 775. (b) Ruwisch, L. M., Dürichen, P., Riedel, R. *Polyhedron.*, 2000, 19: 323.
- [4] Weimer, W. *Carbide, Nitride and Boride Materials Synthesis and Processing*, Chapman & Hall, London, UK, 1997.
- [5] Paine, R. T., Sneddon, L. G. *Chemtech.*, 1994, 24: 29. (b) Yajima, S., Okamura, K., Hayashi, J. Omori, M. *J. Am. Ceram. Soc.*, 1976, 58: 324.
- [6] Kim, D. P., Economy, J., *Chem. Mater.*, 1993, 5: 1216.
- [7] Kho, J. G., Moon, K. T., Nouet, G., Ruterana, P., Kim, D. P. *Thin Solid Films*, 2001, 389: 78.
- [8] Sermen, J., Loop, J. G. *Ceram. Eng. Sci. Prod.*, 1991, 12: 1967.
- [9] (a) Baldus, H. B., Jansen, M., Wagner, O. *Key. Eng. Mater.*, 1994, 75: 89. (b) Riedel, R., Kienzle, A., Dressler, W., Ruwisch, L. M., Bill, J., Aldinger, F. *Nature*, 1996, 382: 796.
- [10] Takamizawa, M., Kobayashi, T., Hayashida, A., Takeda, Y. U.S. Patent, 4, 604, 367 (1986).
- [11] (a) Seyferth, D., Plenio, H. *J. Am. Ceram. Soc.*, 1990, 73: 2131. (b) Seyferth, D., Plenio, H., Rees, W. S., Büchner, K. *Frontiers of Organosilicon Chemistry*, Bassindale, A. R., Gaspar, P. P., Eds. Royal Society of Chemistry, Cambridge, 1991.
- [12] (a) Su, K., Remsen, E. E., Zank, G. A., Sneddon, L. G. *Chem. Mater.*, 1993, 5: 547. (b) Su, K., Remsen, E. E., Zank, G. A., Sneddon, L. G. *Polym. Prepr (Am. Chem. Soc., Div. Polym. Chem.)*, 1993, 34: 334. (c) Wideman, T., Su, K., Remsen, E. E., Zank, G. A., Sneddon, L. G. *Chem. Mater.*, 1995, 7: 2203. (d) Fazen, P. J., Remsen, E. E., Beck, J. S., Carroll, P. J., McGhie, A.

- R., Sneddon, L. G. *Chem. Mater.*, 1995, 7: 1942. (e) Wideman, T., Su, K., Remsen, E. E., Zank, G. A., Sneddon, L. G. *Mater. Res. Soc. Symp. Proc.*, 1996, 410: 185. (f) Wideman, T., Cortez, E., Remsen, E. E., Zank, G. A., Carroll, P. J., Sneddon, L. G. *Chem. Mater.*, 1997, 9: 2218.
- [13] Fazen, P. J., Sneddon, L. G. *Organometallics*, 1994, 13: 2867.
- [14] Schuhmacher, J., Berger, F., Weinmann, M., Bill, J., Aldinger, F., Müller, K. *Appl. Organometal. Chem.*, 2001, 15: 809.
- [15] Volger, K. W., Kroke, E., Gervais, C., Saito, T., Babonneau, F., Riedel, R., Iwamoto, Y., Hirayama, T. *Chem. Mater.*, 2003, 15: 755.
- [16] Weinmann, M., Kamphowe, T. W., Schuhmacher, J., Müller, K., Aldinger, F. *Chem. Mater.*, 2000, 12: 2112.
- [17] Weinmann, M., Kamphowe, T. W., Fischer, P., Aldinger, F. *Organomet. Chem.*, 1999, 583: 115.
- [18] (a) Gérardin, C., Taulelle, F., Bahloul, D. J. *Mater. Chem.*, 1997, 7: 117. (b) Gérardin, C., Taulelle, F., Livage, J. *Chem. Phys.*, 1992, 89: 461.
- [19] Jones, R., Myers, J. K. *Organomet. Chem.*, 1972, 34: C9.
- [20] Schuhmacher, J., Weinmann, M., Bill, J., Aldinger, F., Müller, K. *Chem. Mater.*, 1998, 10: 3913.
- [21] Schmidt, W. R., Narsavage-Heald, D. M., Jones, D. M., Marchetti, P. S., Raker, D., Maciel, G. E. *Chem. Mater.*, 1999, 11: 1455.
- [22] Schiavon, M. A., Sorary, G. D., Yoshiyda, I. V. P. *J. Non-Crystalline Solids*, 2002, 304: 76.
- [23] Kortobi, Y. E., Shihi, H., Legrand, A. P., Musset, E., Herlin, N., Cauchetier, M. *Colloid. Surface*, 1996, A115: 319.
- [24] Narula, C. K. *Ceramic Precursor Technology and Its Applications*. Marcel Dekker, New York, 1995.
- [25] (a) Rushkin, I. L., Shen, Q., Lehman, S. E., Interrante, L. V. *Macromolecules*, 1997, 30: 3141. (b) Ayache, J., Bonnamy, S., Bourrat, X., Oberlin, A., Bacque, E., Pillot, J. P. *J. Mater. Sci. Lett.*, 1998, 7: 885.
- [26] Greil, P. *J. Am. Ceram. Soc.*, 1995, 78: 835.
- [27] Petrovic, J. J., Vasudevan, A. K. *Mater. Sci. Eng.*, 1999, A261: 1.
- [28] Yamada, K., Kamiya, N. *Mater. Sci. Eng.*, 1999, A261: 270.
- [29] Mu, Y., Laine, R. M., Harrod, J. F. *Appl. Organomet. Chem.*, 1994, 8: 95.
- [30] Moon, K. T., Min, D. S., Kim, D. P. *Bull. Kor. Chem. Soc.*, 1998, 19: 222.
- [31] Kim, D. P., Min, D. S., and Kho, J. G. *J. Mater. Sci. Lett.*, 2000, 19: 303.
- [32] Kim, D. P. *Mat. Res. Bull.*, 2001, 36: 2497.
- [33] Lee, J. I., Hecht, N. L., Mah, T. J. *Am. Ceram. Soc.*, 1998, 81: 421.
- [34] (a) Krishnarao, R. V., Ramarao, V. V., Mahajan, Y. R. *J. Mater. Res.*, 1997, 12: 3322. (b) Aldrich, D. J., Jones, K. M., Govidrajan S., Moore, J. J., Ohno, T. R. *J. Am. Ceram. Soc.*, 1998, 81: 1471. (c) Wei, W. C., Lee, J. S. *J. Eur. Ceram. Soc.*, 1998, 18: 509.
- [35] Paine, R. T., Narula, C. K. *Chem. Rev.*, 1990, 90: 73.
- [36] (a) Arnell, R. D., Colligon, J. S., Minnebaev, K. F., Yurasova, V. E. *Vacuum*, 1996, 47: 425. (b) Losbichler, P., Mitterer, C., Gibson, P. N., Gissler, W., Hofer, F., Warbichler, P. *Surf. Coat. Technol.*, 1997, 94: 297. (c) Hammer, P.,

- Steiner, A., Villa, R., Baker, M., Gibson, P. N., Haupt, J., Gissler, W. *Surf. Coat. Technol.*, 1994, 68: 194.
- [37] Su, K., Nowakowski, M., Bonnell, D., Sneddon, L. G. *Chem. Mater.*, 1992, 4: 1139.
- [38] Kim, D. J., Hong, L. Y., Kim, D. P. *J. Ind. Eng. Chem.*, 2004, 10: 821.
- [39] Zhang, G. J. *J. Chin. Ceram. Soc.*, 1993, 21: 182.
- [40] Millet, P., Hwang, T. J. *Mater. Sci.*, 1996, 31: 351.
- [41] Dou, D., Ketchum, D. R., Hamilton, E. J., Florian, P. A., Vermillion, K. E., Gradinetti, P. J., Shore, S. G. *Chem. Mater.*, 1996, 8: 2839.
- [42] Riedel, R. *Adv. Mater.*, 1994, 6: 549.
- [43] Bae, D. S., Han, K. S., Choi, S. H. *J. Korean Ceram. Soc.*, 1996, 33: 524.
- [44] Rice, R. W. *Bull. Am. Ceram. Soc.*, 1983, 62: 889.
- [45] Dhas, N. A., Gedanken, A. *Chem. Mater.*, 1997, 9: 3144.
- [46] Wade, T., Park, J., Garza, E. G., Ross, C. B., Smith, D. M., Crooks, R. M. *J. Am. Chem. Soc.*, 1992, 114: 9457.
- [47] Deppisch, C., Liu, G., Hall, A., Xu, Y., Zangvil, A., Shang, J. K., Economy, J. *J. Mater. Res.*, 1998, 3: 3485.
- [48] Rebholz, C., Schneider, J. M., Voevodin, A. A., Steinebrunner, J., Charitidis, C., Thetidis, S. Logo, Leyland, A., Matthews, A. *Surf. Coat. Technol.*, 1999, 113: 126.
- [49] Vippola, M., Keranen, J., Zou, X., Hovmoller, S., Lepisto, T., Mantyla, T. *J. Am. Ceram. Soc.*, 2000, 83: 1834.
- [50] Park, K. C., Park, K. W. *J. Kor. Ceram. Soc.*, 1981, 18: 192.
- [51] Morris, J. H., Perkins, P. G., Rose, A. E. A., Smith, W. E. In *Industrial Alumina Chemistry: The Chemistry and Binding Properties of Aluminum Phosphates* (ACS Monograph, American Chemical Society, Washington D.C., 1986.
- [52] (a) Arclanova, N. I., Bushgev, U. H., Kamalov, A. D., Kirillov, V. N., Pronin, B. F., Furchina, X. K., Chuirul, N. P., Chistiakov, A. M. RU Patent 2015948, 1978. (b) Bautista, F. M., Campelo, J. M. *Catal. Lett.*, 1995, 35: 143.
- [53] Morrison, R. T., Boyd, R. N. *Organic Chemistry*, Prentice Hall International Inc., New Jersey, 1992.
- [54] Kreidl, N. J., Weyl, W. A. *J. Am. Ceram. Soc.*, 1941, 24: 372.
- [55] Chiou, J. M., Chung, D. D. L. *J. Mater. Sci.*, 1993, 28: 1435.
- [56] (a) Buckley, J. D. *Am. Ceram. Soc. Bull.*, 1988, 67: 364. (b) Fitzer, E. *Carbon*, 1987, 25: 163.
- [57] Gee, S. M., Little, J. A. *J. Mater. Sci.*, 1991, 26: 1093.
- [58] Haggerty, J. S., Chuang, Y. M. *Ceram. Eng. Sci. Prod.*, 1990, 11: 757.
- [59] Fazen, P. J., Beck, J. S., Lynch, A. T., Remsen, E. E., Sneddon, L. G. *Chem. Mater.*, 1990, 2: 96.
- [60] (a) Mamantov, G., Margrave, J. L. *J. Inorg. Nucl. Chem.*, 1961, 20: 348. (b) Laubengayer, A. W., Moews, P. C., Porter, R. J. *Am. Chem. Soc.*, 1961, 83: 1337.
- [61] Hirano, S., Yogo, T., Asada, S., Naka, S. *J. Am. Ceram. Soc.*, 1989, 72: 66.
- [62] Lim, Y. S., Lee, B. I. *J. Mater. Sci.*, 1991, 26: 1039.

- [63] Carlsson, L. A., Pipes, R. B. *Experimental Characterization of Advanced Composite Materials*, Prentice Hall, Englewood Cliffs, NJ, 1987.
- [64] Marshall, D. B., Evans, A. G. *J. Am. Ceram. Soc.*, 1985, 68: 225.
- [65] Fitzer, E. *Carbon*, 1989, 27: 621.
- [66] Rice, R. W. *Ceram. Eng. Sci. Proc.*, 1981, 2: 661.
- [67] Coffèr, C. G. *Doctoral Thesis. University of Illinois, Urbana, IL*, 1995.
- [68] Arya, S. P. S., Amico, A. D. *Thin Solid Films*, 1988, 157: 267.
- [69] Chan, V. Z. H., Rothman, J. B., Palladino, P., Sneddon, L. G., Composto, R. J. *J. Mater. Res.*, 1996, 11: 373.
- [70] Wideman, T., Sneddon, L. G. *Inorg. Chem.*, 1995, 34: 1002.
- [71] Colombo, P., Paulson, T. E., Pantano, C. G. *J. Am. Ceram. Soc.*, 1997, 80: 2333.
- [72] (a) Matsuda, T. *J. Mater. Sci.*, 1989, 24, 2353. (b) Akkerman, Z. L., Kosinova, M. L., Fainer, N. I., Rumjantsev, Y. M., Ysoeva, N. P. *Thin Solid Films*, 1995, 260: 156.
- [73] Elena, M., Guzman, L., Calliari, L., Moro, L., Steiner, A., Miotello, A., Bonelli, M., Capelletti, R., Ossi, P. M. *Thin Solid Films*, 1994, 253: 78.
- [74] Coffèr, C. G. *Economy, J. Carbon*, 1995, 33: 389.
- [75] Kim, D. P., *Economy, J. Chem. Mater.*, 1994, 6: 395.
- [76] Kim, D. P., Coffèr, C. G., *Economy, J. J. Am. Ceram. Soc.*, 1995, 78: 1546.
- [77] Davis, R. F., Kester, D. J., Ailey, K. S. *Molecular Beam Epitaxy of Boron Nitride Thin Films and Their Analytical Characterization, in Chemical Vapor Deposition of Refractory Metals and Ceramics III. Materials Research Society Symposium Proceedings (Boston, M. A., November 1994)*. Gallois, B. M., Lee, W. Y., Pickering, M. A., Eds. *Materials Research Society: Pittsburgh, P. A.*, 1995, pp 139-149.
- [78] (a) Duclaux, L., Nysten, B., Issi, J. P. *Phys. Rev. B*, 1992, 46: 3362. (b) Sprague, J. L. *IEEE Trans. Compon. Hybrids, Manuf. Technol.*, 1990, 13: 390.
- [79] (a) Zhu, X., Jiang, D., Tan, S. *Mater. Res. Bull.*, 2002, 37: 541. (b) Kwon, S., Son, G., Suh, J., Kim, K. T. *J. Am. Ceram. Soc.*, 1994, 77: 3137. (c) Geis, S., Fricke, J., Löbmann, P. *J. Eur. Ceram. Soc.*, 2002, 22: 1155. (d) Peng, H. X., Fan, Z., Evans, J. R. G., Busfield, J. J. C. *J. Eur. Ceram. Soc.*, 2000, 20: 807. (e) Zhang, F. Z., Kato, T., Fuji, M., Takahashi, M. *J. Eur. Ceram. Soc.*, 2006, 26: 667.
- [80] (a) Sung, I. K., Yoon, S. B., Yu, J. S., Kim, D. P. *Chem. Comm.*, 2002, p 1480. (b) Wang, H., Yu, J. S., Li, X. D., Kim, D. P. *Chem. Comm.*, 2004, p 2352. (c) Wang, H., Li, X. D., Kim, T. S., Kim, D. P. *Applied Phy. Lett.*, 2005, 86: 1. (d) Wang, H., Zheng, S. Y., Li, X. D., Kim, D. P. *Micropor. Mesopor. Mat.*, 2005, 80: 357.
- [81] Quin, J., Wang, J., Jin, Z., Qiao, G. *Mat. Sci. Eng. A*, 2003, 358: 304.
- [82] Wang, H., Li, X. D., Yu, J. S., Kim, D. P. *J. Mat. Chem.*, 2004, 14: 1383.
- [83] Caruso, F., Shi, X., Caruso, R. A., Susha, A. *Adv. Mater.*, 2001, 13: 740.
- [84] Pham-Huu, C., Bouchy, C., Dintzer, T., Ehret, G., Estournes, M., Ledoux, M. J., *Appl. Catal. A*, 1999, 180: 385.



- [85] Parmentier, J., Patarin, J., Dentzer, J., Vix-Guterl, C. *Ceram. Inter.*, 2002, 28: 1.
- [86] Krawiec, P., Weidenthaler, C., Kaskel, S. *Chem. Mater.*, 2004, 16: 2869.
- [87] Park, K. H., Sung, I. K., Kim, D. P. *J. Mater. Chem.*, 2004, 14: 1.
- [88] Zhao, D. Y., Feng, J. L., Huo, Q. S., Melosh, N., Fredrickson, G. H., Chmelka, B. F., Stucky, G. D. *Sci.*, 1999, 279: 548.
- [89] Schmidt-Winkel, P., Lukens, W. W. Jr., Zhao, D. Y., Yang, P. D., Chmelka, B. F., Stucky, G. D. *J. Am. Chem. Soc.*, 1999, 121: 254.
- [90] Yan, J., Wang, A., Kim, D. P. *J. Phys. Chem. B*, 2006, 110: 5429.
- [91] Shi, Y. F., Meng, Y., Chen, D. H., Cheng, S. J., Chen, P., Yang, H. F., Wan, Y., Zhao, D. Y. *Adv. Funct. Mater.*, 2006, 16: 561.
- [92] Dibandjo, P., Bois, L., Chassagneux, F., Cornu, D., Letoffe, J. M., Toury, B., Babonneau, F., Miele, P. *Adv. Mat.*, 2005, 17: 571.
- [93] Vinu, A., Terrones, M., Golberg, D., Hishita, S., Ariga, K., Mori, T. *Chem. Mater.*, 2005, 17: 5887.
- [94] Iijima, S. *Nature*, 1991, 354: 56.
- [95] Wu, G., Zhang, L., Cheng, B., Xie, T., Yuan, X. *J. Am. Chem. Soc.*, 2004, 126: 5976.
- [96] (a) Dai, H., Wang, E. W., Lu, Y. Z., Fan, S. S., Lieber, C. M. *Nature*, 1995, 375: 769. (b) Keller, N., Pham-Huu, C., Ehret, G., Keller, V., Ledoux, M. J. *Carbon*, 2003, 41: 2132.
- [97] Hong, L. Y., Kim, D. P. *Key Eng. Mat.*, 2005, 287: 323.
- [98] Dat, Q., Pham, A. T., Kim, D. P. *Mat. Sci. Forum*, 2006, 774: 510.
- [99] (a) Liew, L., Liu, Y., Luo, R., Cross, T., An, L., Bright, V. M., Dunn, M. L., Daily, J. W., Raj, R. *Sensor Actuat. A*, 2002, 95: 120. (b) Liew, L., Zhang, W., Bright, V. M., An, L., Dunn, M. L., Raj, R. *Sensor Actuat. A*, 2001, 89: 64. (c) Shah, S. R., Raj, R. *J. Eur. Ceramic Soc.*, 2005, 25: 243.
- [100] Sung, I. K., Christian, M. M., Kim, D. P., Kenis, P. J. A. *Adv. Funct. Mater.*, 2005, 15: 1336.

---

# Chemical and Biological Sensors Based on Porous Silicon Nanomaterials

**Honglae Sohn\*, Seunghyun Jang**

Department of Chemistry, Chosun University, Gwangju 501-759, the Republic of Korea

Tel.: +82-62-230-7372, Fax: +82-62-230-7372

\*E-mail: hsohn@chosun.ac.kr

## 5.1 Introduction

The porous silicon (PSi) material, an electrochemical derivative of silicon, is a natural nano-structured material that can be prepared easily without much sophistication. The history of PSi research is quite remarkable. This material was accidentally discovered by Ulhir at Bell Labs, USA, in 1956<sup>[1]</sup>, followed by Turner<sup>[2]</sup> during a study on the electropolishing of silicon in hydrofluoric acid solution. After the discovery, only a small amount of interest in the field developed as a result of the poor understanding of the porous structure. In the 1970's, it was found that by thermal oxidation the porous structure could be easily transformed into silicon dioxide and used as an isolation dielectric material.<sup>[3,4]</sup> Further advances in electronic isolation technology by Japanese groups in the 1980's led to the development of full isolated porous oxidized silicon (FIPOS)<sup>[5]</sup> and the silicon-on-insulator (SOI)<sup>[6]</sup> process.

It was not until 1990, when L. T. Canham first reported efficient, tunable, room temperature luminescence in the visible range from PSi<sup>[7]</sup> that interest in the field grew exponentially. From this point on, a large number of academic and industrial researchers from all over the world began to study the PSi pore structure,<sup>[8,9]</sup> light emission mechanism,<sup>[10,11]</sup> surface chemistry,<sup>[12,13]</sup> and feasibility for optoelectronic applications.<sup>[14,15]</sup>

The many favorable characteristics and the vast interest in PSi have given

rise to a variety of new applications, such as light-emitting devices,<sup>[15]</sup> multilayer structure,<sup>[16]</sup> solar energy conversion,<sup>[17]</sup> chemical and biological sensors,<sup>[18-23]</sup> drug delivery application,<sup>[24]</sup> ultrasound generators,<sup>[25]</sup> microengineering,<sup>[26]</sup> astrophysics,<sup>[27]</sup> signal processing,<sup>[28]</sup> and nuclear science.<sup>[29]</sup> Due to these multifunctional applications of PSi, recently it has been proposed that it can be used as an educational vehicle for introducing nano-technology and inter-disciplinary materials science by eminent scientists in the field.<sup>[30]</sup>

## **5.2 Interferometric Sensors Based on Porous Silicon Nanomaterials**

We know that porous silicon (PSi) material, an electrochemical derivative of silicon, is a natural nano-structured material that can be prepared easily without much sophistication. In this section, we mainly talk about interferometric sensors based on porous silicon nanomaterials, including fabrication of porous silicon, chemical sensing applications of porous silicon and biological sensing applications of porous silicon.

### **5.2.1 Fabrication of Porous Silicon**

Porous silicon can be produced in many different ways. In this part, we will introduce seven topics dealing with the fabrication of porous silicon: the etching mechanism, electrochemical etching setup, anodization parameters, properties of porous silicon, stabilization of porous silicon, the multi-structure of porous silicon and encoding of porous silicon.

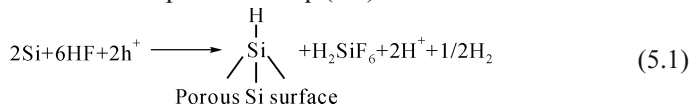
#### **5.2.1.1 Etching Mechanism**

PSi can be produced in many different ways. The most common way is the anode electrochemical etching of crystalline silicon in hydrofluoric acid solution. Although there is still some discussion regarding the surface dissolution mechanism, it is commonly agreed that holes are required for the dissolution mechanism to begin. The required holes are present in *p*-type crystalline silicon, but they need to be supplied for the dissolution process to be initiated in *n*-type crystalline silicon. Illumination is the most common way of supplying holes.

In normal anodization conditions, the surface of crystalline silicon is inert against hydrofluoric acid at low pH values. In 1991, Lehmann and Gösele<sup>[31]</sup> proposed a reaction model of the dissolution chemistry for the formation of PSi. This formation mechanism is illustrated in Fig. 5.1. This model is well accepted and proposes that when silicon is under anodic bias and holes reach the surface,

nucleophilic attack of the silicon-hydrogen bonds by fluorine ions occurs. This attack gives rise to a silicon-fluorine bond as shown in step (a) of Fig. 5.1. Once fluorine is attached, its large electronegativity polarizes the structure making it possible for another fluorine ion to bond to the surface. During this process, an electron is ejected into the electrode and hydrogen is released, as shown in step (b) of Fig. 5.1. At this point, the large polarization of two silicon-fluorine bonds lowers the electron density from the silicon-silicon bonds, making them weak and vulnerable to be attacked by hydrofluoric acid and water, as shown in steps (c) and (d) of Fig. 5.1. This results in the removal of a silicon atom in the form of the soluble ion  $\text{SiF}_6^{2-}$  and leaves the remaining silicon atoms hydrogen terminated, as shown in step (e) of Fig. 5.1.

The overall reaction can be expressed as Eq. (5.1).<sup>[32]</sup>



The removal of the silicon atom creates an atomic size dip or irregularity in the once atomically flat surface. The change in surface geometry concentrates the electric field lines on the irregularity site. PSi pore formation and side-wall dissolution will be inhibited by the depletion of holes. The depletion is caused by quantum confinement of charge carriers that result from the small dimensions of the pore walls. The quantum confinement increases the effective band-gap energy, making it more difficult for holes to enter the silicon region between the etched pores.<sup>[31]</sup>

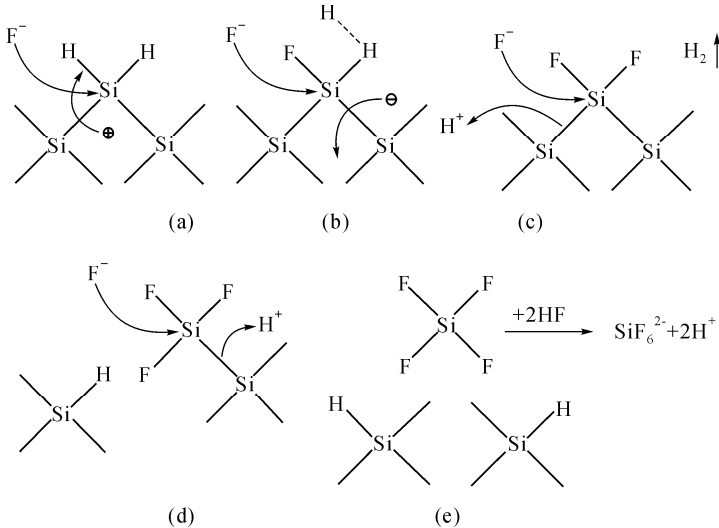


**Fig. 5.1.** Dissolution mechanism of crystalline silicon in hydrofluoric acid associated with the formation of porous silicon. Steps (a) through (e) represent the sequence of steps in the dissolution process (Redrawn from Ref. 31)

### 5.2.1.2 Electrochemical Etching Setup

Fig. 5.2 shows a picture of experimental setup to produce PSi. The anodization cell is made of Teflon, which is resistant to attack from the hydrofluoric acid electrolyte. The aluminum foil serves as the anode and it is sandwiched between the top and bottom parts of the Teflon cell. For a better contact, a platinum wire is placed against the silicon wafer, where leads can be connected. The cathode is a circular platinum wire that is submerged in the hydrofluoric acid electrolyte. The cathode is held in place, three wing nuts hold the entire anodization cell together during the electrochemical etching process. The hydrofluoric acid electrolyte is placed inside the top part of the Teflon cell. Enough electrolyte must be present to supply the required fluorine ions and to cover the platinum wire cathode. The top part of the Teflon cell has a circular window of area  $1.2 \text{ cm}^2$  which exposes the silicon to hydrofluoric acid and forms the PSi. The entire electrochemical process is carried out under constant current supplied by a computer controlled Keithley 2420 power sourcemeter.

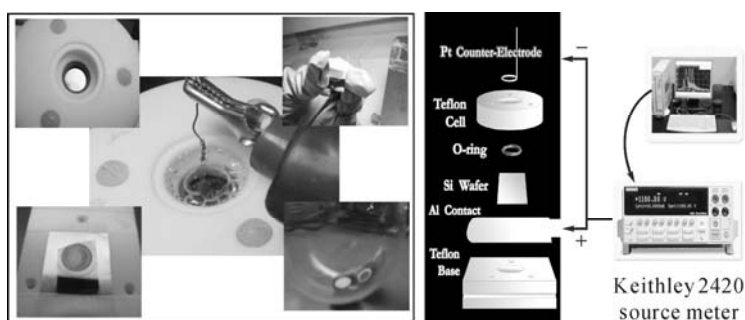


**Fig. 5.2.** Experimental setup to produce porous silicon. Anodization is conducted under a constant current with the hydrofluoric acid electrolyte in the top portion of the Teflon cell. The aluminum foil serves as the anode and the platinum wire as the cathode

### 5.2.1.3 Anodization Parameters

In this section, we mainly describe three main anodization parameters: current density, concentration of etching solution and anodization time.

#### 5.2.1.3.1 Current Density

PSi is produced by the anodic etching of crystalline silicon under a constant current density. By varying the anodization current density, some general trends with respect to porosity and the etching rate for a fixed hydrofluoric acid electrolyte concentration can be observed. As the current density increases, the silicon dissolution rate increases, resulting in higher porosity and etching rate. Fig. 5.3 shows linear dependence of PSi porosity and etching rate as a function of current density.

The size of pores formed during anodization is predominantly controlled by the current density,<sup>[33]</sup> with an increase in the pore size corresponding to an increase in the current density. At low current densities, the pores are randomly directed. When the current density gradually increased, the diameter of PSi pores increased. Fig. 5.4 shows that surface images of etched PSi with different current densities are measured by field emission-scanning electron microscope (FE-SEM, Hitachi-4800S).

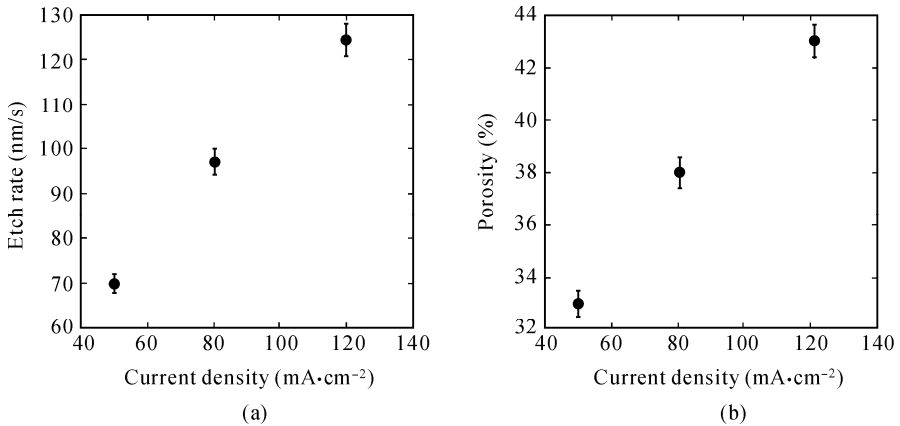


**Fig. 5.3.** PSi porosity (top) and etch-rate (bottom) dependence versus current density for *p*-type crystalline silicon substrate anodized in 35% hydrofluoric acid concentration electrolyte

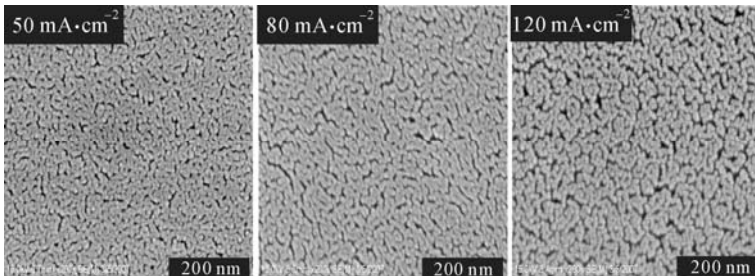


**Fig. 5.4.** Surface FE-SEM images of PSi with different current densities

#### 5.2.1.3.2 Concentration of Etching Solution and Anodization Time

The composition of HF solution determines the etching process. In the anodization of PSi, hydrofluoric acid with ethanol as an etchant solution is typically used. When aqueous HF solutions are used in the formation of PSi, the hydrogen bubbles evolved stick to the surface. To improve the surface uniformity in PSi, the hydrogen bubbles must be removed. The ethanol solution ensures the uniformity of the PSi by removing the hydrogen bubbles from the PSi surface and enables HF penetration into the pores.

Concentration of the hydrofluoric acid and etching time determine the PSi

porosity and thickness. For a given time, porosity is inversely proportional to the HF concentration.<sup>[34]</sup> Therefore, lowering the HF concentration increases the PSi porosity. Since PSi thickness is related to HF concentration, an increase in the HF concentration causes an increase in the PSi thickness, which in turn leads to a reduction of the PSi porosity for a fixed time.<sup>[35]</sup>

As the etching time is varied, the thickness and porosity of the PSi layers change. Fig. 5.5 shows the thickness of the PSi layer as a function of anodization time<sup>[36]</sup> for a *p*-type substrate that is etched at a constant current density of  $50 \text{ mA} \cdot \text{cm}^{-2}$  in a 35% hydrofluoric acid solution. Fig. 5.5 shows a linear relationship between the etching time and the thickness of the PSi layer.

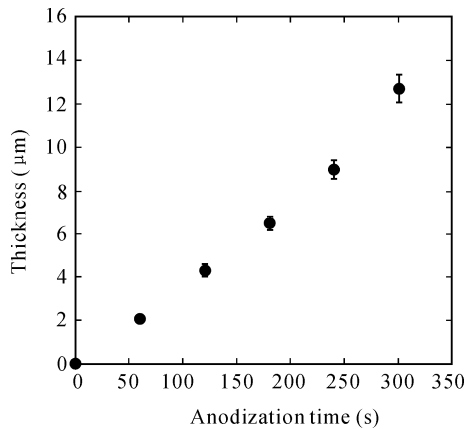


**Fig. 5.5.** Thickness of PSi with different anodization time for *p*-type crystalline silicon substrates anodized at a fixed current density of  $50 \text{ mA} \cdot \text{cm}^{-2}$  (Adapted from Ref. 36. Copyright (1995), with permission from Springer-Verlag)

### 5.2.1.4 Properties of Porous Silicon

Some properties, such as porosity, refractive index, thickness, pore diameter, multi-structures, and optical properties, strongly depend on the anodization process parameters. These parameters include HF concentration, current density, anodization time, and silicon wafer type and resistivity.

#### 5.2.1.4.1 Substrate Properties

Silicon substrates are identified by properties such as dopant type (i.e., *n*-type or *p*-type), substrate resistivity, dopant concentration, and substrate orientation. During anodization, dopant of the silicon substrate plays a significant role. Since holes ( $\text{h}^+$ ) are the most important element in the chemical reaction leading to the formation of PSi, the use of *p*-type wafer is the most popular. However, *n*-type wafer can be used with external illumination.

Substrate resistivity determines the achievable thickness of PSi. For example,

a very low resistivity wafer ( $<0.01 \text{ m}\Omega\cdot\text{cm}^{-2}$ ) is capable of producing thicker PSi compared to a wafer with a higher resistivity ( $>10 \text{ m}\Omega\cdot\text{cm}^{-2}$ ) under the same anodization conditions.

The morphology of the PSi can be grouped into four categories based on doping concentration:  $p$ ,  $p^+$ ,  $p^{++}$ ,  $n$ ,  $n^+$ , and  $n^{++}$ .<sup>[33]</sup> For  $p$ -type silicon wafer, the pore diameters and interpore spacing are very small (20 – 100 Å). As the dopant concentration increases, the pore diameter and spacing increase slightly (100 – 1000 Å). For  $n$ -type silicon, the pore diameters are considerably larger than those of the  $p$ -type substrate. Substrate orientation is also important in the structure of the PSi morphology. The main pore growth direction is essentially the same irrespective of the substrate orientation, dopant concentration or anodization conditions.<sup>[37-38]</sup>

#### 5.2.1.4.2 Porosity

The most important quantity, when characterizing a porous material, is the porosity which is defined as the ratio of the empty pore volume to the total volume. The porosity of a PSi can be calculated gravimetrically using Eq. (5.2).<sup>[39]</sup>

$$\text{Porosity (\%)} = \frac{m_1 - m_2}{m_1 - m_3} \quad (5.2)$$

Where  $m_1$  is the mass of the initial silicon wafer in grams,  $m_2$  is the mass of the silicon wafer after anodization in grams, and  $m_3$  is the mass of the silicon wafer after dissolution of the porous layer in grams. The dissolution of PSi is performed using a  $0.1 \text{ mol}\cdot\text{L}^{-1}$  aqueous solution of sodium hydroxide (NaOH). This gravimetric method is applicable in cases where the PSi layer is sufficiently thick ( $> 5 \mu\text{m}$ ). The difference in masses is larger than the amount of errors induced in the measurements. However, when the PSi layer is thin ( $< 200 \text{ nm}$ ), the mass difference is in the same order of magnitude as the error in measurements, and the porosity value obtained is unreliable.

#### 5.2.1.4.3 Thickness

The thickness of PSi can be determined using either non-destructive or destructive techniques. One non-destructive technique is the use of an ellipsometer which requires the extensive understanding of the refractive index. For the PSi samples, the index is difficult to determine since the porosity varies vertically with depth. There are two available destructive techniques that can be used with significant ease. One determines the approximate PSi thickness using Eq. (5.3).

$$\text{Thickness} = \frac{M_1 - M_3}{S \cdot d} \quad (5.3)$$

where  $M_1$  is the mass of the original silicon wafer,  $M_3$  is the wafer with anodized material removed,  $S$  is the area of the PSi sample, and  $d$  is the density of the silicon substrate. The second and more accurate technique uses a field emission



scanning electron microscope (FE-SEM) after scribing the PSi sample to visualize a cross sectional view. This technique can resolve the thickness of PSi to a few nanometers as well as provide additional information on the PSi morphology.

#### 5.2.1.4.4 Refractive Index

The refractive index is one of the important properties of PSi. This property controls the reflection and transmission of wave incident on the PSi-air interface. There are many approximations that predict the refractive index of PSi based on porosity.<sup>[40-41]</sup> However, none of them covers the entire porosity range with the same degree of high accuracy. The refractive index of PSi is calculated by using the Bruggeman approximation as described in Eq. (5.4).

$$(1-P) \frac{\epsilon_{\text{silicon}} + \epsilon_{\text{porous silicon}}}{\epsilon_{\text{silicon}} + 2\epsilon_{\text{porous silicon}}} + (P) \frac{\epsilon_{\text{air}} + \epsilon_{\text{porous silicon}}}{\epsilon_{\text{air}} + 2\epsilon_{\text{porous silicon}}} = 0 \quad (5.4)$$

where  $P$  is the porosity of porous silicon,  $\epsilon_{\text{silicon}}$  is the dielectric constant of silicon,  $\epsilon_{\text{air}}$  is the dielectric constant of air, and  $\epsilon_{\text{porous silicon}}$  is the dielectric constant of porous silicon.

#### 5.2.1.4.5 Optical Properties and Bench Setup

The optical properties of PSi are discussed in a wide spectral range from the infrared to the ultraviolet. PSi has two optical properties such as photoluminescence (PL) for  $n$ -type with external illumination (300 W tungsten lamp) and optical reflectivity (Fabry-Pérot fringe) for  $p$ -type, as shown in Fig. 5.6. The ability of PSi to emit and reflect in visible range is the most attractive property of the material. One explanation for the visible luminescence is based on the nanometer-size crystalline structure for PSi.<sup>[31,43-45]</sup>

The PL spectrum of PSi has been obtained with Ocean Optics LS-1 (blue LED). The optical reflectivity spectrum of PSi showing Fabry-Pérot fringe pattern has been measured by using a tungsten-halogen lamp and an Ocean Optics S2000 charge-coupled detector (CCD) spectrometer fitted with a fiber optic input. The reflected light collection end of the fiber optic is positioned at the focal plane of the optical microscope, as described in Fig. 5.7.

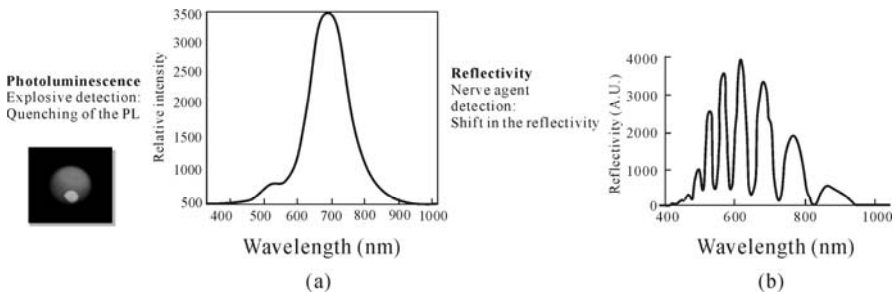


Fig. 5.6. Optical properties of porous silicon, photoluminescence (a) and reflectivity (b)

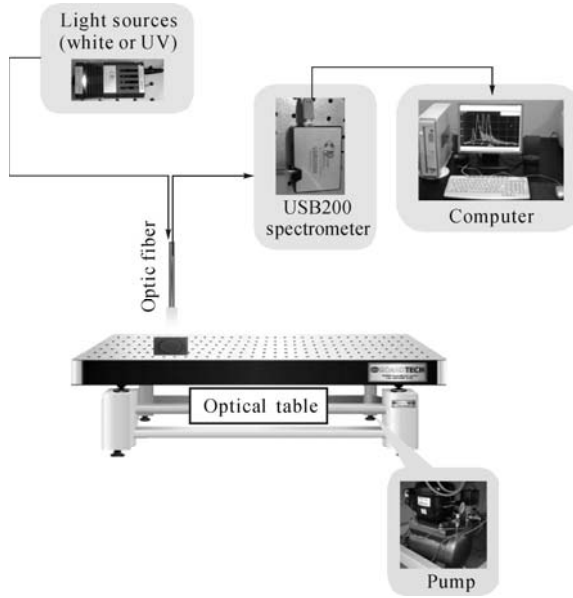


Fig. 5.7. Optical bench setup for obtaining the optical properties of porous silicon

### 5.2.1.5 Stabilization of Porous Silicon

In order to stabilize porous silicon, freshly etched PSi should require another two processes: oxidation and surface-derivatization.

#### 5.2.1.5.1 Oxidation

Freshly etched PSi is covered by hydrogen atoms that are covalently attached to the silicon surface. The attached hydrogen species are in the form of Si-H, Si-H<sub>2</sub>, and Si-H<sub>3</sub> and can be characterized by Fourier transform infrared spectroscopy (FT-IR). The hydrogen covered surface provides a good electron passivation layer. After the PSi is exposed to air, a slow oxidation of the surface takes place. Replacing the hydrogen by oxygen (oxidation) is one of the most common ways to passivate the electronic properties of PSi. Oxidation can occur by exposing the sample to air, anodic oxidation in a non-fluoride electrolyte,<sup>[46]</sup> chemical oxidation,<sup>[47]</sup> or by thermal oxidation.<sup>[48-51]</sup> Thermal oxidation is the most commonly used because it produces reproducible and controlled oxide layers of good quality. Thermal oxidation is the method used to passivate or oxidize the PSi structure. Thermal oxidation performed in a furnace at temperatures between 300 – 600 °C results in the loss of hydrogen and the production of PSi with poor electronic properties. The solution is to oxidize at higher temperatures resulting in better passivation, but running the risk of converting the PSi structure into silicon dioxide (SiO<sub>2</sub>). Fig. 5.8 shows an experimental setup for thermal oxidation and a comparison of FT-IR spectra between freshly etched PSi and thermally oxidized PSi.

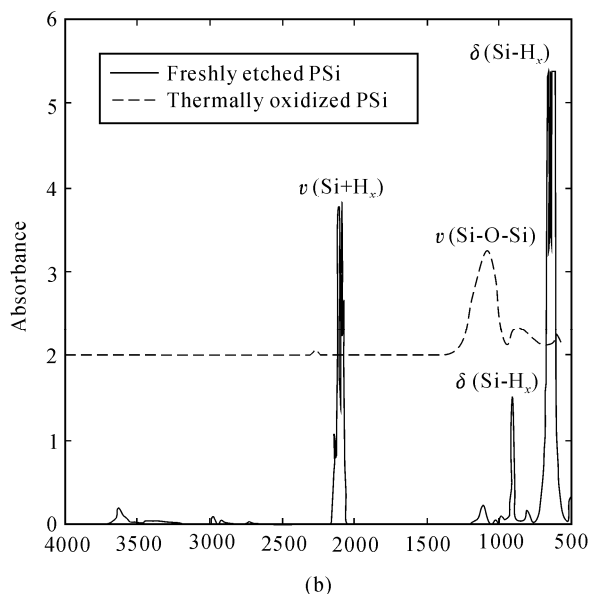
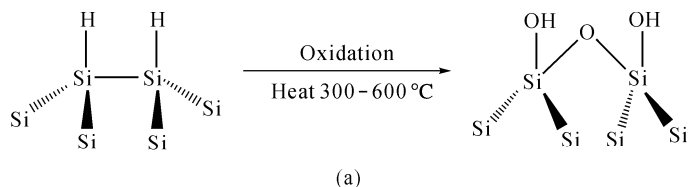


**Fig. 5.8.** Chemical scheme for the thermal oxidation (a) and comparison of FT-IR spectra between freshly etched PSi and thermally oxidized PSi (b) (Redrawn from Ref. 52)

#### 5.2.1.5.2 Surface-Derivatization (Hydrosilylation)

The hydride-terminated surfaces in general offer many advantages, including their excellent chemical homogeneity (>99% H termination) and strong FT-IR stretching modes ( $\sim 2100\text{ cm}^{-1}$ ) which can provide information as to surface flatness and makeup. The use of the Si-H terminated surface for many applications is precluded due to its propensity to oxidize, but it can be easily handled in air for a few minutes to tens of minutes without measurable degradation. Rapid and efficient preparation of Si-H hydride-terminated flat surfaces has been known for over 10 years.<sup>[53,54]</sup>

Hydrosilylation involves the insertion of an unsaturated bond onto a silicon-hydride group. Alkene and alkyne hydrosilylation on Si-H-terminated surfaces produce alkyl and alkenyl termination, respectively, as shown in Fig. 5.9. One of the hydrosilylation methods is thermally induced hydrosilylation. Thermally induced hydrosilylation of alkenes and alkynes has been applied to Si-H-terminated PSi surface.<sup>[55-57]</sup> It is initially reported that refluxing PSi for 18 – 20 h at 110 – 180 °C in an aliphatic alkyne or alkene yields alkyl monolayers.<sup>[55]</sup> Further investigation

of thermally induced hydrosilylation of 1-dodecene on PSi is examined, and derivatized surfaces are characterized by FT-IR as shown in Fig. 5.9.

Another hydrosilylation method is photochemical hydrosilylation using UV irradiation. UV irradiation can promote hydrosilylation of unsaturated compounds<sup>[58]</sup> due to homolytic cleavage of Si-H bonds. UV photoinduction, however, takes place at room temperature and thus a way to avoid thermal input that can be harmful to delicate or small features on a silicon chip.

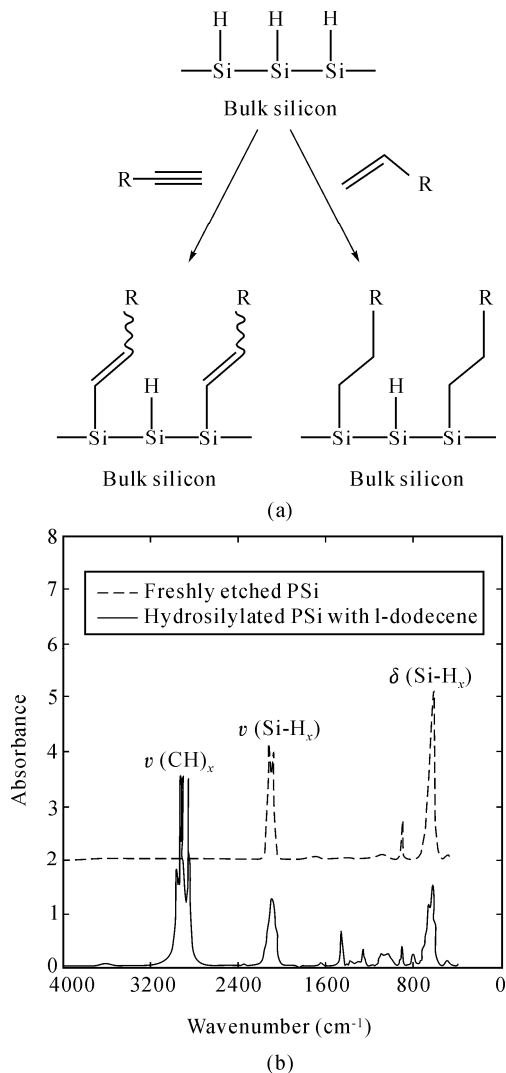


**Fig. 5.9.** Schematic hydrosilylation chemistry. Hydrosilylation involves the insertion of an unsaturated bond, alkyne or alkene, into the Si-H bond, resulting in Si-C bond formation and formation of alkenyl or alkyl groups, respectively (a) and comparison of FT-IR spectra between freshly etched PSi and hydrosilylated PSi with 1-dodecene (b) (Redrawn from Ref. 59)

### 5.2.1.6 Multi-Structures of Porous Silicon

First, we will introduce the theory of multilayer structures. Then, properties of multilayer structures will also be described.

#### 5.2.1.6.1 Theory of Multilayer Structures

The multilayer structures based on PSi open the door for a variety of new applications. Some of the possible applications of these structures are in the areas of interference filters,<sup>[60]</sup> waveguides,<sup>[61]</sup> photodiodes,<sup>[62]</sup> and microcavities.<sup>[63]</sup> For all these applications, strict control over the reflectance and transmission properties of the PSi multilayer is required.

The advantage of a dielectric multilayer structure is the multiple interference light beams undergo when reflected at each interface. A qualitative representation of this is described in Fig. 5.10, where interference from a single film is compared to a multilayer structure. The light beam is reflected at each interface between the two materials containing two different refractive indices. In a single layer (neglecting the multiple reflections of light between interfaces) the reflected light is composed of two reflectivity beams, one across the air-film interface and the other across the film-substrate interface (Fig. 5.10(a)). In the case of the multilayer structure, the reflected light is a combination of all the reflectivity beams at each of the interfaces (Fig. 5.10(b), 5 reflected beams are observed). By simply choosing the thickness and refractive index of each of the layers, it is possible to control the constructive and destructive interference of the light across a multilayer structure, which dictates its reflectivity spectrum.

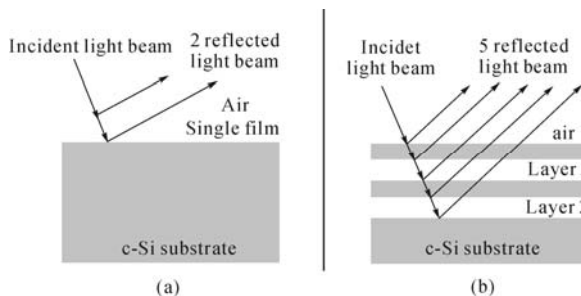


**Fig. 5.10.** Multiple interference of thin film structure. Representation of the reflection and transmission of light by a single (a) and a multilayer structure (b)

#### 5.2.1.6.2 Properties of Multilayer Structures

PSi multilayers consist of alternating layers of different refractive index. PSi multilayer structures are easily manufactured using a periodic current density square waveform for distributed Bragg reflectors (DBR)<sup>[64-68]</sup> and sinusoidal waveform for rugate<sup>[69-72]</sup> during the electrochemical etching process as described in Fig. 5.11. The difference in porosity profile, corresponding to a variation in current density, is attributed to a difference in refractive index.

DBR PSi exhibits a high reflectivity band with a Bragg wavelength  $\lambda_{\text{Bragg}}$ .

depending on the thickness of the layers ( $d_1, d_2$ ) and the corresponding refractive indices ( $n_1, n_2$ ). The  $m$ th order of the Bragg peak is given in Eq. (5.5).

$$m\lambda_{\text{Bragg}} = 2(d_1 n_1 + d_2 n_2) \tag{5.5}$$

Typical etch parameters for the DBR PSi structure involve using a periodic square-wave current between low and high current densities.

Rugate PSi has been successfully prepared using a periodic galvanostatic electrochemical etch of crystalline silicon by applying a sine wave current. The applied current density is modulated with a pseudo sine wave to generate a periodically varying porosity gradient. For the fabrication of rugate PSi, the waveform used involves a sine component, which is represented in Eq. (5.6).

$$Y = A \cdot \sin(k_t) + B \tag{5.6}$$

where  $Y$  represents a temporal sine wave of amplitude  $A$ , frequency  $k$ , time  $t$ , and an applied current density  $B$ . The position of the reflection band depends on the frequency.

Multistructured PSi, DBR or rugate, exhibit unique optical properties providing the reflection of a specific wavelength in the optical reflectivity spectrum. This reflective wavelength can be controlled by tuning of the many etching parameters and can appear anywhere in the visible range. Fig. 5.12 shows a demonstration for the fabrication of specific reflectors or filters in full color. Fig. 5.13 shows a cross-sectional SEM image of a PSi multilayer where the different layers present alternating porosity (refractive index) layers. The two parameters that govern the optical properties of the multilayers are the thickness and refractive index of the alternating layers, so control over these properties is critical. Other properties like interface roughness and depth homogeneity also affect the quality of the multilayer structures.

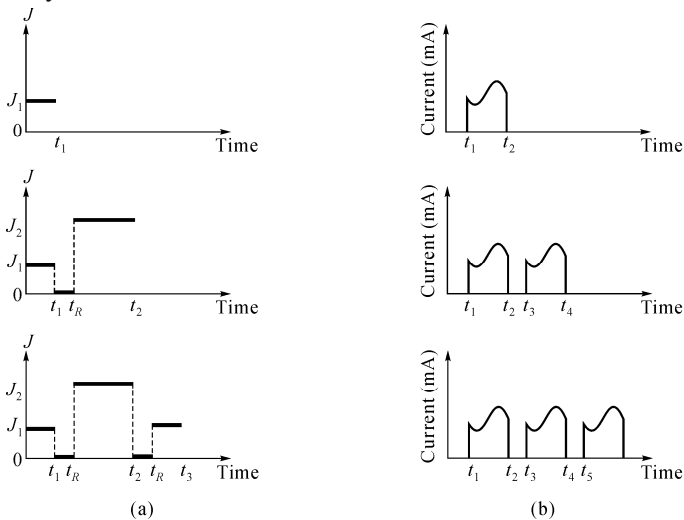


**Fig. 5.11.** Schematic pictures of the formation of PSi multilayer structures. By pulsing between two different current densities, two different porosity PSi layers can be formed (a) and step-functions used to approximate the sinusoidal variation of the refractive index (b)

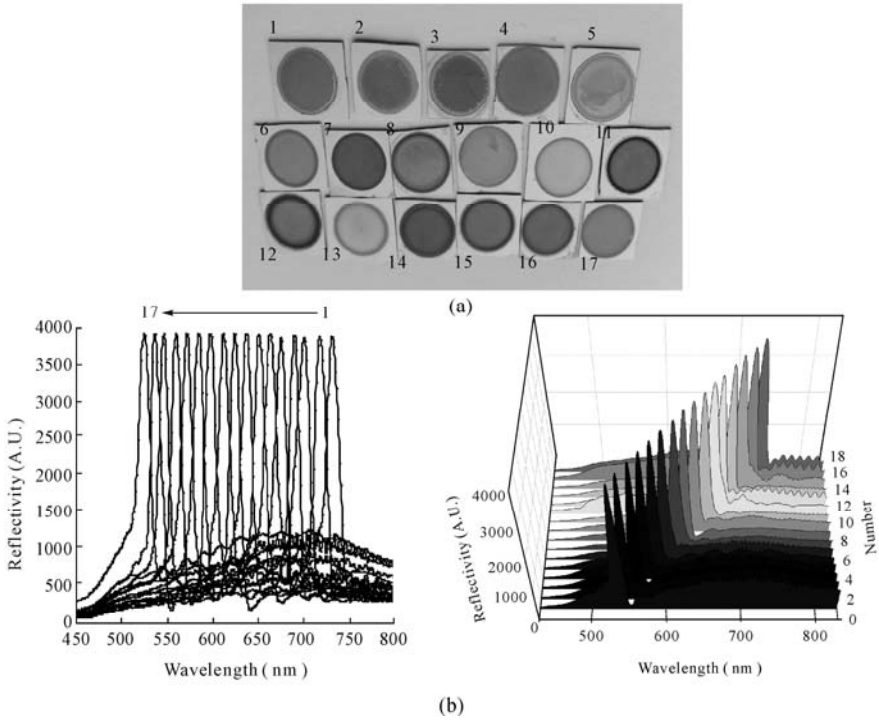


**Fig. 5.12.** Photo (a) and optical reflectivity spectra (b) of specific reflectors or filters anywhere in the visible range. This reflective wavelength can be controlled by tuning many etching parameters

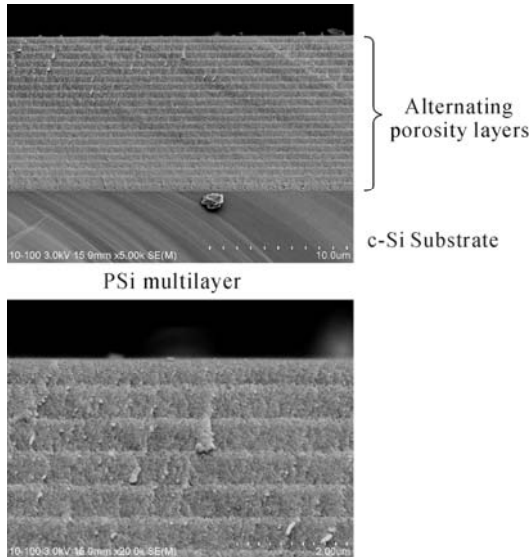


**Fig. 5.13.** Cross-sectional SEM images of PSi multilayer where the different layers present alternating porosity (refractive index) layers (Redrawn from Ref. 73-74)

### 5.2.1.7 Encodings of Porous Silicon

One of the most unique features for multilayer PSi is that its reflective spectral band is much narrower than the fluorescence spectrum obtained from an organic dye or core-shell quantum dot. Thus, more spectral lines can be placed in a narrower spectral window with the photonic structures. Rugate filters possess a sinusoidally varying porosity gradient in the direction perpendicular to the plane of the filter. The waveform used in the present work involves an individual sine component.

Strategies to encode multiple rugate structures have been investigated. Multiple rugate structures can be etched on a silicon wafer and placed in the same physical location, showing that many sharp spectral lines can be obtained in the optical reflectivity spectrum. Two methods are used to generate multiple rugate structures. First, a set of five sine components (Fig. 5.14(a)), combining each individual sine component, was used to create multiple rugate structures (Fig. 5.14(b)). Second, all of the individual sine components are added together to create the composite waveform shown in Fig. 5.14(c).

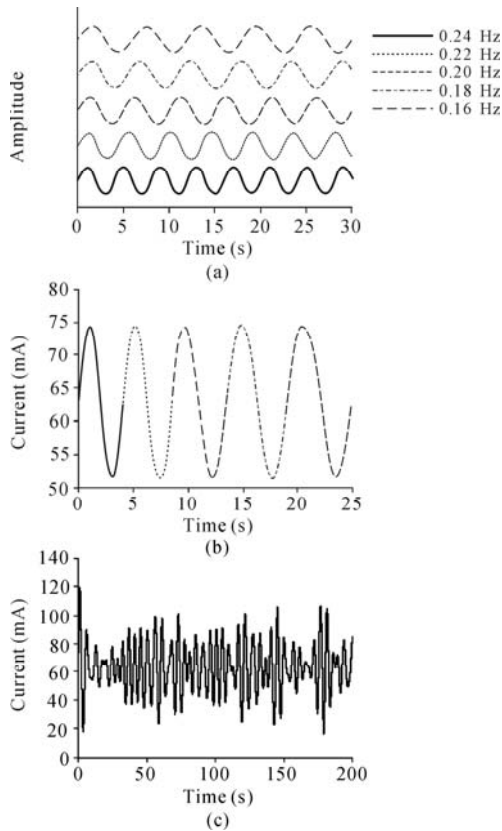


**Fig. 5.14.** Representation of the encoding method. (a) Five individual sine components; (b) A set of five consecutive sine components; (c) A composite waveform sum of five individual sine components (Redrawn from Ref. 75)



Eqs. (5.7) and (5.8), containing all the encoding information, can be converted to an analog current-time waveform for etching by using a computer-controlled digital galvanostat.

$$y_{\text{comp}} = (y_1, y_2, \dots, y_n) \quad (5.7)$$

$$y_{\text{comp}} = A_1 \sin(k_1 t) + A_2 \sin(k_2 t) + \dots + A_n \sin(k_n t) + B \quad (5.8)$$

A waveform containing five separate frequency components was investigated. The values of  $k_i$  for each of the sine components varied from 0.16 to 0.24 Hz, with a spacing of 0.02 Hz between each sine component. The values of  $A_i$  and  $B$  for every sine component were 11.55 and 63.05 mA, respectively. The reflectivity spectra of multiple rugate-structured PSi etched continuously with five separate periodicities using a former method were obtained and displayed five peaks as shown in Fig. 5.15 (a), but the rugate peaks were not placed in the same physical locations. Multiple rugate structures were successfully generated by using Eq. (5.8) and displayed five peaks as shown in Fig. 5.15 (b). The resulting rugate PSi film exhibited a porosity depth profile that related directly to the current-time profile used in the etching. Each of the main peaks in the optical reflectivity spectrum corresponded to one of the sine components of the composite waveform, indicating that the reflectivity spectrum represented the Fourier transform of the composite current-time waveform.

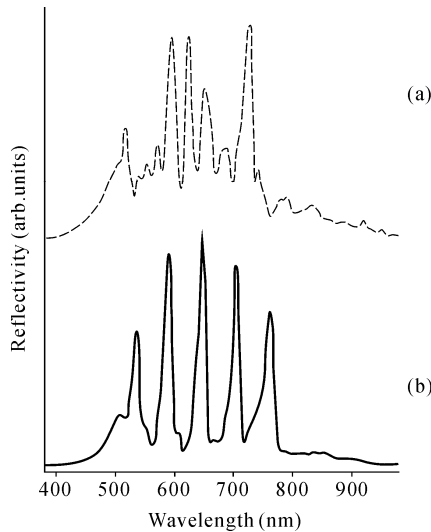


**Fig. 5.15.** Reflectivity spectra of multiple rugate porous silicon: (a) a set of five consecutive sine components and (b) a composite waveform sum of five individual sine components (Adapted from Ref. 75. Copyright (2007), with permission from the Korea Physical Society)

The reflectance spectra of five encoded PSi samples was obtained and showed five-bit encoding. The spectra shown in Fig. 5.16 are divided into five regions, and

the bit representation of each peak in the spectrum is superimposed over each peak. In the latter case, both the wavelengths and the amplitudes of the spectral peaks are controllable by changing the etching parameters and could be useful for encoding information. A complete deletion of a peak, shown in Fig. 5.16, was achieved and demonstrated the capability of this method for creating binary codes while the wavelengths and relative amplitudes of the remaining peaks were fixed. The presence or absence of a spectral line can be recognized as an on-state or an off-state, respectively.

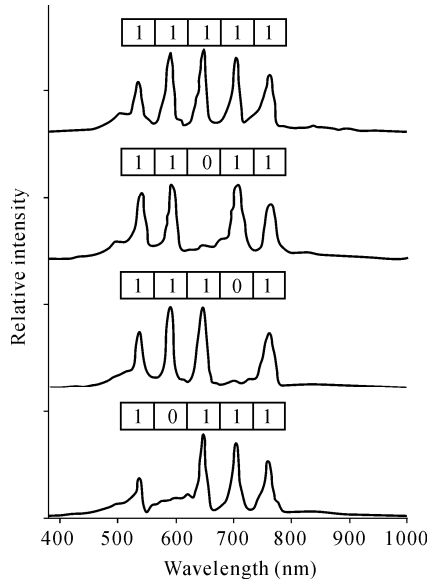


**Fig. 5.16.** Reflectance spectra of encoded PSi samples (Adapted from Ref. 75. Copyright (2007), with permission from the Korea physical Society)

## 5.2.2 Chemical Sensing Application of Porous Silicon

Porous silicon has wide applications in many areas. In this section, we only introduce some applications in chemical sensing.

### 5.2.2.1 Detection of Chemical Nerve Agent Gases

The nerve agent mimics such as diethylchlorophosphate (DCP), triethylphosphate (TEP), dimethylmethylphosphonate (DMMP), and diethylethylphosphonate (DEEP) are among the most toxic substances and are thus commonly used as chemical warfare agents (CWA) and pesticides. There is an urgent need for innovative analytical tools for the detection of CWA due to the toxicity of these compounds. Rapid detection of

sarin, soman, and nerve agents is currently of great interest. There are growing concerns about their use as chemical weapons for terrorists or for use in war (in May 1995, terrorists released sarin gas in the Tokyo subway, killing 12 and injuring 5,500 persons). A G-type nerve agent is lethal depending on both concentration and exposure time. The  $LC_{50}$  for sarin by inhalation of the vapor form is 100 milligrams of sarin per cubic meter of air for one minute.<sup>[76]</sup>

The main method currently used to detect nerve agents is based on a surface acoustic wave (SAW) device.<sup>[77-78]</sup> Other methods using enzymes,<sup>[79]</sup> single-walled carbon nanotubes,<sup>[80]</sup> metal oxides,<sup>[81]</sup> and organic polymers<sup>[82]</sup> have been recently reported. PSi is also an alternative method to detect chemical nerve agents.<sup>[83-84]</sup> Photonic crystals of PSi have been a topic of interest because of their unique properties, including surface area and convenient surface chemistry, as well as their optical signal transduction capability. These properties have led to their use in chemical and biological sensors,<sup>[19,85-87]</sup> biomaterials,<sup>[88]</sup> and optical devices.<sup>[89]</sup> Multi-structured rugate PSi has been recently investigated in terms of possible applications.<sup>[90-95]</sup> DBR (distributed Bragg reflectors) PSi exhibits unique optical properties providing the reflection of a specific wavelength in the optical reflectivity spectrum. DBR structured porous silicon, having the photonic structure of a Bragg filter, has been developed by applying a computer generated square current density waveform.<sup>[96]</sup> Electrochemical etching of single crystalline silicon can easily control the pore morphology, thickness, and porosity by appropriate adjustment of the preparation conditions.<sup>[97]</sup> Biological or chemical molecules can be detected based on changes in the spectral interference pattern.<sup>[19]</sup> Photonic crystals containing rugate structure result in a mirror with high reflectivity in a specific narrow spectral region and are prepared by applying a computer-generated pseudo-sinusoidal current waveform. Rugate filters possess a sinusoidally varying porosity gradient in the direction perpendicular to the plane of the filter. Multiple rugate-structured PSi showing many sharp independent reflection peaks has been also reported.<sup>[98]</sup>

All nerve agent mimics such as DCP, DMMP, DEEP, and TEP are commercially purchased from Sigma-Aldrich, Inc. and used without further purification. Optical reflectivity spectra of a multi-structured PSi interferometer have been measured by using a tungsten-halogen lamp, LED ( $\lambda_{em}=520, 590$  nm), and laser ( $\lambda_{em}=530$  nm) and an Ocean Optics S2000 CCD spectrometer fitted with a fiber optic input. The reflected light collection end of the fiber optic was positioned at the focal plane of the optical microscope. SEM images have been obtained by a cold field emission scanning electron microscope (FE-SEM).

DBR PSi samples were prepared by electrochemical etching of heavily doped  $p^{++}$ -type silicon wafers (boron doped, polished on the  $\langle 100 \rangle$  face, resistivity,  $0.8 - 1.2$   $m\Omega \cdot cm^{-2}$ ). The etching solution consists of a 3:1 volume mixture of aqueous 48% hydrofluoric acid and absolute ethanol. Galvanostatic etching was carried out in a teflon cell applying 20 cycles of a two-electrode configuration. DBR PSi has been prepared by using a square wave current between  $5$   $mA \cdot cm^{-2}$  for 90 s and  $50$   $mA \cdot cm^{-2}$  for 3 s for single reflectivity and  $10$   $mA \cdot cm^{-2}$  for 90 s and  $100$   $mA \cdot cm^{-2}$  for 3 s for double reflectivity. Encoded rugate PSi samples having three photonic

band gaps were also prepared by an identical process as described in procedure of DBR PSi sample. However, in the case of encoded rugate PSi, a composite waveform, the sum of three computer-generated pseudo-sinusoidal current waveforms varying between 51.5 and 74.6 mA·cm<sup>-2</sup> (100 s periodicity, 30 repeats) was applied as an anodization current. Each sine component varied from 0.42 to 0.30 Hz, with a spacing of 0.06 Hz between each sine component. The anodization current was supplied by a Keithley 2,420 high-precision constant current source which was controlled by a computer to allow the formation of PSi multilayers. To prevent the photogeneration of carriers, the anodization was performed in the dark. After formation, the samples were rinsed with absolute ethanol and dried with nitrogen gas.

Typical etch parameters for a DBR PSi structure involves using a periodic square wave current between low and high current densities. The dissolution times for a  $\lambda/4$  layer of Bragg structures are typically from 5 s to 90 s. Its reflection band has a narrow full-width at half maximum (FWHM) of 20 nm at 520 nm. DBR PSi with two reflection peaks has been obtained, when the current densities of a single DBR structure increase twice as shown in Fig. 5.17. The photonic feature of the latter DBR PSi exhibits high reflectivities at both 560 and 717 nm. The first and second reflection bands of DBR PSi have a FWHM of 15 and 20 nm, respectively. DBR PSi samples are placed in an exposure chamber fitted with an optical window.

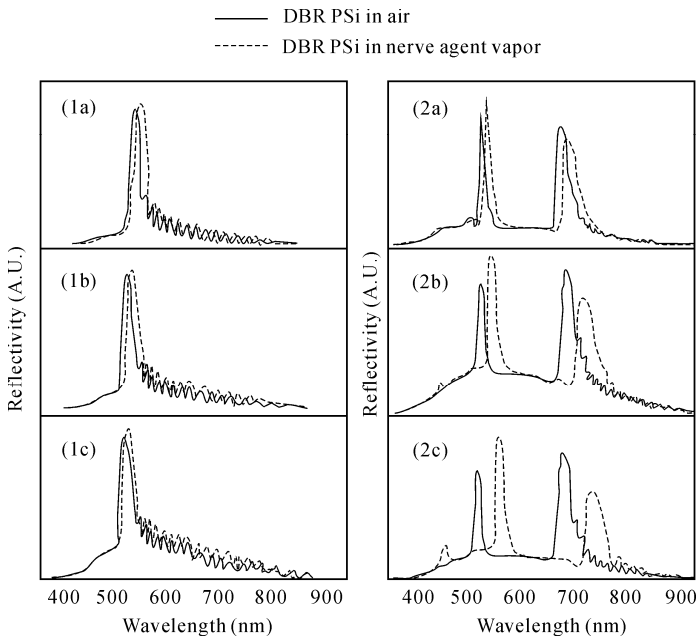


**Fig. 5.17.** Reflectivity spectra of DBR PSi samples. DBR PSi showing single or two reflection peaks recorded for 30 s using the tungsten-halogen lamp as a light source. A red-shift of reflectivity for single reflection DBR PSi, (1a) TEP, 25 nm, (1b) DMMP, 10 nm, (1c) DEEP, 10 nm and double reflection DBR PSi, (2a) TEP, 13 nm for the first DBR peak and 18 nm for the second DBR peak, (2b) DMMP: 22 nm and 32 nm, (2c) DEEP, 39 nm and 52 nm are observed (Adapted from Ref. 73. Copyright (2008), with permission from the Korea physical Society)

The samples are exposed to a flux of DMMP (partial pressure of 0.22 torr or  $290 \times 10^{-6}$ ) in air with a flow rate of  $5 \text{ L} \cdot \text{min}^{-1}$ . Fig. 5.18 shows reflectivity spectra of DBR PSi with one or two reflection bands, while exposing the detector to the nerve agent vapors. Reflection spectra from DBR PSi, with one reflection peak for the detection of the nerve agent, were recorded for 1 min under the exposure of vapor of each analyte. 25 nm (1a), 10 nm (1b), and 10 nm (1c) red-shift of reflectivity were observed for the air-saturated vapor of TEP ( $135 \times 10^{-6}$ ), DEEP ( $135 \times 10^{-6}$ ), and DMMP, respectively. DBR PSi with two reflection peaks has been also used and exposed to a flux of nerve agent vapors in identical conditions. Reflection spectra from DBR PSi with two reflection bands have been recorded for 30 s. Capillary condensation causes both reflection peaks to shift to longer wavelengths by 13 nm for the first DBR peak (shorter wavelength) and 18 nm for the second peak (longer wavelength) under the exposure TEP vapor. Red-shifts of 22 nm and 32 nm for the detection of DMMP were observed for the first and second DBR peaks in the reflectivity spectrum, respectively.

The reflectivity spectrum of triple rugate structured PSi shown in Fig. 5.18 (a) displays three reflection peaks at 554, 632, and 745 nm, respectively. Each of the main peaks in an optical reflectivity spectrum corresponds to one of the sine components of the composite waveform, indicating that the reflectivity spectrum represents the Fourier transform of the composite current-time waveform.

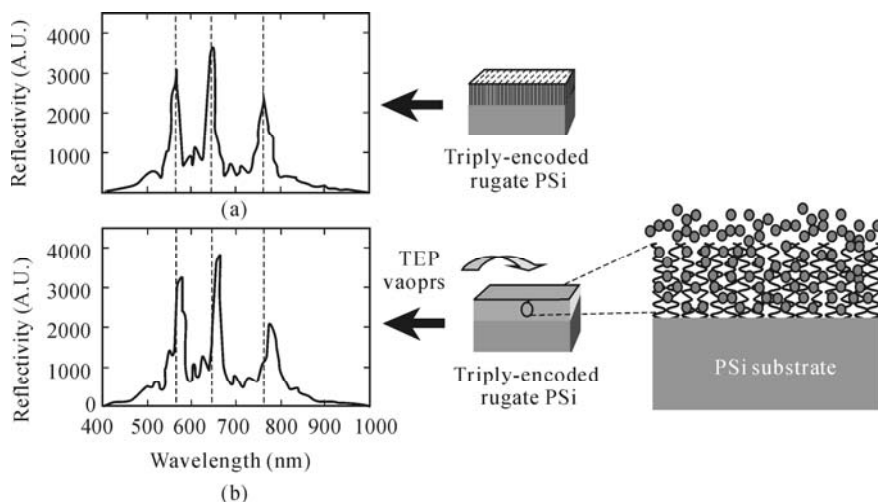


**Fig. 5.18.** Optical reflectivity spectra of triple rugate-structured PSi in air (a) and under the exposure nerve agent mimics (b) for 1 min (Modified from Ref. 99)

An effective refractive index of rugate PSi depends directly on porosity. An electrochemical etching offers an opportunity to modulate the porosity in depth and allows the fabrication of structures with any refractive index profile. When the current is gradually modulated, a smooth index profile of rugate PSi can be achieved. A triple rugate-structured PSi sample is placed in an exposure chamber

fitted with an optical window. The sample is then exposed to a flux of nerve agent such as DMMP, DCP, TEP, and DEEP in air with a flow rate of  $5 \text{ L}\cdot\text{min}^{-1}$  as shown in Fig. 5.19. When the PSi sample is exposed to analytes in the gas phase, capillary condensation causes an increase in its effective refractive index by the replacement of air to liquid of analyte. The positions of three reflection peaks are monitored as a function of time after an analyte vapor is introduced. Diffusion and capillary condensation effects determine the response, because the pressure of analyte is constant.

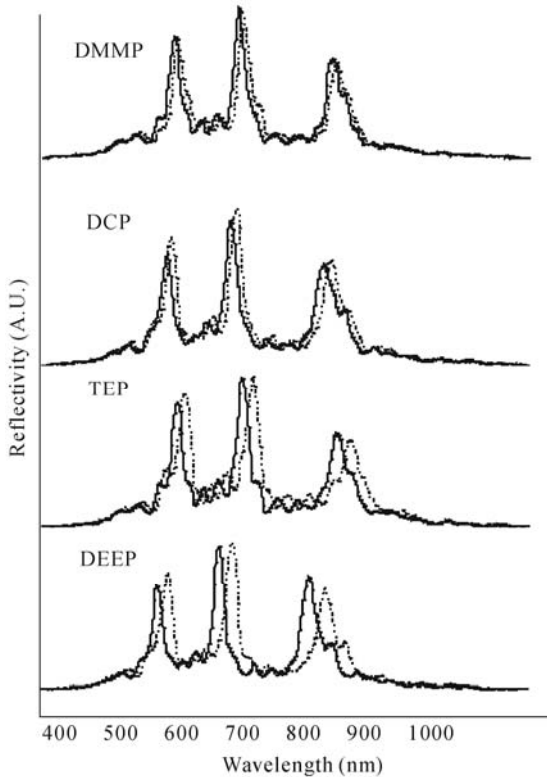


**Fig. 5.19.** Optical reflectivity spectra of triple rugate-structured PSi in air (solid line) and under the exposure of nerve agent mimics (dotted line) for 1 min (Adapted from Ref. 99. Copyright (2008), with permission from ASP)

The surface and cross-sectional SEM images of PSi samples were obtained by a cold field emission scanning electron microscope. FE-SEM images of DBR PSi displaying single reflection peak (a) and double reflection peak (b) are shown in Fig. 5.20.

The cross-sectional images of single and double DBR PSi shown illustrates that the multilayer DBR PSi has a depth of a few microns. A repeating etching process results in two distinct refractive indices. However, triply encoded

rugate-structured PSi illustrates that it possesses a depth of 100 micron without such a gradient porosity depth profile due to the composite current waveform as shown in Fig. 5.20(c).

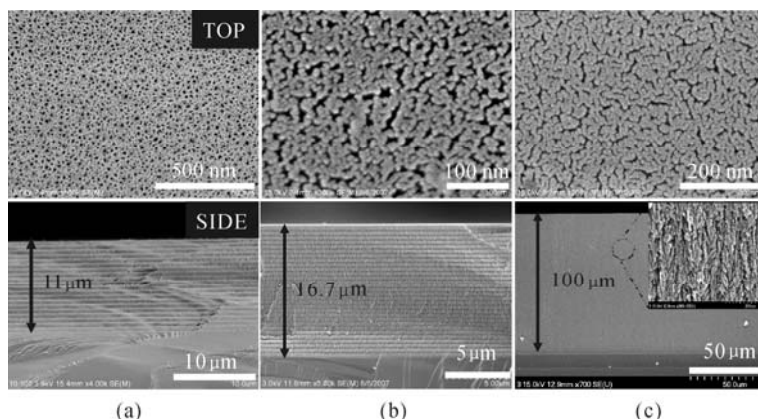


**Fig. 5.20.** Surface and cross-sectional SEM images of single DBR PSi (a), double DBR PSi (b) and triply encoded rugate-structured PSi (c)

Another DBR PSi sample was prepared using a periodic square wave current between  $5 \text{ mA}\cdot\text{cm}^{-2}$  for 100 s and  $50 \text{ mA}\cdot\text{cm}^{-2}$  for 3 s to match the emission wavelength of the LED (520 nm and 590 nm, FWHM = 15 nm) with its reflection band at 520, 590 nm. When a LED was used as the incident light source instead of the tungsten-halogen lamp, a dramatic decrease in the reflectivity, resulting from the red-shift, was observed in the reflectivity spectrum. Fig. 5.21 shows reflectivity spectra recorded every few seconds, in situ, while exposing DBR PSi to nerve agent vapors. A dramatic decrease (75%) in reflection intensity can be observed within 15 s for TEP (Fig. 5.21(a)).

In the case of DMMP, detection of DMMP vapors using laser ( $\lambda_{\text{em}}=530 \text{ nm}$ ) as a light source was much faster and greater due to the narrower FWHM compared to LED light source by 2.5 times for 1 min as shown in Fig. 5.21(d).

DMMP is a stimulant for G-type nerve agents such as sarin. Vapor of sarin has a lethality that is indicated by both concentration and exposure time. If a group of people breathed a concentration of 100 mg of sarin per cubic meter of air for one minute, this would be a lethal dose for 50% of a group. At  $1 \text{ mg}\cdot\text{m}^{-3} = 0.17 \times 10^{-6}$  for sarin,  $100 \text{ mg}\cdot\text{m}^{-3}$  is equal to  $17 \times 10^{-6}$ .<sup>[84]</sup> This is shown in Fig. 5.22. The detection limit ( $1.5 \times 10^{-6}$ ) of DMMP using DBR PSi was  $8.8 \text{ mg}\cdot\text{m}^{-3}$  for 1 min when a tungsten-halogen lamp was used as a light source. However, the detection limit ( $150 \times 10^{-9}$ ) of DMMP could be increased by changing a LED and laser light sources. This result indicates that the detection of nerve agent mimics using DBR PSi exhibits a couple of hundreds times better detection limits compared with single layer PSi ( $800 \times 10^{-6}$  of DFP for 5 min)<sup>[19]</sup> or rugate structured PSi ( $31 \times 10^{-6}$  of DMMP for 1 min).<sup>[84]</sup>

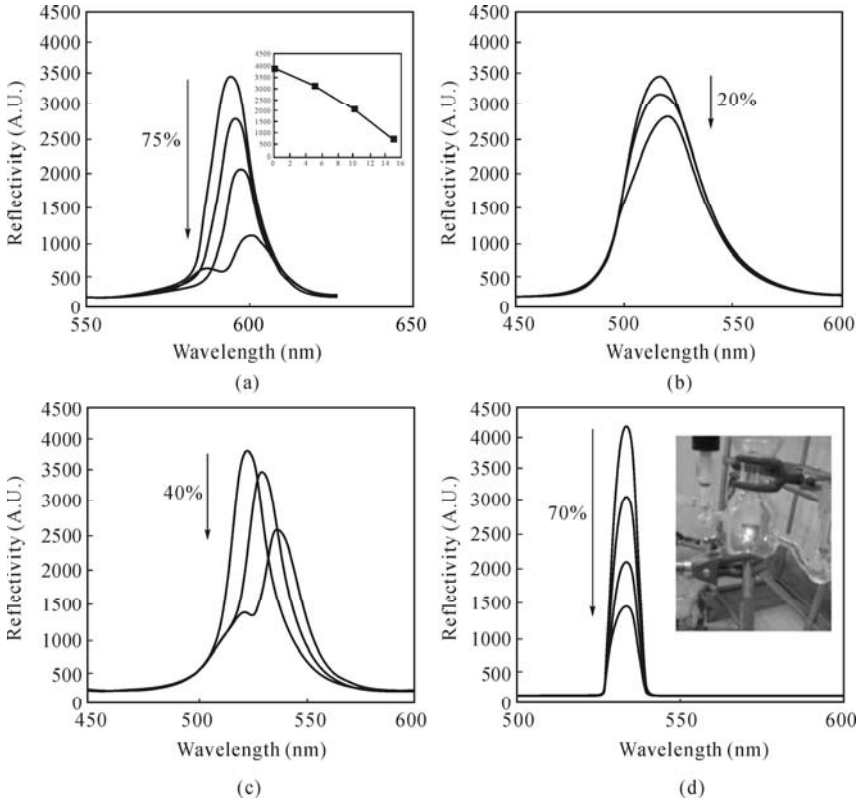


**Fig. 5.21.** Reflectivity spectra of DBR PSi samples under a flux of TEP(a), DMMP (b), DEEP (c) in air when a LED ( $\lambda_{em}=520, 590$  nm) is used as a light source and DMMP (d) in air when a laser ( $\lambda_{em}=532$  nm) is used as a light source (Modified from Ref. 74)

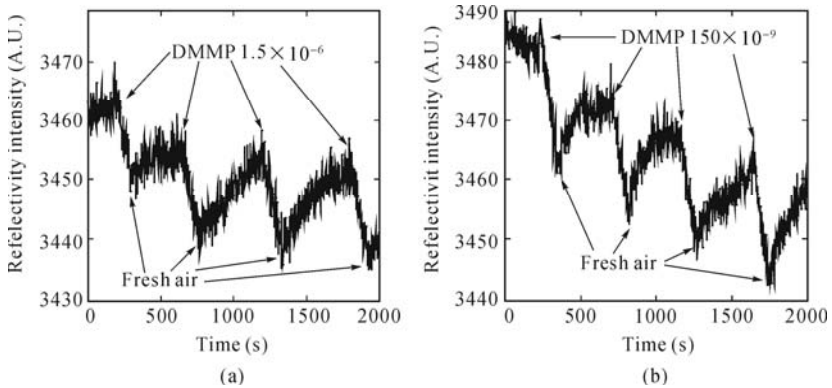


**Fig. 5.22.** Plots for showing the detection limits of DMMP at  $8.8 \text{ mg}\cdot\text{m}^{-3}$  ( $1.5 \times 10^{-6}$ ) by using DBR PSi when a tungsten-halogen lamp is used as a light source and at  $0.88 \text{ mg}\cdot\text{m}^{-3}$  ( $150 \times 10^{-9}$ ) by using DBR PSi when LED and laser are used as a light source (Adapted from Ref. 96. Copyright (2007), with permission from the TTP)



### 5.2.2.2 Detection of VOCs (Volatile Organic Compounds)

PSi is an ideal candidate for gas- or liquid-sensing applications, since it has a very large specific surface area in the order of a few hundred  $\text{m}^2 \cdot \text{cm}^{-3}$ , corresponding to about thousand times the surface area of a polished silicon wafer. The direction of pores and pore diameters depend on surface orientation, doping level and type, temperature, the current density, and the composition of the etching solution. The main techniques investigated to achieve signal transduction are capacitance, resistance, photoluminescence, and reflectivity.

Typically, PSi prepared from *p*-type silicon wafer under dark conditions exhibits well-defined Fabry-Perot interferometric fringes in the optical reflectivity spectrum. Condensation of molecules in the pores can lead to a shift in the Fabry-Perot interference fringes by modification of the refractive index of the PSi films. Luminescent PSi samples can be usually prepared by a galvanostatic photoetch of *n*-Si. PSi from *n*-type silicon has a high surface area network of Si nano-crystallites produced by an electrochemical etch. The material consists of an ensemble of interconnected nanometer-sized silicon crystallites, which can have dimensions small enough to exhibit quantum confinement effects. Carriers generated by UV excitation are confined in the silicon nanocrystallites. The gap of the bulk silicon (1.1 eV) is then increased by the confinement energy and a visible red photoluminescence is observed with an external quantum efficiency of up to 5%. Organic vapors have been detected quantitatively by quenching of photoluminescence of the quantum-confined Si crystallites in PSi. Since the photoluminescence from PSi prepared from *p*-type silicon occurs in the near infrared region (above 700 nm), the intensity of the visible light from porous Si is very weak for sensing purposes.

PSi samples displaying both strong photoluminescence in the visible region and well-defined Fabry-Perot interferometric fringes in the optical reflectivity spectrum were successfully prepared. It was demonstrated how PSi chips were prepared and integrated in chemical sensors. Both photoluminescence and reflectivity were reported to constitute efficient transduction modes for sensing compounds in the gas phase: condensation of molecules in the pores led to a quenching of the photoluminescence by energy or electron transfer and a shift in the Fabry-Perot interference fringes by the change in the refractive index of PSi.

Optical reflectance and photoluminescence spectroscopy were used to investigate the optical properties of PSi. Prepared PSi displayed well-resolved Fabry-Perot fringes in the reflectometric interference spectrum. Photoluminescence spectra were measured and collected at room temperature as shown in Fig. 5.23. The maximum intensity of the emission spectrum was centered at 605 nm, with an excitation wavelength of 380 nm.

The surface of PSi was characterized by FT-IR measurement as shown in Fig. 5.24. FT-IR spectra of fresh PSi displayed vibrational bands in the fingerprint region of the spectra. Vibrations associated with the surface Si-H species of fresh PSi were observed at  $\nu(\text{Si-H}) = 2,090$ ,  $\nu(\text{Si-H}_2) = 2,115$ ,  $\nu(\text{Si-H}_3) = 2,140$ , and  $\delta(\text{Si-H}) = 908 \text{ cm}^{-1}$ , respectively. Thermal oxidation of the PSi resulted in the appearance of the characteristic large and broad Si-O-Si vibrational band around

$1,100\text{ cm}^{-1}$  in the FT-IR. The oxidized PSi exhibited vibrational bands characteristic of  $\nu(\text{OSi-H})$  and  $\nu(\text{Si-OH})$  vibrational modes observed at  $2,265$  and  $3,700\text{ cm}^{-1}$ , respectively.

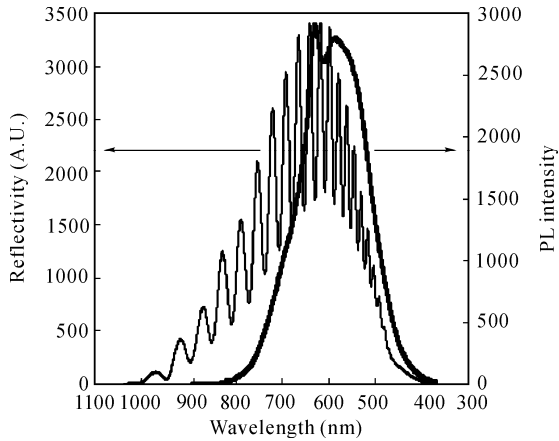


**Fig. 5.23.** Reflectivity and photoluminescence spectra of fresh PSi (Adapted from Ref. 110. Copyright(1997), with permission from Elsevier)

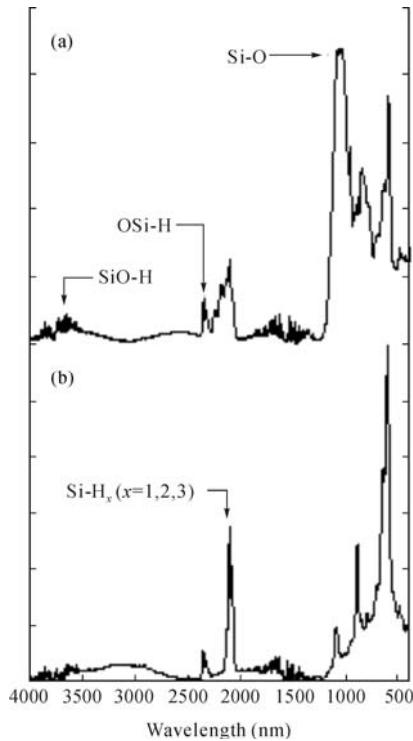


**Fig. 5.24.** FT-IR spectra of fresh PSi (b) and oxidized PSi (a) (Adapted from Ref. 119. Copyright (2008), with permission from ASP)

A plot for the relationship between the vapor pressure of analytes and quenching photoluminescence (%) was obtained. Results from these studies indicated that quenching photoluminescence depended on the vapor pressure of analytes, not on the degree of hydrophilicity/hydrophobicity which was imparted to increase the ability of chloroform to quench the photoluminescence from the material, even though the P*Si* had a hydrophobic Si-H surface. Analyte, having higher vapor pressure, exhibited the higher degree of quenching photoluminescence. The results were summarized in Table 5.1.

**Table 5.1** Change in reflectivity and quenching photoluminescence under the exposure of different analytes (Adapted from Ref. 100. Copyright (2007), with permission from the Korean Science & Technology Center)

Analytes	Vapor pressure (mmHg)	Shift of reflectivity (nm)		Quenching PL (%)	
		Fresh P <i>Si</i>	Oxidized P <i>Si</i>	Fresh P <i>Si</i>	Oxidized P <i>Si</i>
Acetone	184.54	38	17	48	52
<i>n</i> -Hexane	121.26	9	15	20	24
Methanol	97.48	13	7	46	50
Toluene	1.86	10	3	11	6

Fig. 5.25 showed the 2D map obtained from Table 5.1. P*Si* sample was exposed to each analyte three times. Each analyte was represented by a cluster of points. The smaller the area of the clusters indicated the better the reproducibility, and the larger the distance between different clusters indicated the better the discrimination. These results demonstrated the potential of P*Si* sensors for artificial electronic noise applications.

### 5.2.3 Biological Sensing Application of Porous Silicon

Porous silicon has wide applications in many areas. In this section, we only introduce some applications in biological sensing.

The development of new technology, to build such a device on a nanometer is of great interest, because it is too complex to fabricate using a conventional lithographic method. Since the discovery of P*Si*,<sup>[1]</sup> it has been intensively investigated for a variety of applications such as chemical<sup>[19]</sup> and biological sensors,<sup>[101]</sup> medical diagnostics,<sup>[102]</sup> optical band pass filters,<sup>[103]</sup> micro chemical reactors,<sup>[104]</sup> and micro fuel cells<sup>[105]</sup> due to very high surface area as well as unique photonic properties. In particular, optical devices based on multi-structured P*Si* have been brought to the attention of scientists. Multilayer P*Si*, such as DBR P*Si* or rugate P*Si*, exhibits unique optical properties providing a reflection band at a specific wavelength in the optical reflectivity spectrum. The direction of pores and pore diameters depend on surface orientation, doping level and type, temperature, current density, and composition of the etching solution. For applications in high throughput drug discovery and disease diagnostics, label-free biosensors would be important due to the advantage of easy sample

preparations.<sup>[106-107]</sup> Two main optical transduction methods for label-free biosensors were both optical interferometric methods based on interferometers,<sup>[108]</sup> evanescent wave devices,<sup>[109]</sup> and grating couplers,<sup>[110]</sup> and surface Plasmon methods based on metal films<sup>[111]</sup> and colloids.<sup>[112]</sup> Biosensors based on a PSi interferometer had a great advantage due to a large surface area matrix for immobilization of a variety of biomolecules such as enzymes,<sup>[113]</sup> protein,<sup>[114]</sup> and DNA fragments.<sup>[115]</sup>

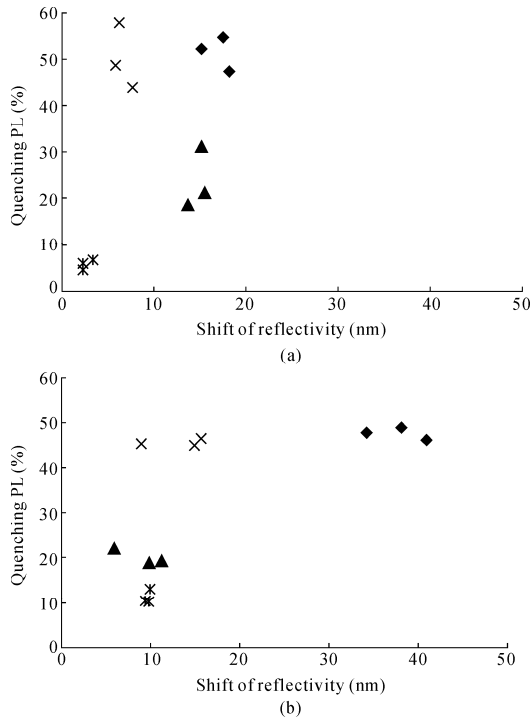


**Fig. 5.25.** 2D map for four different analytes. (a) Oxidized PSi; (b) Fresh PSi (◆: acetone; ▲: hexane; ×: methanol; \*: toluene) (Adapted from Ref. 100. Copyright (2007), with permission from the Korean Science & Technology Center)

DBR PSi samples were prepared by an electrochemical etching of a heavily doped  $p^{++}$ -type silicon wafer. The etching solution consisted of a 3:1 volume mixture of aqueous 48% hydrofluoric acid and absolute ethanol. A galvanostatic etching was carried out in a Teflon cell applying 30 cycles of a two-electrode configuration and performed in a dark room. DBR PSi was prepared by using a periodic pseudo-square wave current between  $30 \text{ mA} \cdot \text{cm}^{-2}$  for 11 s and  $300 \text{ mA} \cdot \text{cm}^{-2}$  for 1.5 s. The resulting DBR PSi were removed from the silicon substrate by applying an electropolishing current at  $460 \text{ mA} \cdot \text{cm}^{-2}$  for 100 s in a solution of 48% aqueous HF and ethanol (3:1 by volume) and  $29 \text{ mA} \cdot \text{cm}^{-2}$  for 200 s in a solution of 48% aqueous HF and ethanol (1:15 by volume) to obtain a free-standing DBR PSi film.

The surface of a free-standing DBR PSi film was predominantly hydride-terminated after the etching procedure. This surface was sensitive to oxidation and hydrolysis upon exposure to aqueous solution. Thermally oxidized DBR PSi samples were obtained by heat treatment in a furnace. Preparation of DBR smart particles was accomplished by placing the oxidized DBR PSi films in ethanol in a Schlenk flask under argon atmosphere. The free-standing DBR PSi films were then made into particles by ultrasonic fracture in organic solution.

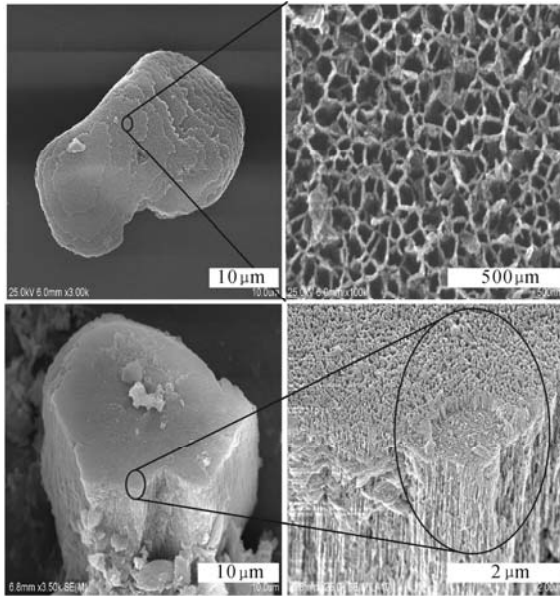
For the biotinylated DBR smart particles, biotin tetrafluorophenyl ester was prepared by a previously known method.<sup>[116]</sup> For surface derivatization of oxidized DBR smart particles, dihydroxysilole was prepared by a previously described method<sup>[117]</sup> and (3-aminopropyl)trimethoxysilane was chemically attached to the surface of the oxidized DBR smart particles. Resulting DBR smart particles were incubated in biotin tetrafluorophenyl ester.

FT-IR spectra were acquired with a Nicolet model 5700 FT-IR instrument in the diffuse reflectance mode. The FT-IR sample compartment was purged with nitrogen before each acquisition. The morphology of DBR smart particles was observed with FE-SEM. Photoluminescence of silole/biotin-derivatized DBR smart particles were measured by luminescence spectrometer, and interferometric reflectance spectra were recorded. Spectra were recorded with a CCD detector in the wavelength range of 400 – 1200 nm.

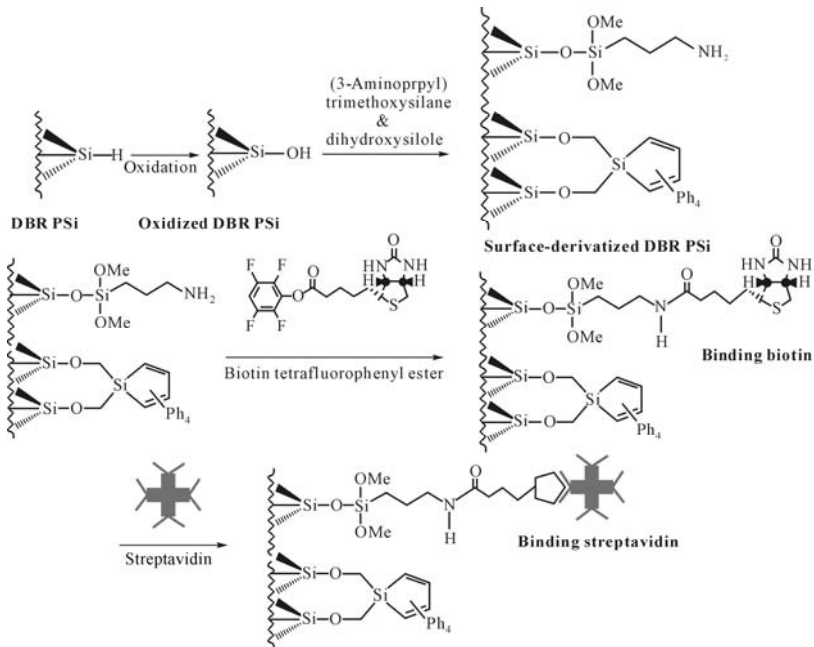
Multilayered DBR PSi prepared by applying a square current waveform exhibits high reflectivity in a specific narrow spectral region. The reflectivity can be tuned to appear anywhere in the visible to near-infrared spectral range, depending on the programmed etched waveform. The electrochemical process generates an optically uniform layer of PSi: the thickness and porosity of a given layer is controlled by the current density, the duration of the etching cycle, and the composition of the etchant solution. High current densities result in the desired well-defined macropores (diameter,  $d > 50$  nm), rather than the random orientation of highly interconnected micropores ( $d < 2$  nm). DBR PSi films have been removed from the silicon wafer by applying an electropolishing current and then ultrasonicated to create particles. Particles with sizes ranging from several hundred nanometers to a few hundred micrometers were generated depending on the duration of ultrasonication. Fig. 5.26 showed the SEM images of DBR PSi particles (so called “smart particle”). The size of the DBR smart particle ranged from 20 to 40 nm. The surface image of DBR smart particles indicated that the pore size of the particle retained a good porosity without destruction of the porous structure during ultrasonication. The prepared DBR smart particles had cylindrical macropores with an average pore size of 100 nm, which could be suitable for the detection of streptavidin and avidin due to their size of  $54 \text{ \AA} \times 58 \text{ \AA} \times 48 \text{ \AA}$  and  $56 \text{ \AA} \times 50 \text{ \AA} \times 40 \text{ \AA}$ , respectively.<sup>[118]</sup>

Fig. 5.27 described the process for chemical functionalization of DBR smart particles with biotin terminated (3-aminopropyl)trimethoxysilane and dihydroxysilole. The thermal oxidation of DBR smart particles at 300 °C for 3 h converted the hydride-terminated surface into the hydroxyl terminated surface. Biotin terminated (3-aminopropyl)trimethoxysilane and dihydroxysilole were used for the surface

modification of oxidized DBR smart particles for the detection of streptavidin



**Fig. 5.26.** Surface and three-dimensional images of DBR smart particle (Adapted from Ref. 119. Copyright (2008), with permission from ASP)



**Fig. 5.27.** Schematic process for surface modification of DBR smart particles with biotin and silole (Adapted from Ref. 119. Copyright (2008), with permission from ASP)

Fig. 5.28 showed that biotin/silole-derivatized DBR smart particles displayed both photoluminescence ( $\lambda_{em} = 505$  nm) with 360 nm of excitation wavelength and reflectivity ( $\lambda_{max} = 607$  nm) under tungsten-halogen lamp. Photograph of samples demonstrated that biotin/silole-derivatized DBR smart particles exhibited dual optical properties.

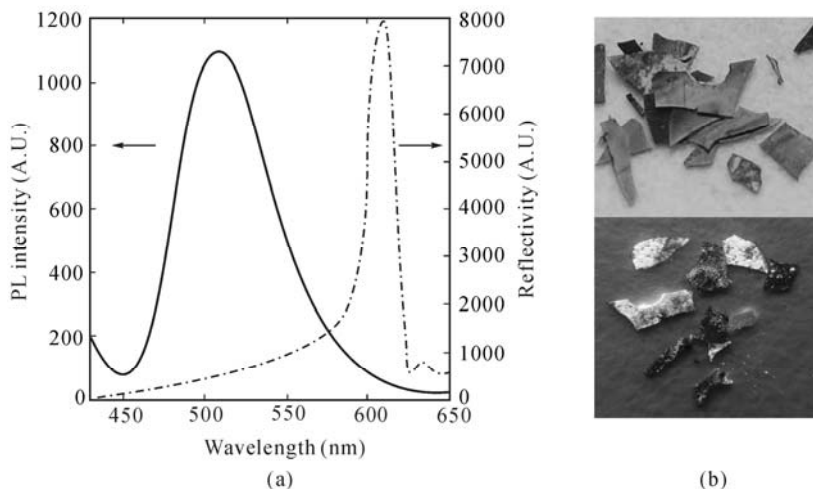


**Fig. 5.28.** (a) Optical reflectivity (dotted line) and photoluminescence (solid line) spectrum of biotin/silole-derivatized DBR smart particles; (b) Photographs of biotin/silole-derivatized DBR smart particles under white light (top) and black light (bottom) (Adapted from Ref. 119. Copyright (2008), with permission from ASP)

Diffuse reflectance FT-IR spectroscopy was used to monitor the oxidation and functionalization reaction of DBR smart particles sample. Fig. 5.29(a) showed that the FT-IR spectrum of DBR smart particle immediately after an anodization of the silicon wafer displayed a characteristic broad-band centered at  $2,115$  and  $908$   $\text{cm}^{-1}$  for the  $\nu(\text{Si-H})$  stretching vibration and  $\delta(\text{Si-H})$  bending vibration. After the thermal oxidation of DBR smart particles, the presence of silicon oxide was determined by FT-IR measurement as shown in Fig. 5.29(b). Thermal oxidation of the DBR smart particles resulted in the appearance of the characteristic large and broad Si-O-Si vibrational band around  $1100$   $\text{cm}^{-1}$  in the FT-IR. The oxidized DBR smart particles exhibited vibrational bands characteristic of  $\nu(\text{OSi-H})$  and  $\delta(\text{OSi-H})$  vibrational modes observed at  $2,277$  and  $883$   $\text{cm}^{-1}$ , respectively. Thermal oxidation of DBR smart particles led to a decrease of the Si-H vibrational band and the appearance of the OSi-H vibrational band. Condensation of the Si-OH surface of DBR smart particles with (3-aminopropyl)trimethoxysilane generated a surface-bound amino group. The FT-IR spectrum shown in Fig. 5.29(c) displayed additional bands characteristic of the linker (the amide band of  $\nu(\text{N-H})$  broad-band centered at  $3,300$   $\text{cm}^{-1}$  and  $\delta(\text{N-H})$  at  $1,579$   $\text{cm}^{-1}$  and the aliphatic  $\nu(\text{C-H})$  stretching bands at  $2,858$  and  $2,954$   $\text{cm}^{-1}$ ). Surface derivatization led to the complete disappearance of the OSi-H vibrational band. The subsequent

reaction with biotin, as shown in Fig. 5.27, led to the desired biotin-functionalized surface which was used in the streptavidin-binding studies (Fig. 5.29(d)). The band at  $1,685\text{ cm}^{-1}$  was assigned to the carbonyl stretching vibration of the biotin head group.

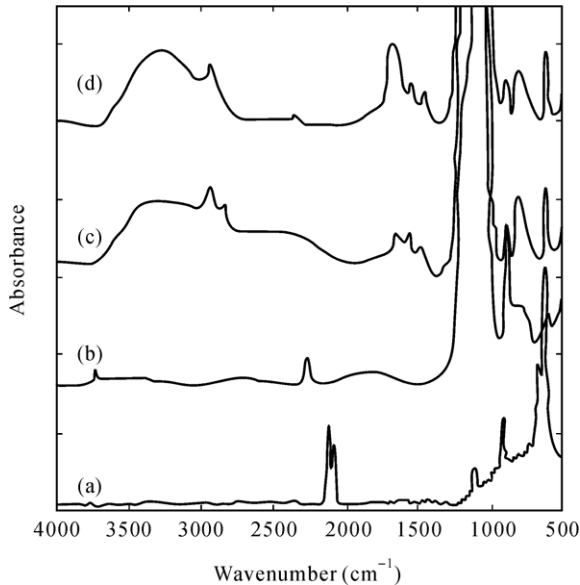


**Fig. 5.29.** Diffuse reflectance FT-IR spectra of: (a) a freshly etched DBR smart particle; (b) oxidized DBR smart particle at  $300\text{ }^{\circ}\text{C}$  for 3 h; (c) functionalized DBR smart particle with (3-aminopropyl) trimethoxysilane; (d) subsequent reaction of the surface with biotin (Adapted from Ref. 119. Copyright (2008), with permission from ASP)

Fresh DBR PSi displayed a very sharp line at  $624\text{ nm}$  with sidelobes around the reflectance peak in the optical reflectivity spectrum as shown in Fig. 5.30. The spectral bands of DBR smart particles had a full-width at half-maximum (FWHM) of about  $20\text{ nm}$ . The thermal oxidation of DBR PSi resulted in the reflectivity at  $580\text{ nm}$  shifting to shorter wavelengths by  $44\text{ nm}$  due to the decrease in the refractive index of silicon dioxide from silicon. Condensation of the Si-OH surface of DBR smart particles with (3-aminopropyl)trimethoxysilane generated a surface-bound amino group. The amine-functionalized DBR smart particles resulted in the reflectivity at  $600\text{ nm}$  shifting to longer wavelengths by  $20\text{ nm}$  due to the increase in the refractive index upon introduction of the amine group into the pores of DBR smart particles. The subsequent reaction with biotin led to the desired biotin-functionalized DBR smart particles which were used in the streptavidin-binding studies. The biotin-functionalized DBR smart particles resulted in the reflectivity at  $610\text{ nm}$  shifting to longer wavelengths due to the increase in the additional refractive index.

The surface functionalized DBR smart particles were placed in the flow cell.



Aqueous phosphate buffer solution (PBS) was flushed to perform for an initial measurement of reflectivity. The surface was rinsed thoroughly with PBS buffer solution to ensure a covalent attachment to the surface and to check the stability of the reflectivity measurement. The biotin-functionalized DBR smart particles in PBS buffer solution resulted in the reflectivity at 665 nm shifting to longer wavelengths by 55 nm due to the increase in the refractive index upon introduction of the PBS buffer solution into the pores of DBR smart particles. The cell was then flushed with a constant flow rate of  $0.8 \text{ mL}\cdot\text{min}^{-1}$  of PBS containing streptavidin ( $20 \mu\text{mol}\cdot\text{L}^{-1}$ ), which coupled to the biotin-modified DBR smart particles surface.

Fig. 5.30 showed the change in the reflection spectrum under the exposure of streptavidin to the biotin-functionalized DBR smart particles. An increase in the reflection wavelength in the reflectivity spectrum by 14 nm was observed, indicative of a change in refractive indices induced by binding of the streptavidin into the biotin-derivatized DBR smart particles. This increase was attributed to the replacement of some of the aqueous phase with streptavidin. The replacement changed the mean refractive indices of the DBR smart particles. They were observed as an increase in the reflection wavelength in the reflectivity.

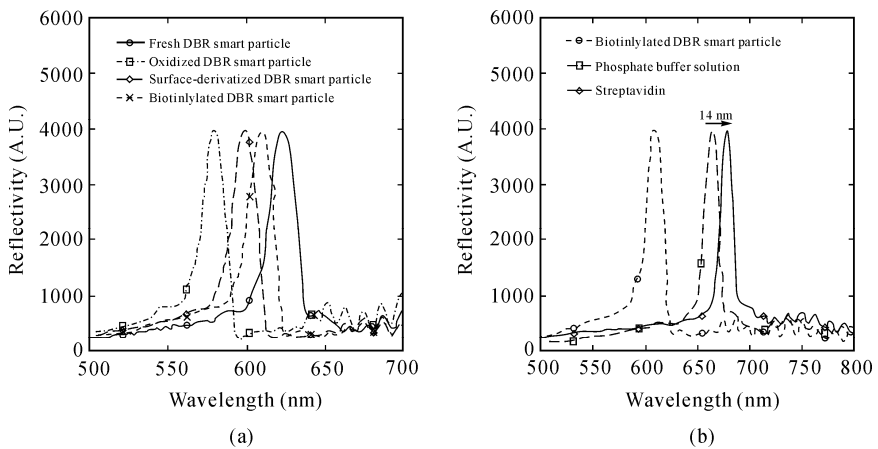


**Fig. 5.30.** Optical reflectivity spectra of fresh, oxidized, surface-functionalized, and biotin derivatized DBR smart particle (a) and sensing of streptavidin based on biotin derivatized DBR smart particle in PBS (b) (Adapted from Ref. 119. Copyright (2008), with permission from ASP)

Fig. 5.31 also showed the change in the reflection spectrum under the exposure of avidin to the biotin-functionalized rugate PSi chip. An increase in the reflection wavelength in the reflectivity spectrum by 18 nm was observed, indicative of a change in the refractive index induced by binding of the avidin into the biotin-derivatized rugate PSi film.



reflection of a specific wavelength in the optical reflectivity spectrum. The fabrication, optical characterization, and surface derivatization of PSi were described. Various detection methods using multi-structured materials such as DBR, rugate, and multi-encoded rugate PSi for sensing G-type nerve agent mimics and VOCs have been developed. The detection methods involve the shift of DBR or rugate peaks in reflectivity spectra under the exposure of vapors of nerve agent simulants and VOCs. Rapid detections have been achieved in a few seconds, in situ, and observed by the red-shift of the reflection peak resulting from the increase in refractive indices in PSi. Real-time detection for the nerve gases indicates that the measurement is reversible. The detection efficiency for nerve agent mimics also increased when a light emitting diode (LED) and laser are used as an incident light source. Detection of DMMP vapors using laser ( $\lambda_{em}=530$  nm) as a light source was much faster and greater due to the narrower FWHM compared to LED light source by 2.5 times for 1 min. The detection limit ( $150 \times 10^{-9}$ ) for DMMP vapors has been enhanced to be a couple of hundred times better than previous detection limits. For the detection of the bio-molecule, the reflection spectra of biotin-modified PSi were used in the avidin and streptavidin-binding studies. When the PBS buffer solution containing avidin and streptavidin was flushed into the biotin-functionalized PSi in the cell, a red-shift of reflectivity by 18 and 14 nm in the reflectivity spectrum was observed, respectively. This result indicated the binding of the avidin and streptavidin into the biotin-derivatized PSi.

## References

- [1] Uhlir, A. *Bell Synt. Tech. J.*, 1956, 35: 333.
- [2] Turner, D. R. *J. Electrochem. Soc.*, 1958, 105: 402.
- [3] Arita, Y., Kato, K., Sudo, T. *IEEE T. Electron Dev.*, 1977, 24: 757.
- [4] Unagami, T., Kato, K. *Jpn. J. Appl. Phys.*, 1977, 16: 1635.
- [5] Imai, K. *Solid State Electron*, 1981, 24: 159.
- [6] Otoi, F., Anzai, K., Kitabayashi, H., Uchiho, K., Mizokami, Y. *J. Electrochem. Soc.*, 1984, 131: C319.
- [7] Canham, L. T. *Appl. Phys. Lett.*, 1990, 57: 1046.
- [8] Cullis, A. G., Canham, L. T. *Nature*, 1991, 353: 335.
- [9] Sui, Z., Leong, P. P., Herman, I. P., Higashi, G. S., Temkin, H. *Appl. Phys. Lett.*, 1992, 60: 2086.
- [10] Delerue, C., Allan, G., Lannoo, M. *Phys. Rev. B*, 1993, 48: 11024.
- [11] Koch, F., Petrova-Koch, M., V. T., Nikolov, A., Gavrilenko, V. *Mater. Res. Soc. Symp. Proc.*, 1993, 298: 319.
- [12] Lee, E. J., Bitner, T. W., Ha, J. S., Shane, M. J., Sailor, M. J. *J. Am. Chem. Soc.*, 1996, 118: 5375.
- [13] Buriak, J. M., Allen, M. J. *J. Am. Chem. Soc.*, 1998, 120: 1339.
- [14] Richter, A., Steiner, P., Kozlowski, F., Lang, W. *IEEE Electron Device Lett.*, 1991, 12: 691.

- [15] Hirschmann, K., Tsybeskov, D. L., Dutttagupta, S. P., Fauchet, P. M. *Nature*, 1996, 384: 338.
- [16] Mazzoleni, C. Pavesi, L. *Appl. Phys. Lett.*, 1995, 67: 2983.
- [17] Smestad, G., Kunst, M., Vial, C. *Sol. Energy Mater. Sol. Cells*, 1992, 26: 277.
- [18] Lauerhaas, J. M., Sailor, M. J. *Science*, 1993, 261: 1567.
- [19] Sohn, H., Letant, S., Sailor, M. J., Trogler, W. C. *J. Am. Chem. Soc.*, 2000, 122: 5399.
- [20] Letant, S., Sailor, M. J. *Adv. Mater.*, 2001, 13: 355.
- [21] Chan, S., Horner, S. R., Fauchet, P. M., Miller, B. L. *J. Am. Chem. Soc.*, 2001, 123: 11797.
- [22] Sohn, H., Calhoun, R. M., Sailor, M. J., Trogler, W. C. *Angew. Chem. Int. Ed.*, 2001, 40: 2104.
- [23] Sohn, H., Sailor, M. J., Magde, J. D., Trogler, W. C. *J. Am. Chem. Soc.*, 2003, 125: 3821.
- [24] Li, X., Coffey, J. L., Chen, Y. D., Pinizzotto, N. R. F. J., Canham, L. T. *J. Am. Chem. Soc.*, 1998, 120: 11706.
- [25] Koshida, N., Nakajima, T., Yoshiyama, M., Ueno, K., Nakagawa, T., Shinoda, H. *Mater. Res. Soc. Symp. Proc.*, 1999, 536: 105.
- [26] Bell, T. E., Gennissen, P. T. J., Demunter, D., Kuhl, M. J. *Micromech. Microeng.*, 1996, 6: 361.
- [27] Zubko, V. G., Smith, T. L., Witt, A. N. *Astrophys. J.*, 1998, p 501.
- [28] Parkhutik, V. P., Matveeva, E., Perez, R., Alamo, J., Beltraán, D. *Mater. Sci. Engn. B*, 2000, pp 69-70, 53.
- [29] Bondarenko, V. P., Bogatirev, Y. V., Colinge, J. P., Dolgyi, L. N., Dorofeev, A. M., Yakovtseva, V. A. *IEEE. Trans. Nucl. Sci.*, 1997, 44: 1719.
- [30] Parkhutik, V. P., Canham, L. T. *Phys. Stat. Sol. A*, 2000, 182: 591.
- [31] Lehmann, V., Gösele, U. *Appl. Phys. Lett.*, 1991, 58: 856.
- [32] Sailor, M. J., Heinrich, J. L., Lauerhaas, J. M. *Stud. Surface Sci. Cat.*, 1996, 103: 209.
- [33] Smith, R. L., Collins, S. D. *J. Appl. Phys.*, 1992, 71: R1.
- [34] Hossain, S. M., Das, J., Chakraborty, S., Dutta, S. K., Saha, H. *Semicon. Sci. Tech.*, 2002, 17: 55.
- [35] Itoia, I. K., Drayton, R. F. *IEEE Antenn. Propag. Soc.*, 2003, 2: 663.
- [36] Halimaoui, A. *Porous Silicon Science and Technology*, Vial, J. C., Derrien, J., Eds. Springer-Verlag, New York, 1995, p 33.
- [37] Christopersen, M., Carstensen, J., Foll, H. *Phys. Stat. Sol. A*, 2000, 182: 601.
- [38] Chuang, S. F., Collins, S. D., Smith, R. L. *Appl. Phys. Lett.*, 1989, 55: 675.
- [39] Brumhead, D., Canham, L. T., Seekings, D. M., Tufton, P. J. *Electrochi. Acta*, 1993, 38: 191.
- [40] Bergman, D. J. *Phys. Rep. C*, 1978, 43: 377.
- [41] Looyenga, H. *Physica*, 1965, 31: 401.
- [42] Brunauer, S., Emmett, P. H., Teller, E. *J. Am. Chem. Soc.*, 1938, 60: 309.
- [43] Sawada, S., Hamada, N., Ookubo, N. *Phys. Rev. B*, 1994, 49: 5236.
- [44] Read, A. J., Needs, R. J., Nash, K. J., Canham, L. T., Calcott, P. D. J., Qteish, A. *Phys. Rev. Lett.*, 1992, 69: 1232.
- [45] Kanemitsu, Y., Uto, H., Masumoto, Y., Futagi, T., Mimura, H. *Phys. Rev. B*,

- 1993, 48: 2827.
- [46] Hory, M., Herino, A. R., Ligeon, M., Muller, F., Gaspard, F., Mihalcescu, I., Vial, J. C. *Thin Solid Films*, 1995, 255: 200.
- [47] Nakahima, A., Itakura, T., Watanabe, S., Nakayama, N. *Appl. Phys. Lett.*, 1992, 64: 46.
- [48] Yan, J., Shih, S., Jung, K. H., Kwong, D. L., Kovar, M., White, J. M., Gnade, B. E., Magel, L. *Appl. Phys. Lett.*, 1994, 64: 1374.
- [49] Walter, L., Peter, S., Frank, K., Peter, R. *Thin Solid Films*, 1995, 255: 224.
- [50] Hirschmann, K. D., Tsybeskov, L., Duttagupta, S. P., Fauchet, P. M. *Nature*, 1996, 384: 338.
- [51] Pap, A. E., Kordás, K., George, T. F., Leppävuori, S. *J. Phys. Chem. B*, 2004, 108: 12744.
- [52] Kim, S. G., Kim, S., Ko, Y. C., Cho, S., Sohn, H. *Colloids Surf. A*, 2008, pp 313-314, 398
- [53] Higashi, G. S., Chabal, Y. J., Trucks, G. W., Raghavachari, K. *Appl. Phys. Lett.*, 1990, 56: 656.
- [54] Higashi, G. S., Becker, R. S., Chabal, R. S., Becker, A. J. *Appl. Phys. Lett.*, 1991, 58: 1656.
- [55] Bateman, J. E., Eagling, R. D., Worrall, D. R., Horrocks, B. R., Houlton, A. *Angew. Chem. Int. Ed. Engl.*, 1998, 37: 2683.
- [56] Boukherroub, R., Morin, S., Wayner, D. D. M., Bensebaa, F., Sproule, G. I. Baribeau, J. M., Lockwood, D. J. *Chem. Mater.*, 2001, 13: 2002.
- [57] Bateman, J. E., Eagling, R. D., Horrocks, B. R., Houlton, A. J. *Phys. Chem. B*, 2000, 104: 5557.
- [58] Fleming, I. In: *Comprehensive Organic Chemistry*, Jones, N., Ed., Pergamon: New York, 1979, 3: 568.
- [59] Buriak, J. M. *Chem. Rev.*, 2002, 102: 1271.
- [60] Berger, M. G., Dieker, C., Thonissen, M., Vescan, L., Luth, H. Munder, H. J. *Phys. D*, 1994, 27: 1333.
- [61] Loni, A., Canham, L. T., Berger, M. G., Arens-Fisher, R., Munder, H., Luth, H., Arrand, H. F., Benson, T. M. *Thin Solid Films*, 1996, 276: 143.
- [62] Hruger, M., Berger, M. G., Marso, M., Reetz, W. T., Eickhoff, L. R., Vescan, L., Thonissen, M., Luth, H., Arens-Fisher, R., Hilbrich, S., Theiss, W. *Jpn. J. Appl. Phys.*, 1997, 36: L24.
- [63] Pavesi, L. *La Rivista del Nuovo Cimento, della Società Italiana di Fisica*, Frabetti, Marangon, S. P., Missiroil, M., Rucci, P, Bologna, Marangon, M., Eds., 1997, p 1.
- [64] Mazzoleni, C., Paves, L. *Appl. Phys. Lett.*, 1995, 67: 2983.
- [65] Berger, M. G., Arens-Fischer, R., Thonisson, M., Kruger, M., Billat, S., Luth, H., Hilbrich, S., Theiss, W., Grosse, P. *Thin Solid Films*, 1997, 297: 237.
- [66] Cazzanelli, M., Vinegoni, C., Pavesi, L. *J. Appl. Phys.*, 1999, 85: 1760.
- [67] Lehmann, V., Stengl, R., Reisinger, H., Detemple, R., Theiss, W. *Appl. Phys. Lett.*, 2001, 78: 589.
- [68] Agrawal, V., Del Rio, J. A. *Appl. Phys. Lett.*, 2003, 82: 1512.
- [69] Bovard, B. G. *Appl. Opt.*, 1993, 32: 5427.
- [70] Nolte, A. J., Rubner, M. F., Cohen, R. E. *Langmuir*, 2004, 20: 3304.

- [71] Dorvee, J. R., Derfus, A. M., Bhatia, S. N., Sailor, M. J. *Nat. Mater.*, 2004, 3: 896.
- [72] Ilyas, S., Böcking, T., Kilian, K., Reece, P. J., Gooding, J. K., Gaus, G. M. *Opt. Mater.*, 2007, 29: 619.
- [73] Jang, S., Koh, Y., Kim, J., Sohn, H. *J. Kor. Phys. Soc.*, 2008, 52: 212.
- [74] Jang, S., Koh, Y., Kim, J., Park, J., Park, C., Kim, S. J., Cho, S., Ko, Y. C., Sohn, H. *Mater. Lett.*, 2008, 62: 552.
- [75] Park, J., Cho, S., Ko, Y. C., Sohn, H. *J. Kor. Phys. Soc.*, 2007, 50: 695.
- [76] Office of the special assistant for Gulf War Illness, Department of Defense, Fact Sheet on Exposure Limits for Sarin (GB), 1997.
- [77] Nieuwenhuizen, M. S., Hartevelde, J. L. N. *Sens. Actuators B*, 1997, 40: 167.
- [78] Williams, D., Pappas, G. *Field Anal. Chem. Technol.*, 1999, 3: 45.
- [79] LeJeune, K. E., Wild, J. R., Russell, A. J. *Nature*, 1998, 395: 27.
- [80] Snow, E. S., Perkins, F. K., Houser, E. J., Badescu, S. C., Reinecke, T. L. *Science*, 2005, 307: 1942.
- [81] Taranenko, N., Alarie, J. P., Stokes, D. L., Vo-Dinh, T. *J. Raman Spectrosc.*, 1996, 27: 379.
- [82] Hopkins, A. R., Lewis, N. S. *Anal. Chem.*, 2001, 73: 884.
- [83] Letant, S. E., Kane, S. R., Hart, B. R., Hadi, M. Z., Cheng, T. C., Rastogi, V. K., Reynolds, J. G. *Chem. Commun.*, 2005, p 851.
- [84] Dorvee, J., Sailor, M. J. *Phys. Stat. Sol.*, 2005, 202: 1619.
- [85] Chan, S., Horner, S. R., Miller, B. L., Fauchet, P. M. *J. Am. Chem. Soc.*, 2001, 123: 11797.
- [86] Pacholski, C., Yu, C., Miskelly, G. M., Godin, D., Sailor, M. J. *J. Am. Chem. Soc.*, 2006, 128: 4250.
- [87] Snow, P. A., Squire, E. K., Russell, P. S. J., Canham, L. T. *J. Appl. Phys.*, 1999, 86: 1781.
- [88] Pacholski, C., Sartor, M., Sailor, M. J., Cunnin, F., Miskelly, G. M. *J. Am. Chem. Soc.*, 2005, 127: 11636.
- [89] Canham, L. T., Stewart, M. P., Buriak, J. M., Reeves, C. L., Anderson, M. E., Allcock, K. P., Snow, P. A. *Phys. Status Solidi A*, 2000, 182: 521.
- [90] Lehmann, V., Stengl, R., Reisinger, H., Detemple, R., Theiss, W. *Appl. Phys. Lett.*, 2001, 78: 589.
- [91] Schmedake, T. A., Cunin, F., Link, J. R., Sailor, M. J. *Adv. Mater.*, 2002, 14: 1270.
- [92] Cunin, F., Schmedake, T. A., Link, J. R., Li, Y. Y., Koh, J., Bhatia, S., Sailor, M. J. *Nat. Mater.*, 2002, 1: 39.
- [93] Yoon, M. S., Ahn, K. H., Cheung, R. W., Sohn, H., Link, J. R., Cunin, F., Sailor, M. J. *Chem. Commun.*, 2003, p 680.
- [94] Sailor, M. J., Link, J. R. *Chem. Commun.*, 2005, p 1375.
- [95] Li, Y. Y., Cunin, F. J., Link, R., Gao, T., Betts, R. E., Reiver, S. H., Chin, V. S., Bhatia, N., Sailor, M. J. *Science*, 2003, 299: 2045.
- [96] Lee, B. J., Jang, S., Sohn, H. *Solid State Phenom.*, 2007, pp 124-126, 491.
- [97] Janshoff, A., Dancil, K. P. S., Steinem, C. D., Greiner, P., Lin, V., Gurtner, S. Y., Motesharei, C. K., Sailor, M. J., Ghadiri, M. R. *J. Am. Chem. Soc.*, 1998, 120: 12108.

- [98] Meade, S. O., Yoon, M. S., Ahn, K. H., Sailor, M. J. *Adv. Mater.*, 2004, 16: 1811.
- [99] Jang, S., Kim, J., Koh, Y., Ko, Y. C., Woo, H. G., Sohn, H. J. *Nanosci. Nanotechnol.*, 2007, 7: 4049.
- [100] Koh, Y., Kim, S. J., Jang, S., Park, C., Sohn, H. J. *Kor. Vac. Soc.*, 2007, 16: 99.
- [101] Lin, V. S.-Y., Motesharei, K., Dancil, K. P. S., Sailor, M. J., Ghadiri, M. R. *Science*, 1997, 278: 840.
- [102] Simion, M., Kleps, I., Neghina, T., Angelescu, A., Miu, M., Bragaru, A., Danila, M., Condac, E., Costache, M., Savu, L. J. *Alloy. Compd.*, 2007, 434: 830.
- [103] Ilyas, S., Böcking, T., Kilian, K., Reece, P. J., Gooding, J., Gaus, K., Gal, M. *Opt. Mater.*, 2007, 29: 619.
- [104] Khan, M. A., Haque, M. S., Naseem, H. A., Brown, W. D., Malshe, A. P. *Thin Solid Films*, 1998, 332: 93.
- [105] Létant, S. E., Content, S., Tan, T., Zenhausem, T. F., Sailor, M. J. *Sensor Actuat. B-Chem.*, 2000, 69: 193.
- [106] Brecht, A., Gauglitz, G. *Sensor. Actuat. B-Chem.*, 1997, 38: 1.
- [107] Janata, J., Josowicz, M., Devaney, D. M. *Anal. Chem.*, 1994, 66: 207R.
- [108] Piechler, J., Brandenburg, I., Brecht, A. A., Wagner, E., Gauglitz, G. *Appl. Opt.*, 1997, 36: 6554.
- [109] Abel, A. P., Weller, M. G., Duvencek, G. L., Ehart, M., Widmer, H. M. *Anal. Chem.*, 1996, 68: 2905.
- [110] Polzius, R., Diessel, E., Bier, F. F., Bilitewski, U. *Anal. Biochem.*, 1997, 248: 269.
- [111] Homola, J., Yee, S. S., Gauglitz, G. *Sensor. Actuat. B-Chem.*, 1999, 54: 3.
- [112] Nikitin, P. I., Beloglazov, A. A., Kochregin, V. E., Valeiko, M. V., Ksenevich, T. I. *Sensor. Actuat. B-Chem.*, 1999, 54: 43.
- [113] Drott, J., Lindstrom, K., Rosengren, L., Laurell, T. J. *Micromech. Microeng.*, 1997, 7: 14.
- [114] Laurell, T., Drott, J., Rosengren, L., Lindstrom, K. *Sensor. Actuat. B-Chem.*, 1996, 31: 161.
- [115] Beattie, K. L., Beattie, W. G., Mengm, L., Turner, S. L., Coral-Vazquez, R., Sith, D. D., McIntyre, P. M., Dao, D. D. *Clin. Chem.*, 1995, 41: 700.
- [116] Gamper, H. B., Reed, M. W., Cox, T., Viroscio, J. S., Adams, A. D., Gall, A. A., Scholler, J. K., Meyer, R. B. *Nucleic Acids Res.*, 1993, 21: 145.
- [117] Touloukhonov, I., Zhao, R., Kozee, M., West, R. *Main Group Met. Chem.*, 2001, 24: 737.
- [118] Hendrickson, W. A., Pahler, A., Smith, J. L., Satow, Y., Merritt, E. A., Phizackerley, R. P. *Proc. Natl. Acad. Sci.*, 1989, 86: 2190.
- [119] Jang, S., Kim, J., Koh, Y., Park, J., Woo, H. G., Kim, S., Sohn, H. J. *Nanosci. Nanotechnol.*, 2008, 8: 5166.
- [120] Koh, Y., Kim, S. J., Park, J., Park, C., Cho, S., Woo, H. G., Ko, Y. C., Sohn, H. B. *Kor. Chem. Soc.*, 2007, 28: 2083.
- [121] Stuchbury, T., Shipton, M., Norris, R., Malthouse, J. P. G., Brocklehurst, K., Herbert, J. A. L., Suschitzky, H. *Biochem. J.*, 1975, 151: 417.

---

# Microbial Fuel Cells as the Real Source of Sustainable Energy

## Sung-Hee Roh

Research Institute of Advanced Engineering Technology and Department of Chemical and Biochemical Engineering, Chosun University, Gwangju 501-759, the Republic of Korea

Tel.: +82-62-220-2653; Fax: +82-62-230-7226

E-mail: rohsh@chosun.ac.kr

## 6.1 Introduction

The fuel cell (FC) could be one of the most promising discoveries for solving the fossil resources shortage and global environmental problems. FC is a pollution-free and highly efficient energy production source that emits little harmful gas and directly transforms a chemical reaction into electrical energy. In particular, microbial fuel cells (MFCs) have provided new ways of utilizing renewable energy sources. The microbial energy conversion technology with resort to MFCs that convert the chemical energy stored in organic compounds to electrical energy, achieved through the catalytic reactions by microorganisms, has attracted considerable interest among energy researchers.<sup>[1-5]</sup> The technology is based on the electrochemically active microorganisms that grow by oxidizing the biodegradable material to both CO<sub>2</sub> and protons while transferring the electrons to a solid electrode.<sup>[6]</sup>

MFC technology has not yet been applied to the practical treatment of waste material primarily because it is an emerging technology and much time is still needed for technical maturation. Another reason is that its process performance is considered to be low when compared to its competitors (e.g., methanogenic anaerobic digesters) because of considerable difficulty in constructing large-scale, highly efficient MFC reactors.<sup>[7]</sup> Pham et al. reviewed the advantages and disadvantages of MFCs compared to the conventional anaerobic digestion



technology for the production of biogas as renewable energy.<sup>[8]</sup> As a way of increasing the performance of MFCs, there has been considerable work on MFC configurations, their physical and chemical operating conditions, the choice of microorganisms and optimization of the microbial metabolism to increase electron donation to the electrodes.<sup>[6,9-14]</sup>

In recent years, as a result of the rapid advances in MFC research, several valuable reviews on MFCs have appeared in the literature. These include the following: MFC designs, characterizations and performance,<sup>[6]</sup> the recent advances in MFC configurations and performances,<sup>[15]</sup> the microbial metabolism and parameters defining the performance of MFC,<sup>[16]</sup> electricity-producing bacterial communities,<sup>[17]</sup> the primary mechanism for electron transfer of electricigens to electrodes,<sup>[18]</sup> the characteristics of electrochemically active bacteria in a mediator-less system,<sup>[19]</sup> microbial physiology and engineering approaches regarding Benthic Unattended Generators (BUGs) for powering remote-sensing or monitoring devices,<sup>[20]</sup> the inherent constraints of MFCs and suggestions for MFC performance improvement,<sup>[21]</sup> the anodic electron transfer mechanisms in electrochemically active bacteria,<sup>[22]</sup> improved cathode reactions<sup>[23]</sup> and the application of new electrode materials.<sup>[24]</sup> This review article covers a critical perspective on the recent advances in MFC with an emphasis on the performances of MFC, materials, operational factors and applications of MFCs in the future.

## **6.2 Configurations and Designs of Microbial Fuel Cells**

In recent years, as a result of the rapid advances in MFC research, several valuable reviews on MFCs have appeared in the literature. In this section, we will introduce one of these valuable reviews, MFC configurations and designs.

### **6.2.1 MFC Components**

In order to increase the power output of MFCs, many research efforts have been made to alter their designs to overcome the barriers to electron and proton transport and to enhance the surface area and reactivity of the electrodes. The essential physical components of MFCs are the anode, cathode and proton exchange membrane (PEM), or more precisely a cation exchange membrane (CEM), as shown in Fig. 6.1. This configuration is a typical two-chambered MFC with an oxygen cathode. A single-chambered MFC eliminates the need for the cathodic chamber by exposing the cathode directly to the air atmosphere. The use of a PEM is optional. Electrochemically active bacteria in the anode chamber oxidize the substrate and separate the electrons from protons. These electrons and protons travel to the cathode, the former through an external circuit, and the latter by diffusing through the electrolyte and a PEM. The protons and electrons

subsequently combine at the cathode with oxygen, aided by a catalyst such as platinum, to form water. The final electron acceptors are as diverse as oxygen, ferricyanide, hydrogen peroxide and nitrate. The electrons retrieved from the microbial oxidation of the substrate are transferred to the anode in diverse ways such as by (1) direct electron transfer from the attached bacteria, (2) highly conductive nanowires produced by specific bacteria as a long distance transfer, and (3) an exogenous mediator or bacterial-origin mediator.

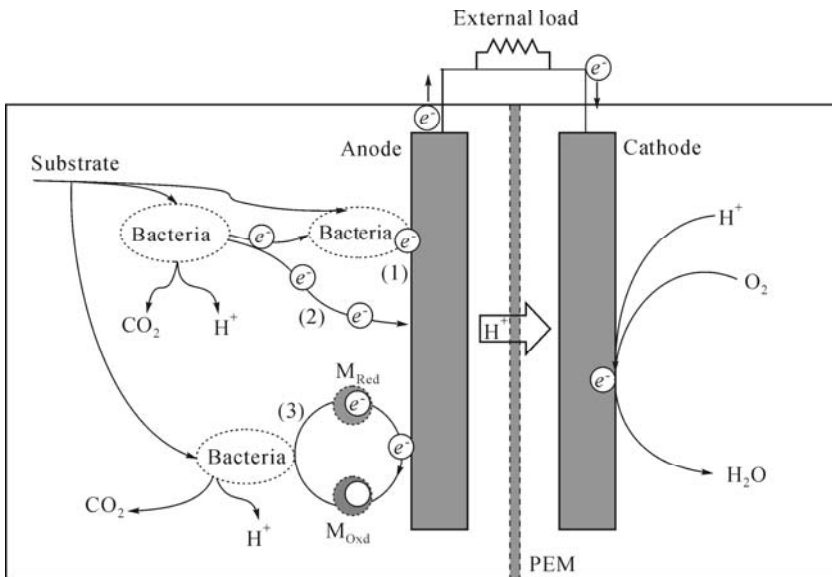


**Fig. 6.1.** Schematic diagram of a typical two-chambered microbial fuel cell PEM: proton exchange membrane;  $M_{\text{Red}}$ : reduced mediator;  $M_{\text{Oxd}}$ : oxidized mediator

### 6.2.2 Two-Chambered MFCs

A number of configurations for MFCs have been developed, which are run in batch, fed-batch, or continuous mode, having a variety of shapes. A two-chambered configuration is a typical MFC, which consists of an anode and a cathode chamber separated by a PEM such as Nafion<sup>[25,26]</sup> or Ultrex<sup>[27,28]</sup> so as to create a potential difference between them. The compartments can take various practical shapes.<sup>[29,30]</sup> The schematic diagrams of two-chambered MFCs are shown in Fig. 6.2. Organics are injected into the anode chamber under anaerobic conditions, while oxygen is supplied to the cathode chamber. Two-chambered MFCs are typically run in batch mode often with a chemically defined medium such as glucose or acetate solution to generate energy.

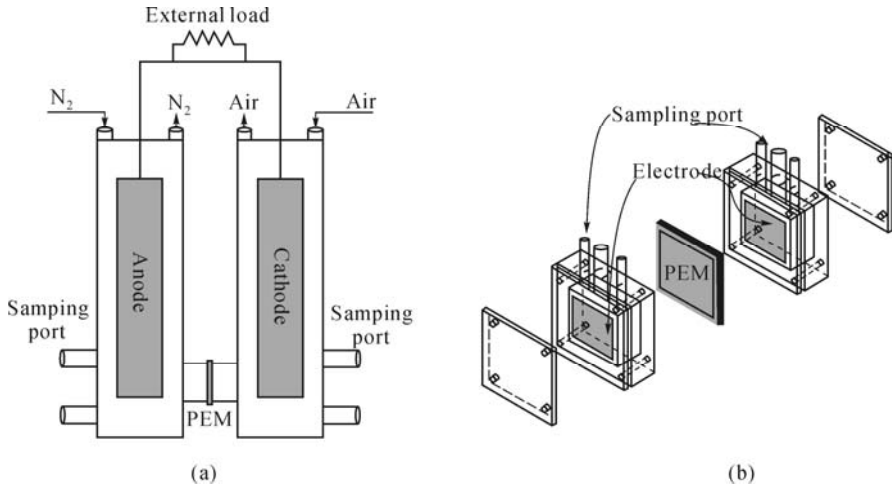


**Fig. 6.2.** Schematic diagrams of a two-chambered MFC in cylindrical shape (a) and rectangular shape (b)

### 6.2.3 *Single-Chambered MFCs*

MFCs are difficult to scale up, even though they can be operated in either batch or continuous mode. Single-chambered MFCs are quite attractive for increasing the power output because they can be run without artificial aeration in an open air cathode system and can reduce the internal ohmic resistance by avoiding the use of a catholyte as a result of combining two chambers. Very recently, Rabaey et al.<sup>[31]</sup> designed a single-chambered MFC consisting of an anode using graphite granules in a tubular anode chamber anode coupled with an outer cathode that is exposed directly to the air as shown in Fig. 6.3. In the absence of a cathodic chamber, catholyte is supplied to the cathode by dripping an electrolyte over the outer woven graphite material to keep it from drying up. The use of sustainable, open-air cathodes is critical to the practical implementation of such MFCs.

The membrane less configuration is the most significant advantage of single-chambered MFCs. However, many single-chambered MFCs still use Nafion as a physical separator, where Nafion is either hot-pressed directly onto the cathode or works as a membrane electrode assembly.<sup>[13,32]</sup> In this case, the use of a catholyte can be avoided but a Nafion membrane is still used normally. The undesirable back diffusion of oxygen from the cathode to the anode and microbial contamination of the cathode are the two major concerns with single-chambered MFCs. A substantial increase in oxygen transfer into the anode chamber in the absence of a PEM was reported.<sup>[13]</sup>

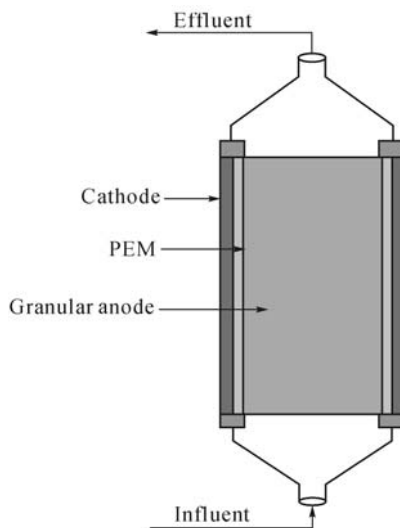


**Fig. 6.3.** Schematic diagram of a single-chambered MFC with outer cathode and inner anode consisting of graphite granules (Adapted from Ref. 31. Copyright (2005), with permission from ACS Publications)

### 6.2.4 Up-Flow Mode MFCs

Up-flow mode MFCs as shown in Fig. 6.4 are more suitable for wastewater treatment because they are relatively easy to scale up. On the other hand, fluid recirculation is used in this case. The energy cost of pumping fluid around is much greater than its power output. Therefore, its primary function is not power generation, but rather wastewater treatment. The MFC design in Fig. 6.4(a) offers a low internal resistance of  $4 \Omega$  because the anode and cathode are in close proximity over a large PEM surface area.<sup>[33]</sup> Jang et al. recently provided another design (Fig. 6.4(b)) of a MFC working in continuous flow mode.<sup>[9]</sup> A Plexiglas cylinder was partitioned into two sections by glass wool and glass bead layers. These two sections served as anodic and cathodic chambers, respectively. The disk-shaped graphite felt anode and cathode were placed at the bottom and at the top of the reactor, respectively.

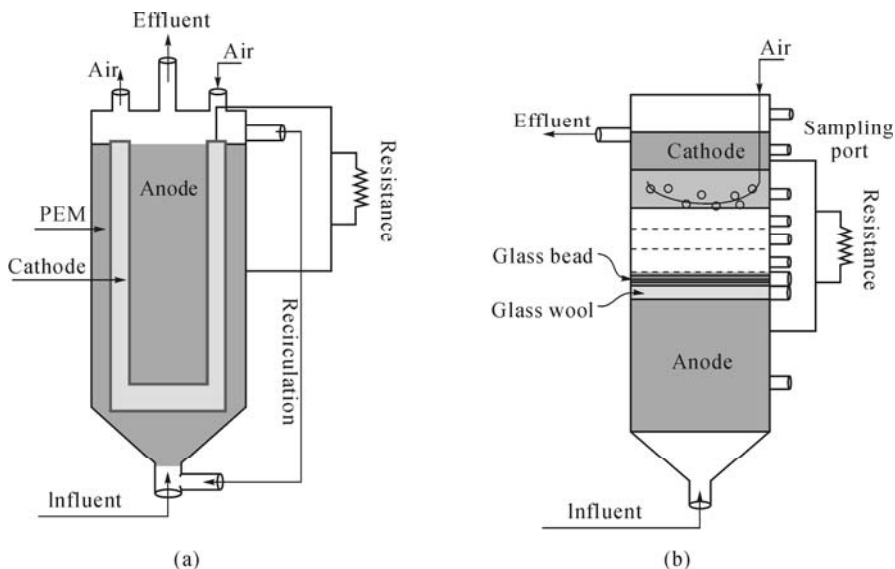


**Fig. 6.4.** Schematic diagrams of an up-flow MFC with cylindrical shape (Adapted from Ref. 9. Copyright (2004), with permission from Elsevier)

### 6.2.5 Stacked MFCs

The maximum theoretical power generated in an MFC can be calculated based on the substrate and catholyte. For example, the open circuit voltage (OCV) for acetate oxidation linked with oxygen utilization at the cathode is calculated to be  $\sim 1.1$  V.<sup>[6]</sup> However, a single MFC typically produces an OCV less than 0.8 V, and a working voltage of  $\sim 0.5$  V due to energy utilization by bacteria, electrode over potentials and high internal resistance. In order to increase overall voltage, MFCs can be stacked together (i.e., linked together in series) resulting in a nearly additive increase in total voltage.<sup>[34,35]</sup> A stacked MFC is shown in Fig. 6.5 for investigating performances of several MFCs connected in series and in parallel. Enhanced voltage or current output can be attained by connecting several MFCs in series or in parallel. Aelterman et al. found that 2.2 V (255 mA) could be generated using a six-cell MFC stack with ferricyanide as the catholyte (no mediator). While performance was sustained using continuous feeding, in some tests at high current densities they observed cell charge reversal, whereby the voltage in one cell abruptly reversed polarity.<sup>[34]</sup> The parallel-connected stack has higher short circuit current than the series connected stack, implying that a higher maximum bioelectrochemical reaction rate is allowed in the connection of MFCs in parallel than in series.

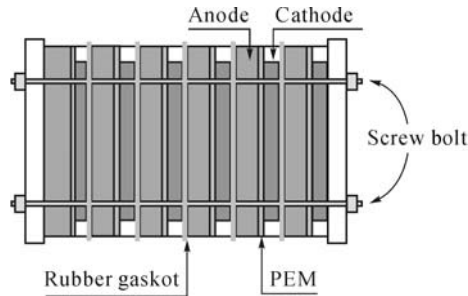


**Fig. 6.5.** Schematic diagram of stacked MFCs consisting of six individual units with granular graphite anode

## 6.3 Electrode Materials and Catalysts

In this section, two subjects will be introduced, including electrode materials and cathodic catalysts.

### 6.3.1 Electrode Materials

The MFC is currently considered to be a very popular and promising bio-source, producing electrochemical power for directly recovering electrical energy from carbohydrates as well as organics in wastewater.<sup>[36,37]</sup> However, the power output of the MFC is too low for practical applications, which is mainly due to the difficult electron transfer between bacterial cells and the extracellular electrode.<sup>[4,38]</sup> Therefore, a high-performance electrode material is most essential for practical applications. In particular, the anode material and its structure can directly affect the bacteria attachment, electron transfer and substrate oxidation. The specific materials for each compartment used in MFCs can affect the power density and coulombic efficiency (CE). The CE is defined as the ratio of total electrons recovered as current to maximum possible electrons, if all substrate removal produced current. Table 6.1 shows a summary of the basic components and materials of MFCs. The materials for the anode electrode must be non-corrosive, conducting, biocompatible and chemically stable in an electrolyte.<sup>[6,27]</sup>

To date, carbon materials such as carbon cloth and carbon paper are applied in most MFC electrodes because of their good stability in the microbial inoculum mixture, high conductivity and high specific surface area. Nonetheless, they have little electrocatalytic activity for the electrode microbial reactions. Modification of the carbon materials is the main approach for improving their performance. Many attempts have been made to increase the anode performance by adapting chemical and physical modification of electrode materials. Schörder et al. proposed a novel

MFC concept using polyaniline-modified platinum as an anode, which boosted the power output of the MFC to reach current density far above that described before.<sup>[39]</sup> Although the power density is high, this MFC system requires improvements to overcome the inherent drawbacks, such as the need for a potential-pulse operation to maintain the catalytic activity of the anode.<sup>[39]</sup> Recently, they investigated the properties of tungsten carbide as an anodic electrocatalyst for MFC application.<sup>[40,41]</sup> Qiao and co-workers reported the feasibility by using carbon nanotube/polyaniline composite as anode material for MFCs.<sup>[42]</sup>

Carbon nanotubes (CNTs) have emerged as new class nanomaterials because of their unique structure, high conductivity and high surface-to-volume ratio. Although such properties make them extremely attractive for fabricating electrodes,<sup>[43-45]</sup> CNTs have a cellular toxicity that could lead to proliferation inhibition and death of cells.<sup>[46,47]</sup> Hence, they are not suitable for MFCs unless modified to reduce the cellular toxicity. Recently, conducting polymer/CNTs composites have received great attention because the incorporation of CNTs in conducting polymers can lead to the production of new composite materials possessing the properties of each component with a synergistic effect.<sup>[48]</sup>

**Table 6.1** Basic components and materials for MFCs

Components	Materials	Remarks	References
Anode	Stainless steel mesh, Graphite, graphite felt, carbon paper, carbon-cloth, Pt, Pt black, reticulated vitreous carbon	Necessary	11,26,27,49
Cathode	Graphite, graphite felt, carbon paper, carbon-cloth, Pt, Pt black	Necessary	6,18,50,51
Anodic-chamber	Glass, polycarbonate, Plexiglas	Necessary	6,18,50,51
Cathodic-chamber	Glass, polycarbonate, Plexiglas	Optional	6,18,50,51
Ion exchange membrane	Proton exchange membrane: Nafion, Ultrex, polyethylene.poly (styrene-co-divinylbenzene); salt bridge, porcelain septum, or solely electrolyte	Necessary	28,29
Electrode catalyst	Pt, Pt black, MnO <sub>2</sub> , Fe <sup>3+</sup> , polyaniline, electron mediator immobilized on anode	Optional	52,53

### 6.3.2 *Cathodic Catalysts*

Expensive catalysts, such as platinum, are generally used to reduce the high overpotential for oxygen reduction in the cathode compartment.<sup>[52]</sup> Thus, researchers have searched for alternative cheaper catalysts that are as efficient as platinum in the MFC cathode reaction. The alternatives include ferric iron,<sup>[54,55]</sup> manganese oxides,<sup>[56]</sup> iron complexes<sup>[57]</sup> and cobalt complexes.<sup>[52,57]</sup> Recently,

noble metal-free catalysts, such as pyrolyzed iron phthalocyanine (FePc) or cobalt tetramethoxyphenylporphyrin (CoTMPP), and even non-catalysts showing comparable performance to a catalyzed cathode, have been applied with successful current generation,<sup>[53]</sup> as summarized in Table 6.2. In single-chambered MFCs, the effects of cathode catalysts (platinum and CoTMPP) and polymer binders (Nafion and polytetrafluoroethylene (PTFE), used for binding catalysts to the carbon surface) on power density have been analyzed.<sup>[52]</sup> The results suggested that the two catalysts showed similar performance; however, Nafion was superior to the other binders. It was also shown that the amount of Pt loaded on the cathode (from 0.1 to 2 mg·cm<sup>-2</sup>) did not substantially affect power density,<sup>[52]</sup> suggesting that cathodes used in MFCs can contain minimal Pt, and that Pt can be replaced with a non-precious metal catalyst, such as CoTMPP, with only slightly reduced performance. In another study, Zhao et al. compared oxygen reduction-dependent cathode currents with Pt, pyrolyzed iron(II) phthalocyanine (pyr-FePc), and pyr-CoTMPP as catalysts,<sup>[57]</sup> and also showed that the performance differences were not large. However, it is likely that these conclusions may not be applicable to more efficient MFCs not affected by other critical rate-limiting steps. For example, Zhao and co-workers also suggested that the physical and chemical environments (e.g., pH and ionic concentrations) severely affect the thermodynamics and kinetics of cathode oxygen reduction.<sup>[57]</sup>

**Table 6.2** Comparison of the power density and Coulombic efficiency obtained from MFCs with different cathodic catalysts (Adapted from Ref. 53. Copyright (2007), with permission from Elsevier)

Cathode material	Catalyst	Electron acceptor	Electrode sur-face area (cm <sup>2</sup> )	CE (%)	Power density (W·m <sup>-2</sup> )	Reference
Carbon paper	None	Air	11.3	NM <sup>a</sup>	0.064	14
Carbon paper	Pt (0.5 mg·cm <sup>-2</sup> )	Air	11.3	63 – 78	0.312	14
Carbon cloth	CoTMPP (2 mg·cm <sup>-2</sup> )	Air	30	NM <sup>a</sup>	13.88 <sup>b</sup>	62
Carbon cloth	None	Air	7	10-20	0.093 (W·m <sup>-2</sup> )	52e
Carbon cloth	Pt (0.5 mg·cm <sup>-2</sup> ) + CoTMPP(0.6 mg·cm <sup>-2</sup> )	Air	7	7.9 – 16.3	0.369 (W·m <sup>-2</sup> )	52e
Carbon cloth	CoTMPP (0.5 mg·cm <sup>-2</sup> )	Air	7	19.7	0.483 (W·m <sup>-2</sup> )	63e
Carbon cloth	FePc-KJB <sup>c</sup> (0.5 mg·cm <sup>-2</sup> )	Air	7	28.29	0.53 (W·m <sup>-2</sup> )	63e
Carbon cloth	Pt (1 mg·cm <sup>-2</sup> )	Air	7	19.6	0.474 (W·m <sup>-2</sup> )	63e
Graphite foil	FePc (2 mg·cm <sup>-2</sup> )	Air	30	NM <sup>a</sup>	14.32 <sup>b</sup>	62
Graphite foil	Pyr-FePc <sup>d</sup> (1 mg·cm <sup>-2</sup> )	Air	60	NM <sup>a</sup>	9.20	57e
Graphite granule	None	Air	1260	65	21	53

<sup>a</sup> NM: not mentioned; <sup>b</sup> Acidified catholyte (pH 3.3) was used; <sup>c</sup> FePc on Ketjenblack (KJB) carbon; <sup>d</sup> Pyrolyzed FePc; <sup>e</sup> Single-chambered MFC



Another MFC cathode option would be a biocathode, in which microorganisms catalyze cathodic reactions.<sup>[58]</sup> Biocathodes may have advantages over abiotic cathodes. For example, (1) construction and operation costs may be reduced, since costly catalysts (e.g., platinum) and mediators are not required and (2) denitrification could be coupled with the cathode reaction.<sup>[59]</sup> Interestingly, aerobic bacteria can also be used as cathode catalysts, so-called biocathodes. To date, several studies have examined the utility of biocathodes in MFCs.<sup>[23,60]</sup> Clauwaert et al. reported the combination of the anode of an acetate-oxidizing tubular MFC with an open-air biocathode for electricity production.<sup>[23]</sup> The biomineralization of manganese oxide and its resolubilization at the cathode surface had taken place in a biocathode chamber.<sup>[56,61]</sup> Rhoads and co-workers have shown that biomineralized manganese oxides, deposited by *Leptothrix discophora*, were electrochemically reduced at the cathode, demonstrating that these oxides are superior to oxygen when used as cathodic reactants in MFCs.<sup>[56]</sup>

## 6.4 Performance of Microbial Fuel Cells

In order to know the performance of MFCs, we should know the key parameters that define the performance of MFCs, and also should pay much attention to the effects of conditions when operating MFCs.

### 6.4.1 Parameters Defining the Performance of MFCs

The performance of MFCs is affected by various operational parameters such as substrate, electrode, PEM and electrolyte strength. The power output cannot reach the theoretical value due to the overpotential related to ohmic, activation and concentration losses. These losses can be reduced by optimizing the reactor configuration, such as minimizing the electrode spacing, applying a high protons-selective membrane, increasing the electrode surface area and improving catalyst activity.<sup>[64,65]</sup> Fig. 6.6 summarizes the potential losses that occur during electron transfer in an MFC.

**The substrate conversion rate:** The ideal performance of an MFC could be affected mainly by the electrochemical reactions that occur between the organic substrate at a low potential such as glucose and the final electron acceptor with a high potential, such as oxygen.<sup>[16]</sup> Concentration polarization is a loss of potential due to the inability to maintain the initial substrate concentration in the bulk fluid. A good MFC bioreactor should minimize concentration polarization by enhancing mass transfer. This depends on the amount of bacterial cells, the mixing and mass transfer phenomena in the reactor, the bacterial kinetics ( $\mu_{max}$ , the maximum specific growth rate of the bacteria, and  $K_s$ , the bacterial affinity constant for the

substrate), the biomass organic loading rate (g substrate per g biomass present per day),<sup>[28]</sup> the efficiency of the PEM for transporting protons and the potential over the the MFC.<sup>[9,13]</sup>

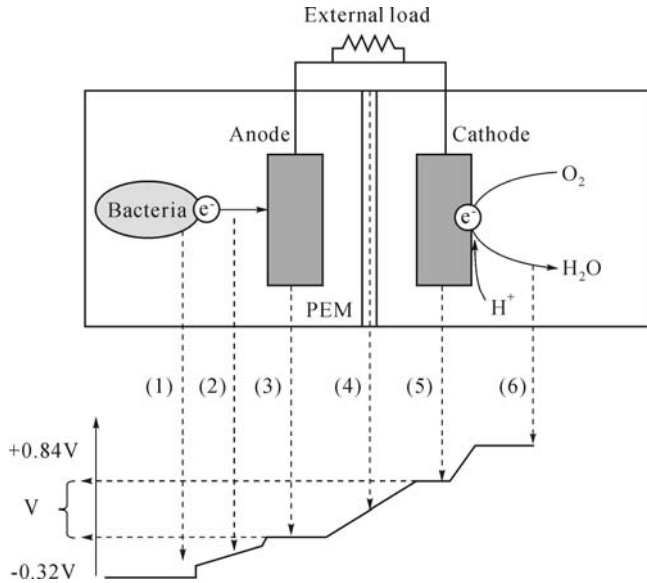


**Fig. 6.6.** Various potential losses during electron transfer in an MFC. (1) Losses due to bacterial electron transfer; (2) Losses due to electrolyte resistance; (3) Losses at the anode; (4) Losses at the MFC resistance and membrane resistance losses; (5) Losses at the cathode; (6) Losses due to electron acceptor reduction

**Overpotentials at the anode:** Parameters influencing the overpotentials are the electrode surface, the electrochemical characteristics of the electrode, the electrode potential and the kinetics, together with the mechanism of the electron transfer and the current of the MFC. In order to achieve a better performance of MFCs, the anode material should have a larger surface area with relatively fewer activation losses.<sup>[27]</sup> Carbon-based materials (e.g., carbon cloth or graphite felt) are frequently used for anodes because of their stability in microbial culture media, high electric conductivity and large surface area. In some cases, carbon-based anodes modified with metals and/or metal oxides increased power production in MFCs.

**Overpotentials at the cathode:** Cathodic overpotential caused by a lack of dissolved-oxygen (DO) for the cathodic reaction confines the power density output of some MFCs.<sup>[14]</sup> Similar to the losses observed at the anode, the cathode exhibits significant potential losses. To remedy this, several researchers have used hexacyanoferrate solutions.<sup>[26,28,66]</sup> However, hexacyanoferrate is not completely reoxidized by oxygen in the air, and should be considered as an electron acceptor rather than a mediator.<sup>[67]</sup> To be sustainable, MFC cathodes should be open-air cathodes.<sup>[14,68,69]</sup>

**The proton exchange membrane performance:** Although Nafione PEMs are used in most MFC studies, Nafione PEMs are sensitive to biofouling (e.g., by ammonium). The best result was obtained using an Ultrex PEM.<sup>[29]</sup> The ratio of PEM surface area to system volume is important for the power output. The PEM surface area has a large impact on maximum power output if the power output is below a critical threshold. The MFC internal resistance decreases with increasing PEM surface area over a relatively large range.<sup>[70]</sup>

**Internal resistance of the MFC:** The internal resistance of the MFC depends on both the resistance of the electrolyte between the electrodes and by the membrane resistance (in fact, Nafione has the lowest resistance). The resistance to the flow of ions in electrolytes and the electron flow between the electrodes cause Ohmic losses. Dominant ohmic loss in electrolytes can be reduced by shortening the distance between the two electrodes and by increasing the ionic conductivity of the electrolytes.<sup>[71]</sup> PEMs produce a transmembrane potential difference that also constitutes a major resistance. For optimal operation, anode and cathode need to be together as close as possible.<sup>[69]</sup> Proton migration also significantly influences resistance-related losses.<sup>[11]</sup> Proper mixing could minimize these losses.

#### 6.4.2 *Effects of Conditions When Operating MFCs*

The performance of an MFC is affected by many factors including microbe type, fuel biomass type and concentration, electrode material, proton exchange system, pH, DO concentration, ionic strength and reactor configuration.<sup>[72]</sup> Table 6.3 summarizes the performance obtained from various studies. With a given MFC system, the following operating parameters can be regulated to decrease the polarizations, in order to enhance the performance of an MFC. Several studies showed at least one order of magnitude difference in the power density, even in cases of MFCs using a similar seed culture and substrate.

**Table 6.3** Performances obtained from the various operating conditions of MFCs

MFC Configuration	Operating mode	Electron donor (g COD·L <sup>-1</sup> )	Electron acceptor	PEM	CE (%)	Power density <sup>c</sup>	Ref.
Two-chambered	Fed-batch	Acetate (0.056)	Air	Nafion 117	82	14 mW·m <sup>-2</sup>	73
Two-chambered	Fed-batch	Glucose (1.92)	Ferricyanide	Nafion 117	81	31 mW·m <sup>-2</sup>	27
Two-chambered	Continuous	Glucose (1.0)	Air	Nafion 117	14	220 mW·m <sup>-2</sup>	69 <sup>b</sup>
Two-chambered	Continuous	Glucose (1.0)	Ferricyanide	Ultrex	20	37 W·m <sup>-3</sup>	74 <sup>c</sup>

(Continued)

MFC Configuration	Operating mode	Electron donor (g COD·L <sup>-1</sup> )	Electron acceptor	PEM	CE (%)	Power density <sup>e</sup>	Ref.
Two-chambered	Continuous	Acetate (1.61)	Ferricyanide	Ultrex	65	21 W·m <sup>-3</sup>	53 <sup>c</sup>
Two-chambered	Fed-batch	Ethanol (0.093)	Air	Nafion 117	61	40 mW·m <sup>-2</sup>	32
Two-chambered	Continuous	Wastewater (4.316)	Ferricyanide	Nafion 117	NM <sup>a</sup>	119.3 mW·m <sup>-2</sup>	75
Two-chambered	Continuous	Wastewater (4.316)	Air	Nafion 117	NM <sup>a</sup>	82.3 mW·m <sup>-2</sup>	75
Single-chambered	Fed-batch	Glucose (NM <sup>b</sup> )	Air	Nafion 117	28	262 mW·m <sup>-2</sup>	13
Single-chambered	Fed-batch	Glucose (NM <sup>b</sup> )	Air	None	20	494 mW·m <sup>-2</sup>	13
Single-chambered	Continuous	Wastewater (0.2)	Air	Nafion 117	12	26 mW·m <sup>-2</sup>	76
Single-chambered	Fed-batch	Acetate (0.76)	Air	None	31	506 mW·m <sup>-2</sup>	12
Single-chambered	Fed-batch	Glucose (0.54)	Air	None	32	766 mW·m <sup>-2</sup>	77
Single-chambered	Fed-batch	Acetate (0.95)	Air	None	61	1,970 mW·m <sup>-2</sup>	78
Single-chambered	Fed-batch	Ethanol (0.47)	Air	None	10	488 mW·m <sup>-2</sup>	32
Single-chambered	Fed-batch	Acetate (0.95)	Air	None	60	2,400 mW·m <sup>-2</sup>	79 <sup>d</sup>
Up-flow	Continuous	Sucrose (0.57)	Hexa-Cyanoferrate	Ultrex	51	29 W·m <sup>-3</sup>	58 <sup>c</sup>

<sup>a</sup> Not mentioned; <sup>b</sup> Flat plate microbial fuel cell; <sup>c</sup> Granular graphite as the anode material; <sup>d</sup> Graphite fiber brush anode electrode was installed to obtain much higher surface area; <sup>e</sup> mW·m<sup>-2</sup>: surface power density unit; W·m<sup>-3</sup>: volume power density unit.

#### 6.4.2.1 Effect of Electrode Material

In order to achieve a better performance of MFCs, the anode material should have a larger surface area with relatively fewer activation losses.<sup>[27]</sup> The level of current generation is proportional to the electrode surface areas: a threefold higher current was generated with graphite felt (200 cm<sup>2</sup> as geometric surface area) than with graphite rods (65 cm<sup>2</sup>).<sup>[27]</sup> Using better performing electrode materials can improve the performance of an MFC because different anode materials result in different activation polarization losses. Pt and Pt black electrodes are superior to graphite, graphite felt and carbon cloth electrodes for both anode and cathode constructions, but their costs are much higher. Schröder et al. reported that a

current of 2 – 4 mA could be achieved with platinumized carbon cloth anode in an agitated anaerobic culture of *E. coli* using a standard glucose medium at  $0.55 \text{ mmol}\cdot\text{L}^{-1}$ , while no microbially facilitated current flow is observed with the unmodified carbon cloth with the same operating conditions.<sup>[39]</sup> Pt also has a higher catalytic activity with regard to oxygen than graphite materials. MFCs with Pt or Pt-coated cathodes yielded higher power densities than those with graphite or graphite felt cathodes.<sup>[2,9,14]</sup>

Modification of the anode with conductive polymers has also been conducted. Among these polymers, polyaniline (PANI) has been used most frequently. Schröder and co-workers reported that a platinum electrode covered with PANI achieved a current density one order of magnitude higher than that of an untreated electrode in an MFC inoculated with *E. coli*.<sup>[39]</sup> Modified PANI polymers, such as fluorinated PANI,<sup>[80]</sup> PANI/carbon nanotube composite<sup>[42]</sup> and PANI/titanium dioxide composite<sup>[81]</sup> were employed to yield higher current densities.

Electrode modification is actively investigated by several research groups to improve MFC performances. Park and Zeikus reported an increase of 100-fold in current output by using neutral red (NR)-woven graphite and Mn(IV) graphite anode compared to the woven graphite anode alone.<sup>[54,66]</sup> NR and Mn(IV) served as mediators in their MFC reactors. Doping ions such as Fe(III) and/or Mn(IV) in the cathode also facilitated the cathodic reactions, resulting in improved electricity generation. A four times higher current can be achieved with the combination of Mn(IV)-graphite anode and  $\text{Fe}^{3+}$  graphite cathode compared to plain graphite electrodes.<sup>[4,26,66]</sup> One drawback of using Pt or Pt black electrodes is that their activities are reduced by the formation of a PtO layer at the electrode surface at positive potentials. As another approach, a gold electrode was coated with a self-assembled monolayer and used as an anode in an MFC inoculated with *Shewanella putrefaciens*.<sup>[82]</sup> Currents produced with gold electrodes coated with various alkanethiol SAMs were compared to those produced with glassy carbon electrodes.<sup>[82]</sup> It was revealed that current production correlated to monolayer molecular chain length and head-group, with certain head groups enhancing electronic coupling to the bacteria. Recently, a graphite felt coated with a polymer (polyethyleneimine) and a mediator (9,10-anthraquinone-2,6-disulfate) was used as an anode in a *Geobacter*-inoculated MFC, and showed a current density of  $1.2 \text{ A}\cdot\text{m}^{-1}$ .<sup>[2,83]</sup>

#### 6.4.2.2 Effect of Proton Exchange Membrane

In MFCs, the efficiency of proton transfer from the anode to the cathode significantly affects the power output. Electrons migrate to the cathode depending on the potential gradient, while protons are transferred to the cathode by diffusion, which is slower than the electron transfer. Thus, proton transfer is the rate-limiting step and a major cause of internal resistance.<sup>[6,84]</sup> In addition, although a PEM is necessary for generating a potential gradient between the anode and the cathode

chambers, it also acts as a proton transfer barrier.

Nafion (manufactured by DuPont, Wilmington, Delaware, USA) is the most popular membrane because of its highly selective permeability of protons. Despite many attempts by researchers to look for less expensive and more durable substitutes, Nafion is still the best choice. However, the side effect of other cations transport is unavoidable during the MFC operation even with Nafion. In a batch accumulative system, for example, transportation of cation species other than protons by Nafion dominates the charge balance between the anodic and cathodic chambers because the concentrations of  $\text{Na}^+$ ,  $\text{K}^+$ ,  $\text{NH}_4^+$ ,  $\text{Ca}^{2+}$ , and  $\text{Mg}^{2+}$  are much higher than the proton concentrations in the anolyte and catholyte.<sup>[85]</sup> In this sense, Nafion as well as other PEMs used in the MFCs are not necessarily proton-specific membranes but actually cation-specific membranes.

The ratio of PEM surface area to system volume is also important because it governs the internal resistance of an MFC as a consequence of mass transport (e.g., protons and ions) through the PEM. Oh and Logan reported that the power density increases with increasing PEM surface area ( $45 \text{ mW}\cdot\text{m}^{-2}$  at  $3.5 \text{ cm}^2$ ,  $68 \text{ mW}\cdot\text{m}^{-2}$  at  $6.2 \text{ cm}^2$ , and  $190 \text{ mW}\cdot\text{m}^{-2}$  at  $30.6 \text{ cm}^2$ ).<sup>[70]</sup>

### 6.4.2.3 Effect of pH Buffer and Electrolyte

Proton-transfer efficiency counts on the type of PEM (or a similar membrane that separates the anode and cathode), the type and concentration of buffer, and the distance between the two electrodes.<sup>[7]</sup> Slow proton transfer also affects reaction rates at the anode and cathode. The accumulation of protons may suppress microbial activity related to organic oxidation at the anode,<sup>[84]</sup> while low proton availability reduces the cathode reaction. Very recently, Torres and co-workers investigated how proton transport inside a biofilm can limit electrical current generation by anode-respiring bacteria.<sup>[84]</sup> The researchers focused on the mechanism of protons transfer, and revealed that they were mainly transported out of the biofilm by protonating the conjugate base of the buffer system (e.g., phosphate and carbonate). If a buffer solution is not used in a working MFC, there will be a clear pH difference between the anodic and cathodic chambers, though theoretically there will be no pH shift when the reaction rate of protons, electrons and oxygen at the cathode equals the production rate of protons at the anode.

The PEM is responsible for a transport barrier to the cross membrane diffusion of the protons, and proton transport through the membrane is slower than its production rate in the anode and its consumption rate in the cathode chambers at the initial stage of MFC operation, thus brings a pH difference.<sup>[11]</sup> However, the pH difference increases the driving force of the proton diffusion from the anode to the cathode chamber and finally a dynamic equilibrium forms. Gil and co-workers found a pH difference of 4.1 (pH 9.5 at cathode and pH 5.4 in anode) after 5 h operations with an initial pH of 7 without buffering. With the addition of a phosphate buffer (pH 7.0), pH shifts at the cathode and anode were both less than 0.5 unit and the current output increased *ca.* 1 fold to 2 folds.<sup>[11]</sup> The buffer

treatment compensated the slow proton transport rate and improved the proton availability for the cathodic reaction.

A decrease in pH in the anodic chamber due to proton accumulation during substrate degradation and a corresponding increase in pH in the cathodic chamber of prolonged-run MFCs is a common PEM-associated problem.<sup>[42,83]</sup> Recently, lower activation energy for oxygen reduction and enhanced power output was suggested at a relatively lower pH of the catholyte.<sup>[39,60]</sup> Jang et al. found that the current output increased by about one fold when an HCl solution was added to the cathode.<sup>[9]</sup> This again confirms the fact that the proton availability to the cathode is a limiting factor in electricity generation.

#### 6.4.2.4 Operating Conditions in the Anodic Chamber

The electrochemically active bacteria on the anode in MFCs are widely referred to as electricigens,<sup>[18]</sup> anodophilic bacteria<sup>[6]</sup> and exoelectrogens,<sup>[17]</sup> based on their capability for exocellular transfer electrons to the electrodes without resort to exogenous mediators. They can completely oxidize organic compounds to carbon dioxide with the electrode serving as the sole electron acceptor. Fuel biomass type, concentration and feed rate are important factors that impact the performance of an MFC. With a given microbe or microbial consortium, power density varies greatly using different substrates. Table 6.4 shows the applications of some MFCs operated using different microbes and substrates. Many systems have shown that electricity generation is dependent on substrate concentration both in batch and continuous-flow mode MFCs. Usually, a higher substrate concentration gives a higher power output in a wide concentration range.

Electron transfer can occur either through membrane-associated components,<sup>[28]</sup> soluble electron shuttles generated by specific bacteria,<sup>[85]</sup> or highly conductive nanowires.<sup>[86]</sup> The mechanisms for electron transfer to the electrodes recently were reviewed respectively by Lovley<sup>[18]</sup> and Schröder<sup>[22]</sup>. The properties of well-known electrochemically active bacteria, such as *Shewanella putrefaciens*, *Geobacteraceae sulfurreducens* and *Geobacter metallireducens* are well described.<sup>[54,85,87]</sup>

Park and Zeikus reported that a higher current level was attained with increasing lactate (fuel) concentration up to a point in excess of 200 mmol·L<sup>-1</sup> in a single-compartment MFC inoculated with *S. putrefaciens*.<sup>[54]</sup> Moon et al. investigated the effects of substrates concentration on the performance of an MFC.<sup>[2]</sup> The study also demonstrated that the power density increased with the increase in substrate concentration.<sup>[2]</sup> Gil and co-workers found that the current increased with a wastewater concentration up to 50 mg·L<sup>-1</sup> in their MFC.<sup>[11]</sup> Interestingly, the electricity generation in an MFC often peaks at a relatively low level of feed rate before heading downward. This may be because a high feed rate promoted the growth of fermentative bacteria faster than those of the electrochemically active bacteria in a mixed culture.<sup>[2,28,29]</sup>

**Table 6.4.** Microbes and substrates used in MFCs

Microbes	Substrate	Application	Reference
<i>Actinobacillus succinogenes</i>	Glucose	Neutral red or thionin as electron mediator	4,26
<i>Aeromonas hydrophila</i>	Acetate	Mediator-less MFC	90
<i>Clostridium butyricum</i>	Starch	Fermentative bacterium	80
<i>Desulfovibrio desulfuricans</i>	Sucrose	Sulphate/sulphide as mediator	91
<i>Erwinia dissolvens</i>	Glucose	Ferric chelate complex as mediators	92
<i>Escherichia coli</i>	Glucose	Methylene blue as mediator	39,91,93
<i>Geobacter metallireducens</i>	Acetate	Mediator-less MFC	29
<i>Geobacter sulfurreducens</i>	Acetate	Mediator-less MFC	86
<i>Gluconobacter oxydans</i>	Glucose	HNQ, resazurin or thionine as mediators	94
<i>Klebsiella pneumoniae</i>	Glucose	HNQ as mediator biominedralized manganese as electron acceptor	56
<i>Lactobacillus plantarum</i>	Glucose	Ferric chelate complex as mediators	92
<i>Proteus mirabilis</i>	Glucose	Thionin as mediator	3
<i>Pseudomonas aeruginosa</i>	Glucose	Pyocyanin and phenazine-1-carboxamide as mediators	88
<i>Rhodospirillum rubrum</i>	Glucose	Mediator-less MFC	27
<i>Shewanella oneidensis</i>	Lactate	Anthraquinone-2,6-disulfonate (AQDS) as mediator	95
<i>Shewanella putrefaciens</i>	Lactate	Mediator-less MFC	54,96
<i>Streptococcus lactis</i>	Glucose	Ferric chelate complex as mediators	92

#### 6.4.2.5 Operating Conditions in the Cathodic Chamber

Reaction efficiency of a cathode depends on the concentration and species of the oxidant (electron acceptor), proton availability, catalyst performance and electrode structure. Oxygen is most commonly used as an electron acceptor in MFCs for the cathodic reaction, since it is free from toxic end products. Power output of an MFC greatly counts on the concentration level of electron acceptors. Several studies indicated that DO was a major limiting factor when it remained below the air-saturated level.<sup>[11,14,68]</sup> Surprisingly, a catholyte sparged with pure oxygen that gave 38 mg·L<sup>-1</sup> DO did not further increase the power output compared to that of the air-saturated water (at 7.9 mg·L<sup>-1</sup> DO).<sup>[14,68,69]</sup> The rate of oxygen diffusion toward the anodic chamber goes up with the DO concentration. Thus, part of the substrate is consumed directly by the oxygen instead of transferring the electrons through the electrode and the circuit.<sup>[68]</sup>



The cathode reaction is inefficient when plain carbon or graphite is used as the electrode.<sup>[21]</sup> Therefore, it is necessary to coat it with catalysts (e.g., platinum). One study reported that a platinum modification resulted in a 3- to 4-fold higher current than that with a plain graphite cathode.<sup>[68]</sup> Furthermore, the critical oxygen concentration (below which the catalytic reaction decreases) of the Pt-modified cathode was much lower than that of the plain graphite cathode (2.0 mg·L<sup>-1</sup> vs. 6.6 mg·L<sup>-1</sup>).<sup>[68]</sup> This improvement is considered significant, since oxygen diffusion in the cathode chamber can limit the cathode reaction.

Power density increased greatly using ferricyanide as the electron acceptor in the cathodic chamber. So far, reported cases with very high power densities such as 7200 mW·m<sup>-2</sup>, 4310 mW·m<sup>-2</sup> and 3600 mW·m<sup>-2</sup> all used ferricyanide in the cathodic chamber,<sup>[14,28,39]</sup> while power density of less than 1,000 mW·m<sup>-2</sup> was reported in studies using DO regardless of the electrode material. This is likely due to the greater mass transfer rate and lower activation energy for the cathodic reaction offered by ferricyanide.<sup>[14]</sup> As a consequence, aeration is no longer needed for single-chambered MFCs with a cathode that is directly exposed to air.

## 6.5 Metabolism in Microbial Fuel Cells

Theoretically, most microbes can potentially be used as a biocatalyst in MFC. The microbes utilize organic compounds as energy and carbon sources. In order to generate energy for growth, organics are decomposed and chemical energy is released. In addition, high-energy electrons released from organics are transferred to electron acceptors to conserve electrochemical energy produced through the respiration process. In MFCs, electrons released from organics are initially accepted by intercellular electron-shuttling compounds (e.g., nicotinamide adenine dinucleotide (NAD)), and subsequently transferred to electron acceptors via respiratory electron transport chains. If electrons released from organics can be transferred from any step in the intercellular electron transfer pathway to an anode, then microbial oxidation of organics can be coupled with electricity generation (i.e., an MFC).<sup>[7]</sup> At high anodic potentials, bacteria can use the respiratory chain in an oxidative metabolism. Electrons and, concomitantly, protons can be transported through the NADH dehydrogenase, ubiquinone, coenzyme Q or cytochrome.<sup>[97]</sup> The use of this pathway was intensively investigated by Kim et al.<sup>[89]</sup> They observed that the generation of electrical current from an MFC was prevented by various inhibitors in the respiratory chain. The electron transport system in their MFC used NADH dehydrogenase, Fe/S (iron/sulphur) proteins and quinones as electron carriers, but does not use site 2 of the electron transport chain or the terminal oxidase. Processes using oxidative phosphorylation have regularly been observed in MFCs, yielding high energy efficiencies of up to 65%.<sup>[28]</sup> Examples include *Pseudomonas aeruginosa*, *Enterococcus faecium*<sup>[88]</sup> and *Rhodospirillum rubrum*.<sup>[27]</sup> An overview of different bacterial species and their electron transport pathway is given in Table 6.5.

**Table 6.5.** Bacterial species identified in microbial fuel cells and their possible metabolism and pathway of electron transfer

Metabolic type	Transfer type	Examples of organisms	Terminal bacterial electron shuttle	Added redox shuttle	Reference
Oxidative metabolism	Membrane-driven	<i>Rhodospirillum rubrum</i>	Unknown		27
Oxidative Metabolism	Membrane-driven	<i>Geobacter sulfurreducens</i>	89 kDa <i>c</i> -type cytochrome <sup>a</sup>		86
Oxidative Metabolism	Membrane-driven	<i>Aeromonas hydrophila</i>	<i>c</i> -type cytochrome <sup>a</sup>		90
Oxidative Metabolism	Mediator-driven	<i>Escherichia coli</i>	Hydrogenase	Neutral red	98
Oxidative Metabolism	Mediator-driven	<i>Shewanella putrefaciens</i>	Quinones <sup>a</sup>		96,99
Oxidative Metabolism	Mediator-driven	<i>Pseudomonas aeruginosa</i>	Pyocyanin, phenazine carboxamide		31
Oxidative Metabolism	Mediator-driven	<i>Erwinia dissolvens</i>	Unknown	Fe(III) CyDTA (an iron chelator)	92
Oxidative metabolism	Mediator-driven	<i>Desulfovibrio desulfuricans</i>	S <sup>2-</sup>		100
Fermentative metabolism	Membrane-driven	<i>Clostridium butyricum</i>	Cytochromes <sup>a</sup>		101
Fermentative metabolism	Mediator-driven	<i>Enterococcus faecium</i>	Unknown	Pyocyanin	31

<sup>a</sup> Putative

The microbes transfer electrons to the electrode through an electron transport system that either consists of a series of components in the bacterial extracellular matrix or together with electron shuttles dissolved in the bulk solution. *Geobacter* belongs to dissimilatory metal-reducing microorganisms, which produce biologically useful energy in the form of adenosine triphosphate (ATP) during the dissimilatory reduction of metal oxides under anaerobic conditions in soils and sediments. The electrons are transferred to the final electron acceptor, such as Fe<sub>2</sub>O<sub>3</sub>, mainly by direct contact of mineral oxides and the metal reducing microorganisms.<sup>[102,103]</sup> Such mediators penetrate bacterial cells in an oxidized form, interact with reducing agents within the cell (e.g., NADH, NADPH and reduced cytochromes) and are reduced. The reduced mediators diffuse out of the cells, and the anode surface is then oxidized by the release of electrons.<sup>[102]</sup>

## 6.6 Applications

New type of electricity production from renewable resources without a net carbon

dioxide emission is greatly desired.<sup>[18]</sup> MFCs are devices that exploit microbial catabolic activities to generate electricity from various materials, including complex organic waste and renewable biomass. These sources provide MFCs with a great advantage over chemical fuel cells that can utilize only purified reactive fuels. Locally supplied biomass can be used to provide renewable power for local consumption. Applications of MFCs in a spaceship are also possible since they can provide valuable electricity while degrading wastes generated onboard. Some scientists envision that in the future a miniature MFC can be implanted in a human body to power an implantable medical device with the nutrients supplied by the human body.<sup>[104]</sup>

In addition, an MFC can harness energy in the form of hydrogen. The MFC can be modified to produce hydrogen instead of electricity. This modified system, which was recently suggested and referred to as biocatalyzed electrolysis<sup>[105]</sup> or a bio-electrochemically assisted microbial reactor process,<sup>[106]</sup> or electrohydrogenesis,<sup>[107]</sup> has been considered an interesting new technology for the production of biohydrogen from organics. The modified MFCs have many advantages over the technologies currently used to generate hydrogen from organic matter. First, the direct conversion of the substrate to hydrogen makes high conversion efficiency possible. In addition, the high purity of hydrogen produced is another advantage over other methods for producing biohydrogen from organic materials containing a diverse mixture of biogases or other impurities (e.g. CH<sub>4</sub>, CO<sub>2</sub>, H<sub>2</sub>S, NH<sub>3</sub>), which require expensive gas purification.<sup>[108]</sup> Another advantage is that hydrogen can be accumulated and stored for later usage to overcome the inherent low power feature of the MFCs. Therefore, MFCs provide a renewable hydrogen source that can contribute to the overall hydrogen demand in a hydrogen economy.<sup>[109]</sup>

MFCs have attracted considerable attention over the last decade as a sustainable technology for simultaneous electricity generation and wastewater treatment. Electricity generation using a variety of biodegradable materials including not only pure chemicals, such as acetate, glucose, cysteine and ethanol, but also wastewater, such as swine wastewater, food processing wastewater, domestic wastewater and corn stover, has been reported.<sup>[12,27,32,38,69,75]</sup> With the great energy demand for wastewater treatment, an MFC-based wastewater treatment system has wide applications because wastewater must be treated and the substrate is free. MFCs can enhance the growth of bioelectrochemically active microbes during wastewater treatment. Thus they have good operational stabilities. Continuous flow and single-chambered MFCs and membrane-less MFCs are favored for wastewater treatment, due to concerns in scale-up.<sup>[9,36]</sup>

One of the most exciting discoveries in MFC research was the development by Reimers and Tender of an MFC that can harvest electricity from the organic matter in aquatic sediments.<sup>[110,111]</sup> MFCs can provide an in situ power source for electronic devices in remote areas, such as the ocean and the bottom of deep-water, where it is difficult to have routine access to replace traditional batteries.<sup>[6,20]</sup> A good example is sediment MFC with the most well-known being the benthic unattached generator (BUG), in which the anode is buried in anoxic or anaerobic marine sediments connected to a cathode suspended in the overlying aerobic water.

Another potential application of MFC technology is to use it as a biosensor for pollutant analysis and in situ process monitoring and control.<sup>[112,113]</sup> The proportional correlation between the Coulombic yield of MFCs and the strength of the wastewater makes it possible to apply MFCs for biological oxygen demand (BOD) sensors.<sup>[114]</sup> A MFC using *Shewanella* as a biocatalyst was demonstrated to be an effective sensor for quantifying the BOD.<sup>[112,113,114]</sup> MFC-type of BOD sensors are advantageous over other types of BOD sensor because they have excellent operational stability and good reproducibility and accuracy.

## 6.7 Summary

MFCs are a hybrid bio-electrochemical system, which converts bio-substrate directly into electricity by the oxidation of organic matter in the presence of bacteria under ambient temperature/pressure conditions. The potential, developed between the bacterial metabolic activity and electron acceptor condition, separated by a manifests bioelectricity generation. The achievable power output from MFCs has increased remarkably by modifying their designs, such as the optimization of the MFC configurations, their physical and chemical operating conditions, and their choice of biocatalyst. More recently, selecting the proper materials, such as the anode-cathode electrodes and a PEM is one of the critical challenges for applications of MFCs. The specific materials for each chamber used in an MFC can affect the power density and coulombic efficiency. Furthermore, the practical application of technologies provides tremendous scope for an increase in cell efficiency by optimizing parameters, like the spacing between the electrodes, cathode suitability for varying MFC designs.

## Acknowledgment

This work was supported by a National Research Foundation of Korea Grant funded by the Korean Government (2009-0066808).

## References

- [1] Allen, R. M., Bennetto, H. P. *Appl. Biochem. Biotechnol.*, 1993, 39: 27.
- [2] Moon, H., Chang, I. S., Kim, B. H. *Bioresource Technol.*, 2006, 97: 621.
- [3] Choi, Y., Jung, E., Kim, S., Jung, S. *Bioelectrochemistry*, 2003, 59: 121.
- [4] Park, D. H., Zeikus, J. G. *Appl. Environ. Microb.*, 2000, 66: 1292.
- [5] Oh, S. E., Logan, B. E. *Water Res.*, 2005, 39: 4673.

- [6] Logan, B. E., Hamelers, B., Rozendal, R., Schroder, U., Keller, J., Freguia, S., Alterman, P., Verstraete, W., Rabaey, K. *Environ. Sci. Technol.*, 2006, 40: 5181.
- [7] Watanabe, K. *J. Biosci. Bioeng.*, 2008, 106: 528.
- [8] Pham, T. H., Rabaey, K., Aelterman, P., Clauwaert, P., De Schampelaire, L., Boon, N., Verstraete, W. *Eng. Life Sci.*, 2006, 6: 285.
- [9] Jang, J. K., Pham, T. H., Chang, I. S., Kang, K. H., Moon, H., Cho, K. S., Kim, B. H. *Process Biochem.*, 2004, 39: 1007.
- [10] You, S. J., Zhao, Q. L., Zhang, J. N., Jiang, J. Q., Zhao, S. Q. *J. Power Sources*, 2006, 162: 1409.
- [11] Gil, G. C., Chang, I. S., Kim, B. H., Kim, M., Jang, J. K., Park, H. S., Kim, H. *J. Biosens. Bioelectron*, 2003, 18: 327.
- [12] Liu, H., Cheng, S., Logan, B. E. *Environ. Sci. Technol.*, 2005, 39: 658.
- [13] Liu, H., Logan, B. E. *Environ. Sci. Technol.*, 2004, 38: 4040.
- [14] Oh, S., Min, B., Logan, B. E. *Environ. Sci. Technol.*, 2004, 38: 4900.
- [15] Du, Z. W., Li, H. R., Gu, T. Y. *Biotech. Adv.*, 2007, 25: 464.
- [16] Rabaey, K., Verstraete, W. *Trends Biotechnol.*, 2005, 53: 291.
- [17] Logan, B. E., Regan, J. M. *Trends Microbiol.*, 2006, 14: 512.
- [18] Lovley, D. R. *Curr. Opin. Biotechnol.*, 2006, 17: 327.
- [19] Chang, I. S., Moon, H., Bretschger, O., Jang, J. K., Park, H. I., Nealsen, K. H., Kim, B. H. *J. Microbiol. Biotechnol.*, 2006, 16: 163.
- [20] Lovley, D. R. *Nat. Rev. Microbiol.*, 2006, 4:497.
- [21] Kim, B. H., Chang, I. S., Gadd, G. M. *Appl. Microbiol. Biotechnol.*, 2007, 76: 485.
- [22] Schörder, U. *Phys. Chem. Chem. Phys.*, 2007, 9: 2619.
- [23] Clauwaert, P., Van der Ha, D., Boon, N., Verbeke, K., Verhaege, M., Rabaey, K., Verstrate, W. *Environ. Sci. Technol.*, 2007, 41: 7564.
- [24] Logan, B. E., Cheng, S., Watson, V., Estadt, G. *Environ. Sci. Technol.*, 2007, 20: 567.
- [25] Li, Z., Yao, L., Kong, L., Liu, H. *Bioresource Technol.*, 2008, 99 :1650.
- [26] Park, D. H., Zeikus, J. G. *J. Bacteriol.*, 1999, 181: 2403.
- [27] Chaudhuri, S. K., Lovley, D. R. *Nat. Biotechnol.*, 2003, 21: 1229.
- [28] Rabaey, K., Lissens, G., Siciliano, S. D., Verstraete, W. *Biotechnol. Lett.*, 2003, 25: 1531.
- [29] Min, B., Cheng, S., Logan, B. E. *Water Res.*, 2005, 39: 1675.
- [30] Delaney, G. M., Bennetto, H. P., Mason, J. R., Roller, S. D., Stirling, J. L., Thurston, B. F. *J. Chem. Tech., Biotechnol.*, 1984, 34B: 13.
- [31] Rabaey, K., Clauwaert, P., Aelterman, P., Verstraete, W. *Environ. Sci. Technol.*, 2005, 39: 8077.
- [32] Kim, J. R., Jung, S. H., Regan, J. M., Logan, B. E. *Bioresour. Technol.*, 2007, 98: 2568.
- [33] He, Z., Wagner, N., Minteer, S. D., Angenent, L. T. *Environ. Sci. Technol.*, 2006, 40: 5212.
- [34] Aelterman, P., Rabaey, K., Pham, H. T., Boon, N., Verstraete, W. *Environ. Sci. Technol.*, 2006, 40: 3388.

- [35] Shin, S. H., Choi, Y., Na, S. H., Jung, S., Kim, S. *Bull. Korean Chem. Soc.*, 2006, 27: 281.
- [36] He, Z., Minteer, S. D., Angenent, L. T. *Environ. Sci. Technol.*, 2005, 39: 5262.
- [37] Yu, E. H., Cheng, S., Scott, K., Logan, B. J. *Power Sources*, 2007, 171: 275.
- [38] Logan, B. E., Murano, C., Scott, K., Gray, N. D., Head, I. M. *Water Res.*, 2005, 39: 942.
- [39] Schörder, U., Niebn, J., Scholz, F. *Angew. Chem. Int. Ed.*, 2003, 42: 2880.
- [40] Rosenbaum, M., Zhao, F., Schörder, U., Scholz, F. *Angew. Chem. Int. Ed.*, 2006, 45: 6658.
- [41] Rosenbaum, M., Zhao, F., Quaas, M., Wulff, H., Schörder, U., Scholz, F. *Appl. Catal. B Environ.*, 2007, 74: 261.
- [42] Qiao, Y., Li, C. M., Bao, S. J., Bao, Q. L. *J. Power Sources*, 2007, 170: 79.
- [43] Danilov, M. O., Melezhyk, A. V. *J. Power Sources*, 2006, 163: 376.
- [44] Jeng, K. T., Chien, C. C., Hsu, N. Y., Huang, W. M., Chiou, S. D., Lin, S. H. *J. Power Sources*, 2007, 164: 33.
- [45] An, G., Yu, P., Mao, L., Sun, Z., Liu, Z., Miao, S. *Carbon*, 2007, 45: 536.
- [46] Magrez, A., Kasas, S., Salicio, V., Pasquier, N., Seo, J. W., Celio, M. *Nano Lett.*, 2006, 6: 1121.
- [47] Wu, Z., Feng, W., Feng, Y., Qiang, Liu., Xu, X., Sekino, T. *Carbon*, 2007, 45: 1212.
- [48] Zou, Y., Xiang, C., Yang, L., Sun, L. X., Xu, F., Cao, Z. *J. Hydrogen Energy*, 2008, 33: 4856.
- [49] Freguia, S., Rabaey, K., Yuan, Z., Keller, J. *Environ. Sci. Technol.*, 2007, 41: 2915.
- [50] Rabaey, K., Boon, N., Hofte, M., Verstraete W. *Environ. Sci. Technol.*, 2005, 39: 3401.
- [51] Bullen, R. A., Arnot, T., Lakeman, J. B., Walsh, F. C. *Biosens. Bioelectron.*, 2006, 21: 2015.
- [52] Cheng, S., Liu, H., Logan, B. E. *Environ. Sci. Technol.*, 2006, 40: 364.
- [53] Freguia, S., Rabaey, K., Yuan, Z., Keller, J. *Electrochim. Acta*, 2007, 53: 598.
- [54] Park, D. H., Zeikus, J. G. *Appl. Microbiol. Biotechnol.*, 2002, 59: 58.
- [55] Ter Heijne, A., Hamelers, H. V. M., de Wilde, V., Rozendal, R. A., Buisman, C. J. N. *Environ. Sci. Technol.*, 2006, 40: 5200.
- [56] Rhoads, A., Beyenal, H., Lewandowski, Z. *Environ. Sci. Technol.*, 2005, 39: 4666.
- [57] Zhao, F., Harnisch, F., Schröder, U., Scholz, F., Bogdanoff, P., Herrmann, I. *Environ. Sci. Technol.*, 2006, 40: 5193.
- [58] He, Z., Angenent, L. T. *Electroanalysis*, 2006, 18: 2009.
- [59] Clauwaert, P., Rabaey, K., Aelterman, P., de Schampelaire, L., Pham, T. H., Boeckx, P., Boon, N., Verstraete, W. *Environ. Sci. Technol.*, 2007, 41: 3354.
- [60] Chen, G. W., Choi, S. J., Lee, T. H., Lee, G. Y., Cha, J. H., Kim, C. W. *Appl. Microbiol. Biotechnol.*, 2008, 79: 379.
- [61] Nguyen, T. A., Lu, Y., Yang, X., Shi, X. *Environ. Sci. Technol.*, 2007, 41:

- 7987.
- [62] Zhao, F., Harnisch, F., Schroder, U., Scholz, F., Bogdanoff, P., Herrmann, I. *Electrochem. Commun.*, 2005, 7: 1405.
- [63] Hao Yu, E., Cheng, S., Scott, K., Logan, B. J. *Power Sources*, 2007, 171: 275.
- [64] Bard, A. J., Faulkner, L. R. *Electrochemical methods: fundamentals and applications*. New York: Wiley, 1980.
- [65] Larminie, J., Dicks, A. *Fuel Cell Systems Explained*. New York: Wiley, 2003.
- [66] Park, D. H., Zeikus, J. G. *Biotechnol. Bioeng.*, 2003, 81: 348.
- [67] Park, D. H. *Biotechnol. Lett.*, 2000, (22): 1301.
- [68] Pham, T. H., Jang, J. K., Chang, I. S., Kim, B. H. *J. Microbiol. Biotechnol.*, 2004, 14: 324.
- [69] Min, B., Logan, B. E. *Environ. Sci. Technol.*, 2004, 38: 5809.
- [70] Oh, S. E., Logan, B. E. *Appl. Microbiol. Biotechnol.*, 2006, 70: 162.
- [71] Cheng, S., Liu, H., Logan, B. E. *Environ. Sci. Technol.*, 2006, 40: 2426.
- [72] Liu, H., Cheng, S., Logan, B. E. *Environ. Sci. Technol.*, 2005, 39: 5488.
- [73] Bond, D. R., Holmes, D. E., Tender, L. M., Lovley, D. R. *Sci.*, 2002, 295: 483.
- [74] Rabaey, K., Ossieur, W., Verhaege, M., Verstraete, W. *Water Sci. Technol.*, 2005, 52: 515.
- [75] Venkata Mohan, S., Saravanan, R., Raghavulu, S. V., Mohanakrishna, G., Sarma, P. N. *Bioresour. Technol.*, 2008, 99: 596.
- [76] Liu, H., Ramnarayanan, R., Logan, B. E. *Environ. Sci. Technol.*, 2004, 38: 2281.
- [77] Cheng, S., Liu, H., Logan, B. E. *Electrochem. Commun.*, 2006, 8: 489.
- [78] Cheng, S. A., Logan, B. E. *Electrochem. Commun.*, 2007, 9: 492.
- [79] Logan, B., Cheng, S. *Environ. Sci. Technol.*, 2007, 41: 3341.
- [80] Niessen, J., Schröder, U., Rosenbaum, M., Scholz, F. *Electrochem. Commun.*, 2004, 6: 571.
- [81] Qiao, Y., Bao S. J., Li, C. M., Cui, X. Q., Lu, Z. S., Bao, J. *ACS Nano.*, 2008, 2: 113.
- [82] Crittenden, S. R., Sund, C. J., Sumner, J. J. *Langmuir*, 2006, 22: 9473.
- [83] Adachi, M., Shimomura, T., Komatsu, M., Yakuwa, H., Miya, A. *Chem. Commun.*, 2008, 7: 2055.
- [84] Torres, C. I., Kato Marcus, A., Rittmann, B. E. *Biotechnol. Bioeng.*, 2008, 100: 872.
- [85] Rozendal, R. A., Hamelers, H. V. M., Buisman, C. J. N. *Environ. Sci. Technol.*, 2006, 40: 5206.
- [86] Bond, D. R., Lovley, D. R. *Appl. Environ. Microbiol.*, 2003, 69: 1548.
- [87] Reguera, G., McCarthy, K. D., Mehta, T., Nicoll, J. S., Tuominen, M. T., Lovley, D. R. *Nature*, 2005, 435: 1098.
- [88] Rabaey, K., Boon, N., Siciliano, S. D., Verhaege, M., Verstraete, W. *Appl. Environ. Microbiol.*, 2004, 70: 5373.
- [89] Kim, B. H., Park, H. S., Kim, H. J., Kim, G. T., Chang, I. S., Lee, J. *Appl.*

- Microbiol. Biotechnol., 2004, 3: 672.
- [90] Pham, C. A., Jung, S. J., Phung, N. T., Lee, J., Chang, I. S., Kim, B. H. FEMS Microbiol. Lett., 2003, 223: 129.
- [91] eropoulos, I.A., Greenman, J., Melhuish, C., Hart, J. Enzyme Microb. Tech., 2005, 37: 238.
- [92] Vega, C. A., Fernandez, I. Bioelectrochem. Bioenerg., 1987, 17: 217.
- [93] Grzebyk, M., Pozniak, G. Sep. Purif. Technol., 2005, 41: 321.
- [94] Lee, S. A., Choi, Y., Jung, S., Kim, S. Bioelectrochemistry, 2002, 57: 173.
- [95] Ringeisen, B. R., Henderson, E., Wu, P. K., Pietron, J., Ray, R., Little, B. Environ. Sci. Technol., 2006, 40: 2629.
- [96] Kim, B. H., Kim, H. J., Hyun, M. S., Park, D. H. J. Microbiol. Biotechnol., 1999, 9: 127.
- [97] Nevin, K. P., Lovley, D. R. Appl. Environ. Microbiol., 2002, 68: 2294.
- [98] McKinlay, J. B., Zeikus, J. G. Appl. Environ. Microbiol., 2004, 70: 3467.
- [99] Hernandez, M. E., Newman, D. K. Mol. Life Sci., 2001, 58: 1562.
- [100] Cooney, M. J., Roschi, E., Marison, I. W., Comninellis, C., Stockar, U. Enzyme Microb. Technol., 1996, 18: 358.
- [101] Park, H. S., Kim, B. H., Kim, H. S., Kim, H. J., Kim, G. T., Kim, M., Chang, I. S. Anaerobe, 2001, 7: 297.
- [102] Lovley, D. R., Holmes, D. E., Nevin, K. P. Adv. Microb. Physiol., 2004, 49: 219.
- [103] Vargas, M., Kashefi, K., Blunt-Harris, E. L., Lovley, D. R. Nature, 1998, 395: 65.
- [104] Chia, M. A Miniaturized Microbial Fuel Cell, Technical Digest of Solid State Sensors and Actuators Workshop: Hilton Head Island, 2002, p 59.
- [105] Rozendal, R. A., Hamelers, H. V. M., Molenkmp, R. J., Buisman, J. N. Water Res., 2007, 41: 1984.
- [106] Liu, H., Grot, S., Logan, B. E. Environ. Sci. Technol., 2005, 39: 4317.
- [107] Cheng, S., Logan, B. E. Proc. Natl. Acad. Sci. U. S. A., 2007, 104: 18871.
- [108] Nath, K., Das, D. Current Sci., 2003, 85: 265.
- [109] Holzman, D. C. Environ. Health Persp., 2005, 113: A754.
- [110] Reimers, C. E., Tender, L. M., Fertig, S., Wang, W. Environ. Sci. Technol., 2001, 35: 192.
- [111] Tender, L. M., Reimers, C. E., Stecher, H. A., Holmes, D. E., Bond, D. R., Low, D. A., Piblobello, K., Fertig, S., Lovley, D. R. Nat. Biotechnol., 2002, 20: 821.
- [112] Chang, I. S., Moon, H., Jang, J. K., Kim, B. H. Biosens. Bioelectron., 2005, 20: 1856.
- [113] Chang, I. S., Jang, J. K., Gil, G. C., Kim, M., Kim, H. J., Cho, B. W. Biosens. Bioelectron., 2004, 19: 607.
- [114] Kim, B. H., Chang, I. S., Gil, G. C., Park, H. S., Kim, H. J. Biotechnol. Lett., 2003, 25: 541.





---

## Index

(3aminopropyl)trimethoxysilane, 184, 186, 187  
(*R, R*)-binaphehyl diamine, 49  
1,5-dioxpan-2-one (DXO), 43  
2,2'-bis (trifluoromethyl)-4,4'-diaminobiphenyl (TFDB), 19  
2,2'-bis-(3,4-dicarboxyphenyl) hexafluoropropane dianhydride (6FDA), 19  
2,4,6-trimethyl-2,4,6-trivinylcyclosilazane(VSZ) 106  
2-thiopyridone, 189  
3,3', 4,4'-biphenyltetracarboxylic anhydride (BPDA)-phenylenediamine (PDA), 20  
3,3'-4,4'biphenyl tetracarboxylic dianhydride (BPDA)-4,4'-oxydianiline(ODA), 21  
3-aminopropyltriethoxysilane (3-APS), 21  
4-pyrrolidinopyridine, 55

### A

acrylonitrile-butadiene-styrene (ABS) terpolymer, 1  
activated monomer cationic polymerization, 45  
adamantane (tricycle [3.3.3.1.1.<sup>3,7</sup>] decane), 10  
AHPCS, 45  
Al metal filler, 122  
Al-B-N nanocomposite, 151

AlCl<sub>3</sub>, 78, 121, 122, 124, 151  
Al-Cr-phosphate, 125  
aliphatic polyimides, 4, 10-14, 31  
aliphatic polyimidosiloxanes, 12, 13  
allyhydridopolycarbosilane, 145  
AlN phase, 121-123  
 $\alpha$ -MoSi<sub>2</sub> phase, 114  
 $\alpha$ -SiC ceramics, 113  
aluminum alkoxides, 49  
aluminum isopropoxide, 49  
aluminum-Salen complex, 50  
amplitude, 169  
anionic ROP, 45, 46  
anodization, 158, 160-163, 175, 186  
antitumor, 91  
aramid fibres, 1  
arginine metabolism, 158  
amorphous BN phase, 119  
amorphous phase, 121, 125  
amorphous preceramic network, 109  
aromatic polyimides, 2, 4, 9, 17, 31  
autoclave, 124, 125  
Avidin, 184, 188, 190

### B

back-biting chain transfers, 48  
back-biting process, 92  
band pass filters, 183  
batteries, 70, 91, 214  
 $\beta$ -MoSi<sub>2</sub> phase, 114  
biocatalyst, 212, 215  
biodegradable material, 195, 214  
biodegradable, 37-42, 60, 195, 214

biogenic guanidines, 58  
biohydrogen, 214  
biological sensors, 143, 158, 174, 183  
biomass, 205, 206, 210, 214  
bio-resorbable surgical sutures, 61  
biosensor, 215  
biotin tetrafluorophenyl ester, 184  
BN film, 137, 139  
BN ceramic composites, 76, 90  
BN precursor oligomers, 131  
BN/TiN/TiB<sub>2</sub> composite, 118, 119  
bone screws, 61  
Borazine, 89, 90, 105, 137  
boron nitride-like material, 131  
BPDA-ODA PI, 22  
Bruggeman, 164  
buffer, 19, 137, 139, 188, 190, 209

## C

capability, 19, 173, 174, 210  
Capillary condensation, 176  
Carbon cloth, 203  
Carbon nanotube, 202  
carbon paper, 201-103  
carbonization, 143  
carbothermal reduction, 121, 144, 147  
cationic ROP, 44, 45  
ceramic line patterns, 148  
ceramic microstructures, 148  
ceramic phase, 108  
Ceramic yield, 104  
ceramics, 75, 89, 148  
CH<sub>2</sub>(SiH<sub>3</sub>)<sub>2</sub>, 78, 79  
chain-extension technique, 41  
charge transfer (CT), 5  
chemical reactors, 183  
chemical sensors, 180  
chemical warfare agents(CWA), 173  
Child law, 18  
coefficient of thermal expansion (CTE), 8  
composite, 24, 31, 111, 128  
composite waveform, 171, 175, 189  
controlled cationic ROP, 45  
coordination-insertion ROP, 47

copolymer, 24, 50, 81, 85, 88, 106  
core-shell quantum dot, 171  
coulombic efficiency, 201, 215  
Cp<sub>2</sub>TiMe<sub>2</sub>, 77  
Cp<sub>2</sub>ZrCl<sub>2</sub>, 69, 70, 80, 83, 88  
Cp<sub>2</sub>ZrMe<sub>2</sub>, 84  
crack-free ceramic microchannel, 49  
creatine, 58  
creatinine, 58  
cross-linking reaction, 121  
crosslinking, 25, 76, 81, 82, 90  
cross-polycondensation, 39  
crystalline ceramic, 108  
crystallization, 40, 114, 125, 128, 129  
current density, 160, 168-169, 208  
CVD process, 89, 151  
cyclic boron hydride, 150  
cyclic oligosilane, 68

## D

D, L-lactide (DLLA), 42  
Dehydrocatenation, 67, 70, 74, 75, 77  
dehydrocoupling, 69, 70, 75, 80, 113  
dehydrogenation, 105  
dehydrolytic condensation, 127, 128  
dehydropolymerization, 74, 84, 88, 89  
dehydrosilylation, 105  
diamine, 4, 8, 12-14, 17, 28, 49  
dianhydride 4, 12-14, 18, 19  
dibenzylsilane, 79  
dichlorometallocene, 69, 70  
dichloromethylsilane, 112  
dielectric constant, 5, 8, 15, 31, 164  
diethylchlorophosphate (DCP), 173  
diethylethylphosphonate (DEEP), 173  
dihydroxysilole, 184  
diisocyanates, 42  
dimensional stability, 2, 23, 118  
dimethylmethylphosphonate (DMMP), 173  
dimethyltitanocene, 67  
dimethylzirconocene, 67  
disilanes, 78, 83  
distributed Bragg reflector, 168, 174  
dithiothreitol(DTT), 189

D-lactide (DLA), 42  
 DMAP, 155  
 dopant, 162, 163  
 dry gas-phase processes, 117

**E**

elastomeric character, 91  
 electrical conductivity, 19, 117, 151  
 electrical energy, 195, 201  
 electrically conducting, 105, 112  
 Electricity generation, 214  
 Electrochemical etching, 174  
 electrochemically active bacteria, 196, 210  
 Electroluminescent, 71  
 electrolyte, 160, 165, 196, 198, 206  
 Electron transfer, 210  
 electroredox, 65  
 ellipsometer, 163  
 encoding, 158, 172, 173  
 enzymes, 42, 174, 183  
 Enzyme-catalyzed polcondensations, 42  
 Enzyme-catalyzed ROP, 60  
 epimerization, 55  
 evanescent wave devices, 183  
 excited state, 186  
 exothermic phenomenon, 121  
 exothermic reaction, 113

**F**

Fabry-Pérot fringe, 164  
 Fe(II)-alkoxide complex, 46  
 ferricyanide, 197, 200, 212  
 flat panel displays (FPDs), 19  
 flexible substrates, 19, 31  
 fluorescence, 20, 171  
 foam-like porous ceramic structure, 119, 151  
 Food and Drug Administration (FDA), 24  
 four-center transition states, 68, 83  
 frequency, 169, 172  
 fuel cell, 92, 195  
 full isolated porous oxidized silicon (FIPOS), 157

full-width at half maximum, 175

**G**

Galvanostatic, 174  
 GC/MS, 78  
*Geobacter*, 210, 213  
 glycolide (GA), 42  
 GPC, 14, 68, 72, 84  
 graphite felt, 199, 207, 208  
 graphite granules, 198  
 graphite, 7, 103, 198, 205, 208, 212  
 grating couplers, 183  
 Grignard reagent, 71  
 ground state, 86  
 guanidine, 58, 59, 61

**H**

hafnium, 77  
 hardening chemistry, 125  
 heterotactic polylactide, 50  
 hexabutyl guanidinium acetate, 59  
 (hexagonal) phase, 114  
 high density polyethylene (HDPE), 2  
 high performance polymers, 1, 2, 31  
 high temperature micro-reactor, 149, 152  
 H NMR, 45, 53, 54, 58, 68, 77, 107  
 hollow spheres, 122, 143  
 homodehydrocoupling, 89  
 homogeneity, 166, 169  
 hybrid precursor, 118, 119, 151  
 hydroborated aliphatic carbon, 108  
 hydroboration, 106-108, 110, 150  
 hydrofluoric acid, 23, 157-162, 183  
 hydrogermation, 88  
 hydrophilicity, 37, 182  
 hydrophobic, 24, 91, 182  
 hydrophobicity, 182  
 hydrosilane, 67, 75, 86, 88  
 hydrosilapolymerization, 85-88  
 hydrosilation, 85, 87, 88  
 hydrosilylation, 85, 166, 167  
 hydrostannation, 88  
 hyperbranched polysilane, 81, 82

**I**

Inorganic hydride, 68, 78  
inorganic polymer, 67  
interference filters, 168  
intermetallic phase, 119  
intermolecular transesterifications, 48  
intramolecular transesterification, 47  
isocyanates, 78  
isotactic stereoblock polylactide, 51

**K**

Kapton<sup>®</sup>, 3, 5  
Kevlar, 28, 29

**L**

lactams, 78  
lactide (LA), 38  
lactones, 38, 42, 60  
LCt<sub>50</sub>, 174  
lethality, 178  
lime sulfur, 25  
lipase CA, 60  
Lipase PS, 60  
lipase, 42  
liquid crystal display (LCD), 17  
living ROP, 47, 55  
L-lactide (LLA), 42  
low density polyethylene (LDPE), 2  
Low temperature curable binder, 124

**M**

macropore, 141  
mass transfer, 204, 212  
mediator, 91, 197, 200, 205, 208  
medical devices, 24  
medical diagnostics, 183  
melt/solid polycondensation, 40  
membranes, 9, 24, 209  
MEMS device, 147  
MeSiH<sub>3</sub>, 78  
*meso*-lactide, 50  
mesoporous BN, 146  
mesoporous materials, 141  
mesoporous SiC, 144-146, 151

metabolism, 54, 55, 58, 196, 212  
metal oxides, 174, 205, 213  
metallocene, 67-70, 77, 83  
methyl trifluoromethane sulfonate  
(MeOTf), 44  
microbe, 206, 210  
microchannel, 149  
microorganisms, 195, 196, 204, 213  
micropores, 141, 145, 184  
mold transfer technique, 148  
morpholinediones, 38, 42  
morphology, 21, 50, 141, 174, 184

**N**

Nafion, 197, 198, 203, 206, 209  
nanocomposites 118, 119, 151  
nanohybrids, 31  
nanoparticle, 89  
nanowires, 197, 210  
natural rubber, 25  
near net shape processing techniques,  
105, 141  
nerve agent mimics, 173, 178, 190  
net shape processing techniques, 105,  
141  
N-heterocyclic carbene (NHC), 56  
NMR spectroscopy, 13, 46, 72, 76, 77,  
108  
non-oxide ceramics, 75, 89, 103, 120  
non-toxic metal, 38  
*N*-selectride, 69, 72, 81, 82  
nylon, 28  
nylon 6, 38

**O**

OLED, 17, 19, 67, 70  
olefins, 78, 85  
oligocarbosilane, 76  
oligomer, 40, 41, 69, 77, 80, 84, 132  
oligosilanes, 68, 79, 80  
one-pot, 11, 74, 75  
ordered assembly, 143  
organic dye, 171  
Organic Light-Emitting Devices  
(OLEDs), 17

organosilazane, 105, 150  
 overpotential, 202, 204, 205  
 oxidation resistance, 111, 130, 141, 151

## P

P(DLLA-GA), 38  
 passivation, 4, 9, 17, 18, 165  
 PDMS, 75, 148, 149  
 periodic squarewave, 175, 178  
 phenylsilene, 81  
 PhGeH<sub>3</sub>, 77  
 phosphate buffer solution (PBS), 188  
 photodiode, 168  
 photoelectronics, 67  
 photogeneration, 175  
 photoluminescence, 164, 180, 182, 184, 186  
 photoluminescent, 71, 72  
 photonic crystals, 174  
 photopolymerization, 86-88, 148  
 photoresist, 31  
 photoresistors, 67  
 photosensitive polyimide (PSPI), 18  
 plastic substrate, 17  
 platinum wire, 160  
 P-MAS-NMR, 129  
 polarization, 159, 204, 207  
 poly (butylene terephthalate) (PBT), 2, 22  
 poly (ethylene terephthalate) (PET), 2  
 poly (vinyl chloride) (PVC), 2  
 Poly(4,4'-oxydiphenylene pyromellitimide) (PMDA-ODA PI), 3  
 Poly(alkoxysilane)s, 74  
 poly(amic acid)(PAA), 11  
 poly(amide-imide)s, 1  
 poly(chlorophenylsilane), 70  
 poly(dioxanone) (PDO), 38  
 poly(hydrosilane)s, 67, 76, 87, 88, 89, 90  
 poly(L-lactide) (PLLA), 40  
 poly(methyl methacrylate) (PMMA), 2

Poly[*N,N'*-diphenyl-*N,N'*-bis (4-aminobiphenyl)-(1,1'-biphenyl)-4,4'-diamine pyromellitimide] (PMDA-DBABBD PI), 18  
 polyacetal, 1  
 polyamic acid silyl ester (PASE), 12  
 polyamide (PA), 2  
 polybenzimidazoles, 1  
 Polyborazine, 89, 104, 137  
 polycarbonate (PC), 2  
 polycarbosilane, 75, 103, 111, 138, 145  
 polychloroprene, 25  
 polycondensation, 38-43, 112  
 polydispersity index (PDI), 14, 40, 72  
 polyetheretherketon (PEEK), 2, 22  
 Polyethersulfone (PES), 24  
 Polyethylene, 1, 2  
 polygermanes, 66, 67, 77, 83, 93  
 polygermole, 71, 73  
 polyglycolic acid (PGA), 37  
 Polyimides, 3, 8, 9, 16  
 polyisoprene, 25  
 polylactic acid (PLA), 37  
 polymeric phase, 106, 108  
 Polymethylsilane, 111, 141, 147, 151  
 polynorbornene (PNB), 22  
 polyoxymethylene (POM), 2  
 polyphenylene oxide, 29  
 polyphenylsilanes, 68, 69, 92  
 Polyphosphazenes, 91, 92  
 Polypropylene, 1  
 Polysilanes, 67, 70  
 polysiloxanes, 66, 74, 91, 103  
 polystannanes, 66, 67, 77, 83, 84, 93  
 polysulfides, 25  
 polysulphones, 1  
 polytetrafluoroethylene (PTFE), 7, 203  
 polyvinylsilsequioxane (PVSSQ), 21  
 pore diameter, 162, 163  
 pore size distribution, 140, 141, 146  
 Porosity, 163  
 porous silica materials, 141, 145  
 Porous silicon (PSi), 157, 158, 164

- post-polycondensation, 40  
 Potassium methoxide, 45  
 Power density, 212  
 preceramic polymer, 89, 111, 121, 145, 148, 149  
 precursor, 18, 20, 67, 75, 76, 91, 105, 113  
 prosthetics, 61  
 pseudo poly(amino acid)s, 39  
 Pt/Ru alloy nanoparticles, 147  
*p*-toluene sulfonic acid (TSA), 40  
 PVS, 76  
 Pyrolysis, 111
- Q**
- quenching, 180, 182
- R**
- rac*-LA, 42, 51, 56  
 Red-Al, 52, 53  
 reduced shrinkage, 118  
 Reflection, 176  
 reflectivity, 92, 164, 168-170, 172, 174, 176  
 refractive index, 15, 27, 162, 164  
 refractive indices, 15, 169, 188, 190  
 renewable energy, 195, 196  
 Resistance, 8  
 resistivity, 162, 163, 174  
 rhodium complex, 74  
 ring-opening metathesis polymerization (ROMP), 30  
 ring-opening polymerization (ROP), 38, 42  
 roughness, 138, 169  
 Rugate, 169, 171, 174
- S**
- sacrificial carbon templates, 144  
 Salen ligand, 49  
 sarin, 174, 178  
 sc-PLA, 51  
 selected area electron diffraction (SAED), 115  
 Selectrides, 68, 72  
 self-polycondensation, 39  
 self-reinforced (SR), 38  
 semi-aromatic polyimides, 4  
 semi-conducting polyimides, 17  
*Shewanella*, 208, 210, 215  
 shock-sensitive, 92  
 $\text{Si}_3\text{N}_4$ , 89, 111, 150  
 Si-C bond, 79  
 SiC ceramics, 76, 85, 103, 111, 145, 146  
 SiC crystallite, 145  
 SiC macroporous, 141  
 SiC porous monoliths, 149  
 SiC tubes, 147  
 SiC/MoSi<sub>2</sub> composite, 111, 114, 151  
 Si-C-B-N, 105, 150  
 SiCN ceramic sphere, 143  
 sigma-bond, 68, 73, 81, 83  
 Si-H bond, 73, 85  
 $\text{SiH}_4$ , 78, 79, 81  
 silazane ring, 110  
 silica, 15, 20, 27, 141, 145  
 SILICONIT<sup>®</sup>, 117  
 silicon-on-insulator (SOI), 157  
 Si NMR, 109, 110  
 smart particle, 184, 186  
 $\text{SnCl}_2 \cdot 2\text{H}_2\text{O}$ , 40  
 softlithography, 141, 147-149  
 sol-gel reaction, 20, 75  
 solid state reaction, 119, 121  
 solid-state post-polycondensation, 40  
 soluble polymeric precursor, 105  
 soman, 174  
 space charge limited current (SCLC) regime, 18  
 SR-PLLA, 38  
 stannous 2-ethylhexanoate, 47  
 stannous octoate, 47  
 stereocomplex of PLLA-PDLA, 51  
 stereospecific ROP, 42, 58  
 stoichiometric SiC precursors, 111  
 Streptavidin, 183, 188, 190  
 Substitution reaction, 91, 147  
 super-hydride, 68, 69, 72  
 surface acoustic wave (SAW), 174

Surface area, 143  
Surfacederivatization, 186  
syndiotactic polylactide, 150

## T

tailored porous SiC and SiCN  
microchannels, 149  
Teflon cell, 160, 183  
Tetragonal phase, 114  
TGA, 76, 80, 81, 82, 86, 112  
THF, 46, 70, 78, 118, 138  
thickness, 9, 116, 132, 138, 162  
three-step polycondensation, 40  
Ti-B-N composite, 104, 117  
Titania, 20, 22  
*trans*-4-hydroxy-L-proline, 39  
transesterification, 44, 47-49, 54, 55  
transmission, 19, 27, 103, 164, 168  
tribenzylsilane, 79  
triethoxyphenylsilane, 74  
triethylphosphate (TEP), 173  
trifluoromethane sulfonic acid  
(HOTf), 44  
Tungstenhalogen lamp, 164, 174, 178,  
186

## U

Ultem, 5  
ultra high molecular weight  
polyethylene (UHMWPE), 2

ultrasonication, 184  
UV photoinduction, 167  
UV-vis spectrum, 71

## V

voltage, 200

## W

wastewater treatment, 199, 214  
waveguides, 168  
weight loss, 16, 112, 118, 136  
wood ceramic, 141  
Wurtz-type coupling, 66, 67

## Z

Zeigler-Natta catalyst, 1  
zeolite, 76  
zinc acetate dihydrate, 40  
zirconium, 77  
ZSM-5, 76  
zwitterionic structure, 69  
 $\alpha$ -hydroxyacid, 39  
 $\beta$ -butyrolactone ( $\beta$ -BL), 43  
 $\beta$ -diketiminatate ligands, 54  
 $\beta$ -propiolactone ( $\beta$ -PL), 42  
 $\gamma$ -butyrolactone ( $\gamma$ -BL), 42  
 $\delta$ -valerolactone ( $\delta$ -VL), 43  
 $\omega$ -caprolactone ( $\omega$ -CL), 43